University of Arkansas, Fayetteville
ScholarWorks@UARK

Theses and Dissertations

12-2018

GeSn Thin Film Epitaxy and Quantum Wells for Optoelectronic Devices

Perry Christian Grant
University of Arkansas, Fayetteville

Follow this and additional works at: https://scholarworks.uark.edu/etd

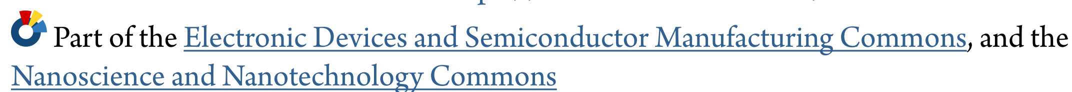
Part of the Electronic Devices and Semiconductor Manufacturing Commons, and the Nanoscience and Nanotechnology Commons

Recommended Citation
Grant, Perry Christian, "GeSn Thin Film Epitaxy and Quantum Wells for Optoelectronic Devices" (2018). *Theses and Dissertations*. 3096.
https://scholarworks.uark.edu/etd/3096

This Dissertation is brought to you for free and open access by ScholarWorks@UARK. It has been accepted for inclusion in Theses and Dissertations by an authorized administrator of ScholarWorks@UARK. For more information, please contact scholar@uark.edu, ccmiddle@uark.edu.

GeSn Thin Film Epitaxy and Quantum Wells for Optoelectronic Devices

A dissertation submitted in partial fulfillment
of the requirements for the degree of
Doctor of Philosophy in Microelectronics-Photonics

by

Perry C. Grant
Southern Arkansas University
Bachelor of Science in Engineering Physics, 2011
University of Arkansas
Master of Science in Microelectronics-Photonics, 2013

December 2018
University of Arkansas

This dissertation is approved for recommendation to the Graduate Council.

Shui-Qing Yu, Ph.D.
Dissertation Director

Hameed Naseem, Ph.D.
Committee member

Gregory Salamo, Ph.D.
Committee member

Madga O. El-Shenawee, Ph.D.
Committee member

Rick Wise, Ph.D.
Ex-Officio Member

The following signatories attest that all software used in this dissertation was legally licensed for use by Perry Grant for research purposes and publication.

___________________________________ ___________________________________

Perry C. Grant, Student Dr. Shui-Qing Yu, Dissertation Director

This dissertation was submitted to http://www.turnitin.com for plagiarism review by the TurnItIn company's software. The signatories have examined the report on this thesis that was returned by TurnItIn and attest that, in their opinion, the items highlighted by the software are incidental to common usage and are not plagiarized material.

___________________________________ ___________________________________

Dr. Rick Wise, Program Director Dr. Shui-Qing Yu, Dissertation Director

Abstract

Group IV photonics is an effort to generate viable infrared optoelectronic devices using group IV materials. Si-based optoelectronics have received monumental research since Si is the heart of the electronics industry propelling our data driven world. Silicon however, is an indirect material whose optical characteristics are poor compared to other III-IV semiconductors that make up the optoelectronics industry. There have been major efforts to integrate III-V materials onto Si substrates. Great progress on the integration of these III-V materials has occurred but incompatibility with CMOS processing has presented great difficulty in this process becoming a viable and cost-effective solution. Germanium has also been studied and shown to produce direct bandgaps through tensile strain but have limited wavelength coverage. Research into group IV photonics has produced Sn-based materials which have shown promise in achieving efficient infrared optoelectronic devices on Si substrates. The GeSn material has already shown to be direct bandgap with a number of optically active devices already demonstrated.

The work presented in this dissertation was focused on the development of ultra-high vacuum chemical vapor deposition of epitaxially grown high optical quality GeSn material. Low temperature Ge and dilute GeSn films were grown directly on Si. Development of Ge buffers on Si for high optical quality GeSn was also accomplished. Growth of GeSn on Ge buffers started under a Sn over-pressure condition. Reduction of the $SnCl_4$ molar flow fraction led to high quality optical material. Material and optical characterization were carried out using x-ray diffraction, transmission electron microscopy, photoluminescence and other methods to determine the Sn composition and optical and material qualites.

Additionally, GeSn and SiGeSn barriered GeSn quantum wells grown using a commercial reduced pressure chemical vapor deposition chamber were characterized. The

structures were grown on Ge and GeSn buffered Si with up to 9.5% Sn in the buffer. The bandstructure was simulated and compared against optical characterization to verify the simulation results and estimate the carrier confinement in the structures. Increasing the Sn in the GeSn buffer puts more Sn in the well, and wide wells provide enhanced confinement, suggesting a route toward efficient mid-infrared emitters.

Acknowledgement

I would to thank my advisor, Dr. Shui-Qing (Fisher) Yu, for his unending support in completion of this dissertation. His continuous encouragement and thought-provoking discussions have truly helped me become a better researcher. His drive, enthusiasm, and imagination are inspirational. I could not imagine having had any other advisor see me through this work. I would like to thank Dr. Baohua Li, President of Arktonics LLC., for the opportunity to perform this research in support of the company goals. I would like to thank Dr. Wei Du for his help with paper writing. His help with wording and figure building truly helped with the writing process. I would like to thank Dr. Hameed Naseem for his unique support of the research and Dr. Salamo for the opportunity to work in his lab and learn the ultra-high vacuum equipment, upkeep, and maintenance procedures. This experience was invaluable on upkeeping of the ultra-high vacuum chemical vapor deposition system used to complete this research. I would like to thank Dr. El-Shenawee and Dr. Wise for being on the dissertation committee as well. All members of the committee are instrumental in their suggestions to make this a better work. I would like to thank Mr. Ken Vickers who recruited me to the microelectronics-photonics program and taught me much about management and how research becomes the next product on the market. I would like to thank Mr. David Monk who taught me the skills to work on ultra-high vacuum systems that I will employ throughout my career. I would like to thank Dr. Aboozar Mosleh for teaching me the operation of the UHV-CVD used to complete the growth part of this research. I would like to thank Dr. Seyed Amir Ghetmiri whose instruction on the optical characterization techniques and setups was used for this research. I would like to thank the Institute for Nanoscience and Engineering for use of the characterization tools as well as Dr. Andrian Kuchuk for the quantum well simulations. Special thanks go to Dr. Mourad Benemara

for his upkeep and imaging with the transmission electron microscope.

Finally, I would like to thank all the lab members that shared information, helped with measurements, went through group meetings, and shared in genuine joy of seeing positive results from our work. I am especially thankful for the growth team members who dealt with me over the years and worked very hard to keep up with the pace we operated at.

This work was funded in part by the Air Force Office of Scientific Research (AFOSR) # FA9550-16-C-0016, Air Force Office of Scientific Research (AFSOR) # FA9550-14-1-0205, the National Aeronautics and Space Administration Established Program to Stimulate Competitive Research (NASA EPSCoR) # NNX15AN18A, and the National Science Foundation (NSF) #DMR-1149605. Any opinions, findings, and conclusions or recommendations expressed in this material are those of the author and do not necessarily reflect the views of the Air Force, NASA, or NSF. Research was performed through the use of the High-Density Electronics Center at the University of Arkansas to grow samples as well as ASM America Inc. where quantum wells were deposited with their CVD reactors in a collaborative effort for this research.

Last but not least, I would like to thank those who are closest to me. My dad and Ms. Judy, and my brother as their support has made this effort possible. They have always been an ear to vent to when stress was high and pat on the back when it all works out. I also would like to thank Dr. Abdel Bachri from Southern Arkansas University who showed me I had the ability to complete a dream I never thought possible. Thanks to all my friends for the amazingly fun times we have had and while we may separate in the future, we will always be close.

Dedication

To my dad, for his guidance to always do more, to my brother as a push to further his own successes, and to my son as an inspiration on how far you can go with dedication and hard work.

Table of Contents

Chapter 1 Introduction/Background 1

1.1 Motivation 1

1.1.1 Group IV Epitaxy 2

1.1.2 SiGeSn for Infrared Optoelectronics 2

1.1.3 Bandgap Engineering 4

1.1.4 Commercial Integration 4

1.2 Scope of Dissertation 5

1.2.1 Ultra-High Vacuum Chemical Vapor Deposition Growth 5

1.2.2 Quantum Well Characterization 5

1.3 Semiconducting Sn and GeSn alloys 6

1.3.1 Semiconducting Alpha-Sn 6

1.3.2 GeSn Alloy: The Potential Realized 8

1.4 GeSn Quantum Wells 11

1.5 Summary 12

Chapter 2 UHV-PE-CVD System and Thin Film Characterizations 13

2.1 Vacuum System 13

2.2 Unique System Capabilities 14

2.2.1 Plasma Enhancement 15

2.2.2 Hotwire Enhancement 15

2.2.3 Gas Mixing and Delivery 15

2.3 Thin Film Characterizations 17

2.3.1 Ellipsometry 17

2.3.2 Raman Spectroscopy 18

2.3.3 Photoluminescence 20

2.3.4 X-ray Diffraction 21

2.3.5 Transmission Electron Microscopy 22

Chapter 3 UHV-CVD Growth on Si substrate 23

3.1 A Comparison Study of the Low Temperature Growth of Dilute GeSn and Ge 23

3.1.1 Growth and Characterization of Dilute Sn Films 24

3.1.2 Dilute GeSn Material and Optical Properties 26

3.1.3 Exothermic Reaction During the Growth of GeSn Using $SnCl_4$ 31

3.1.4 Summary and Conclusion 31

3.2 Ge Buffers on Si Substrate 32

3.2.1 Limiting Factor of Strain on Incorporation 32

3.2.2 LT/HT Growth Method 33

3.2.3 Optical/Material Characterizations 34

3.2.4 UHV-CVD Grown Buffers on Si for GeSn Growth 38

3.3 Plasma Enhanced Growth of GeSn on Si substrate 38

3.3.1 Plasma Enhancement 38

3.3.2 Results/Discussion 39

3.3.3 Plasma Enhanced Growth of GeSn near 5% Sn on Si 42

3.4 Summary 42

Chapter 4 UHV-CVD Growth of GeSn on Ge Buffers 44

4.1 GeSn on Ge Buffered Si substrate 44

4.2 Growth Method 45

4.3 Growth Temperature Dependence with $SnCl_4$ Overpressure 47

4.4 Growth Optimization 50

4.5 UHV-CVD Growth of GeSn up to 10% Sn 56

4.6 Comparisons to Commercial Grown Material 58

4.7 GeSn Photoconductors 61

4.8 Discussion on Growth Technology and Precursors 63

4.9 Summary 65

Chapter 5 GeSn/GeSn Quantum Wells 66

5.1 Direct Bandgap Type I GeSn/GeSn SQW on Ge Buffered Si Substrate 66

5.1.1 Growth and Material Characterization 66

5.1.2 Band Structure Calculation 69

5.1.3 Photoluminescence Characterization 70

5.1.4 Interlayer Formation 73

5.1.5 Conclusion 75

5.2 GeSn/GeSn DQW with Increased Sn% in the Buffer 75

5.2.1 Experimental Details 77

5.2.2 Results and Discussion 79

5.2.3 Band Structure and Optical Transition Analysis 82

5.2.4 Photoluminescence Spectra Analysis 85

5.2.5 Conclusion 91

5.3 Summary 92

Chapter 6 SiGeSn/GeSn Quantum Wells 93

6.1 Introduction 93

6.2 Experimental Details 94

6.2.1 Material Growth and Calculations 94

6.2.2 Band Structure Calculation 95

6.2.3 Photoluminescence Study 95

6.3 Single Quantum Wells (SQW) 96

6.3.1 Material Characterizations 96

6.3.2 Band Structure and Optical Transition Analysis 101

6.3.3 Photoluminescence Spectra Analysis 106

6.3.4 Conclusion 109

6.4 Double Quantum Wells (DQW) 110

6.4.1 Material Characterizations 110

6.4.2 Band Structure and Optical Transition Analysis 113

6.4.3 Photoluminescence Spectra Analysis 115

6.4.4 Conclusion 116

6.5 Multiple Quantum Wells 4x (MQW) 117

6.5.1 Material Characterizations 117

6.5.2 Band Structure and Optical Transition Analysis 121

6.5.3 Photoluminescence Spectra Analysis 122

6.5.4 Conclusion 123

6.6 Summary 124

Chapter 7 Dissertation Summary, Conclusion, and Future Work 125

7.1 Summary 125

7.2 Conclusion 128

7.3 Future work 129

7.3.1 Ex-situ Gas Mixing 129

7.3.2 GeSn on Ge substrate 129

7.3.3 Plasma Enhanced GeSn on Ge Buffered Si substrate 130

7.3.4 Growth of SiGeSn 130

References 131

Appendix A: Description of Research for Popular Publication 154

Appendix B: Executive Summary of Newly Created Intellectual Property 157

Appendix C: Potential Patent and Commercialization Aspects of Listed Intellectual 158

C. 1 Patentability of Intellectual Property (Could Each Item be Patented) 158

C. 2 Commercialization Prospects (Should Each Item Be Patented) 158

C. 3 Possible Prior Disclosure of IP 158

Appendix D: Broader Impact of Research 158

D. 1 Applicability of Research Methods to Other Problems 159

D. 2 Impact of Research Results on U.S. and Global Society 159

D. 3 Impact of Research Results on the Environment 160

Appendix E: Microsoft Project for MS MicroEP Degree Plan 161

Appendix F: Identification of All Software Used in Research and Dissertation Generation 162

Appendix G: All Publications Published, Submitted and Planned 163

List of Figures

Figure 1-1: Periodic table representation of Groups III thru V. Colored regions show the region of interest. 2

Figure 1-2: Diagram of semiconductors and alloys plotting the bandgap energy vs the lattice constant [4]........ 3

Figure 2-1: Schematic diagram of UHV-CVD system used in this research. 14

Figure 2-2: Schematic diagram of the Raman system. The diagram is for illustration and is not to scale........ 19

Figure 2-3: Photoluminescence system schematic incorporating the used lasers, detectors, and dual beam path for room temperature and low temperature measurements. The diagram is for illustration and is not to scale. 21

Figure 3-1: Thickness dependence on the growth time of low temperature growth of (a) Ge and (b) GeSn. The solid points are measured data and the solid lines are linear fitting to extract the average growth rate. 26

Figure 3-2: (a) The derived growth rate for low temperature Ge and dilute GeSn film growth. (b) The extracted nucleation times of the films and their dependence on decreased temperature. 27

Figure 3-3: XRD 2θ-ω scans of (a) Ge and (b) GeSn films. A high-quality relaxed Ge reference grown on Si using an optimized two step growth recipe was also plotted for comparison. 28

Figure 3-4: X-ray diffraction reciprocal space maps along (-2-24) plane of (a) sample A and (b) sample B. The R=1 and R=0 lines indicate the full relaxation and pseudomorphic (lattice match to Si). 29

Figure 3-5: Stacked PL spectra of two selected dilute GeSn samples. The PL of Ge bulk reference is also poltted for comparison. The black and red curves are measured data and Gaussian fittings, respectively. The clear PL peaks at 1625 and 1650 nm were observed. 30

Figure 3-6: Room temperature PL from Ge bulk reference and Ge buffer. 34

Figure 3-7: Temperature dependent PL of the Ge buffer. 35

Figure 3-8: (a) The extracted integrated PL Intensity and (b) peak energy. The peak energy has been fit using a Varshni fitting. 35

Figure 3-9: (a) Room temperature power dependence and (b) integrated PL Intensity vs. pumping power on Ge buffer. 36

Figure 3-10: Scanning electron microscope image of pits that were etched in the surface. The pit counting visible with dots and #1 beside the pit.. 37

Figure 3-11: Temperature dependence of a) GeSn film thickness and b) relative Raman shift for the GeSn grown films.. 39

Figure 3-12: a) Plasma enhanced GeSn film thickness with increasing flow rates of $SnCl_4$. b) Example PL from the GeSn plasma enhanced growth. 40

Figure 3-13: The XRD rocking curve of the edge of GeSn plasma enhanced growth. 41

Figure 4-1: Growth matrix of GeSn on Ge buffers. Matrix narrowing from growth understanding is illustrated. A starting point and path to high quality GeSn is shown. 46

Figure 4-2: a) PL of growth temperature dependent GeSn. b) Selected XRD of growth temperture dependent GeSn. 47

Figure 4-3: XRD RSM and TEM of 0613 grown at 300 °C for 30 mins. 48

Figure 4-4: XRD RSM and TEM of 0616 grown at 270 °C for 30 mins. 49

Figure 4-5: XRD RSM of 0621 grown at 270 °C for 1 hour. 49

Figure 4-6: Images of the sample surface after each Sn reduction test. a) Initial state, b) Test 1, c) Test 2, and d) Test 3. 51

Figure 4-7: PL of the Sn reduction testing. 52

Figure 4-8: XRD rocking curves of the Sn reduction tests. Vertical dashed lines are used for ease of the eye to align the peak position. The GeSn peak angle is noted next to the curve. 54

Figure 4-9: SEM imaging of selected sample surfaces: a) cloudy surface from the initial state, b) hazy surface Test 1, and c) clear surface from Test 3. 55

Figure 4-10: Images of the sample surfaces for the second batch of samples. a) 270 °C, b) 260 °C, and c) 250 °C. 56

Figure 4-11: Normalized PL spectra from second batch of GeSn Growth. 57

Figure 4-12: XRD rocking curves from the second batch of GeSn growth. 57

Figure 4-13: XRD rocking curves spectra comparing growth in this work to commercial material. 58

Figure 4-14: Room temperature PL of 260 °C growth under the improved growth conditions using the 1064 nm pulsed and 532 nm continuous wave pump lasers. 59

Figure 4-15: Temperature dependent PL of the a) commercial and b) grown sample. 60

Figure 4-16: a) Spectral analysis and b) I-V curves for co-planar GeSn photoconductors fabricated from the first batch of samples. 62

Figure 4-17: a) Spectral analysis and b) I-V curves for 12-24 Interdigitated photoconductors fabricated from the first batch of samples. 62

Figure 4-18: Photoconductor detectivity from optimized growth plotted again best GeSn and state of the art detectors. 63

Figure 5-1: (a) HRXRD 2θ-ω scan of QW sample. The black and red curves are measured data and simulation results, respectively. Inset: The RSM contour plot of the QW structure; (b) TEM image of the GeSn/GeSn QW. The SIMS profile is overlaid with the TEM image to illustrate the Sn composition in every layer. 68

Figure 5-2: Band diagram calculated based on measured material data, showing the carrier confinement and the possible band-to-band optical transitions between (a) Γ-HH; (b) Γ-LH; (c) L-HH; and (d) L-LH. (Unit: meV). 70

Figure 5-3: (a) Temperature-dependent PL spectra of the GeSn QW sample. The PL peaks were annotated by peak 1, 2, and 3, respectively; (b) PL peak positions of peak 1 and 2. The reference samples are plotted for comparison; (c) integrated PL intensities of peak. 72

Figure 5-4: (a) SIMS and (b) calculated band diagram of GeSn QW showing the comparison between compensated and uncompensated Sn incorporation growth approaches. 74

Figure 5-5: Cross section (not to scale) of GeSn QW: (a) sample A and (b) sample B. 77

Figure 5-6: SIMS profiles of a) sample A and b) sample B. 79

Figure 5-7: High-resolution XRD rocking curves with corresponding sample structure simulation for a) Sample A and b) Sample B. 80

Figure 5-8: XRD-RSM measurements of a) Sample A and b) sample B. 80

Figure 5-9: TEM imaging of a) Sample A and b) Sample B. The layer thicknesses are labeled for the specific layer. 81

Figure 5-10: Top: for sample A. Band diagram calculated based on measured material data, showing the carrier confinement and the possible band-to-band optical transitions between (a) Γ-HH; (b) Γ-LH; (c) L-HH; and (d) L-LH. (Unit: meV). Bottom: for sample B. (e)-(h) The similar band diagram and optical transition calculations. 83

Figure 5-11: Temperature dependent PL of sample A using multiple pumping sources. a) 532 nm, b) 1550 nm, and c) 1064 nm. 86

Figure 5-12: Temperature dependent PL using multiple laser pumping a) 532 nm, b)1550 nm, and c) 1064 nm. 90

Figure 5-13: Integrated PL intensity of (a) sample A; and (b) sample B. 91

Figure 6-1: Sample structures for the single quantum wells... 96

Figure 6-2: SIMS profile for sample A.. 97

Figure 6-3: SIMS profile for sample B.. 97

Figure 6-4: SIMS profile for sample C.. 98

Figure 6-5: a) HRXRD rocking curve with simulation. b) RSM of sample A. 98

Figure 6-6: a) HRXRD rocking curve with simulation. b) RSM of sample B. 99

Figure 6-7: a) HRXRD rocking curve with simulation. B) RSM of sample C......................... 100

Figure 6-8: TEM image of sample C. 100

Figure 6-9: Bandedge diagram for sample A.. 102

Figure 6-10: Bandedge diagram for sample B. 104

Figure 6-11: Bandedge diagram for sample C. 105

Figure 6-12: Temperature dependent PL spectra for (a) sample A, (b) sample B, and (c) sample C.. 106

Figure 6-13: Peak positions of QW samples. Varshni fitting for each sample......................... 108

Figure 6-14: Normalized integrated PL intensity and FWHM of the PL spectra..................... 109

Figure 6-15: Nominal sample structure for the SiGeSn/GeSn DQW 110

Figure 6-16: SIMS profile of the SiGeSn/GeSn DQW.. 111

Figure 6-17: HRXRD rocking curve with simulation and RSM of sample D......................... 111

Figure 6-18: TEM image of sample D. 112

Figure 6-19: Bandedge diagram for sample D... 114

Figure 6-20: Temperature dependent PL of sample D.. 115

Figure 6-21: Nominal sample structure for the SiGeSn/GeSn MQW. 117

Figure 6-22: SIMS Profile of 4x multiple quantum well sample.. 118

Figure 6-23: HRXRD rocking curve with simulation and RSM of sample E. 118

Figure 6-24: TEM image of sample E. 119

Figure 6-25: Bandedge diagram for Sample E. 121

Figure 6-26: Temperature dependent PL of Sample E. 123

Figure 7-1: Summary of 10 K PL of all studied QW samples.. 127

Lists of Tables

Table 1: Characterization results of the temperature dependent growth of GeSn. 48

Table 2: $SnCl_4$ Gas Supply Ratios for growth optimization 51

Table 3: Parameters of pumping lasers. 79

Table 4: Summary of GeSn/GeSn DQW sample information 82

Table 5: Summary of SiGeSn/GeSn SQW sample information 101

Table 6: Varshni fitting parameters derived from fitting PL spectra peaks. 108

Table 7: Summary of SiGeSn/GeSn DQW sample information 113

Table 8: Summary of SiGeSn/GeSn 4x MQW sample information 120

List of Published Papers Used in This Dissertation

Part of Chapter 3 was originally published as:

Reproduced from ["Comparison study of the low temperature growth of dilute GeSn and Ge" P.C. Grant, W. Dou, B. Alharthi, J. M. Grant, A. Mosleh, W. Du, B. Li, M. Mortazavi, H. A. Naseem, S.-Q. Yu, JVST (B), vol 35, no. 6, 061204, (2017)], with the permission of the American Vacuum Society.

Chapter 4 was originally submitted as:

"UHV-CVD Growth of High Quality GeSn Using SnCl4: From Growth Optimization to Prototype Devices" P.C. Grant, W. Dou, B. Alharthi, J.M. Grant, H. Tran, G. Abernathy, A. Mosleh, W. Du, B. Li, M. Mortazavi, H.A. Naseem, S.Q. Yu, arXiv:1810.02523 [cond-mat.mtrl-sci]

Part of Chapter 5 was originally published as:

"Direct bandgap type-I GeSn/GeSn quantum well on a GeSn- and Ge- buffered Si substrate" P. C. Grant, J. Margetis, Y. Zhou, W. Dou, G. Abernathy, A. Kuchuk, W. Du, B. Li, J. Tolle, J. Liu, G. Sun, R. A. Soref, M. Mortizavi, S.-Q. Yu, AIP Advances, vol. 8, no. 2, (2018)

"Study of Direct Bandgap Type-I GeSn/GeSn Double Quantum Well with Improved Carrier Confinement" P. C. Grant, J. Margetis, W. Du, Y. Zhou, W. Dou, G. Abernathy, A. Kuchuk, B. Li, J. Tolle, J. Liu, G. Sun, R. A. Soref, M. Mortazavi, S.-Q. Yu, Nanotechnology, vol. 29, no. 46, (2018)

Chapter 6 experimentation was identical to the experimentation performed for Chapter 5 except it was for SiGeSn/GeSn quantum wells instead of GeSn/GeSn quantum wells. The formatting, word usage, and sentence structure, therefore, are similar or exactly the same.

Chapter 1 Introduction/Background

The world around us has been transformed by Si electronics. Devices made from this material penetrate every aspect of our modern daily lives. The revolution that Si devices began continues to this day as more and more electronic devices invade our personal lives, from autonomous vehicles, personal electronic devices, and home integration.

1.1 Motivation

The remarkable success of Si as an electronic material has been lessened by the fact that Si displays poor optical qualities. While there are many Si-based photonic devices, detectors, solar cells, etc., these devices have very poor performance with a modern Si solar cell being only 25% efficient [1]. With these levels of efficiency, the chance of achieving efficient, pure Si-based emitters is extremely small. Therefore, optical systems have made use of III-V semiconductors which emit light very efficiently, such as GaAs, InGaAs, InSb, and other like materials. The reason for efficient light emission is that they are direct band gap materials, meaning the lowest valley of the conduction band lines up with the peak of the valence band in momentum space. Si is an indirect material, in that the lowest valley of the conduction band is not in alignment with the highest peak on the valence band. This means that for an emission to occur, phonon interaction is required. This requirement reduces the efficiency of the radiative process for indirect materials.

The issue with III-V materials is that they are traditionally expensive, require special fabrication techniques, and are fragile. This makes them impractical to push electronics farther as Si is cheap, robust, and has highly refined processing methods. This disparity has pushed researchers to look for other avenues to base photonic devices on using Si. This has included III V devices grown on Si [2]. However, it is considered that monolithic integration of Group IV

devices can be more reliable and less costly than the III-V hybrid method [3].

1.1.1 Group IV Epitaxy

Group IV materials began the electronic revolution with Si and Ge being initially used for devices. The use of these materials and production methods have matured over the decades resulting in large companies who innovate advanced designs and fabrication technologies, e.g., Intel or Texas Instruments. Increased interest in Group IV epitaxy helped develop the SiC material, which has become an important material for state of the art high temperature electronics. Figure 1-1 shows the region of interest of this research on the periodic table.

5 B	6 C	7 N
13 Al	14 Si	15 P
31 Ga	32 Ge	33 As
49 In	50 Sn	51 Sb
81 Tl	82 Pb	83 Bi

Figure 1-1: Periodic table representation of Groups III thru V. Colored regions show the region of interest.

While high temperature electronics have looked up in the periodic table (C), photonics researchers have turned their attention downward on the periodic table to look at Ge and Sn and the alloys that can be produced.

1.1.2 SiGeSn for Infrared Optoelectronics

Monolithic integration of Group IV direct bandgap devices on Si substrates are highly

desirable. This opens the possibility for increased computing speed with less heat generation, size reduction of systems, and improved energy conversion. In III-V materials, the decoupling of lattice constant and bandgap energy to tailor the device to specific applications usually requires quaternary materials. However, utilizing only Group IV allows this to be done with ternary materials, suggesting an easier route for tailored semiconductors. The SiGeSn material system has been suggested as a potential candidate to be integrated into multi-junction solar cells as a 1.0 eV material lattice matched to Ge. To illustrate the possibility, the bandgap vs lattice constant is shown in Figure 1-2.

Figure 1-2: Diagram of semiconductors and alloys plotting the bandgap energy vs the lattice constant [4].

The SiGeSn material system can cover infrared wavelengths from 1.6 µm to 12 µm. Active devices in this range can make use of near-infrared (NIR) and mid-infrared (MIR)

atmospheric transmission windows from 1.6 µm to 2.5µm and 3 µm to 5µm, respectively. The material has the potential to achieve direct bandgap and a type-I band alignment for quantum well (QW) structures. The SiGeSn material system has potential in many areas such as night vision cameras, free-space communication, and even laser eye surgery. These possibilities, for low cost commercial, military, and civilian devices demand the material system be thoroughly explored to determine if commercialization is possible.

1.1.3 Bandgap Engineering

Engineering the bandgap of semiconductors is essential to expanding the application of photonic devices. Gas detection is a prime example as individual gases have unique spectral absorption lines, tailoring a semiconductor to specific ranges allows for one material to cover a broad range of applications. In Figure 1-2, the SiGeSn material system can be used at the 0.565 nm lattice constant for lattice matched solar cell layers and can also be used for solar cells along the 0.610 nm lattice constant for direct bandgap materials for the majority of absorbing layers. Bandgap engineering historically regulated to III-V and II-VI materials now has a counterpart in the Group IV materials.

1.1.4 Commercial Integration

One major drawback of III-V and II-VI materials are that they require special fabrication processes that are not compatible with that of standard Si fabrication, known as Complementary Metal Oxide Semiconductor (CMOS) processing. Fabrication of III-IV materials usually requires a high temperature step that damages CMOS circuits. Therefore, a CMOS compatible material is required for commercial integration. The SiGeSn material system requires growth temperatures below 400 °C making the material system fully compatible with CMOS processing. The diamond crystalline structure of SiGeSn matches that of Si, thus reducing the need for

special wafers to battle anti-phase domains. The fact that SiGeSn has been grown in an industrial reduced pressure chemical vapor deposition (RP-CVD) shows its ability to transition from the research to industrial scale [5].

1.2 Scope of Dissertation

This dissertation is divided into two parts with in-house ultra-high vacuum chemical vapor deposition (UHV-CVD) of GeSn comprising the first part and characterization of RPCVD grown QWs provided through a collaborator being the basis for the second part.

1.2.1 Ultra-High Vacuum Chemical Vapor Deposition Growth

The achievement of SiGeSn growth has two pathways: i) start from GeSn and add Si and ii) start from SiGe and add Sn. Regardless of pathway chosen to obtain SiGeSn, the growth of Ge is the initial starting point. This dissertation will start with the introduction to the unique UHV-CVD growth chamber located at the University of Arkansas along with the measurement techniques used to complete this work in Chapter 2. The GeSn pathway has generated tremendous interest over the last 10 years as it holds more promise for efficient emitters than the SiGe path. Therefore, this work follows the GeSn path toward SiGeSn. Chapter 3 describes: i) the 1st generation of GeSn growth occurring directly on Si; ii) plasma enhanced GeSn on Si; and iii) development of Ge buffers for further development of GeSn material growth. Chapter 4 details the specific growth of GeSn on the developed Ge buffers.

1.2.2 Quantum Well Characterization

Corroboration with other facilities improves research in the field as in-house material development isn't a limiting factor of progress. Chapter 5 documents type-I direct bandgap QWs using a GeSn/GeSn structure. The QWs were divided into separate generations of samples with

Chapter 5 reporting generations 1 and 2. Chapter 6 focuses on the third generation of QWs that utilize the SiGeSn/GeSn structure. All QW structures studied were grown on relaxed GeSn buffers. Chapter 7 summarizes this work with future research plans to continue improving the in-house material development as well as the continued development of GeSn QWs.

1.3 Semiconducting Sn and GeSn alloys

1.3.1 Semiconducting Alpha-Sn

Elemental Sn undergoes a transformation that, while documented since ancient times (tin pest), was only scientifically studied in the last 160 years. The transformation of white Sn to gray Sn was well known and described in scientific literature prior to 1900 [6]. In Reference 6, the transition from metallic, white or β-Sn, to semiconducting, gray or α-Sn occurred at 20 °C which suggested that all the tin in the world, unless it was in an extreme environment, was likely in a metastable state. In the following 20 years, the volume expansion of the transition was measured [7] and in 1919, α-Sn was studied using x-rays and proved the change in the crystal structure [8–10]. The magnetic properties of the Sn phases were studied during the 1910s-1930s [11–13] with results showing the magnetic properties of Sn are not atomic properties but instead depend on the crystal structure. By 1950, the lattice constant of α-Sn had been determined [14] as well as its semiconducting nature [15]. Research into α-Sn hit a boom in the 1950s with researchers looking at factors that affected the transformation of α-Sn including the inclusion of Ge into the α-Sn crystal lattice increasing the transformation temperature [15–21]. Reference 21 showed a transformation of 13.2 °C. The electronic carrier mobilities and specific heat were measured [22–25] with Ewald giving an effective mass and 0 K bandgap energy of 0.68m and 0.094 eV, respectively [25]. Also demonstrated in this decade was that pure α-Sn is n-type material [26]. Alloying with α-Sn also became prevalent in the 1950s with several studies on

HgSn material or Hg with an α-Sn based alloy [26–28] with Reference 28, specifically mentioning the GeSn alloy. The first non-amalgam growth was accomplished in 1958 using evaporation, with α-Sn only occurring at low growth temperatures and β-Sn occurring at increased temperatures [30]. Along with more experimental study on the formation and properties of α-Sn [30–36], the rise of calculations and modeling of the band structure began in the 1960s [37–43]. Antimony doping of α-Sn also began during this time with non-parabolic conduction band and spin splitting being observed [44–46]. Continued calculations and modeling of material properties, such as bandstructure, quantum effect, electron distribution, and lattice dynamics [47, 48, 49–60] followed in the 1970s and early 1980s.

A large step was made in 1981 with the first molecular beam epitaxy (MBE) growth of α-Sn at 25 °C using InSb and CdTe substrates [62]. These growths showed the stabilization temperature was raised to 70 °C. The growth of α-Sn thin films showed a bandgap behavior based on thickness [62, 63]. Further increase in the α-Sn stabilization was shown by alloying with Si, with only 0.75% Si resulting in a transition temperature of 90 °C [65]. It was shown at the same time that by increasing the amount of Ge in the alpha-Sn lattice, the transition temperature could be increased [66]. The growth of α-Sn allowed for improved modeling of the band structure [66–74] as models could be compared to experimental data. The late 1980s produced many growth results including: layer-by-layer growth mode, film thicknesses up to 70 nm, high quality films, and superlattices [75–80]. Growth was performed on different substrates such as InSb, CdTe, Ge, and Si, with varying crystal orientations [76, 77, 81–85]. Growth of superlattices reported the possible out-diffusion of the InSb or CdTe substrate/buffer into the film [81, 82, 86] which was common for InSb/CdTe structures. However, other experimental results [87, 88] suggested that α-Sn prevented the out-diffusion. During the 1990s, efforts were

put into superlattices [89–94], interfaces [95–97], and surfaces [98–101].

The story of α-Sn continues but, for this work, the 100 years of research surveyed provided several key contributions to group IV photonics: i) α-Sn is semiconducting and cubic in crystal structure, ii) α-Sn is suggested to have a bandgap energy of 0 eV or slightly negative, iii) Ge alloying increased the stability temperature, and iv) α-Sn is stable on both Ge and Si surfaces. Most work for α-Sn was geared to long wavelength detectors, however, improvements in growth during the 1980s paved a new path for researchers.

1.3.2 GeSn Alloy: The Potential Realized

Early studies on α-Sn showed that Ge strongly affected the transformation of α-Sn and raised the transition temperature. However, the solid solubility of Ge into Sn and vice versa is quite poor at <1%, thus, only low compositional alloys could be produced. The successful demonstration of α-Sn growth using MBE in 1981, opened the doors to exceeding the solubility limits of alloying with Sn. The GeSn material system was first predicted to have a direct bandgap by Goodman et al., in 1982 [103]. Sputtering of single crystal GeSn alloy was first accomplished in 1987 [104] and followed up with amorphous GeSn in 1988 [104, 105]. It was reported in Reference 105, the change in bandgap energy with Sn incorporation was -12 meV/% Sn.

The first MBE growth of GeSn occurred in 1989 [107]. From that point on, the GeSn material system garnered increasing interest with groups producing GeSn along with their α-Sn research [107–110]. GeSn direct bandgap heterostructures on Si substrates were proposed by Soref and Friedman in 1993 [112]. Research on growth of GeSn using MBE continued throughout the rest of the 1990s while searching for improved growth conditions [112–115]. A breakthrough was made in 2001 with the introduction of a gaseous Sn-based precursor $(Ph)SnD_3$

for CVD growth [117].

A group at Arizona State University (ASU) was a pioneer in this growth technique of GeSn by developing the (Ph)SnD_3 precursor [117, 118] and deuterium-stabilized stannane, SnD_4 [119–123]. Simulations during this time suggested phase separation was suppressed through biaxial strain [125] and a direct bandgap crossover composition of 9% Sn [126]. Throughout the rest of the 2000s, nanowires and quantum dots were grown [126–132], Sn-enhanced epitaxy was accomplished [133, 134], and interface studies [135, 136] were done. This time frame also saw the use of GeSn as a buffer for tensile straining of Ge [137, 138]. The CVD group at ASU continued throughout the 2000s by researching growth using higher order Si-hydride and Si-Ge hybrid precursors [139, 140], produced a compliant layer [141–143], and the first generation of GeSn optoelectronic devices processed under CMOS compatible conditions [144, 145].

These first devices demonstrated in 2008 were the first realization of the true potential of the GeSn material system. It may have been the demonstration of these devices that spurred increased interest in the GeSn material system as a viable infrared semiconductor material system. The last decade has seen an uptick in the amount of research toward the (Si)GeSn material system. The growth of GeSn alloys continued into the 2010s [146–148] with results suggesting reduced carrier concentration of GeSn alloys [150] as well as shifting absorption and PL with increasing Sn incorporation [151, 152]. It was also suggested that deviation in the bandgap bowing from Vegard's law was 2.9 for low composition GeSn alloys [153]. The group at ASU demonstrated the only CVD growth technique using the SnD_4 precursor, however, this changed in 2011 with the addition of $SnCl_4$ to the viable Sn precursors available for CVD growth [154]. The thermal stability of GeSn alloys was also investigated with it being suggested that the alloy was stable up to 500 °C even for high Sn compositions [154–156]. It was also suggested

that the expansion of the lattice constant also deviated from Vegard's law with a bowing parameter of -0.066 Å [158].

The year 2011 saw the first demonstration of the GeSn pMOSFET [159] as well as GeSn p-i-n photodiodes [159, 160]. Growth of GeSn alloy during this time was primarily accomplished using the Ge_2H_6 (digermane) precursor [161, 162], while the group from ASU developed higher order hydrides for growth [164]. However, higher order hydrides are expensive and thus not very applicable to make the material truly commercial. More devices were demonstrated in 2012 including the high mobility pMOSFET [165], the first demonstration of a nMOSFET [166], and the first p-channel Tunneling Field Effect Transistor [167]. A GeSn p-i-n photodiode was also demonstrated with 4% Sn incorporation [168].

The year 2013 saw another increase in the amount of published information on the (Si)GeSn material system. One point of contention with the GeSn material system is the amount at which the bandgap changes with respect to Vegard's law. There have been several studies examining the bandgap bowing with results showing bowing factors from 2.9 to 1.35 [152, 168–170]. It has been suggested that the bowing parameter may be Sn composition dependent. It has been reported that a temperature dependence was also observed with the bandgap bowing parameter [171]. The GeSn material was shown to have optical emission properties of direct bandgap material by Ghetmiri et al. [172]. This critical confirmation of the direct bandgap nature demonstrated the material potential of GeSn to bridge the gap between Si electronics and optoelectronics dominated by III-V materials. However, this required 10% Sn incorporation into the Ge lattice. To increase the directness of the bandgap, several groups grew GeSn with compositions over 10% [4, 172, 173]. Currently the world record Sn incorporation by CVD growth method was recently demonstrated by Dou et al. at 22% Sn [175]. The demonstrated

direct bandgap and method to increase the material composition in a commercial reactor illustrates the GeSn material compatibility to Si-based electronics. Increased control and growth improvements have paved the way to efficient optical devices including lasers [175–177]. Si based systems now have a compatible direct bandgap material clearing a pathway for low cost infrared emitters.

1.4 GeSn Quantum Wells

Proving that GeSn material could work as an efficient emitter only increased the interest in producing more advanced structures for more efficient devices. A couple of device designs for GeSn QW lasers were produced in 2010 [178–180]. QWs are generally acknowledged to produce more efficient devices and, therefore, the SiGeSn material system needs to be fully explored. To maintain all group IV structures a few QW barrier candidates arise: i) Ge, ii) GeSn, and iii) SiGeSn. Heterostructures and devices based on the Ge/GeSn/Ge structure have been demonstrated [181–188]. This research suggested that the strain induced in the QW would prohibit the transition to direct bandgap material in the well. It was suggested that the Ge/GeSn/Ge heterostructure could produce a direct bandgap QW with type one band alignment to the barriers by using a relaxed GeSn buffer [190]. However, these structures had a narrow range to exist and SiGeSn material was suggested as a better barrier layer. The studies on the GeSn/GeSn/GeSn and SiGeSn/GeSn/SiGeSn structures are more limited [190, 191]. The S.-Q. Yu research group has demonstrated GeSn QW structures using both the GeSn and SiGeSn barriers [192–194]. The GeSn/GeSn/GeSn structure was plagued by a Ge interlayer due to the strain effect in the QW depleting the Sn from the interlayer, while the SiGeSn/GeSn/SiGeSn structures remained indirect. Type-I band alignment has been shown for many QW structures, however, direct bandgap QW structures, have still been elusive.

1.5 Summary

Chapter 1 contains the introduction and scope of the dissertation as well a look at the research that laid the foundation for this work. The (Si)GeSn material system makes an ideal candidate system to monolithically integrate infrared optoelectronics onto Si. The material system should be an easier route than using traditional III-V materials for integration. The decoupling of the bandgap and lattice constant can be accomplished using a ternary material instead of the quaternary materials needed for III-V infrared materials. The cubic lattice structure of the (Si)GeSn material system allows for an easier path towards growth on Si as high-quality films can be grown on true Si (001) substrates using standard commercial processes. Experimentally shown direct bandgap GeSn and theoretical direct bandgap SiGeSn materials pave the way for the next generation of Si-based emitters.

Chapter 2 UHV-PE-CVD System and Thin Film Characterization

2.1 Vacuum System

UHV-CVD growth is accomplished using a custom, in-house constructed vacuum system shown in Figure 2-1. The system consists of two identical but separate vacuum chambers connected using a central gate valve. One vacuum chamber serves as the entry-exit chamber for the system. This chamber is pumped using an Edwards (Burgess Hill, UK www.edwardsvacuum.com) turbo vacuum pump and Edwards XDS-10 scroll type mechanical pump and achieves base pressures of ~10^{-8} torr. This chamber also contains a wafer fork and transfer arm for transferring wafers to and from the process chamber. The process (growth) chamber is pumped using an Edwards STP-451C corrosive resistant turbo pump and Edwards QDP-40 corrosive resistant mechanical pump. The process chamber is also pumped using a Marathon (San Leandro, CA www.marathonproducts.com) CP-8 cryopump enabling base pressures as low as 10^{-10} torr. Chamber pressure is measured using a cold cathode gauge (CCG) with an isolating valve to ensure the gauge is not damaged during growth. Sample heating is carried out on a UHV Design (East Sussex, UK www.uhvdesign.com) Epi-Center In-Line deposition stage allowing for growth temperatures up to 1000 °C. Gas flows are controlled using mass flow controllers (MFCs) with flow rates below 100 sccm. The gases mix in a manifold before being injected into the chamber through a single port. Growth pressure is measured by a MKS Baratron® (Andover, MA www.mksinst.com) capacitance manometer. The growth pressure is regulated using a throttle valve connected to a MKS pressure controller. Process gas after deposition is pumped to a Gas Reactor Column (GRC) that transforms the volatile process gas to inert salts using high temperatures with the remaining inert gas exhausted to atmosphere.

Process gases are stored at a gas farm in individual cabinets that are continuously

exhausted to atmosphere. Each cabinet contains a gas manifold with bottle gauges to monitor bottle pressure. Each gas line also contains an emergency shutoff valve as close to the bottle valve as possible. The exhaust for the gas farm has Honeywell Midas® (Lincolnshire, IL www.honeywellanalytics.com) gas detectors (sniffers) installed to sense for leaks in the gas farm. Gas is delivered into the lab using single piece gas lines from the gas farm to the growth chamber gas manifold inside the lab. This gas manifold is also exhausted to the outside with sniffers installed in the exhaust line. The sniffers are connected electrically to a local alarm and building master alarm. The local alarm has been wired to activate the emergency shutoff valves in the event of a gas leak as well as power sirens and lights in the local area. The building master alarm is also triggered which evacuates the entire building.

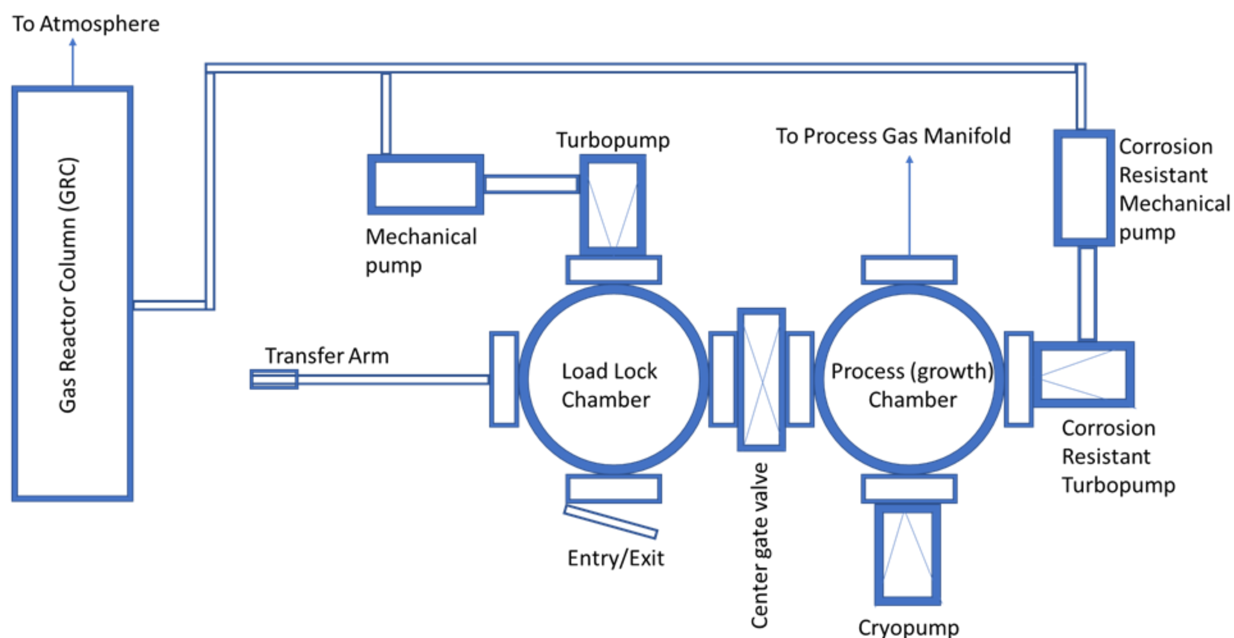

Figure 2-1: Schematic diagram of UHV-CVD system used in this research.

2.2 Unique System Capabilities

The UHV-CVD system constructed at the University of Arkansas has some unique capabilities. These capabilities were implemented to study multiple pathways of possible growth

enhancement of GeSn materials. As well as growth enhancements, a method to provide increased gas control has also been implemented.

2.2.1 Plasma Enhancement

Radio frequency (RF) plasma enhancement was built into the chamber with its initial construction. The deposition stage has a built-in plasma circuit separate from the heating circuit used during growth. The plasma is generated using a Seren (Vineland, NJ www.serenips.com) RF power source coupled with an automatic network matching controller. The plasma system was completed with the addition of a lower plasma electrode that can be raised for growth and lowered for transferring the sample in and out of the process chamber.   The plasma generation increases the amount of available energy for precursor decomposition beyond standard thermal deposition. This increase in energy would enhance the breakdown of the GeH_4 into radicals needed for deposition. A RF grid is installed between the upper plasma electrode and the substrate heater to act as a shield from electromagnetic interference during growth.

2.2.2 Hotwire Enhancement

The hotwire enhancement for the UHV-CVD system uses a tungsten filament as a heating element. A direct electrical current is passed down the filament and, like an incandescent light bulb, the filament releases heat and light. The heat generated by the filament is large enough to break down H_2 into atomic hydrogen and thus useful for enhancing the decomposition of GeH_4 into radicals needed for low temperature growth of GeSn.

2.2.3 Gas Mixing and Delivery

Epitaxial CVD growth of GeSn films require strict gas flow control of the Sn precursor. The UHV-CVD system has been adapted to use either $SnCl_4$ or SnD_4 (deuterium stabilized Sn-

hydride) as the Sn precursor. This research was accomplished using $SnCl_4$ due to its low cost and molecular stability. $SnCl_4$ vapor was directly injected using a 5 sccm MFC. The vapor pressure of $SnCl_4$ at room temperature is 18 torr which is high enough to operate the MFC. However, it was found that even at the lowest set point (<1% of maximum flow) the MFC delivered too much $SnCl_4$ to the system resulting in Sn segregation on the wafer surface and poor material quality. This led to various methods for reducing the $SnCl_4$ fraction during growth including gas dilution, increasing GeH_4 decomposition, and design of a gas mixing and delivery system for precision gas mixture control.

The gas mixing system utilized a 10" vacuum nipple as a gas bottle. The bottom of the nipple was capped with a 10" to 2 ¾" reducer flange. The 2 ¾" remaining port in the bottom was used to feed through a stirring motor that was connected to an impeller inside the nipple. The motor and impeller were used to continuously stir the gasses. The upper side of the nipple was also connected using a 10" to 2 ¾" reducer flange. A valve was mounted to the upper reducer flange to isolate the gas mixing cylinder during no flow operation. A 2 ¾" tee is mounted to the isolation valve to make a port to install an all range pressure gauge as a monitor to gas pressure in the system. A 2 ¾" 4-way was mounted to the tee, with an isolation valve on the upper and lower sides and a reducer to ¼" gas line on the end. The upper side of the 4-way was reserved for a residual gas analyzer (RGA) used to measure partial gas pressures in the mixtures, ensuring correct compositional control for Sn based growths. The lower valve on the 4-way isolated an Edwards 75-DX turbopump used to pump the gas mixing system. This pump removed the residual gas after growth and maintained the system under high-vacuum conditions when not in use. The ¼" gas line connection was used to connect the gas to a mass flow controller to control the rate of gas flow during growth.

2.3 Thin Film Characterization

Characterization of the grown thin films were essential for the material grower. This feedback information was crucial in improving growth recipes to produce better material. Characterization methods used for this growth were primarily focused on telling the grower how much film was produced, the material quality and, in the case of GeSn, the composition of Sn incorporated into the Ge lattice. Every sample grown was subjected to three optical characterization methods such as ellipsometry, Raman spectroscopy, and photoluminescence (PL). Some samples displayed desired properties in the optical characterizations and, therefore, were sent on to other material characterization methods such as x-ray diffraction (XRD) and cross-sectional transmission electron microscopy (TEM). These methods provide a rich assortment of information to understand what has been done and to formulate a strategy to further improve material growth with process iterations.

2.3.1 Ellipsometry

The ellipsometry characterization technique was the first characterization performed on grown samples. This characterization was mainly used to derive the thin film thickness of the grown films. In the case of GeSn the characterization was also used to estimate the Sn composition in the film. Ellipsometry operates off the principle that as electromagnetic waves making up the incident light interacts with a material, the electromagnetic waves change in intensity and phase. Thus, if you start with linearly polarized light (two light waves in phase) then interact it with a material, a change in polarization will occur resulting in either a circular (90° out of phase) or elliptical polarization (arbitrary amplitude and intensity). The ellipsometer is divided into two sections. The first section is for polarized light emission and includes a light source and a polarizer which passes light of only a certain polarization. The second section of

the ellipsometer is the detection section. This consists of a polarization analyzer and a detector. Between the polarized source and detection section is the wafer. Light is emitted to the sample and reflected from the sample to the detection section. The reflected light has changed polarization due to the interaction with the sample. The polarization analyzer is a polarizer that continuously rotates allowing for light of different polarizations to arrive at the detector as it rotates. The change in polarization from the incident is what the ellipsometry measures as Psi and Delta. To accurately describe a thin film from the measurements of Psi and Delta requires using a material model and regression analysis. The ellipsometer has a database of standard materials from which to select, allowing for quick and accurate model building. However, for materials that are not in the database for the ellipsometer, a generalized model must be developed.

For this research, a V-Vase optical spectroscopic ellipsometer from J.A. Wollam (Lincoln, NE www.jawoolam.com) was utilized. The GeSn material system was not in the ellipsometer database. Therefore, a generalized model was developed based off Ge. In fitting the ellipsometry data for GeSn, the developed model was employed by shifting of the bandgap to lower energy. This left many of the optical constants consistent with that of Ge and introduced some error in the measurement. However, with Ge being the base material in GeSn, it was felt the error was small and the measurement itself was only one piece of the puzzle in determining the thickness, Sn composition, and material quality of the grown films.

2.3.2 Raman Spectroscopy

Raman spectroscopy pioneered in the 1920s and 1930s is a characterization technique based on the inelastic light scattering with atoms or molecules. This technique is mainly used to observe low energy interactions such as those involving rotational and vibrational interactions.

Since vibrational energies are unique to a chemical bond, this technique is useful in identifying materials. This technique is accomplished by illuminating the sample with monochromatic light and collecting the scattered light. However, most of the scattered light is Rayleigh scattering caused by elastic collisions of the monochromatic light with the atoms in the sample. Filtering out the Rayleigh scattering using a notch filter allows for the Raman scattered light to be collected. The collected photons will be shifted from the original photon energies due to rotational and vibrational energies. This shifting of photon energies is referred to as Stokes or anti-Stokes shifting. The Raman spectroscopy performed in this research was performed on an in-house built Raman system as shown in Figure 2-2.

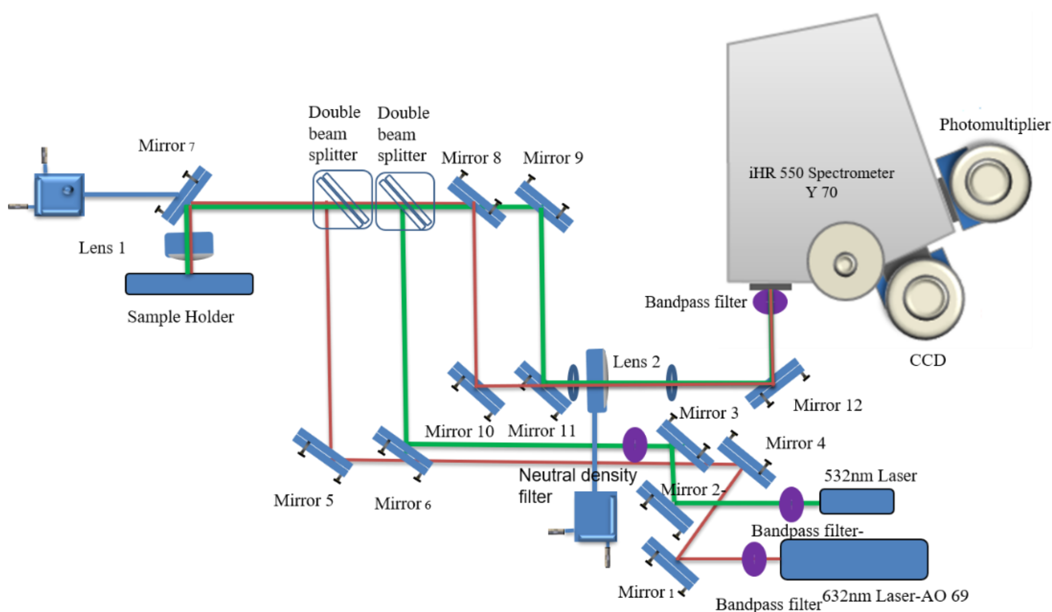

Figure 2-2: Schematic diagram of the Raman system. The diagram is for illustration and is not to scale.

The Raman system could utilize either a 532 nm or 632.8 nm laser as the monochromatic light source. The collected light was dispersed using a grating-based spectrometer with optional LN_2-cooled charged coupled device (CCD) camera or photomultiplier detector. The CCD was the primary detector used while the photomultiplier was used as a backup in-the case of CCD

degrading vacuum and difficulty holding temperature. The system was calibrated to both Si (520 cm^{-1}) and Ge (300 cm^{-1}). With the semiconducting α-Sn Raman shift close to 210 cm^{-1} [196], the Raman shift of GeSn thin films should range between the Raman peaks of Ge and α-Sn. Raman spectroscopy was mainly used in this research to determine the presence of deposited films and their crystallinity.

2.3.3 Photoluminescence

The photoluminescence characterization technique is used to observe and characterize the light emission from optoelectronic materials. Photoluminescence, as its name suggests, is the luminescing of light while using light as a pumping source, or provider of energy. The general process is that, photons of light above the bandgap of the semiconductor are absorbed in the material. As the photons interact with electrons in the material, the electrons are excited to a higher energy state generating an electron-hole pair. Radiative recombination of the electron-hole pair emits a photon with an energy equal to that of the bandgap in the material. These emitted photons are collected and measured using a spectrometer. The photoluminescence technique can provide information about the bandgap of the material, carrier lifetimes, recombination processes, and a host of other information about the material under study. This research was accomplished using an in-house built PL setup as shown is Figure 2-3.

The PL setup was a multi-functional system which possessed six lasers as pumping sources and used different detectors such as InGaAs, PbS, and InSb. The system was used for off-axis PL (both room temperature and low temperature have separate pump and collection paths), micro-PL, and optical pumping of devices. The pumping side of the setup consists of 532 nm continuous wave laser, 1064 nm pulse laser, 1550 nm continuous wave, 2000 nm continuous wave laser, 780 nm pulse Ti-sapphire femtosecond laser, and Nd:YAG laser.

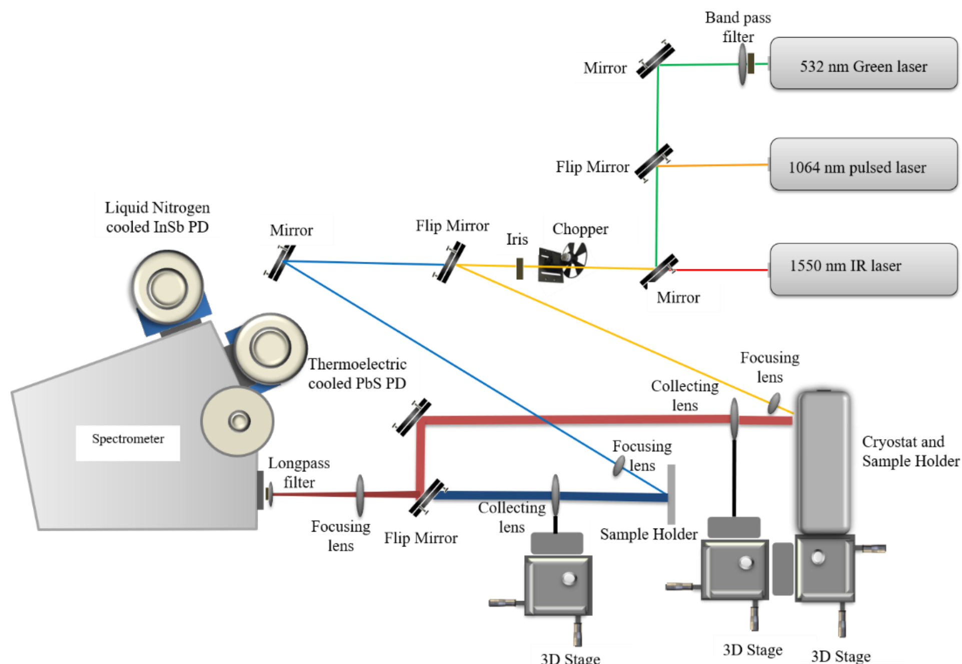

Figure 2-3: Photoluminescence system schematic incorporating the used lasers, detectors, and dual beam path for room temperature and low temperature measurements. The diagram is for illustration and is not to scale.

Detection of the emitted light was accomplished using a Horiba (Kyoto, JA www.horiba.com) grating-based spectrometer in conjunction with either a PbS detector or InSb detector depending on the emitted wavelength. PbS has cutoff at 3.0 µm, therefore, samples with emission near or beyond this wavelength required the InSb detector. The off-axis configuration was used for this research with both the room temperature and low temperature beam paths utilized. Only the 532 nm, 1064 nm, and 1550 nm lasers were used for pumping probes during this work. Detection was mainly accomplished using the PbS detector as most samples measured emitted below 3.0 µm.

2.3.4 X-ray Diffraction

The x-ray diffraction (XRD) characterization technique is a non-destructive technique that uses x-rays to probe the arrangement of atoms in materials. First shown by William

Lawrence Bragg and William Henry Bragg, the diffraction of the x-rays interacting with a material was conditioned by the ordered arrangement of the atoms in the material [197]. Thus, using this spacing they were able to describe the atomic arrangement of materials. This revolutionary process has become one of the dominant methods of characterizing the material structure. Material characterization was performed using Phillips (Malvern, UK www.malvernpanalytical.com) X'pert Pro x-ray diffractometer (XRD). The symmetric (004) 2θ-ω rocking curves and asymmetric (2-24) reciprocal space mapping (RSM) were measured, by which the crystalline material, and in-plane ($a_{\parallel}$) and out-of-plane ($a_{\perp}$) lattice constants were obtained.

2.3.5 Transmission Electron Microscopy

Transmission Electron Microscopy (TEM) is a technique that uses electron diffraction to build an image of the object being imaged. Imaging can be of atoms in a crystal, molecule, viruses, bacteria, and other extremely small objects. The TEM uses high energy electrons (>200 keV), focused onto a thin sample (<100 nm) to generate an image on a phosphor screen. Electrons with this high energy have a wavelength of 0.6 picometers making them ideal to image at the atomic level. The principle of operation between an optical and electron microscope are the same with the source being focused through a sample and projected onto a screen. However, focusing light requires a physical lens such as quartz, while focusing electrons need electromagnetic lenses. The sources are also different, and the optical microscope can be done under ambient conditions while the TEM requires UHV conditions. The TEM used in this research was a FEI Titan (Hillsboro, OR www.fei.com) located in the Institute for Nanoscience and Engineering at the University of Arkansas.

Chapter 3 UHV-CVD Growth on Si substrate

Previous work using the UHV-CVD for the growth of group IV materials demonstrated the ability to produce thin films of (Si)GeSn alloys [198]. However, the growth was only demonstrated directly on Si and had yet to be established on Ge buffers. Furthermore, growth had not been shown to be uniform with adequate control to produce device quality materials. Chapter 3 begins a road to solving those growth issues, by solving the uniformity issue in conjunction with learning material growth. Several studies were carried out including studies of the basic growth conditions, development of a Ge buffer for further work, and one of the potential GeH_4 decomposition enhancements available to use.

3.1 A Comparison Study of the Low Temperature Growth of Dilute GeSn and Ge

Reproduced from ["Comparison study of the low temperature growth of dilute GeSn and Ge" P.C. Grant, W. Dou, B. Alharthi, J. M. Grant, A. Mosleh, W. Du, B. Li, M. Mortazavi, H. A. Naseem, S.-Q. Yu, JVST (B), vol 35, no. 6, 061204, (2017)], with the permission of the American Vacuum Society.

The development of GeSn has given silicon photonics its long awaited true direct bandgap material with complementary metal oxide semiconductor (CMOS) compatibility and bandgap tunability [171, 198, 199], which leads to high performance GeSn devices such as light emitting diodes [200–202], photodetectors [204, 205], and lasers [176, 205]. The rapid success of GeSn optoelectronic devices indicates great commercialization potential.

Growth of GeSn is challenging due to large lattice mismatch between Si and GeSn (>4.2%), low solubility (<0.5%), and the instability of α-Sn above 13 °C. Material growth techniques therefore were developed under non-equilibrium growth conditions such as low temperature growth via either molecular beam epitaxy (MBE) [206–210], or chemical vapor deposition (CVD) [140, 204, 211–213]. The growth of GeSn using CVD technique has been

investigated more than one decade. Various Sn and Ge precursors were used attempting to achieve high Sn incorporation and high material quality. Early growths were carried out using deuterated stannane (SnD_4) as the Sn precursor [141], whose high cost and instability drove the motivation of seeking other Sn precursors. It has been reported that tin-tetrachloride ($SnCl_4$), a low cost, stable, and commercially available precursor, with GeSn material growth being initially demonstrated by Vincent et al [154]. On the other hand, various hydride chemistries have also been explored as a Ge precursor by Kouvetakis et al. [141]. Higher order germanes were commonly used due to their favorable decomposition at low temperatures [212]. Recent progress has allowed for low cost germane (GeH_4) to be used for Ge and GeSn growth via a UHV-CVD system [212–214]. The material characterization results revealed that low temperature Ge growth results in relatively lower material quality, while GeSn grown under the same condition displays much better crystal quality. It has been assumed that the reaction between GeH_4 and $SnCl_4$ is an exothermic reaction that supplies increased energy to the growth of the films [216]. Therefore, the introduction of the diluted $SnCl_4$ could significantly improve the material quality. However, no evidence so far has been given to support this assumption during the growth of GeSn. In addition, since the high Sn incorporation was desired for GeSn-based devices, the study of growth for dilute Sn materials has been overlooked.

In this dissertation, the growth of dilute GeSn using GeH_4 and diluted $SnCl_4$ as Ge and Sn precursors are reported, respectively. The growth of Ge was performed under the same growth conditions for comparison. The ratio of GeH_4 and $SnCl_4$ was held constant at 500:1. The optical and material characterization showed the improved material quality of GeSn compared to that of Ge. Moreover, the exothermic chemical reaction during the GeSn growth was investigated.

3.1.1 Growth and Characterization of Dilute Sn Films

3.1.1.1 Growth

All material growth work was done using p-type Si (001) 4-inch wafers as substrates. The wafers were processed using standard piranha etch and HF dip prior to growth as described in previous work [213]. Material growth was carried out in a cold wall UHV-CVD chamber with base pressures below 10^{-9} torr. Low temperature Ge growth was accomplished using GeH_4 as a precursor and Ar as the carrier gas. The corresponding gas flow rates were kept at 10 sccm and 25 sccm, respectively. The dilute GeSn was grown by introducing $SnCl_4$ with a gas flow rate of 0.02 sccm in addition to the low temperature Ge growth recipe. The growth temperature was kept below 400 °C to be consistent with CMOS process compatibility for all growths. The growth pressure was fixed at 0.5 torr. The growth time varied from 10 minutes to 120 minutes to extract nucleation time and the growth rate.

3.1.1.2 Characterization

A J.A. Woolam spectroscopic ellipsometry V-Vase tool was used to measure the change in the polarization of light as it reflects from a material to extract the film thickness, which was subsequently used to analyze the growth mechanism. Material characterization was performed using a Phillips X'pert Pro x-ray diffractometer (XRD). The symmetric (004) 2θ-ω rocking curves and asymmetric (2-24) reciprocal space mapping (RSM) were measured by which the crystalline material, and in-plane ($a_{\parallel}$) and out-of-plane ($a_{\perp}$) lattice constants were obtained. Room temperature PL measurement was carried out to study the film quality and emission peak shifts due to the Sn incorporation. A 1064 nm pulsed laser with 5 ns pulse duration and 45 kHz repetition rate was used as an excitation source, and the emission was collected by a spectrometer equipped with a thermoelectrically cooled PbS detector with response cut-off at 3.0 μm.

3.1.2 Dilute GeSn Material and Optical Properties

Figure 3-1(a) shows the time-dependent Ge film thickness grown at the temperatures of 320, 340, and 350 °C. The solid points are measured data and the solid lines are linear fitting, which show the well-consistent growth of the films up to 60 minutes. This stability of growth suggests that the decomposition of GeH_4 into GeH_x radicals is constant at a given temperature. As temperature increased, thicker films were obtained as expected.

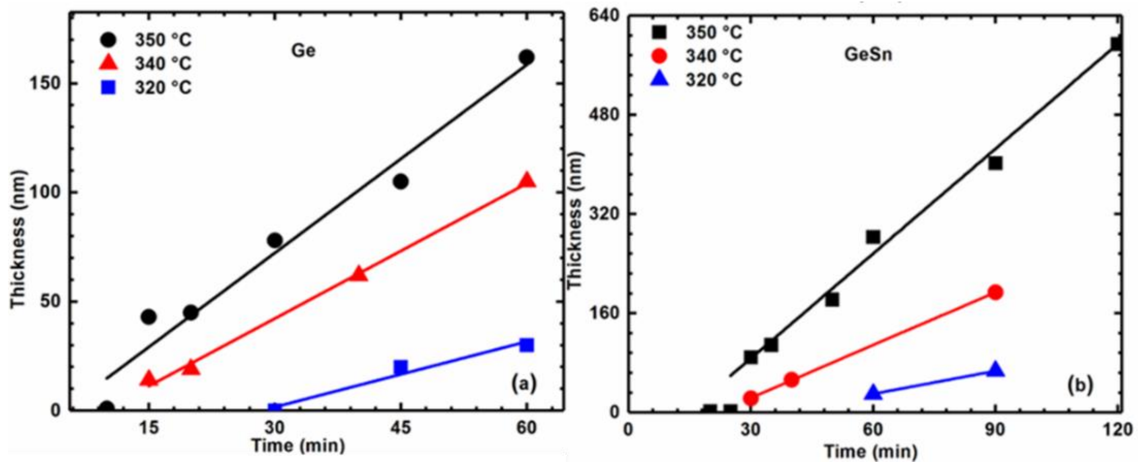

Figure 3-1: Thickness dependence on the growth time of low temperature growth of (a) Ge and (b) GeSn. The solid points are measured data and the solid lines are linear fitting to extract the average growth rate.

Figure 3-1(b) shows the GeSn film thickness grown under the same conditions. The well-consistent growth of the GeSn films was also obtained. Note that the measured GeSn films are much thicker than the Ge films, which is mainly due to the introduction of diluted $SnCl_4$.

Figure 3-2(a) plots the temperature-dependent growth rate that was derived from the linear fitting shown in Figure 3-1. It can be seen that at 350 °C, the growth rate of GeSn is double that of Ge. Decomposition of GeH_4 into GeH_x radicals is expected to be the same for both GeSn and Ge at the same temperature. Therefore, it indicates that incorporation of Sn into

the lattice is responsible for the increased growth rate. Figure 3-2(b) shows the nucleation time during the film growths and their dependence on temperature. The nucleation time was determined by extrapolating the growth rate fit line to zero. The solid points are measured data and the solid lines are linear fitting. The nucleation time for GeSn is always greater than that of Ge at the same growth temperatures.

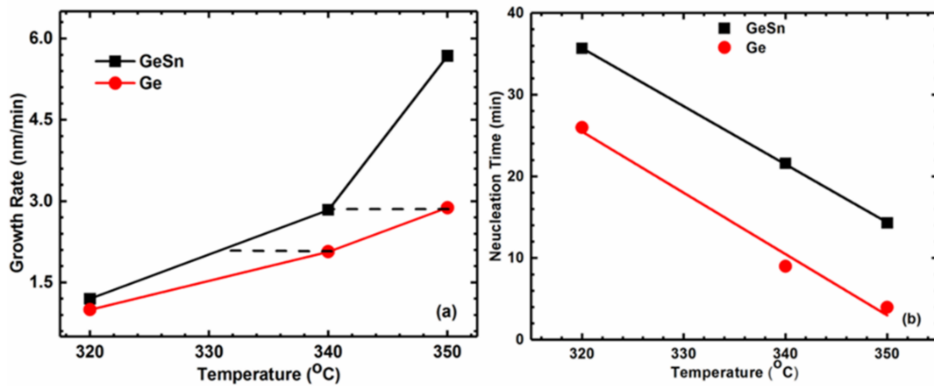

Figure 3-2: (a) The derived growth rate for low temperature Ge and dilute GeSn film growth. (b) The extracted nucleation times of the films and their dependence on decreased temperature.

The increased nucleation time is attributed to dilution of GeH_x radicals by $SnCl_x$ radicals and the HCl byproduct in the system, which is an etchant gas for Ge [217]. As the growth temperature decreases both Ge and GeSn display increased nucleation times. Heirlemann et al. showed that temperature and pressure were two key factors that control the decomposition of GeH_4 [218]. Decrease of the temperature would decrease the amount of GeH_x radicals that are available to nucleate on the surface and, therefore, prolong the time to fully nucleate. The symmetric (004) 2θ-ω scans of low temperature Ge and GeSn are given in Figure 3-3.

The 2θ-ω scans of Ge films with growth temperatures of 350, 340, and 320 °C shown in Figure 3-3(a) exhibit Ge-Ge peak intensities of 264, 42, and 6, respectively. In comparison the 2θ-ω scans of GeSn films plotted in Figure 3-3(b), show the corresponding peak intensities of 3903, 120, 25, respectively. In all cases the peak intensity of GeSn is higher than that of Ge.

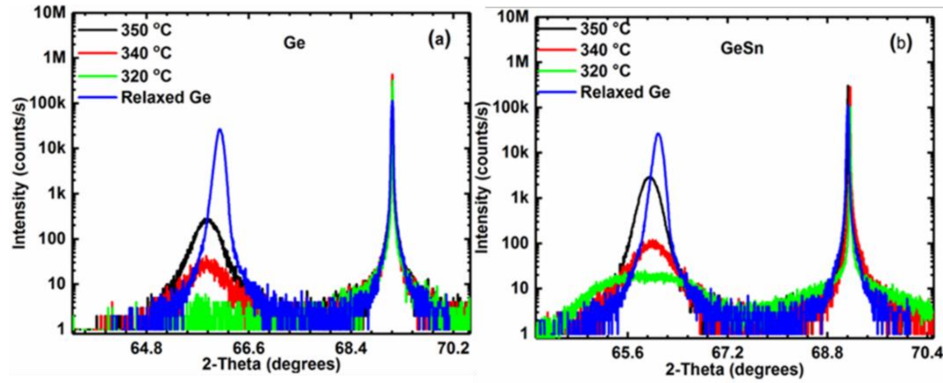

Figure 3-3: XRD 2θ-ω scans of (a) Ge and (b) GeSn films. A high-quality relaxed Ge reference grown on Si using an optimized two step growth recipe was also plotted for comparison.

Moreover, the material quality can be also examined by the full width half max (FWHM) of the Ge or GeSn peaks in XRD rocking curves. Ge exhibits FWHM of 0.357°, and 0.478° at 340 and 350 °C growth temperatures, respectively (the signal–to–noise ratio of the 320 °C peak was too small for an accurate estimation); while the GeSn FWHMs were extracted as 0.246°, 0.287°, and 0.887° at 350, 340, and 320 °C growths, respectively. It is well known that the large lattice mismatch between Ge/GeSn and Si results in high defect density during the material growth at low temperatures. Intuitively, the GeSn would feature lower quality due to the larger lattice mismatch than Ge, however, the opposite phenomena was observed according to the peak intensity and line-width study mentioned above. The increased crystallinity of GeSn can be explained by the presence of Cl on the wafer surface which could act as a surfactant due to its lower surface energy [174]. Surfactants are able to improve the crystal growth in low temperature semiconductors by enhancing the mobility of surface ad-atoms.

Compared to the Ge reference that was grown on Si using an optimized two step recipe, the GeSn peaks for all samples feature a shift toward lower angles, which is a result of Sn incorporation and residual strain.

To further study the strain and optical properties of GeSn, two thick samples with growth

times of 90 and 120 minute and temperature of 350 °C were selected, which feature the film thicknesses of 450 and 600 nm (noted as sample A and B), respectively. To obtain the Sn composition and strain information, the asymmetrical RSM along the (2-24) plane was conducted and shown in Figure 3-4.

The Sn composition and strain in each film was calculated using a method reported elsewhere [219]. For samples A and B, the Sn compositions were calculated as 0.28% and 0.75%, respectively. The calculated compressive strains in sample A and B were 0.13% and 0.06%, which indicates that the GeSn films were almost fully relaxed.

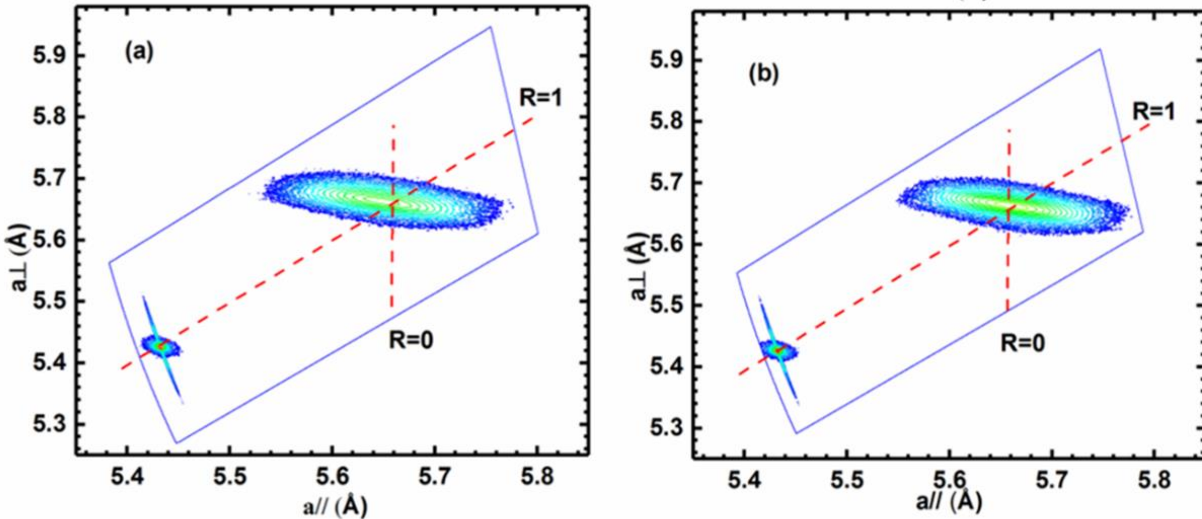

Figure 3-4: X-ray diffraction reciprocal space maps along (-2-24) plane of (a) sample A and (b) sample B. The R=1 and R=0 lines indicate the full relaxation and pseudomorphic (lattice match to Si).

PL characterization was performed on all grown samples. The low temperature grown Ge did not exhibit room temperature PL while GeSn films grown at 350 °C showed clear room temperature PL. Moreover, increase in GeSn film thickness showed increased PL intensity. Figure 3-5 shows the PL spectra of two selected GeSn samples. The black and red curves are measured data and Gaussian fittings, respectively.

In Figure 3-5, the PL peaks at 1625 and 1650 nm for samples A and B were assigned to the direct bandgap transitions according to theoretical study [220]. Compared to the direct peak of Ge at 1575 nm, these peaks shift toward longer wavelengths due to incorporated Sn.

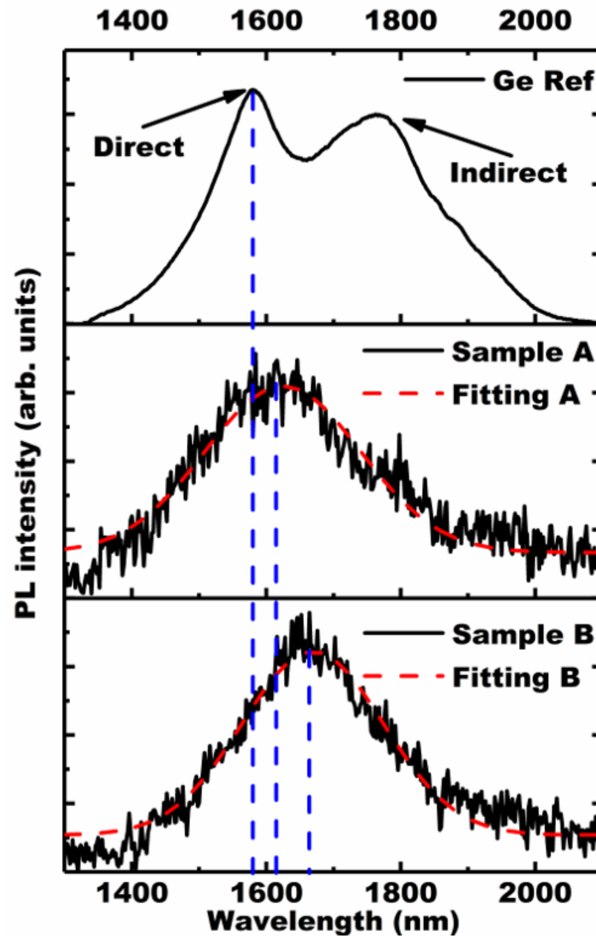

Figure 3-5: Stacked PL spectra of two selected dilute GeSn samples. The PL of Ge bulk reference is also poltted for comparison. The black and red curves are measured data and Gaussian fittings, respectively. The clear PL peaks at 1625 and 1650 nm were observed.

The red-shift of the PL peak associated with sample B compared to sample A was attributed to slight Sn compositional difference and to reduced strain due to the increased film thickness. For samples A and B, since their film thicknesses were beyond the critical thickness of 4.2% lattice mismatch between GeSn and Si [221], the materials became relaxed, and therefore both increased Sn incorporation and relaxation contributed to the peak shifting from

Ge. Unlike Ge bulk reference, the indirect peak was not observed from samples A and B due to their thin film thicknesses. Moreover, the clearly observed PL spectra at room temperature indicated the relative high material quality.

3.1.3 Exothermic reaction during the growth of GeSn using $SnCl_4$

The results show that GeSn had increased crystallinity and higher growth rates compared to Ge. While factors such as Cl surfactant effect or alloy formation temperature can account for increased crystallinity, another important factor such as thermal effect also plays an important role. It has been mentioned that the chemical reactions used in the deposition of Sn-base materials are exothermic in nature [216]. An exothermic reaction could transfer generated heat to nearby GeH_4 molecules allowing for increasing decomposition. This would account for the increased growth rates in GeSn.

The higher growth rates and increased crystallinity of GeSn growth observed in this study suggest that the major reaction, i.e., $GeH_4 + SnCl_4 \rightarrow GeSn + 4\,HCl$, is naturally exothermic. This is observed as a temperature increase in the outflowing gas from the system. Growth rates suggest an effective 10 °C temperature difference in the growth condition between GeSn and Ge within target growth temperatures in this study. For instance, the growth rates of Ge at 340 and 350 °C (2.0 and 2.4 nm/min) are almost equal to that of GeSn at 330 and 340 °C, as shown later by the dashed line in Figure 4-2(a). The generation of heat is expected to be dependent on the $SnCl_4$ flow rate as its decomposition energy is much lower than GeH_4. This suggests increasing $SnCl_4$ incorporation complicates the growth of the material, as the temperature control of substrate during the low temperature growth would be a challenge. However, the excess heat generated offers a possibility to improve the material quality.

3.1.4 Summary and Conclusion

Dilute GeSn was grown at low temperature using diluted $SnCl_4$ (0.02 sccm flow rate) as Sn precursor via cold-wall UHV-CVD and compared with the Ge growth under the same condition. By investigating the temperature-dependent growth rate and nucleation time, the material growth mechanism to explain the improved material quality of GeSn over Ge was provided, and which were confirmed by XRD and PL measurements. In addition, this study provided the evidence of an exothermic reaction occurring during the deposition of GeSn. Based on this analysis, it is believed that this reaction produced HCl as a by-product of the precursor gases. The material and optical characterization results suggested excess heat was provided at the wafer surface to improve the growth conditions [222].

3.2 Ge Buffers on Si Substrate

3.2.1 Limiting Factor of Strain on Incorporation

The incorporation of Sn into the Ge crystalline lattice expands the lattice constant, induces compressive strain in the material, and is a limiting factor in the final Sn composition [223]. The >4.2% lattice mismatch between Si and GeSn inherently increases the strain in the growing films resulting in poor quality and low composition. To overcome this initial barrier to growth Ge buffers are used to provide a larger lattice constant as a virtual substrate for the growth of GeSn or other GeSn based alloys.

There are three main methods of growing high-quality Ge on Si: (i) graded SiGe step buffers, (ii) two-step plus annealing, and (iii) aspect ratio trapping. Graded SiGe step buffers are created by growing multiple layers from low composition SiGe to Ge. These layers have been shown to produce Ge buffers with threading dislocation density (TDD) of ~10^6 cm^{-2} [224]. However, these layers are very thick with average thicknesses of several micrometers. The two-step plus annealing method of producing high-quality Ge on Si involved a low temperature step,

to avoid islanding, followed by a high temperature step and annealing [225]. This method has produced Ge layers with TDD in the mid to upper 10^6 cm^{-2}. The layer thickness of the buffer produced by this method can be 1 um or less. Aspect ratio trapping involved depositing a layer of SiO_2 onto the Si substrate. Once deposited a window needs to be opened to the Si substrate with widow depth over width ratio >1 [226]. The main angle of propagation of threading dislocations generated from the growth of Ge on Si is 45° from the substrate surface. When the depth is greater than the width the 45° threading dislocations terminate at the SiO_2 sidewall. This allows for a layer of defect free material to grow above the defective region. However, this growth method doesn't produce a single high-quality Ge layer for use as a virtual substrate due to defects generated where the lateral over-growth merges.

This research used a two-step method as described above. However, due to technical issues, the annealing step could not be accomplished. Even with this barrier, high-quality Ge buffers on Si were produced.

3.2.2 LT/HT Growth Method

The development of Ge buffers was rapid, and the goal was to produce a suitable platform for the growth of GeSn. It was not to have a fully optimized recipe to produce the best quality material the chamber can produce. A balance had to be found between speed of development and material quality. Therefore, a metric based on desirable properties was developed to include, relaxed film, shiny surface, and PL intensity comparable to bulk Ge substrate.

The first step in the growth was to grow a low temperature step to avoid islanding thus producing a relaxed layer. The second step involved a high temperature step to produce high quality Ge for the upper most layer. The growth performed in this research was at 1 torr of

pressure with a first step growth temperature was between 300 and 400 °C. The second step was grown between 500 and 600 °C. Each growth corresponding to a separate set of conditions for only one of the steps. The GeH_4 flow rate for the high temperature step was half that of the low temperature step.

3.2.3 Optical/Material Characterization

The optimal recipe developed produced a buffer with total thickness just over 1 μm with a low temperature layer thickness of 250 nm. Using 375 °C for the low temperature step and 600 °C for the high temperature step, a smooth shiny surface was produced with good PL (Figure 3-6).

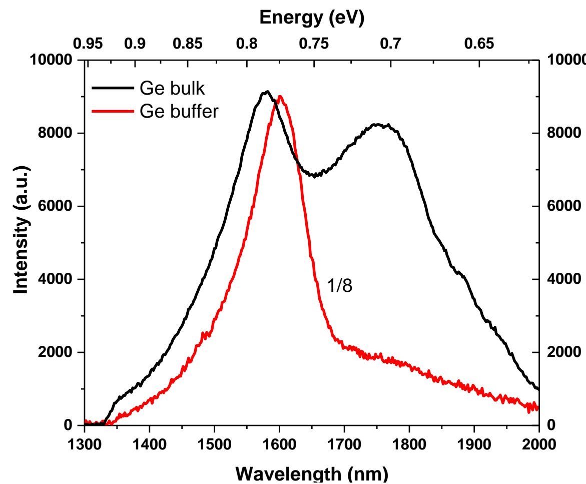

Figure 3-6: Room temperature PL from Ge bulk reference and Ge buffer.

The room temperature PL indicated high quality material because the peak intensity of the Ge buffer was on the same order of magnitude as the Ge bulk reference. The indirect peak was not observed. The shifting of the peak to longer wavelengths was due to tensile strain built up in the layer. This occurred because the thermal expansion coefficient for Si is 2.6 x10^{-6} cm °C^{-1} and for Ge is 5.9 x 10^{-6} cm °C^{-1}. This means that the high temperature growth of the Ge layer results in tensile strain being developed in the material as it cools. Strain in these samples

was estimated to be between 0.15 and 0.2%, which is comparable with the community. [227] Temperature dependence was completed on the sample and shown in Figure 3-7 with extracted information in Figure 3-8.

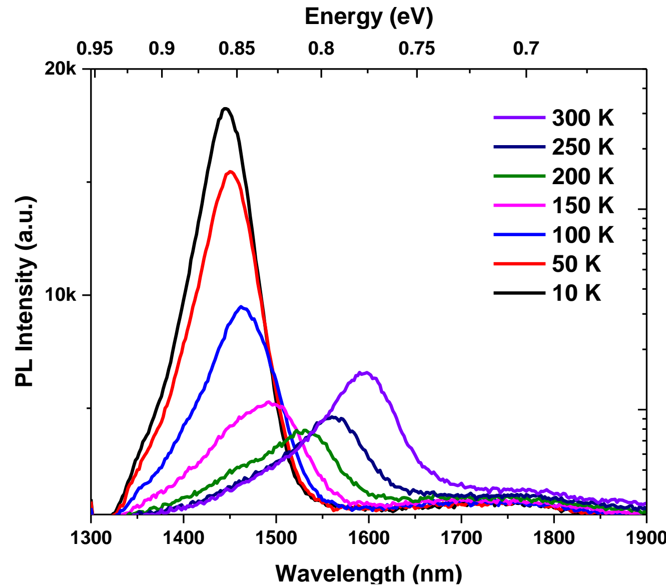

Figure 3-7: Temperature dependent PL of the Ge buffer.

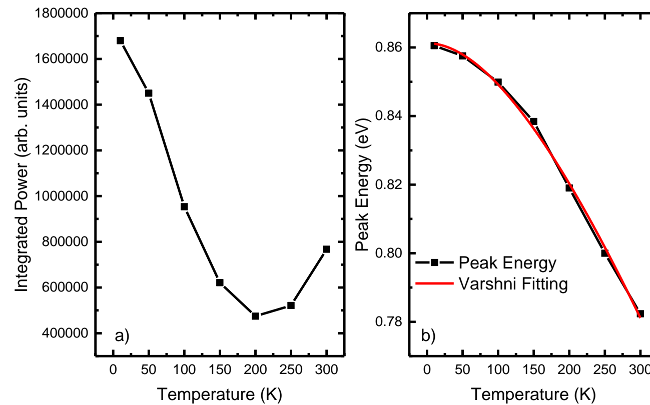

Figure 3-8: (a) The extracted integrated PL Intensity and (b) peak energy. The peak energy has been fit using a Varshni fitting.

The dominant direct bandgap emission peak was fitted for integrated PL intensity and the peak energy. The integrated PL intensity shown in Figure 3-8(a) initially decreased with increasing temperature before rising again. This is typical of indirect bandgap semiconductors

and is explained as follows. Low temperatures freeze out defects allowing for more efficient radiative recombination. As the temperature increased, the defects became more influential thus reducing the integrated PL intensity. Near room temperature thermal energy given to the electrons increased carrier population of the direct band and increased the radiative recombination. The direct bandgap peak was fitted for peak position and fitted with Varshni fitting, Figure 3-8(b).

$$E_g = E_0 + \frac{\alpha T^2}{T+\beta} \qquad \text{(Equation 3-1)}$$

The parameters for the Varshni equation are as follows: E_g is the bandgap energy at a given temperature; $E_0$is the bandgap energy at 0 K; α is the first Varshni parameter; β is the second Varshni parameter; T is the given temperature. The Varshni fitting of the temperature dependent direct bandgap peak position resulted in the following parameters. E_0 is 0.861 eV, α is 6.8 x 10-4 and β is 464. These values are consistent with those produced by the direct bandgap in Ge [228]. The room temperature power dependent PL was accomplished and is shown in Figure 3-9.

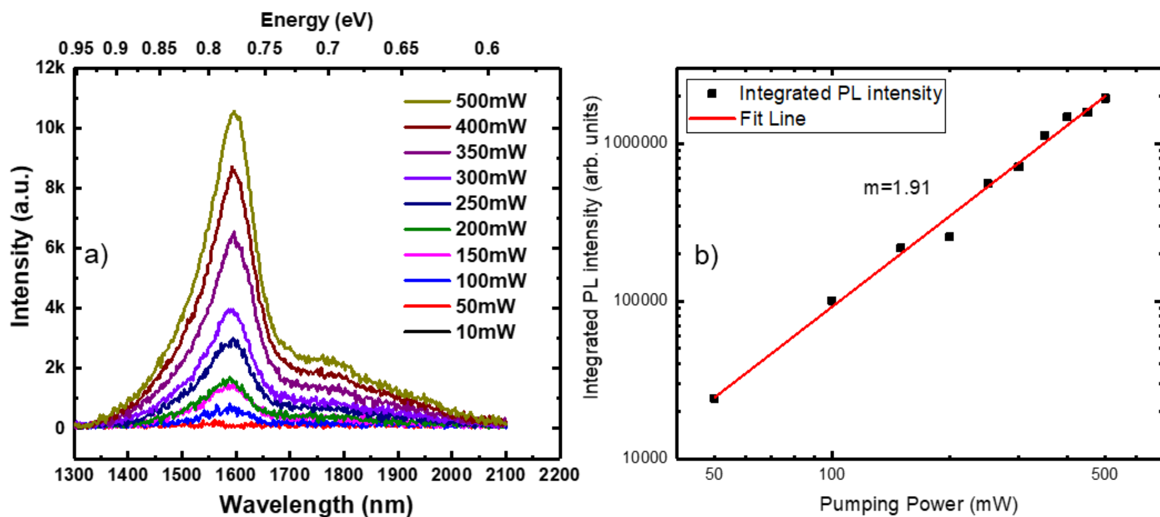

Figure 3-9: (a) Room temperature power dependence and (b) integrated PL Intensity vs. pumping power on Ge buffer.

The room temperature PL pumping power dependence shown in Figure 3-9(a) illustrates high-quality material as the PL signal could still be seen at low pumping powers. During the development phase of growth, most PL was accomplished at 500 mW of pumping power to achieve reasonable signal. However, with the optimized growth condition, the material quality was improved to the point that PL signal could continue to be observed down to 25 mW of pumping power. Figure 3-9(b) shows the log-log plot of the extracted integrated PL as a function of the pumping power. It has been shown by Riordan et al. [229] and Lieten et al. [230] that a fitting slope near 2 shows that the recombination is dominated by Shockley-Reed Hall (SRH) non-radiative recombination.

The PL characterization performed on the Ge buffer suggested high quality material. However, threading dislocation density (TDD) is a better gauge for material quality. It has been shown that optimized growth methods produce TDD in the ~10^5-10^6 range. To perform the estimation of TDD, etch pit counting was performed (Figure 3-10).

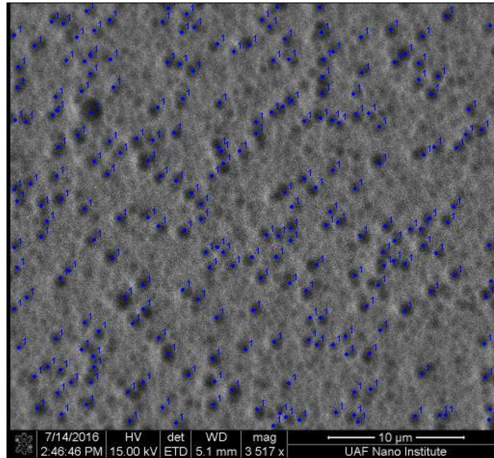

Figure 3-10: Scanning electron microscope image of pits that were etched in the surface. The pit counting visible with dots and #1 beside the pit.

The etch pit counting shown in Figure 3-10, estimated a TDD ~1.1 x 10^7 indicating high-quality Ge buffers grown on Si substrate. The additional annealing step prescribed in the high-

quality Ge buffer growth should result in TDD in the 10^6 range consistent with currently reported high-quality buffers [225]. However, even without the annealing step, the buffer quality should be good enough for growth of GeSn.

3.2.4 UHV-CVD Grown Buffers on Si for GeSn Growth

This section reports on the growth and development of Ge buffers for GeSn growth. An optimized 2-step growth method was successfully developed. Even with the lack of annealing in the samples, the as-grown sample displayed PL intensity only 1/8 of a bulk Ge substrate. Temperature dependence illustrated the nature of indirect materials with an initial decrease in PL integrated intensity until ~200 K before increasing at higher temperatures. Power dependent PL measurement showed SRH non-radiative recombination to be the dominant recombination mechanism in Ge buffers. Etch pit counting in the Ge buffer surface suggested TDD of 1.1 x 10^7. High-quality buffers were successfully developed for the growth of GeSn.

3.3 Plasma Enhanced Growth of GeSn on Si Substrate.

3.3.1 Plasma Enhancement

Growth of GeSn is inherently difficult due to the issues described in Section 3.2.1. Adding to this complexity is that GeH_4 decomposition is extremely poor at low temperatures and has been the main reason for the use of Ge_2H_6 as the Ge precursor in the CVD growth of GeSn. Hierlemann et al showed that temperature and pressure were dominant in the decomposition of GeH_4 [218]. RF plasma was considered to provide localized heating to GeH_4 molecules thus assisting decomposition.

Growth was accomplished similarly to the dilute Sn research described in Section 3.1. In this growth, the plasma system described in Section 2.1 was utilized to generate the plasma. The

temperature effect on growth rate and crystallinity was examined at it gives evidence of increased decomposition of GeH_4 as well as a transition from crystalline to amorphous material. The growth temperature was varied from 225 to 400 °C. The flow rate of $SnCl_4$ was varied to gain insight into changes in the growth due to increasing Sn precursor. All growths were kept at 0.5 torr pressure and 20 minutes growth time to show the enhanced growth rate over that of non-plasma GeSn. For these growths, 50 W of plasma power was used and no sample rotation was performed. Shorting in the plasma system prevented lower power and sample rotation. This was repaired for later growths.

3.3.2 Results/Discussion

The plasma enhanced growth was primarily focused on the increased decomposition of the GeH_4 precursor. It was shown in the dilute GeSn and low temperature Ge comparison completed in Section 3.1 that GeSn grew slowly and growth times took up to an hour to grow several hundred nanometers and at temperatures below 320 °C, no growth occured. Ellipsometry measured thickness and Raman shift for the temperature dependent plasma growths are shown in Figure 3-11.

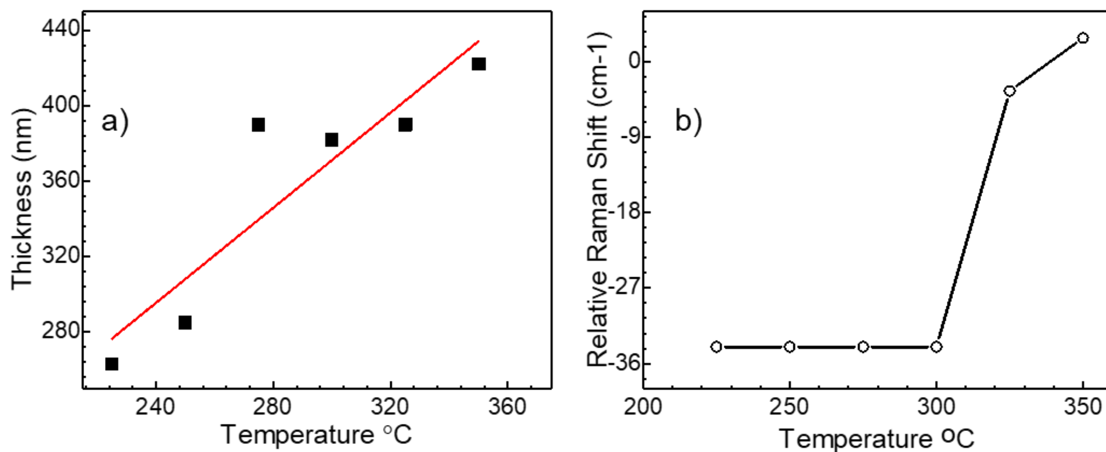

Figure 3-11: Temperature dependence of a) GeSn film thickness and b) relative Raman shift for the GeSn grown films.

In Figure 3-11 a), the film thickness dependence on growth temperature is shown. As the temperature increased, the GeSn films increased in thickness as well. The increase in growth temperature increased the thermal decomposition of GeH_4 allowing for much faster growth rates. It was estimated that the growth rate increased 200 to 400 times over that of non-plasma GeSn growths. The relative Raman shift in Figure 3-11b) shows a reduction in Raman peak position from 350 to 325 °C which could be attributed to Sn incorporation, however, from 300 to 225 °C the relative Raman peak shifts 34 cm^{-1} and remained constant. This was indicative of the crystalline to amorphous transition in Ge [231].

While there is no current study on amorphous GeSn, it is anticipated that low composition GeSn should act similar to Ge. Therefore, while the growth rate was enhanced, single crystallinity was lost at reduced temperatures. The flow of $SnCl_4$ was varied from flow rates used in non-plasma growths to increasing values to examine the effects on the growth. PL was demonstrated from the growth and a sample is shown in Figure 3-12.

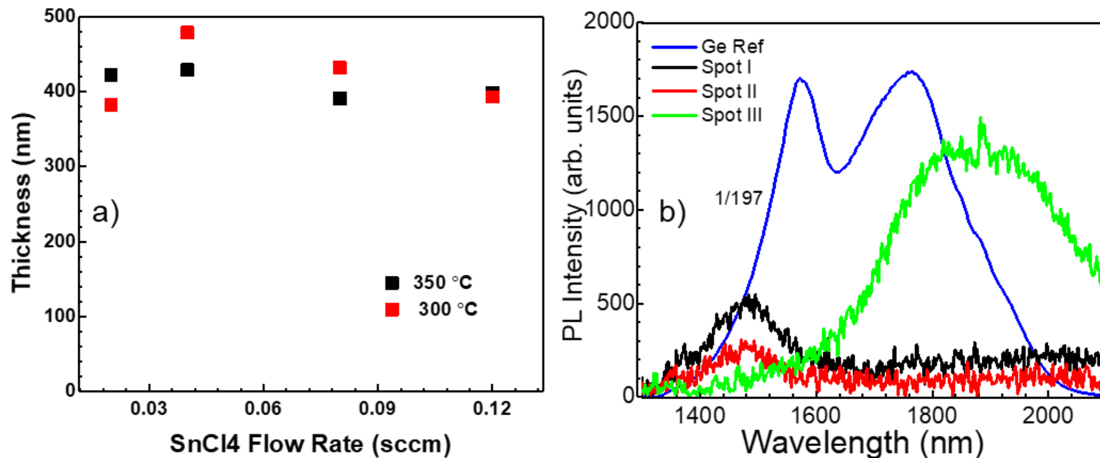

Figure 3-12: a) Plasma enhanced GeSn film thickness with increasing flow rates of $SnCl_4$. b) Example PL from the GeSn plasma enhanced growth.

It was previously shown that applying plasma enhancement breaks down the GeH_4 precursor efficiently resulting in 200 to 400 times growth rate. Examination of the effect of

increasing the $SnCl_4$ flow rate is shown in Figure 3-12a). It can be seen that minor fluctuations in the thickness were noted, however, the overall trend in the thickness range remained constant. While this range was still small, 1 sccm $SnCl_4$ flow rate was attempted with a resulting GeSn film thickness of ~900 nm. This suggests that increasing the $SnCl_4$ flow rate should have increased the film thickness. It has been noted in non-plasma growth that this trend is similar [223]. The PL shown in Figure 3-12b) consists of three consecutive measurements starting in the center and working radially outward. It can be seen that the center and middle of the growth emission was near 1500 nm. However, the edge showed extension of the wavelength to ~1900 nm, which was evidence of Sn incorporation. The edge of the growth was further examined to confirm the shift in wavelength was due to Sn incorporation. The XRD rocking curve for the sample is shown in Figure 3-13.

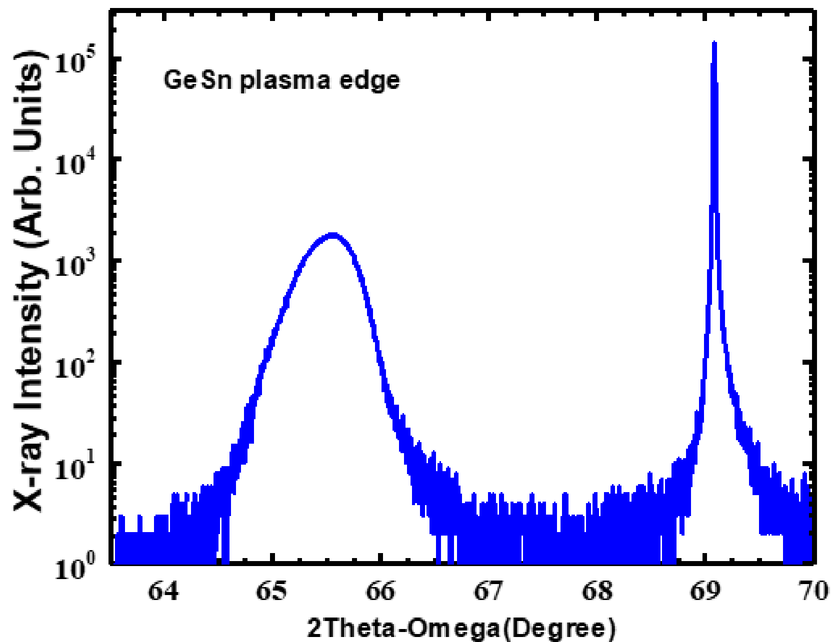

Figure 3-13: The XRD rocking curve of the edge of GeSn plasma enhanced growth.

The XRD rocking curve shown in Figure 3-13 has two distinct peaks. The first peak at ~69 degrees was attributed to the Si substrate while the peak at ~ 65.5 corresponds to the GeSn

peak. This was shifted to lower angles from the Ge peak that would show up ~66 degrees. This was further evidence of Sn incorporation near the edge of the wafer. The XRD intensity was similar to that noted in the dilute growth, however, the FWHM of 0.436° was larger than that of the dilute work. This was evidence of more defective material that could be attributed to using the 50 W plasma.

3.3.3 Plasma Enhanced Growth of GeSn Near 5% Sn on Si

The plasma enhancement did show increased decomposition of GeH_4 evidenced as increased growth rate of GeSn thin film over their non-plasma counterpart. The change in crystallinity below 325 °C could be attributed to high growth rates not allowing Ge and Sn ad-atoms time to find optimal sites to form single crystal material. Large dynamic range of $SnCl_4$ flow rate was observed with increasing thickness at flow rates if 1 sccm. The incorporation of Sn into the growing films was evidenced by PL and XRD rocking curves suggesting a Sn percentage of ~5%. Further refinement of the plasma enhancement technique could result in lower temperature deposition of GeSn films on Si with increased incorporation. This work has shown the potential of the low temperature plasma enhanced growth of GeSn films on Si, thus paving a new avenue toward the growth of the GeSn material.

3.4 Summary

This chapter has described the growth of GeSn on Si. This resulted in material with low Sn compositions. The differences between low temperature grown Ge and GeSn were examined. The growth rate of GeSn was faster under similar conditions but had a delay in the nucleation compared to that of low temperature Ge. GeSn produced higher quality material even to producing PL which was unseen in the low temperature growth of Ge. It is suggested that the $GeH_4 + SnCl_4 \rightarrow GeSn + 4HCl$ reaction is naturally exothermic adding excess heat in the

growing reaction.

The second section described the development of a Ge buffer for high-quality GeSn growth. A standard two-step recipe was used to grow the buffers. However, the annealing step could not be completed. Temperature and pump power dependent PL suggested high-quality Ge buffers with RT PL only being 1/8 of the Ge bulk reference. Etch pit counting suggested TDD of ~ 1.1×10^7 thus adding one more piece of evidence to show high-quality buffer growth.

Lastly, plasma enhanced growth was accomplished on Si substrates. Increased growth rates of 200 to 400 times were observed over the non-plasma growth. Large dynamic range of $SnCl_4$ flow rate was obtained showing increased growth rates with large increases in $SnCl_4$ flow rate. Effective Sn incorporation was shown in PL and XRD measurements with Sn incorporation ~5%.

Chapter 4 UHV-CVD Growth of GeSn on Ge Buffers

4.1 GeSn on Ge Buffered Si substrate

Progress in group IV photonics over recent years has elevated the GeSn material system to the forefront of photonic integration on Si substrates [229–232]. Demonstrations of true direct bandgap GeSn, LED, and lasers show the budding potential of the GeSn material system [176, 205, 215, 235, 236]. Applications based on this technology could flood the photonics market with inexpensive and efficient light emission/detection devices and systems based on these devices.

Growth of GeSn on Ge is difficult due to low solubility (<1%), and instability of α-Sn above 13 °C. In order to grow GeSn material, growth techniques were developed under non-equilibrium growth conditions such as low temperature growth via either MBE [206–210], or CVD [140, 211–214]. The CVD growth of GeSn has been investigated over a decade. Various Sn and Ge precursors in conjunction with carrier gasses were used attempting to achieve high Sn incorporation and high material quality. Early growths were carried out using deuterium-stabalized stannane (SnD_4) as the Sn precursor [141], whose high cost and instability drove the motivation to seek other Sn precursors. It has been reported that tin-tetrachloride ($SnCl_4$) is a low cost, stable, and commercially available precursor and the GeSn material growth was initially demonstrated by Vincent et al. [154]. On the other hand, various hydride chemistries have also been explored as Ge precursor by Kouvetakis et al. [141]. Higher order germanes were commonly used due to their favorable decomposition at low temperatures [212]. Recent progress has allowed for low cost germane (GeH_4) to be used for Ge and GeSn growth via UHV-CVD system [212, 213, 236, 237]. The growth of GeSn material detailed in the previous growths showed the material properties of the grown films, however, no result has yet

demonstrated the entire development to high quality GeSn material. The goal of this work was to detail the development of high-quality GeSn material on the Ge buffer. The effect of growth temperature and the overpressure of $SnCl_4$ were examined. Adjustment of the growth recipes to produce high-quality GeSn was examined in detail. Control in the growth of GeSn was achieved with the dominant mechanisms to produce high-quality films of prescribed thickness and composition identified. While conditions change between different growth chambers, the method used to develop high-quality GeSn could be applicable across chambers.

4.2 Growth Method

All material growth work was done using p-type Si (001) 4-inch wafers as substrates. The wafers were processed using standard piranha etch and HF dip prior to growth as described in our previous work [213]. Material growth was carried out in a cold wall UHV-CVD chamber with base pressures below 10^{-9} torr. Growth was accomplished using GeH_4, $SnCl_4$ as precursors and Ar as the carrier gas. All GeSn growth was accomplished on Ge buffers grown as prescribed in Section 3.2 prior to GeSn thin film growth.

Determination of a starting point for the growth of GeSn on Ge buffers was determined using previous growth studies to understand the mechanism behind the growth. In Section 3.1, understanding of the nature of both low temperature Ge and GeSn were examined. The growth of each of these materials reduced the size of the growth matrix used for GeSn on Ge buffers. The growth of low temperature Ge determined pressure ranges that were useful for GeSn growth. The GeSn growth on Si shown in Section 3.1, developed understanding of the gas supply ratios, temperatures, and time needed for growth to occur. With the understanding of needed parameters, a growth matrix was formed, as shown in Figure 4-1. In Figure 4-1, the narrowed growth window was derived from previous growths shown in Chapter 3. The blue and green

dashed lines represent the narrowing of the growth matrix, with the red dotted lines showing the pathway taken to produce high quality GeSn. Two arrows show the starting point for the growth as well as when a clear surface was achieved. The appearance of the clear surface was the first characteristic of reaching growth conditions required for high quality GeSn material. The growth was divided into two batches with the first batch to examine the growth temperature dependence on Sn incorporation as well as the effect of $SnCl_4$ overpressure.

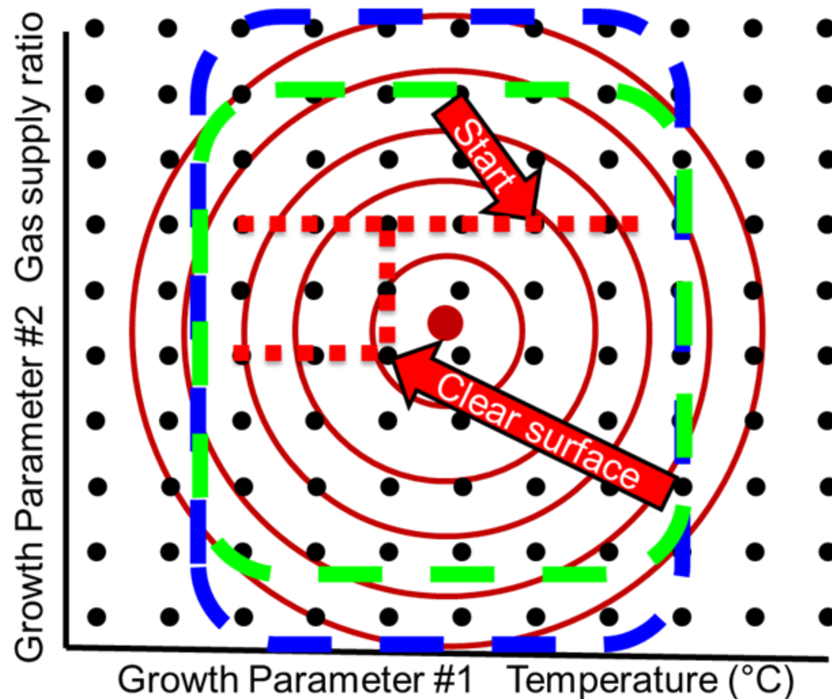

Figure 4-1: Growth matrix of GeSn on Ge buffers. Matrix narrowing from growth understanding is illustrated. A starting point and path to high quality GeSn is shown.

The second batch developed high-quality GeSn, examined the precursor supply fraction ratios, and used the gained information to continue to push Sn incorporation higher. The growth temperature of GeSn was kept below 350 °C consistent with CMOS process compatibility. The growth pressure was fixed at 2 torr. Growth times for the first batch were kept at 30 minutes while the second batch was increased to 60 minutes.

4.3 Growth Temperature Dependence with $SnCl_4$ Overpressure

A series of successive growth were accomplished to verify the temperature dependence on Sn incorporation [5]. These temperatures were varied from the starting point determined by the growth of previous materials shown in Section 3.2. Verification of Sn incorporation was accomplished using PL and XRD with the results shown in Figure 4-2 and tabulated in Table 1.

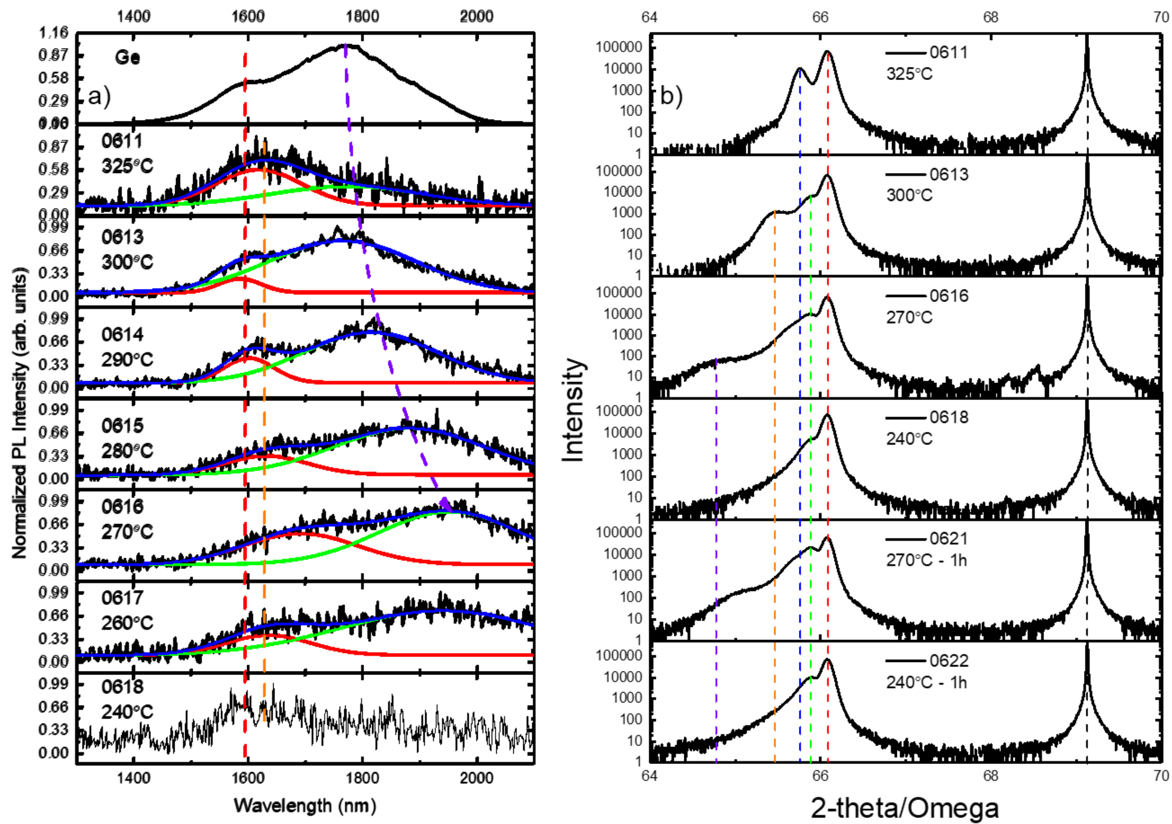

Figure 4-2: a) PL of growth temperature dependent GeSn. b) Selected XRD of growth temperture dependent GeSn.

In Figure 4-2a), the growth temperature dependent PL shows shifting of the PL wavelength to longer wavelengths, however, below 260 °C the PL disappeared. It can be noticed besides the shifting of the wavelength, there seemed to be a separate peak. This was thought to be from the Ge buffer initially, however, the PL wavelength was shifted beyond the buffer emission. This suggests that a separate layer of low composition Sn may have been present.

XRD shown in Figure 4-2b) agrees with the PL in that as the growth temperature decreased the GeSn peak shifts to lower angle, indicating increased Sn incorporation. Below 325 °C, another peak appeared and remained throughout the rest of the temperature reduction. This peak didn't change with growth temperature reduction. Further investigation of this phenomenon was done to understand the effect of $SnCl_4$.

Table 1: Characterization results of the temperature dependent growth of GeSn.

Sample #	Growth temp	PL peak	Ellips cut-off	XRD peak
0611	325°C	1618/1776	1770	65.76
0613	300°C	1586/1764	1770	65.89
0614	290°C	1601/1814	1630	
0615	280°C	1631/1881	1940	
0616	270°C	1691/1952	1840	65.85/64.79
0617	260°C	1636/1939	1790	65.87
0618	240°C	0	2040	65.87
0619	220°C	1590	1570	
0620	240°C	0	2010	
0621	270°C	1874	2130	65.88/65.02
0622	240°C	0	1800	65.87

Selected samples from the first batch were investigated further to better understand the low Sn peak seen in XRD. To further investigate this peak, XRD-RSM was performed as well as TEM. The results from three chosen samples are shown in Figures 4-3, 4-4, and 4-5.

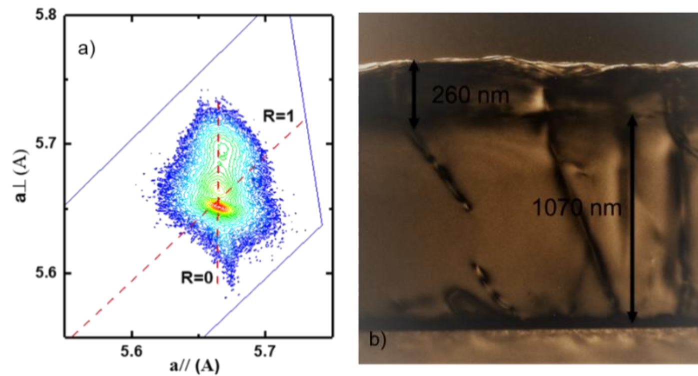

Figure 4-3: XRD RSM and TEM of 0613 grown at 300 °C for 30 mins.

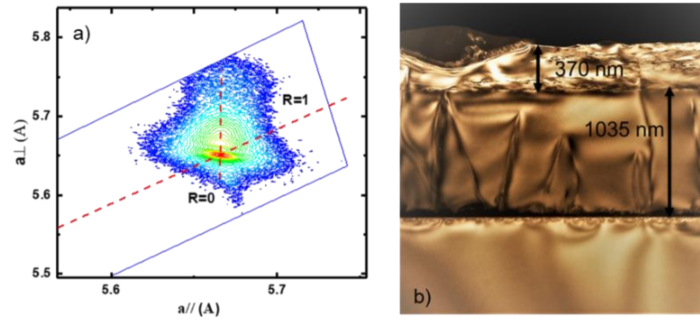

Figure 4-4: XRD RSM and TEM of 0616 grown at 270 °C for 30 mins.

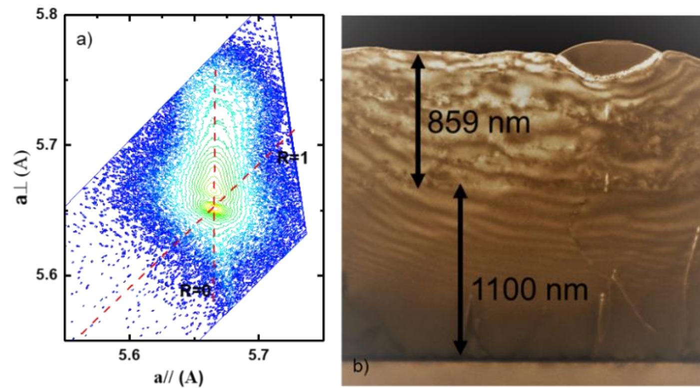

Figure 4-5: XRD RSM of 0621 grown at 270 °C for 1 hour.

The XRD RSM for chosen samples showed a psuedomorphic layer at low composition, (1% Sn), as well as some relaxation in a subsequent layer that corresponded to the growth temperature dependent composition. The maximum composition was measured at ~8% Sn incorporation for the 270 °C growth temperature. The samples were then imaged using TEM to see the structure. It can be seen in Figures 4-3, 4-4, and 4-5, the Ge buffer was consistently grown to be between 1030 and 1100 nm in thickness. Also seen in the TEM are areas of surface segregation of Sn that forms into droplets on the surface. Examination of the layers and surface segregation was performed using the TEM-EDX measurement to estimate the Sn composition in each layer. There was no Sn in the buffer, approximately 1% Sn in the layer, a pure Sn droplet,

and the temperature dependent layer formed between the dot and 1% layer. This suggests that the overpressure of $SnCl_4$ depleted the Sn from the growing layer and segregated it on the surface. This could have been due to lower surface energy of Sn causing it to agglomerate on the surface instead of incorporating into the growing film. To improve growth conditions the amount of $SnCl_4$ available needed to be reduced.

4.4 Growth Optimization

The first batch of GeSn on Ge buffered Si samples was plagued by $SnCl_4$ overpressure. Reduction of this overpressure was required to incorporate more than the 1% Sn layer shown in the first batch of samples. To fully understand the effect of $SnCl_4$ and GeH_4 in the growth of GeSn, the ratio of gas flow rates was calculated. The calculation showed that the first batch was grown under a $SnCl_4$ flow fraction of 2.9×10^{-3}. This value was two orders of magnitude above that which has been reported in the growth of high quality GeSn [240]. Therefore, a series of growths were performed to reduce the $SnCl_4$ gas supply fraction. These growths were done using the same temperature, pressure, and time. The precursor and carrier gas flow rates were adjusted to reduce the $SnCl_4$ partial pressure. In this process, the gas supply fractions were calculated for each step and $SnCl_4$ precursor flow was reduced to the lowest level that could be achieved under the system configuration. The precursor supply ratios are given in Table 2.

It is seen in Table 2, that the $SnCl_4$ gas supply ratio was reduced by an order of magnitude from the starting condition to the clear surface state. The initial growth condition showed Sn surface segregation and, by SnCl4 reduction, resulted in the elimination of surface Sn and gave clear films. The largest disadvantage of the Sn supply reduction was that the Ge supply was also reduced from 25% to 7% of the gas mixture resulting in thinner films. Visual images of the samples are shown in Figure 4-6.

Table 2: $SnCl_4$ Gas Supply Ratios for growth optimization

	Initial state	Test 1	Test 2	Test 3
$SnCl_4$ gas supply ratio	2.9×10^{-3}	1.4×10^{-3}	4.5×10^{-4}	2.3×10^{-4}

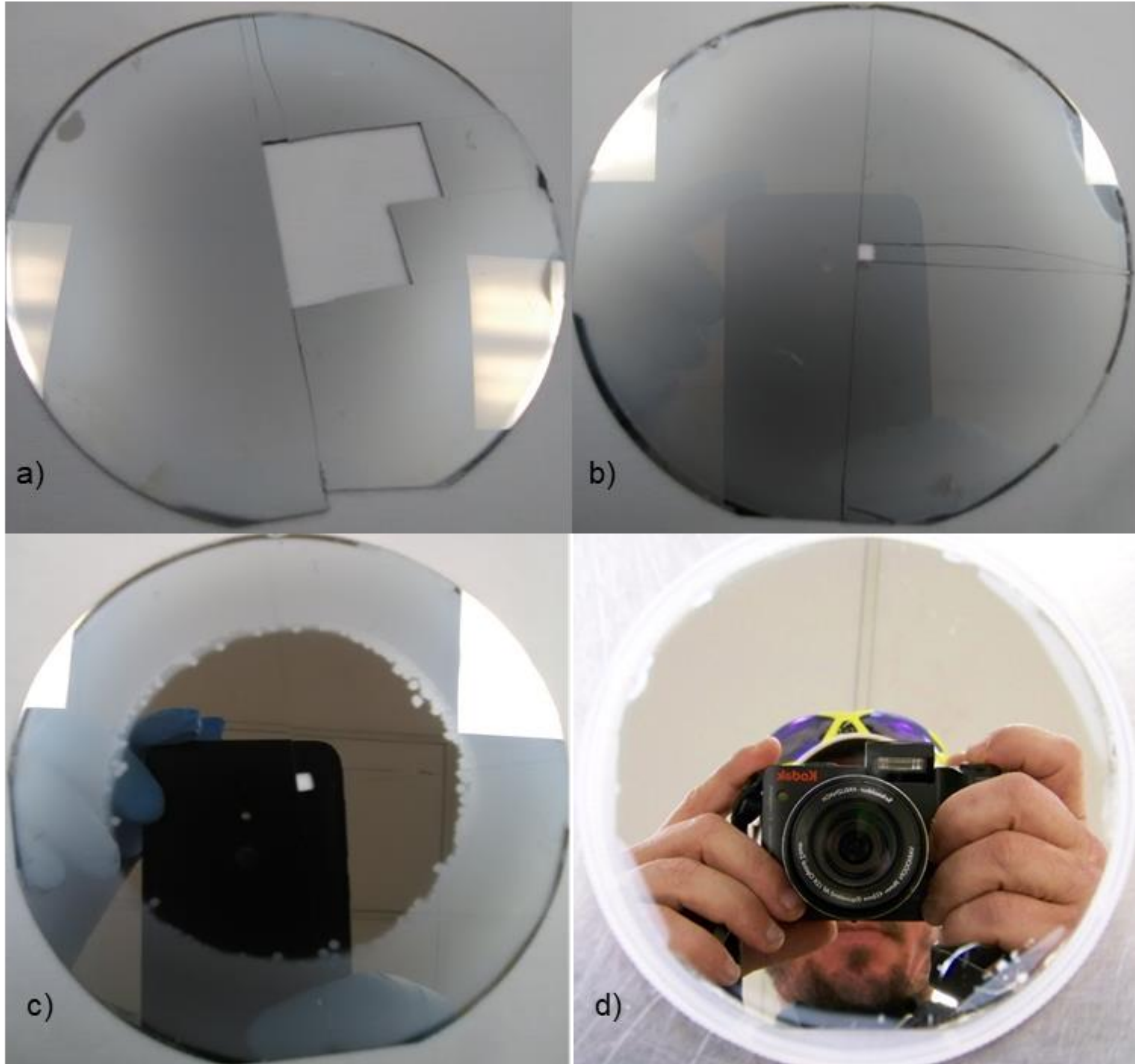

Figure 4-6: Images of the sample surface after each Sn reduction test. a) Initial state, b) Test 1, c) Test 2, and d) Test 3.

Directly imaging the sample surface shown in Figure 4-7 gave evidence of successful Sn reduction. Pieces were taken of initial state, Test 1, and Test 2, for other measurements before

imaging was accomplished. It can be seen in the initial state and Test 1 that the wafer surface was still cloudy with surface Sn segregation. However, by Test 2 the wafer center was clear with only the outer edge being cloudy with surface Sn. Test 3 showed mirror-like sample surface across the full wafer. This showed that there is a window which the upper limit on $SnCl_4$ flow fraction from Test 2 was 4.5 x 10^{-4}. Test 3 showed clearer sample surface so the upper limit $SnCl_4$ flow fraction was just set to show where the surface Sn was removed, and the wafer surface began to clear. This did not verify that all the Sn was removed from the surface. As stated before, Test 3 reduced the $SnCl_4$ flow fraction to the lowest possible level using current precursor control methods. To further reduce the $SnCl_4$ flow fraction another method will need to be adopted that can adjust the precursor flows to acceptable levels. One method to accomplish this will be discussed in a later chapter. To further gauge improvement of optical quality, PL on the samples was completed and shown in Figure 4-7.

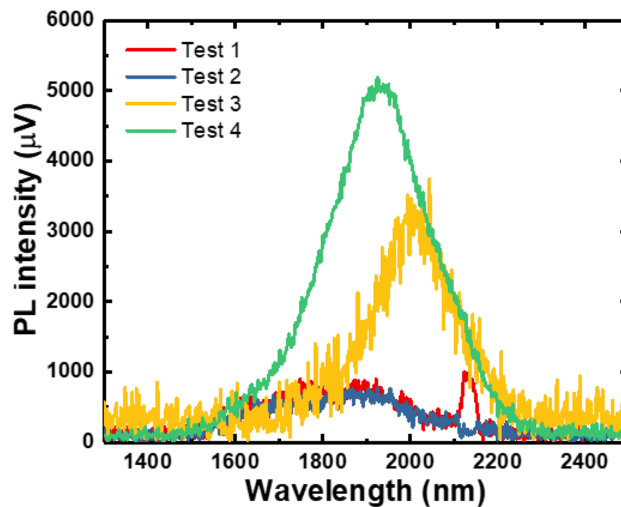

Figure 4-7: PL of the Sn reduction testing.

One gauge of material quality can be seen in the PL from each sample of the Sn reduction tests shown in Figure 4-7. The first two tests have PL signal that is similar. The extra peak seen from Test 1 was due to the second laser harmonic from the 1064 nm pumping laser. Test 2

showed increased PL intensity and shifting to increased wavelengths. This suggests increased incorporation with the Sn surface reduction and higher optical quality of the sample. Test 3 showed increased PL intensity over that of Test 2 indicating higher optical quality, however, the PL peak was shifted back toward shorter wavelengths. The film thickness from Test 2 was more than that of Test 3. Thinner GeSn film should have increased compressive strain which would blue shift the wavelength. Another contribution to the shifting could have been minor compositional changes in the growth. To check for compositional changes, XRD from the Sn reduction testing was completed. Test 1 was omitted from the XRD measurement shown in Figure 4-8 due to the optical properties between the initial state and Test 1 being similar.

The XRD rocking curves contained in Figure 4-8 show similar peak position for all samples regardless of the mass flow fraction of $SnCl_4$ or GeH_4. Since all growths were performed at the same growth temperature, this shows that temperature was the dominant mechanism that determined Sn incorporation when starting from an initial strain state. The change of XRD peak position was <0.1 degrees suggesting the Sn composition between samples varied less than 1% and was most likely attributed to natural process variation in the growth chamber. More intense peaks from Test 2 and Test 4 and the disappearance of the 1% peak show better material quality and suggests that the Sn was incorporated into the growing film instead of agglomerating on the surface. Improvement in the growth conditions allowing for high-quality growth set the stage for continued GeSn growth to further increase the Sn incorporation.

More evidence of the effect of reducing the $SnCl_4$ overpressure can be seen in the surface of the grown samples. It was shown previously that $SnCl_4$ overpressure created droplets on the surface. Visually, as the $SnCl_4$ flow fraction reduced the cloudiness of the sample surface

cleared up and sample optical quality improved. A more in-depth look at the sample surface was accomplished using a scanning electron microscope (SEM). Figure 4-9 shows the SEM imaging of the sample surface of selected samples with different levels of cloudiness.

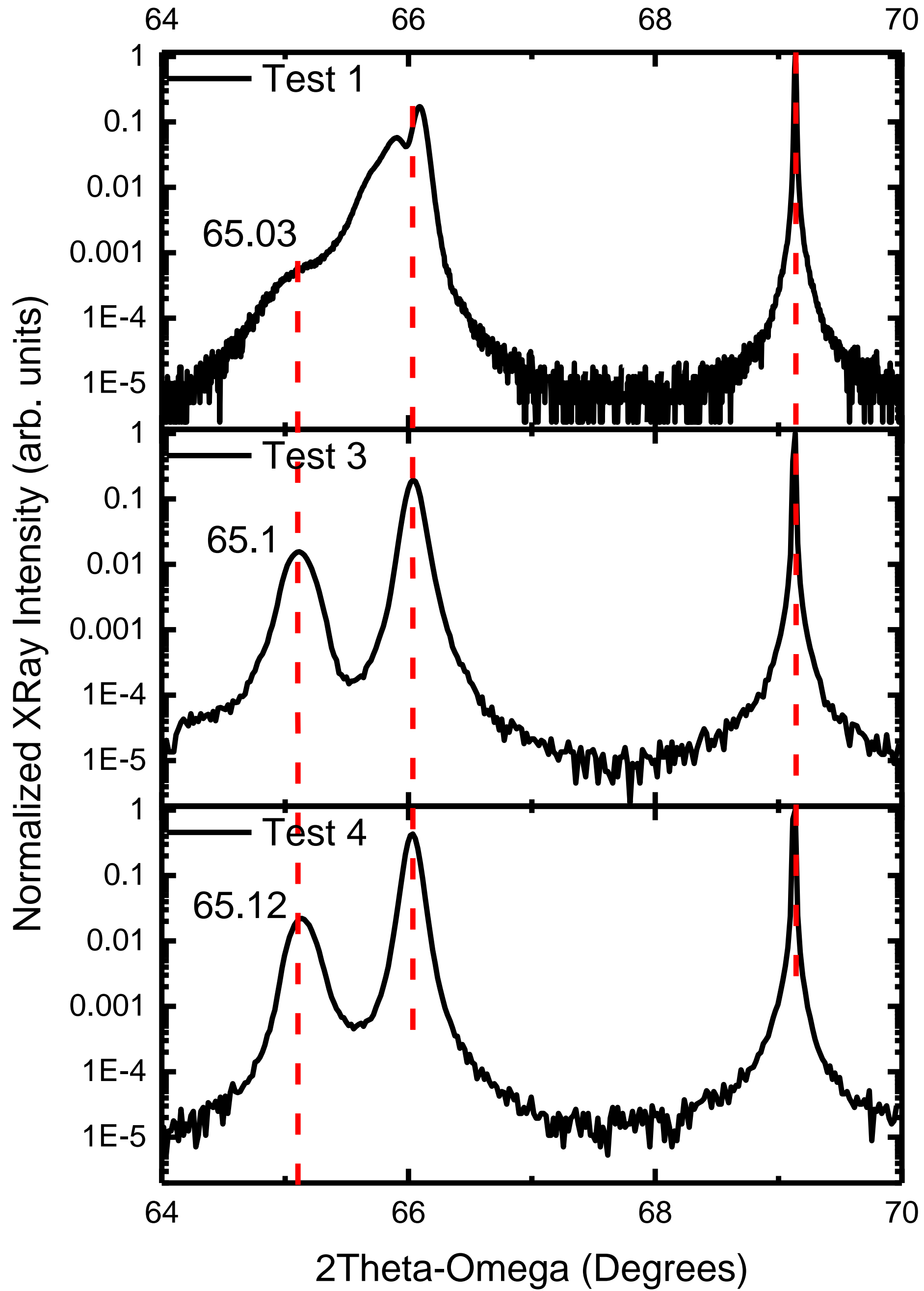

Figure 4-8: XRD rocking curves of the Sn reduction tests. Vertical dashed lines are used for ease of the eye to align the peak position. The GeSn peak angle is noted next to the curve.

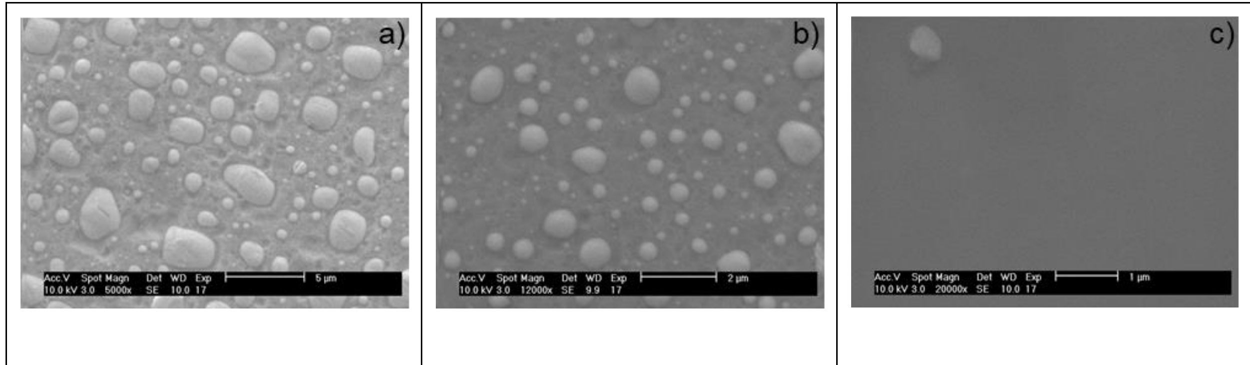

Figure 4-9: SEM imaging of selected sample surfaces: a) cloudy surface from the initial state, b) hazy surface Test 1, and c) clear surface from Test 3.

In Figure 4-9a), it is shown that the droplet size was large – up to 3 µm in diameter. Another interesting feature of the surface in Figure 4-9a) was that the surface appeared to have pits in the surface where Sn droplets look to have been. It is thought that the agglomeration of surface Sn attracted neighboring Sn forming the large clumps on the surface and leaving behind the pits. The hazy surface shown in Figure 4-9b) shows an accumulation of Sn droplets on the surface much like the surface from the initial state. However, the size of the droplet decreased to < 1 µm for the largest of droplets. It can also be seen in this figure that the pits left over were also reduced in size, supporting that the pit was left behind after Sn agglomerated on the sample surface. Figure 4-9c) shows a clear surface with only a single droplet in the image. From the image, it appears as the droplet has moved. This effect has been seen with GeSn and other materials that form droplets; Bi droplets are just one example. While the clear surface appeared to be almost free of droplets, it is fully anticipated that the droplets only continued to reduce in size and a more sensitive tool would be needed to measure them, such as atomic force microscopy (AFM). Improvement in growth conditions and a greater understanding of the precursor ratios required for high-quality growth set the stage for continued GeSn growth to further increase the Sn incorporation.

4.5 UHV-CVD Growth of GeSn up to 10% Sn

Upon optimizing the growth conditions, further growth temperature decreases were accomplished to further push the incorporation of Sn. Having already set the $SnCl_4$ dilution to the lowest possible level using the current system, reduction of the growth temperature resulted in the reduction the amount of GeH_4 decomposition and led to Sn forming back on the surface as shown in Figure 4-10.

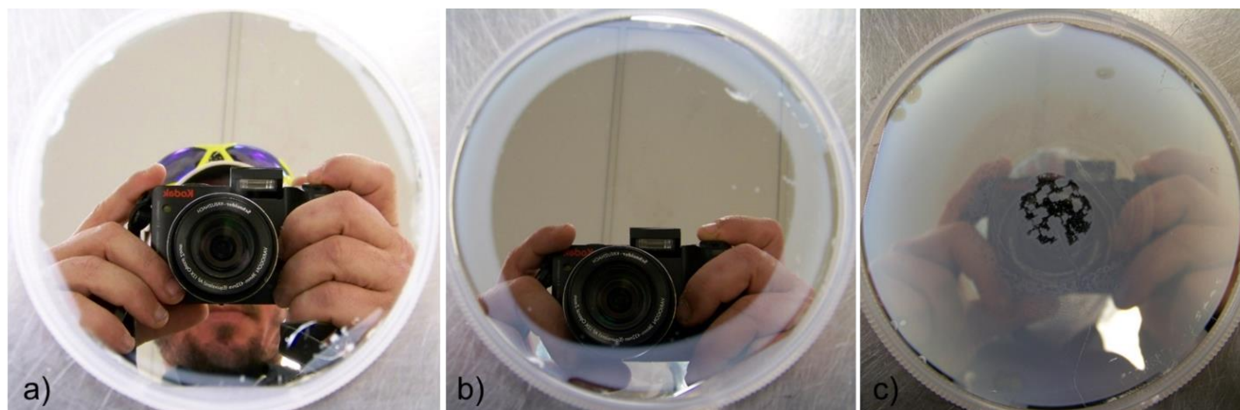

Figure 4-10: Images of the sample surfaces for the second batch of samples. a) 270 °C, b) 260 °C, and c) 250 °C.

It can be seen in Figure 4-10 that reduction of the growth temperature gradually increased the surface Sn, suggesting all $SnCl_4$ was decomposed already with GeH_4 being the limiting factor. The inability to further decrease $SnCl_4$ molar flow fraction limited the amount of temperature decrease to only 250 °C as further decreases would have driven growth back into the $SnCl_4$ overpressure regime. The grown films were further investigated for their optical quality using PL shown in Figure 4-11.

The decrease in growth temperature allows for extension of the PL wavelength. The PL shown Figure 4-11 continued to increase from 1924 nm grown at 270 °C to 2072 nm grown at 250 °C. The estimated Sn composition for 270 °C was ~8% Sn; further extension of the

wavelength suggests increased amounts of Sn incorporation between 9 and 10% Sn. The spectra were normalized due to lower signal intensity from the 250 °C growth as the surface agglomeration of surface Sn increased. Further confirmation of increased Sn incorporation is shown in Figure 4-12.

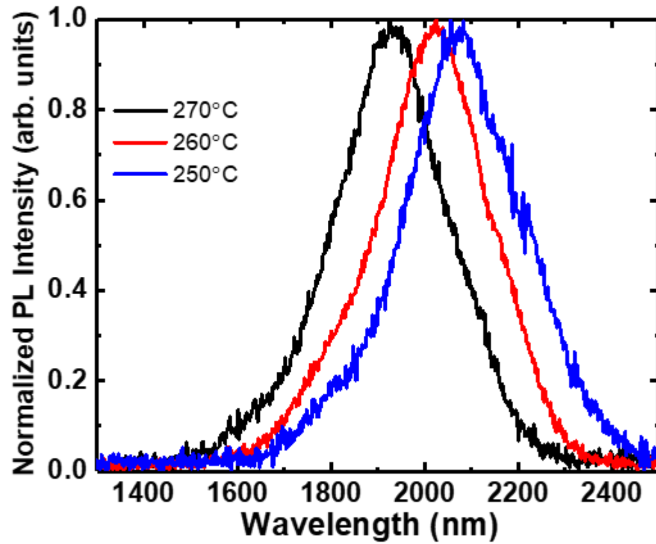

Figure 4-11: Normalized PL spectra from second batch of GeSn Growth.

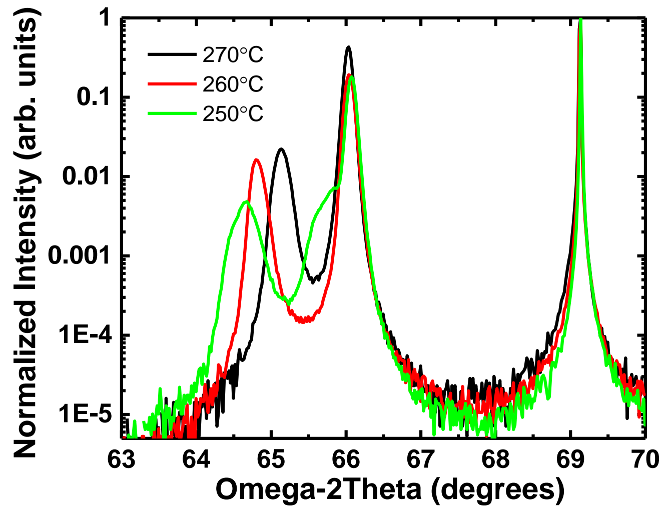

Figure 4-12: XRD rocking curves from the second batch of GeSn growth.

The increased incorporation of Sn is evidenced by the shifting of the XRD rocking curve peaks shown in Figure 4-12 to lower degrees. Once the 1% peak returned to the XRD spectra

the spectra linewidth increased with FWHM of 0.173°, 0.155°, and 0.242° for 270, 260, and 250 °C growths, respectively. It is also seen that with reduction in growth temperature the XRD peak shifted to lower angle supporting the extension of PL wavelength was due to Sn incorporation. It is also noted that the return of the peak near 1% Sn occurred with reduction in growth temperature as more Sn droplets covered the surface. This was evidence of the decreased breakdown of GeH_4 pushing out the limits the GeH_x/$SnCl_x$ incorporable species ratios. Again, this was expected due to the limitation of decreasing the $SnCl_4$ flow fraction.

4.6 Comparisons to Commercially Grown Material

One final metric used to estimate the quality of grown films was to compare those films to commercial films of similar structure and composition. For these comparisons un-doped bulk GeSn thin films were used. These were supplied by ASM America (Phoenix, AZ www.asm.com) and the results have been previously published [214]. Comparison of the XRD from ASM America and in-house grown (UAF, University of Arkansas, Fayetteville) (annotated ASM and UAF, respectively) samples are shown in Figure 4-13.

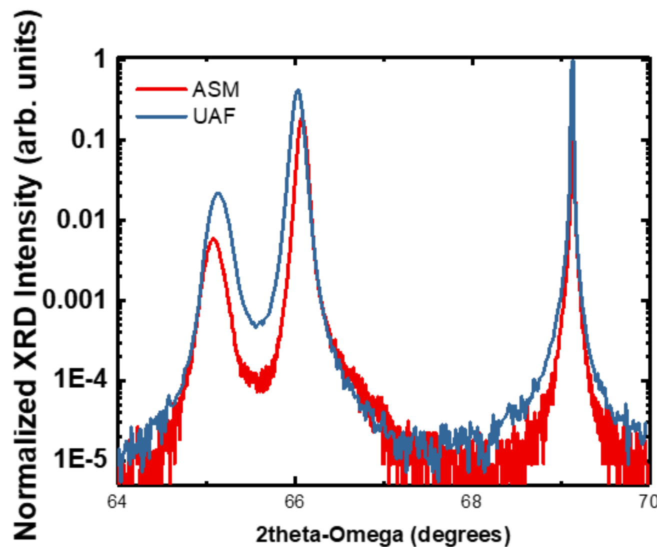

Figure 4-13: XRD rocking curves spectra comparing growth in this work to commercial material.

The XRD rocking curves, shown in Figure 4-13, indicate similar material composition as the GeSn peaks for each sample almost align. The narrower FWHM of the Ge buffer in the commercial sample, 0.080° vs 0.95°, suggests better buffer layers. This was expected as growth in this work did not use post growth annealing. However, the GeSn peak was more intense and had near the same FWHM as the commercial sample, 0.153° vs 0.173°. This suggested that the material quality of the UAF was getting close to that of the commercial sample.

The comparison was also extended to PL to determine how the optical quality compared to the commercial sample. By using this comparison to a growth method that produces device quality material, the quality of this work can be gauged. For the first batch of growths, the comparison could not have been made as different pump and detector combinations made up the PL characterization and did not display good enough quality for room temperature PL using the same pump source used for the commercial samples. After growth condition improvements, room temperature PL was accomplished on the 260 °C grown sample using the normal 1064 nm and 523 nm laser used for the commercial sample measurements as shown in Figure 4-14.

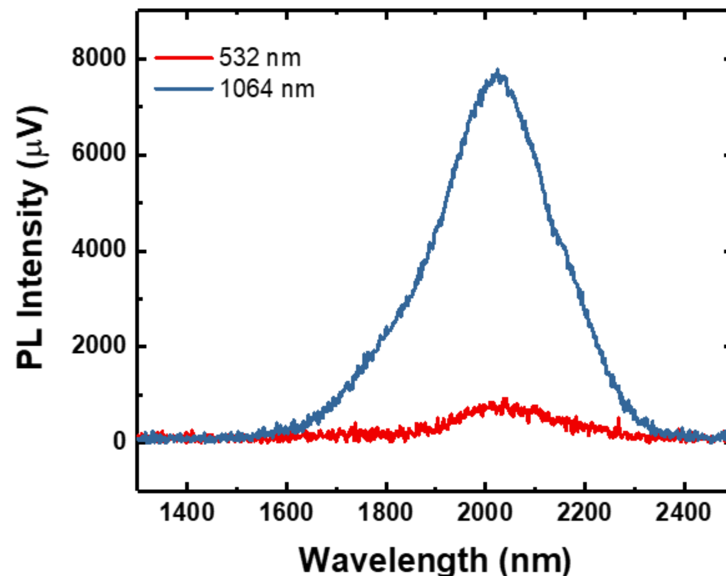

Figure 4-14: Room temperature PL of 260 °C growth under the improved growth conditions using the 1064 nm pulsed and 532 nm continuous wave pump lasers.

Signal strength using the 532 nm laser was more than 10 times less than that of PL signal using the 1064 nm laser, but this was due to the much higher photon injection (3 orders of magnitude) of the 1064 nm pumping laser. Having improved material quality to the point that it could be measured using the 532 nm laser gave a basis to use the same measurement conditions to proceed with the comparison. The temperature dependence of both the commercial and grown sample are shown in Figure 4-15.

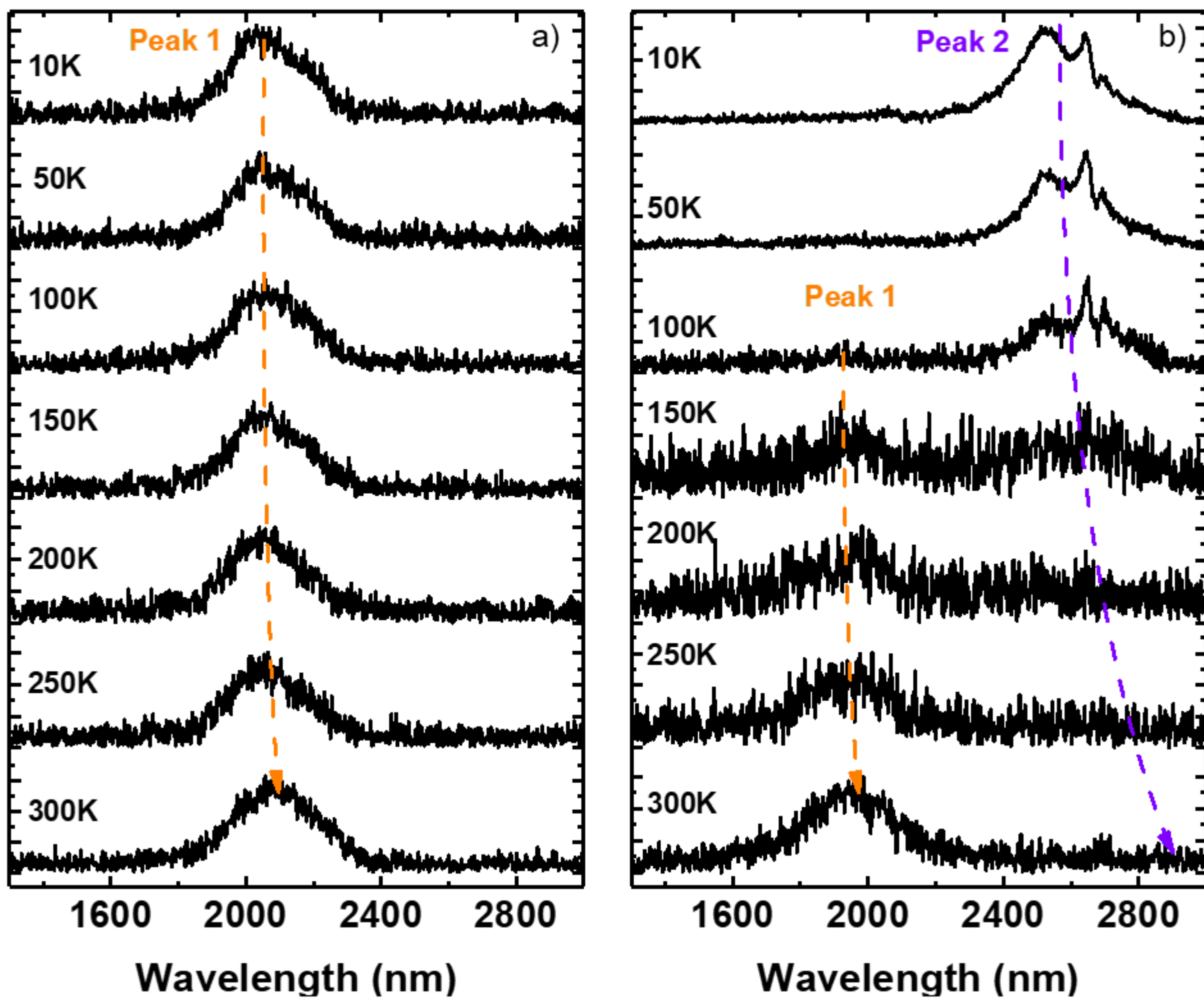

Figure 4-15: Temperature dependent PL of the a) commercial and b) grown sample.

The temperature dependent PL of the commercial sample in Figure 4-15a) shows a single

peak throughout all temperature ranges. However, the grown sample in Figure 4-15b) shows a multipeak spectra with a short wavelength peak showing up at higher temperatures and a long wavelength peak showing up at low temperatures. The single peak spectra in Figure 4-15a) emitted at a longer wavelength at room temperature indicating a bit more Sn incorporation which corroborates the extra shift seen in the x-ray diffraction. The Γ and L valleys may be close enough that there could be competition between the direct and indirect bandgaps.

However, with the multipeak spectra in Figure 4-15b), the Sn composition seen in the x-ray diffraction was less than that of the commercial sample thus suggesting it should be in-direct in nature. This was suggested by the temperature dependent PL seen for the short wavelength peak which increased with increasing temperature.

The long wavelength peak on the other hand decreased with increasing temperature. Since the spectra shifted with temperature, it suggested that the spectra were not defect related. Thus, it could be possible that another compositional layer could have possibly been present. This could be an indication of spontaneous relaxation enhancement shown for the GeSn material [174, 221]. If this did occur, the long wavelength peak could have been from a layer that had 12% Sn and thus be direct bandgap. This would be consistent with the PL measured, however, the sample would require more investigation to be certain.

4.7 GeSn Photoconductors

GeSn photoconductors were fabricated using the grown samples from the first batch of GeSn on Ge buffered Si growth. These devices were more to set a baseline for material growth than for high quality devices. Both coplanar and interdigitated photoconductors were fabricated and shown in Figures 4-16 and 4-17.

The spectral analysis of both sets of devices showed no real extension of the wavelength

with reduced growth temperature. This corroborates the 1% bulk layer suggested with the x-ray diffraction and TEM. All fabricated devices showed linear I-V curves. The interdigitated structures demonstrated higher photo response and lower resistance than the coplanar devices. These results were anticipated with these types of structures.

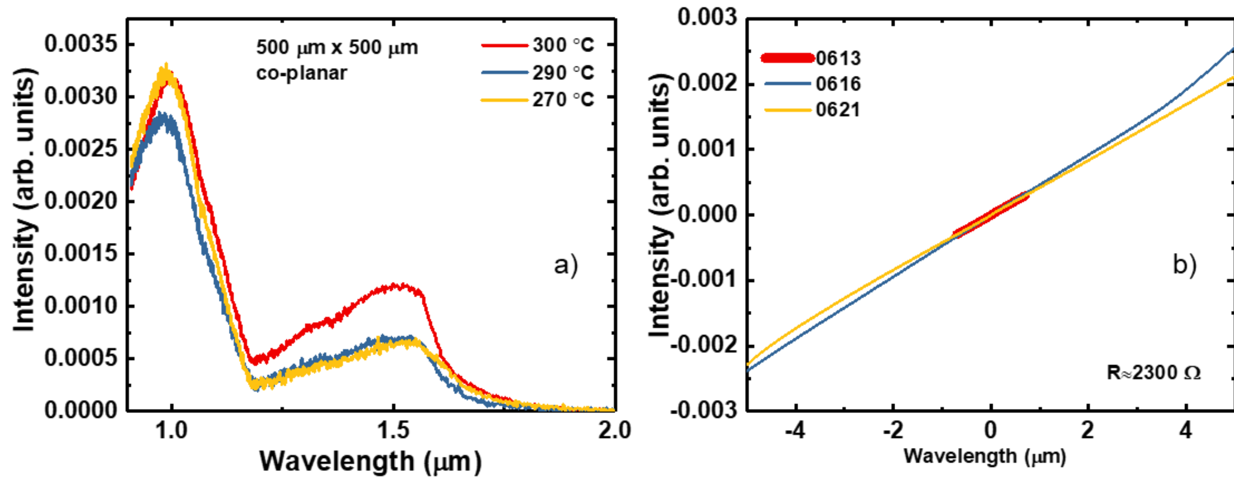

Figure 4-16: a) Spectral analysis and b) I-V curves for co-planar GeSn photoconductors fabricated from the first batch of samples.

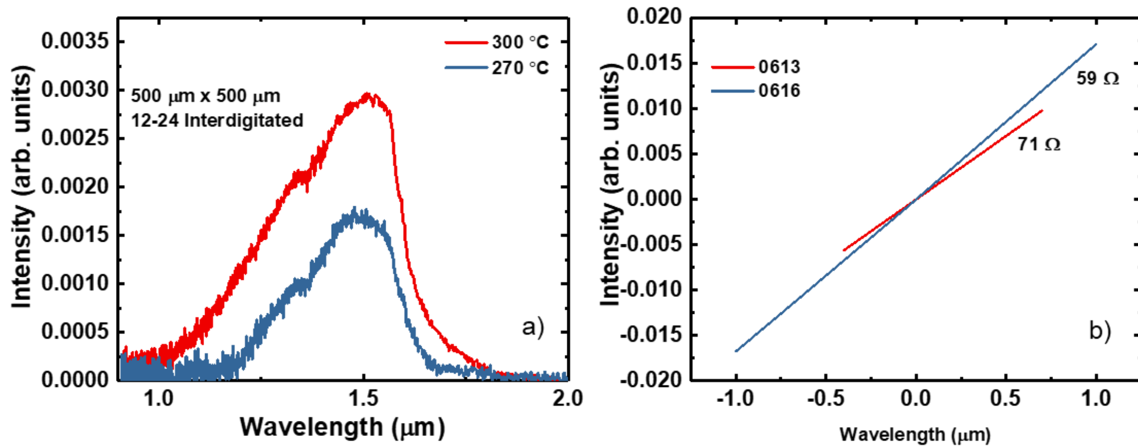

Figure 4-17: a) Spectral analysis and b) I-V curves for 12-24 Interdigitated photoconductors fabricated from the first batch of samples.

One sample after growth optimization was also fabricated into interdigitated photoconductors. The 8.5% sample had the detectivity (D*) calculated and plotted again the best

commercial GeSn currently available as well as the state-of-the-art detectors in Figure 4-18.

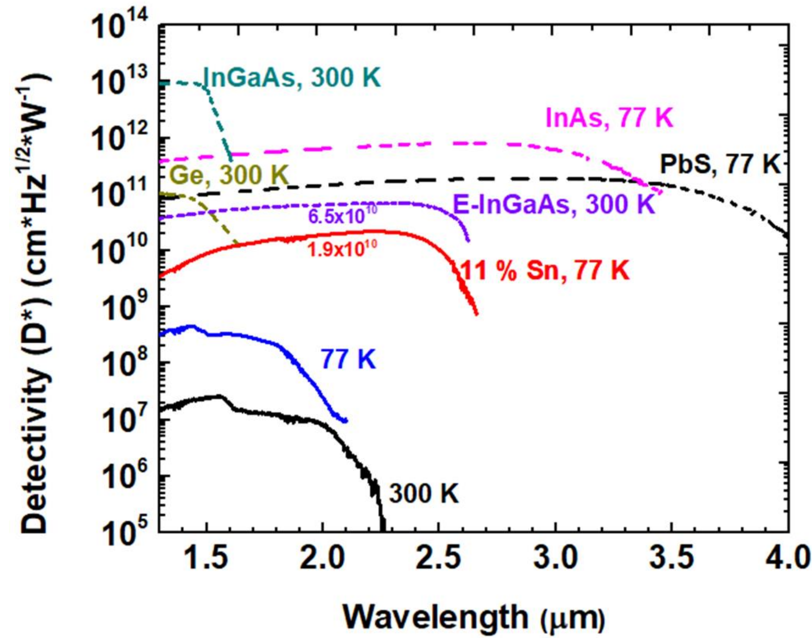

Figure 4-18: Photoconductor detectivity from optimized growth plotted again best GeSn and state of the art detectors.

In Figure 4-18, it is shown that for the grown sample which displayed PL in Figure 4-14, the detectivity was 2.5 $x10^8$. This was two orders of magnitude below the detectivity of the E-InGaAs and 11% GeSn photodetector. This was due to the sample being indirect bandgap and showed there was still room for material improvement. However, this result was comparable to detectivity from earlier work using the commercially grown materials [241]. This result showed growth in this research was on the right direction to catch up to the commercially grown material.

4.8 Discussion on Growth Technology and Precursors

The growth of GeSn has been accomplished in a variety of ways but mainly using MBE and CVD processes. High quality optical devices such as optically pumped lasers have been demonstrated using CVD growth processes. One possibility why MBE has yet to produce high

optical quality devices is that the low growth temperatures needed for MBE growth may limit the surface mobility of the Ge and Sn ad-atoms, thus reducing the optical quality of the material. The use of surfactants, typical for Group IV growth such as arsenic or antimony, could enhance the mobility of the surface adatoms and improve the overall material quality.

It's the conventional wisdom of the growth community that Ge_2H_6 is a better Ge precursor for GeSn growth because it has a lower decomposition temperature. This is evident in that the majority of GeSn growth by the CVD technique uses Ge_2H_6. However, there are some issues with this conventional wisdom: i) the group at ASU formulated higher order Ge precursors, Ge_3H_8 and Ge_4H_{10}, and they saw no increase in the optical quality of their materials, which could be attributed to the instability of SnD_4 under normal growth temperatures [141], ii) it has been seen that regardless of the Ge precursor used the Sn% limit is near 15% unless spontaneous relaxation enhanced epitaxy occurs, suggesting a reaction limit on the growth, and iii) growth with GeH_4 has currently produced the highest Sn composition optical quality films (22% Sn) and highest temperature lasers to date (270 K) [242].

This inconsistency with the conventional wisdom begs to ask if higher order Ge precursors are the correct path or does first order Ge precursor have an advantage. There have been no studies on this question and it is beyond the scope of this dissertation, however, some interesting observations can be made. The SnD_4 precursor requires dry ice conditions to be stored. This suggests that under growth temperatures < 450 °C, the SnD_4 molecule may shed all the deuterium leaving behind only the Sn adatoms on the surface. This in effect would make it similar to the MBE growth. For the Ge precursors, the growth temperature is shown to be high enough to break hydrogen loose from the molecule, thus growth is possible using GeH_4. It is believed that when GeH_4 loses a hydrogen atom, the GeH_3 radical attaches to a hydrogen at the

surface then displaces the surface hydrogen to incorporate. Using this same thought process, when Ge_2H_6 decomposes, there are two GeH_3 radicals to begin with. If they lose a hydrogen atom, they will become GeH_2 and have two open bonding points. The GeH_3 radical should have more surface mobility than that of the GeH_2 radical due to the lower number of open bonding points. Only GeH_4, under the condition that thermal energy causes one hydrogen atom to break away from the molecule, produces only GeH_3 radicals for incorporation.

4.9 Summary

This chapter has discussed the method pursued to grow high quality GeSn on Ge buffered Si. The study started in a growth regime in which $SnCl_4$ overpressure dominated the overall growth of the GeSn material. The detrimental effects of $SnCl_4$ overpressure led to reduction of $SnCl_4$ molar flow fraction. This reduction in $SnCl_4$ molar flow fraction provided better growth conditions to allow Sn to incorporate into the growing film with less agglomeration on the sample surface. Optimal growth conditions were achieved for the 270 °C growth temperature, producing high quality GeSn with a mirror-like surface. Further temperature reduction below 270 °C resulted in increasing surface Sn with decreasing GeH_4 breakdown. GeSn photoconductors were fabricated from the in-house grown materials. The complete process from growth to fabrication was achieved within this research group. Lastly, the question was asked if GeH_4 should be the preferred precursor for GeSn CVD growth and an idea presented about why the higher order precursors do not perform as well as the GeH_4 precursor.

Chapter 5 GeSn/GeSn Quantum Wells

5.1 Direct Bandgap Type I GeSn/GeSn SQW on Ge Buffered Si Substrate

Recent development of group IV-based GeSn light-emitting devices has opened a new avenue for photonic integration on the Si substrate [3, 179, 230, 239–244]. The successful demonstration of direct bandgap GeSn light emitting diodes (LEDs), and optically-pumped GeSn lasers [171, 175, 176, 215, 234, 235] indicates the great potential of GeSn for Si-based light sources. GeSn LEDs with double heterostructures (DHS) [200, 202, 230, 234, 245–249] and quantum wells (QWs) [182, 187, 190, 250–256] have been reported. It is generally acknowledged that the QW structures could be applied to the LEDs and lasers to improve device performance. LEDs based on the Ge/GeSn/Ge QW structure have been demonstrated [190], whose detailed analysis suggested that using Ge as a barrier did not provide the desired carrier confinement and, thereupon, use of the ternary material SiGeSn as the barrier was proposed, since the bandgap energy and lattice constant of SiGeSn alloys can be tuned independently. The SiGeSn/GeSn/SiGeSn QWs were grown and characterized recently [193, 194, 250, 251]. By engineering the Si and Sn composition, using SiGeSn as barrier, the carrier confinement in the QW was improved compared to those using Ge as a barrier. Moreover, the band structure analysis and characterization results indicated that the direct bandgap well could be achieved by using high-Sn GeSn material [250, 251], which is desired for the improvement of the light emission efficiency. However, an in-depth study including detailed band structure calculation and optical transition has not been performed on a direct bandgap GeSn QW so far.

5.1.1 Growth and Material Characterization

In order to obtain the QW structures that can be practically used in efficient GeSn LED and laser devices, the direct bandgap well with type-I band alignment is highly desired. In this

work, a relaxed GeSn layer with 8.5% Sn was utilized as a buffer layer, which could ease the strain of the GeSn well layer with Sn composition of 13.7%. As a result, the direct bandgap well was obtained. In addition, the lower-%-Sn buffer layer also served as a barrier relative to the higher-Sn well. The band structure calculation based on material characterization results indicated that the type-I band alignment was achieved. Furthermore, the clear QW emission was observed from the temperature-dependent PL spectra, which significantly increased peak intensity at lower temperature confirmed the direct bandgap of the GeSn well.

The QW sample studied in this work was grown using an industry standard ASM Epsilon® 2000-Plus RPCVD system. The nominal designed QW structure consisted of a 412-nm-thick $Ge_{0.915}Sn_{0.085}$ buffer (bottom barrier), a 11-nm-thick $Ge_{0.863}Sn_{0.137}$ well, and a 47-nm-thick top $Ge_{0.927}Sn_{0.073}$ barrier. The detailed growth method has been described elsewhere [214]. To assist the analysis of the optical transition properties, two GeSn bulk reference samples, $Ge_{0.92}Sn_{0.08}$ (ref. #1) and $Ge_{0.856}Sn_{0.144}$ (ref. #2) were grown and characterized under the same conditions, aiming to compare with barrier and well, respectively. Although there is ~0.7% difference in Sn composition between the QW and reference samples (which results in a difference in bandgap energy), by comparing their temperature-dependent PL behavior in terms of peak intensity and relative peak shift, the transition mechanism in the QW can be identified. After the growth, the Secondary Ion Mass Spectrometry (SIMS), high-resolution x-ray diffraction (HRXRD) 2θ-ω scan and reciprocal space map (RSM) were employed to identify the Sn compositions and the degree of strain of each layer, where the bowing parameter of -0.066 was used [261]. The layer thickness and material quality were examined by cross-sectional TEM.

The HRXRD 2θ-ω scan is shown in Figure 5-1(a). The black curve is the measured data.

The multipeak at ~65° and the shoulder at ~64.2° correspond to GeSn barriers (7.3% and 8.5% Sn) and well (13.7% Sn), respectively. The multiple oscillations are associated with the thickness of the multi-layered structure (thickness fringes). Their presence indicates the high quality of the interfaces. The XRD simulation was conducted to in-depth analyze the QW, which is shown as the red curve. The lattice constant and layer thickness can be determined by the simulated 2θ-ω scan curve. The RSM shown in Figure 5-1(a) inset shows the clear superposition of two GeSn layers, which correspond to the strain relaxed $Ge_{0.915}Sn_{0.085}$ buffer and the $Ge_{0.863}Sn_{0.137}$ well that is psuedomorphic to the relaxed GeSn buffer. Figure 5-1(b) shows the cross-sectional TEM image of the QW sample. Each layer can be clearly resolved and features low defect density. There were almost no threading dislocations propagating across the QW, resulting in high material quality.

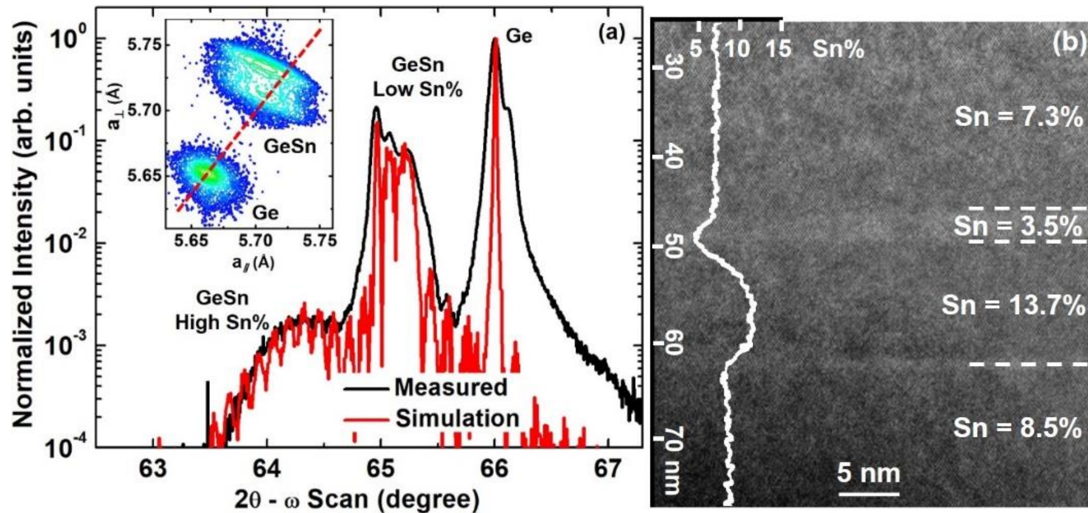

Figure 5-1: (a) HRXRD 2θ-ω scan of QW sample. The black and red curves are measured data and simulation results, respectively. Inset: The RSM contour plot of the QW structure; (b) TEM image of the GeSn/GeSn QW. The SIMS profile is overlaid with the TEM image to illustrate the Sn composition in every layer.

The measured thickness of each layer was consistent with the values from simulated 2θ-ω scan curve, indicating the precisely controlled material growth process. It is worth noting that

according to the SIMS profile and TEM image shown in Figure 5-1(b), a 4.2 nm-thick GeSn interlayer with 3.5% Sn was unintentionally grown after the well layer. The formation mechanism of this layer will be discussed in a later section.

5.1.2 Band Structure Calculation

The band diagram of the QW sample at 300 K, shown in Figure 5-2, was calculated using the measured QW structure data. The effective mass approximation and the propagation matrix approach were used to calculate the electronic band structure and quantized energy levels [193]. Based on Vegard's law with the selected bowing parameters b_{Γ}=1.95 and b_L=0.68 (valid for higher-%-Sn alloy [175, 189]) and considering the strain of -0.95%, the $Ge_{0.863}Sn_{0.137}$ well is a direct bandgap material with the Γ-L valley difference of 24 meV. Due to quantized energy levels in the well, the first energy levels in CB ($n_{1\Gamma}$) and VB (n_{1HH}) were calculated as 19 meV above the Γ valley minimum and 9 meV below the heavy hole (HH) band maximum, respectively [262]. The band offsets for conduction band (CB) and valence band (VB) were calculated following the methods discussed in refs. 256 and 258. The calculation results revealed that the type-I band alignment was achieved. Figure 5-2(a) shows the barrier heights at each interface. In the CB, the barrier height between the GeSn bottom barrier (BB) and the well (ΔE_C^{BB}) was calculated as 20 meV. Due to the existance of the interlayer, which features lower Sn% (3.5%) than the top barrier (TB, 7.3%), the barrier height between well and interlayer (ΔE_C^{I}) is 36 meV. In the VB, the split of the HH and LH bands is the result of the strain. The barrier heights of ΔE_V^{BB} and ΔE_V^{I} are 55 and 116 meV, respectively.

Since the L valley's first quantized energy level is only 9 meV above the $n_{1\Gamma}$ level in the CB in the GeSn well, as shown in Figure 5-2(b), at room temperature the electrons at $n_{1\Gamma}$ could be thermally excited to populate the L valley in the GeSn well and then populate the L valleys in

the bottom barrier and interlayer. Additionally, the 20 and 36 meV barrier heights in the Γ valley do not provide sufficient electron confinement, leading to possible population of electrons in the Γ valley of the bottom barrier and interlayer. The re-distribution of electrons results in optical transitions that could be originated from multiple recombination mechanisms in different layers. The possible transitions from the Γ valley to HH and LH are illustrated in Figures 5-2(a) and (b), respectively. On the other hand, the indirect bandgap transitions with phonon assistance could occur from the L valley to the VB. The corresponding transitions are shown in Figures 5-2(c) and (d). The detailed transition mechanism is discussed in the following via the PL characterization.

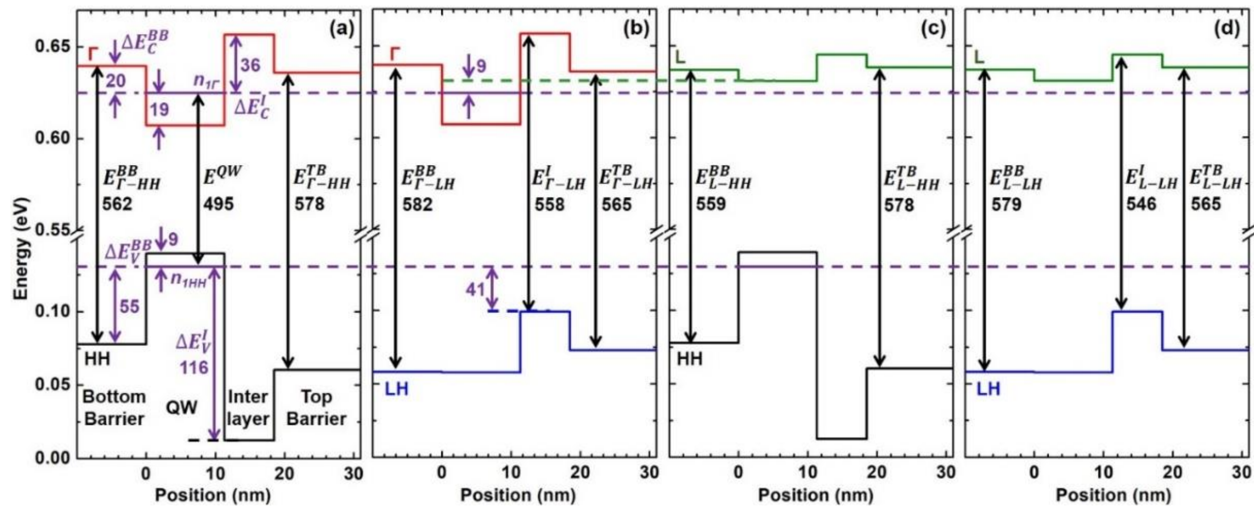

Figure 5-2: Band diagram calculated based on measured material data, showing the carrier confinement and the possible band-to-band optical transitions between (a) Γ-HH; (b) Γ-LH; (c) L-HH; and (d) L-LH. (Unit: meV).

5.1.3 Photoluminescence Characterization

The temperature-dependent PL study was performed using the standard off-axis and lock-in techniques. A 532-nm continuous-wave laser with 500 mW power and 65 µm spot size was used as the pumping source. The emissions were collected using a spectrometer equipped with a thermoelectrically cooled PbS detector with cutoff at 3.0 µm. Figure 5-3(a) shows the

temperature-dependent PL spectra which were stacked for clarity. The multi-peak feature was observed at most temperatures. The Gaussian fitting was used to investigate each peak in terms of peak position, full width at half maximum (FWHM), and integrated PL intensity.

In Figure 5-3(a), a major peak at 2200 nm (0.564 eV, annotated as peak 1) and a small peak at 2500 nm (0.496 eV, annotated as peak 2) were observed at 300 K. As the temperature decreased, both peaks shifted toward shorter wavelength. In addition, a peak located between peak 1 and 2 at ~2250 nm (0.551 eV, annotated as peak 3) was observed at temperatures from 200 to 100 K. For comparison, the PL spectra (not shown here) of reference samples exhibited a clear single peak and peak shift at temperatures from 300 to 10 K. The temperature-dependent peak positions were plotted in Figure 5-3(b). It can be seen that the position shifts of peak 1 and 2 followed a similar trend with reference samples, indicating the validity of the Gaussian fitting method. The discrepancy of energies between peak 1, peak 2 and reference samples is mainly due to two factors: i) different Sn compositions and strain status – the higher Sn composition and lower strain of the reference samples led to their smaller PL peak energies; and, ii) the quantum confinement effect resulted in the transition energy between $n_{1\Gamma}$ and $n_{1\mathrm{HH}}$ in QW being larger than the direct bandgap energy in bulk.

The integrated PL intensities for peak 1 and 2 are shown in Figure 5-3(c). The intensity of peak 2 increases dramatically at lower temperature, while the intensity of peak 1 shows a slight decrease. Peak 2 was assigned to the QW emission as the emission energy at 300 K is consistent with the calculated E^{QW} of 0.495 eV (see Figure 5-2(a)). The significantly increased PL intensity at lower temperature clearly indicated the direct bandgap material feature, which agrees well with band structure calculation. Moreover, the enhanced carrier confinement due to reduced thermal energy k_BT at lower temperature contributes to the increased PL as well.

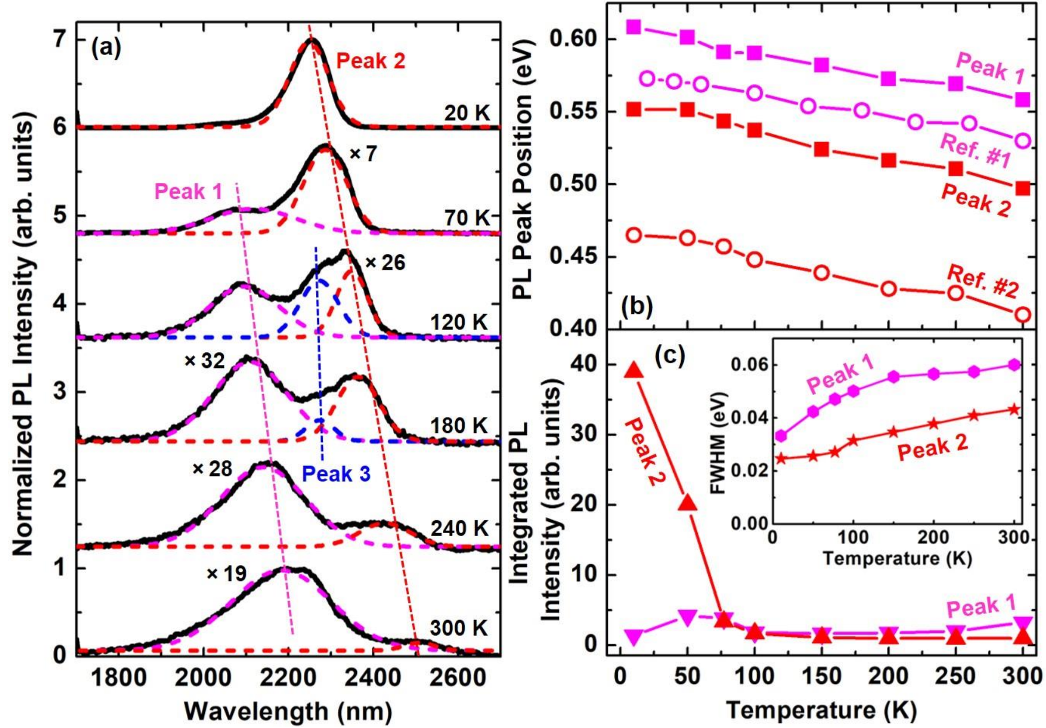

Figure 5-3: (a) Temperature-dependent PL spectra of the GeSn QW sample. The PL peaks were annotated by peak 1, 2, and 3, respectively; (b) PL peak positions of peak 1 and 2. The reference samples are plotted for comparison; (c) integrated PL intensities of peak.

Peak 1 was attributed to emission from the GeSn top barrier and interlayer. As shown in Figure 5-2(b) and (d), the transition energy between the Γ valley and LH in the GeSn top barrier of 0.565 eV was close to the energy of peak 1 at 300 K. However, due to insufficient electron confinement in CB at 300 K, other transitions in the GeSn top barrier and interlayer could also contribute to PL. Figure 5-3(c) inset shows the FWHM of peak 1 and 2. Since the QW emission features the narrower line-width, the FWHM of peak 2 was smaller than that of peak 1 at each temperature. The broadened line-width of peak 1 was also due to its consisting of multiple peaks with partial overlap. According to calculation shown in Figure 5-2, the transitions from the Γ valley to HH in the GeSn top barrier, and from the Γ valley to LH in the GeSn interlayer could have contributed to PL as well. These transitions could not be further identified due to their small energy separation. Note that since the GeSn interlayer acted as a barrier relative to the

GeSn top barrier layer, the major transitions took place in the GeSn top barrier. Therefore, the transitions in that layer dominated the PL at 300 K.

For peak 3, as the temperature decreased, the peak intensity increased, followed by decreases as the temperature further decreased. This peak is possibly attributed to the transition from the L valley to LH in the GeSn interlayer, whose energy is 0.546 eV (2271 nm) at 300 K, as shown in Figure 5-2(d). The behavior of peak 3 can be explained as follows: at relative high temperature, the direct bandgap transition dominates PL, and thus peak 3 cannot be observed. As temperature decreases, the non-radiative recombination rate reduces, resulting in possible electron population of the L valley and enhancement of the optical transition. As the temperature further decreased, the dramatically reduced number of thermally excited electrons and phonon-assisted transition overcompensated the reduced non-radiative recombination, and consequently the PL intensity of peak 3 decreased. The similar phenomenon was also reported elsewhere [190].

Since the penetration depth of the 532-nm laser is only ~20 nm [263], the major absorption occurs only in the GeSn top barrier. To verify the optical transitions in the QW, a 1550-nm CW laser (penetration depth of ~900 nm) with 500 mW power and 24 µm spot size was used as the pumping source. A very similar PL peak feature was observed. At each temperature below 300 K, the PL intensity ratio of peak 2/peak 1 under 1550-nm laser pumping was higher than that under 532-nm laser pumping. This can be interpreted as follows: the deep penetration of 1550-nm laser beam enhances the light absorption in the GeSn bottom barrier. The photo generated carriers would flow into the well region due to the improved carrier confinement at lower temperature because reduced thermal energy, $k_B T$, leads to enhanced QW emission.

5.1.4 Interlayer Formation

The formation mechanism of the unintentionally grown $Ge_{0.965}Sn_{0.035}$ interlayer was investigated. It was found that the Sn incorporation was highly sensitive to the starting growth surface [176, 221]. Both the strain and the Sn composition in the starting surface can affect the Sn incorporation efficiency. As a result, when a nominal $Ge_{0.927}Sn_{0.073}$ layer was grown on QW surface, the introduced strain impaired the Sn incorporation, leading to the formation of a 4.2 nm-thick $Ge_{0.965}Sn_{0.035}$ interlayer between the GeSn well and top barrier. To address this issue, the compensated Sn incorporation approach, i.e., adjusting the $SnCl_4$ flow to compensate the reduced Sn incorporation efficiency, was used to achieve the symmetrical QW structure. Figure 5-4(a) and (b) shows the SIMS and calculated band diagram of a $Ge_{0.93}Sn_{0.07}/Ge_{0.9}Sn_{0.1}/Ge_{0.93}Sn_{0.07}$ QW.

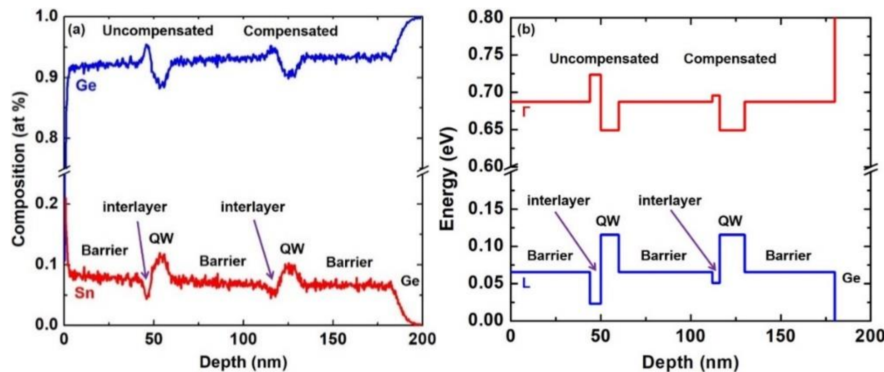

Figure 5-4: (a) SIMS and (b) calculated band diagram of GeSn QW showing the comparison between compensated and uncompensated Sn incorporation growth approaches.

By using a compensated $SnCl_4$ flow, the Sn depletion after well region could be minimized. The change in carrier distribution and QW optical characteristics due to this slight variation of Sn composition thereupon could be neglected. In comparison, a repeat QW structure was grown continuously, in which the Sn composition after well growth was uncompensated. A clear Sn composition drop to ~ 4% was observed, leading to the formation of an interlayer, which cannot be ignored since it considerably affects the QW properties.

5.1.5 Conclusion

In conclusion, a $Ge_{0.92}Sn_{0.08}/Ge_{0.86}Sn_{0.14}/Ge_{0.92}Sn_{0.08}$ single QW was analyzed in depth. The band structure calculation and systematic PL study indicated that by using a relaxed $Ge_{0.92}Sn_{0.08}$ buffer, this QW structure featured direct bandgap material of the well layer and type-I band alignment. At 300 K, the QW emission peak at 2500 nm was observed, and the intensity of the peak increased dramatically as temperature decreased to 20 K. The emissions from the GeSn barriers were also obtained and the peaks were partially overlapped due to small energy separation. Moreover, the formation mechanism of the $Ge_{0.965}Sn_{0.035}$ interlayer was investigated. By using the compensated Sn incorporation approach during material growth, the unintentionally grown interlayer was mostly eliminated and a symmetrical $Ge_{0.93}Sn_{0.07}$/ $Ge_{0.9}Sn_{0.1}/Ge_{0.93}Sn_{0.07}$ QW structure was achieved. [264]

5.2 GeSn/GeSn DQW with Increased Sn% in the Buffer

Silicon-based light sources such as light emitting diodes (LEDs) and lasers have long been desired for optoelectronic integrated circuits [111, 261]. The recent development of group IV-based GeSn technique has opened a new avenue for photonic integration on the Si substrate [3, 178, 229, 239–244]. The successful demonstration of GeSn LEDs and optically-pumped lasers using direct bandgap GeSn materials, indicates the great potential of GeSn for Si-based light sources [171, 175–177, 200, 230, 234, 261]. In the last few years, GeSn LEDs with double heterostructures (DHS) and quantum wells (QWs) have been reported [160, 179, 181, 185, 188, 189, 200, 202, 230, 234, 246–254, 262]. It is generally acknowledged that applying the QW structures to LEDs and lasers could improve their device performance, which motivated the investigation of GeSn LEDs based on the Ge/GeSn/Ge QW structure [188]. However, the detailed analysis suggested that using Ge as a barrier the QW featured type-II band alignment,

and such structure could not provide bandgap directness of QW due to the relative large compressive strain of GeSn layer [190].

To achieve the direct bandgap well with type-I band alignment that can be practically used in efficient GeSn LED and laser devices, the relaxation of GeSn well is a critical issue as the compressive strain pushes the GeSn bandgap towards indirect [193, 194]. Therefore, the use of the GeSn and SiGeSn as the buffer as well as barrier were proposed, which could ease the compressive strain of GeSn well [256, 260]. The SiGeSn/GeSn and GeSn/GeSn QWs were grown and characterized recently [189, 193, 194, 248, 263]. By appropriately selecting the Si and Sn compositions, the SiGeSn and GeSn served as buffer and barrier layers. However, previous study indicated that although direct bandgap well with type-I band alignment was achieved, the carrier confinement was still insufficient, which could reduce the QW light emission efficiency [264]. Hence, a QW structure featuring stronger carrier confinement is highly desirable.

To improve the carrier confinement, further relaxing the GeSn well to make its bandgap exhibit more directness is a viable solution. In this work, the $Ge_{0.91}Sn_{0.09}$ buffer layer was utilized, which features higher Sn composition compared to previous work [264], and therefore could further ease the compressive strain of the GeSn well layer with Sn composition of 15%. Note that the 9%-Sn buffer layer could also serve as the barrier relative to the 15%-Sn well. As a result, the direct bandgap well with improved carrier confinement was obtained despite the residual compressive strain. Two GeSn/GeSn double QW samples, with different well thicknesses were grown and characterized. The temperature-dependent PL spectra were obtained and analyzed, which indicated that: i) both samples featured improved carrier confinement by using higher Sn $Ge_{0.91}Sn_{0.09}$ buffer, as the temperatures of barrier emission disappearing were

observed at 100 and 150 K, respectively, which were higher than previously reported QW of below 70 K [264]; ii) the carrier confinement was further improved with thicker GeSn well sample, as evidenced by the temperature of barrier emission disappearing raising to 150 K, and the QW emission dominates the PL at lower temperature under 1064-nm pulsed laser pumping (barrier emission always dominating PL for thinner well sample and previous QW in ref. 263).

5.2.1 Experimental Details

5.2.1.1 Material Growth and Characterizations

Two QW samples (annotated as A and B) studied in this work were grown using an industry standard RPCVD system. Low-cost commercially available SiH_4, GeH_4, and $SnCl_4$ were used as Si, Ge, and Sn precursors, respectively. The schematic drawing of designed GeSn QW structures are shown in Figure. 5-5.

Sample A	Sample B
Ge cap 17 nm	Ge cap 7 nm
$Ge_{0.85}Sn_{0.15}$ 5 nm	$Ge_{0.85}Sn_{0.15}$ 20 nm
$Ge_{0.91}Sn_{0.09}$ barrier 2 nm	$Ge_{0.91}Sn_{0.09}$ barrier 2 nm
$Ge_{0.85}Sn_{0.15}$ 5 nm	$Ge_{0.85}Sn_{0.15}$ 20 nm
$Ge_{0.91}Sn_{0.09}$ buffer 600 nm	$Ge_{0.91}Sn_{0.09}$ buffer 600 nm
Ge buffer 700 nm	Ge buffer 700 nm
Si substrate	Si substrate

Figure 5-5: Cross section (not to scale) of GeSn QW: (a) sample A and (b) sample B.

The 700-nm-thick Ge buffer layer was grown prior to QW growth by a two-step growth method. The nominal designed QW structures consisted of the following from the bottom to top: i) 600-nm-thick $Ge_{0.91}Sn_{0.09}$ buffer for both samples A and B; ii) two $Ge_{0.85}Sn_{0.15}$ wells (5- and 20-nm-thick for samples A and B, respectively) separated by a 2-nm-thick $Ge_{0.91}Sn_{0.09}$ barrier;

and, iii) the Ge cap layer (17- and 7-nm-thick for samples A and B, respectively). The detailed growth method has been described elsewhere [214].

After the growth, the SIMS, HRXRD 2θ-ω scan, and RSM were employed to identify and cross check the Sn compositions and the degree of strain of each layer. The bowing parameter of -0.066 was used for lattice constant. The layer thickness and material quality were examined by cross-sectional TEM.

5.2.1.2 Band Structure Calculation

The band diagrams of the QW samples at 300 K were calculated using the measured QW structure data. The bowing parameters b_Γ=1.95 and b_L=0.68 were selected to determine the direct and indirect bandgap energies based on Vegard's law, which are valid for the high-Sn material. The effective mass approximation and the propagation matrix approach were used to calculate the electronic band structure and quantized energy levels. The band offsets for conduction band (CB) and valence band (VB) were calculated following the methods discussed in refs. 256 and 258.

5.2.1.3 Photoluminescence Study

The temperature-dependent PL measurements were performed using standard off-axis configuration with lock-in technique (optically chopped at 377 Hz). The emissions were collected using a spectrometer equipped with a thermoelectrically cooled PbS detector with cutoff at 3.0 µm. To pinpoint the optical transitions in QW, three lasers offering various excitation conditions in terms of laser energy and beam penetration depth were utilized in this work: a 532-nm continuous wave (CW) laser, a 1550-nm CW laser, and a 1064-nm pulsed laser (pulse width of 5 ns and repetition rate of 45 kHz). The detailed parameters of pumping lasers are summarized in Table 3.

Table 3: Parameters of pumping lasers.

Laser wavelength (nm)	Laser spot diameter (μm)	Averaged power density (kW/cm^2)	Photon injection density (Photon number/s/cm^2)	Penetration depth in GeSn (nm)
532	65	15	4.1×10^{19}	21 ± 2
1064	52	6*	3.5×10^{22}	418 ± 21
1550	24	160	1.2×10^{21}	916 ± 46

* For 1064 nm pulsed laser, the peak power density is 2.7×10^4 kW/cm^2.

5.2.2 Results and Discussion

5.2.2.1 Material Characterization

Material characterization was performed to fully understand the QW structure to produce simulations that correctly modeled the samples. The SIMS profiles are shown in Figure 5-6.

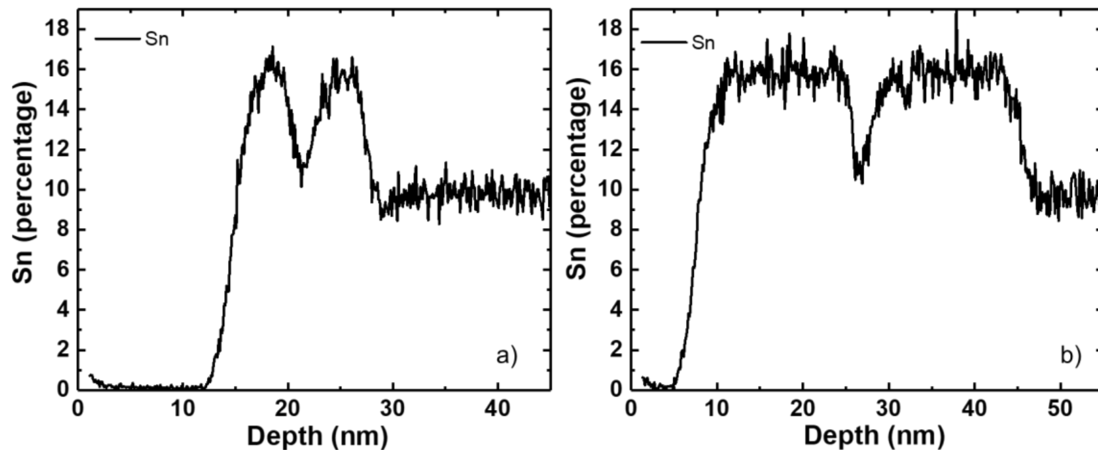

Figure 5-6: SIMS profiles of a) sample A and b) sample B.

Figure 5-6(a) and (b) show the SIMS plots of samples A and B, respectively. It can be seen that the Sn composition in each layer was uniform. Although the transition at each interface was not very abrupt, the GeSn buffer, well, barrier and Ge cap regions can be clearly resolved. The measured Sn compositions agree well with the design, indicating the precisely controlled material growth process. Further confirmation of the sample structures came from XRD

measurements shown in Figures 5-7 and 5-8.

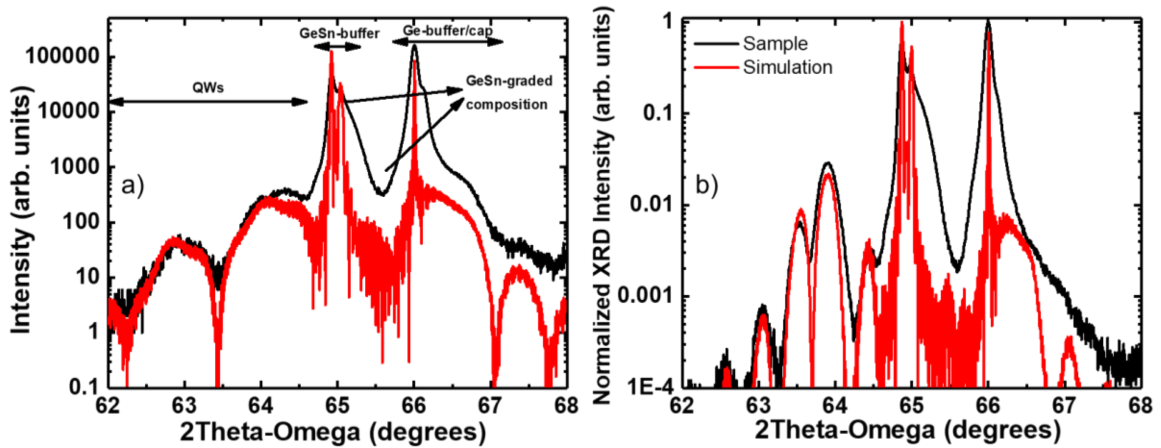

Figure 5-7: High-resolution XRD rocking curves with corresponding sample structure simulation for a) Sample A and b) Sample B.

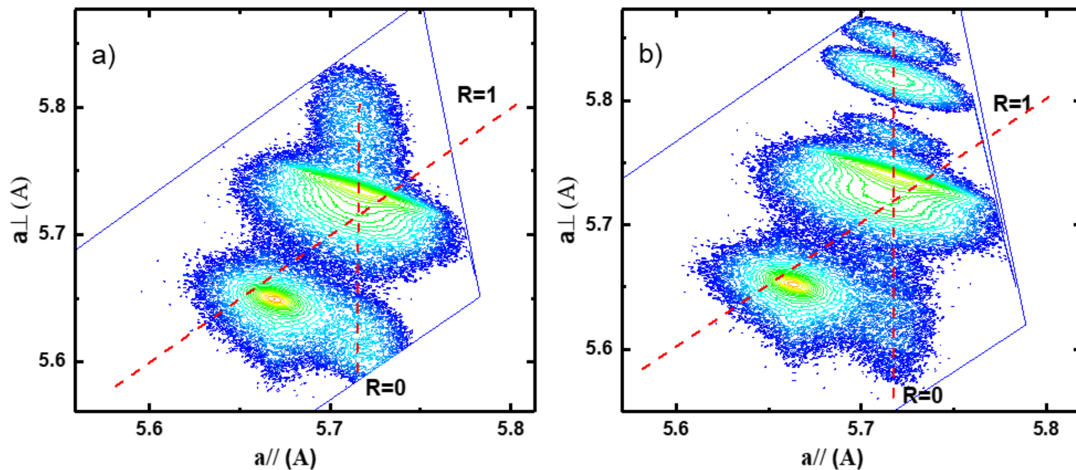

Figure 5-8: XRD-RSM measurements of a) Sample A and b) sample B.

The HRXRD 2θ-ω scans are shown in Figures 5-7(a) and (b) for samples A and B, respectively. The black and red curves are the measured data and simulation results. In Figure 5-7(a), the peak at ~66° indicates the Ge buffer. A small shoulder located at ~66.5° is associated with the tensile strained Ge cap. The peaks at ~65.0° and ~64.2° correspond to GeSn buffer/barrier (measured as 8.8% Sn) and well (measured as 14.7% Sn), respectively. The multiple oscillations are associated with the thickness of the multi-layered structure (thickness

fringes). Their presence indicates the high quality of the layer interfaces. The XRD 2θ-ω simulation was conducted to further analyze the QW, by which the lattice constant and layer thickness can be determined. The RSM shown in Figure 5-7(a) clearly shows three regions. The bottom region corresponds to the superposition of Ge buffer and cap layers. The region above the Ge indicates the contour plot of the almost relaxed $Ge_{0.91}Sn_{0.09}$ buffer/barrier with the residual compressive strain of 0.15%. The top region is the $Ge_{0.85}Sn_{0.15}$ well that was pseudomorphic to the relaxed $Ge_{0.91}Sn_{0.09}$ buffer. Figure 5-7(b) shows the XRD results of sample B. The similar 2θ-ω scan and RSM plot were obtained except the following: i) since the measured Sn compositions in GeSn buffer/barrier (9.4%) and well (15.3%) of sample B were higher than those of sample A, the GeSn peaks in 2θ-ω scan exhibited at ~64.8^{o} and 63.9^{o}, shifted toward lower angles as expected; ii) due to the thicker well of sample B (close to the critical thickness), the layer was partially relaxed, as shown in Fig. 5-8(b). Figure 5-9(a) and (b) show the cross-sectional TEM images of the QW samples.

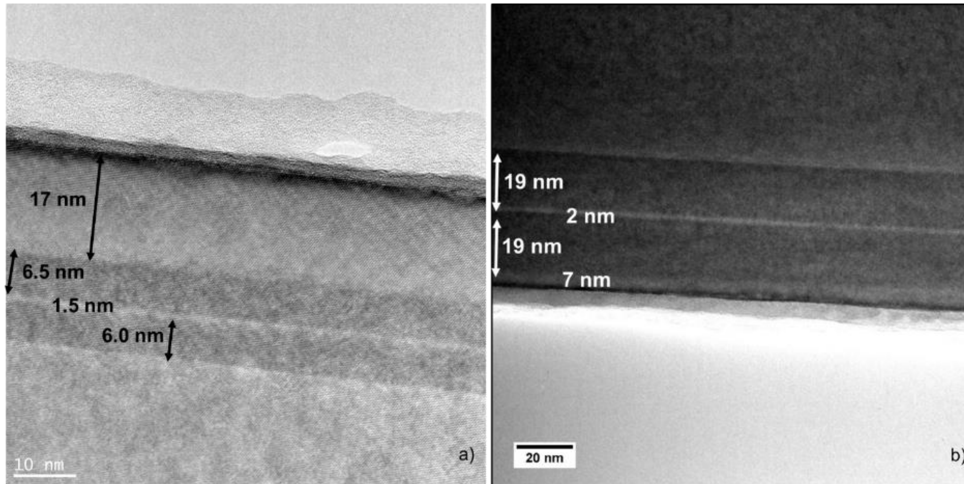

Figure 5-9: TEM imaging of a) Sample A and b) Sample B. The layer thicknesses are labeled for the specific layer.

For both samples, each layer could be clearly resolved. The smooth cross section profile indicated the very low defect density. Particularly, for sample B, even though the $Ge_{0.85}Sn_{0.15}$ well

layers featured partial relaxation, there were almost no threading dislocations propagating across the QW, resulting in high material quality. The measured thickness of each layer from TEM images was consistent with the value that was extracted from the simulated XRD 2θ-ω scan curve. On the other hand, compared to the design, the thicknesses of GeSn wells and barriers, and Ge caps showed very close values for both samples A and B. Such small thickness variation would not affect the QW characteristics in this work. Material characterization results are summarized in Table 4.

Table 4: Summary of GeSn/GeSn DQW sample information

Sample	Layer structure	Sn (%)		Thickness (nm)		Strain (%)
		Designed	Measured	Designed	Measured	
A	Ge cap (top barrier)	0	0	17.0	17.0	0.9
	GeSn well	15	14.7	5.0	6.5	-1.05*
	GeSn barrier	10	8.8	2.0	1.5	-0.26*
	GeSn well	15	14.7	5.0	6.0	-1.05*
	GeSn buffer (bottom barrier)	10	8.8	600	600	-0.14*
	Ge buffer	0	0	700	700	0.2
B	Ge cap (top barrier)	0	0	7.0	7.0	1.15
	GeSn well	15	15.3	20.0	19.0	-0.91*
	GeSn barrier	10	9.4	2.0	2.0	-0.11*
	GeSn well	15	15.3	20.0	19.0	-0.91*
	GeSn buffer (bottom barrier)	10	9.4	600	600	-0.11*
	Ge buffer	0	0	700	700	0.21

* Negative value indicates compressive strain.

5.2.3 Band Structure and Optical Transition Analysis

The band diagram of the QW samples at 300 K were calculated using the measured QW structure data shown in Table 3. Figure 5-10(a)-(d) illustrates the band structures at CB and VB and possible optical transitions of sample A. Using selected bowing parameters and considering

the compressive strain of 1.05%, the direct bandgap $Ge_{0.853}Sn_{0.147}$ well was obtained with the energy difference between Γ-L valley of 26 meV. Due to quantized energy levels in the well, the first energy levels in CB ($n_{1\Gamma}$) and VB (n_{1HH}) were calculated as 24 meV above the Γ valley minimum and 15 meV below the heavy hole (HH) band maximum, respectively. Figure 5-10 shows the barrier heights at each layer interface, which revealed that the type-I band alignment was achieved.

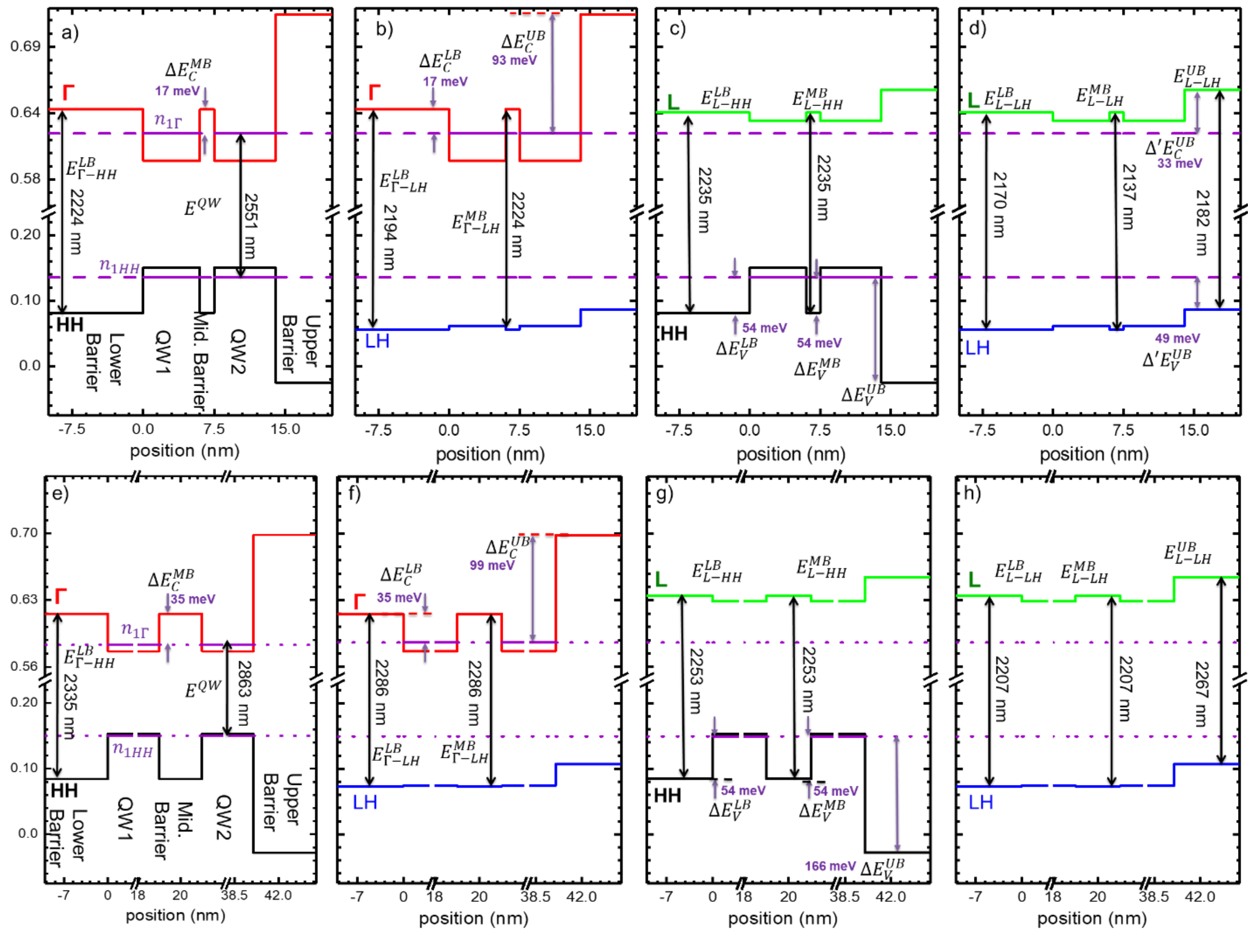

Figure 5-10: Top: for sample A. Band diagram calculated based on measured material data, showing the carrier confinement and the possible band-to-band optical transitions between (a) Γ-HH; (b) Γ-LH; (c) L-HH; and (d) L-LH. (Unit: meV). Bottom: for sample B. (e)-(h) The similar band diagram and optical transition calculations.

In Figure 5-10(a), in the CB, the barrier height between GeSn barriers (including bottom barrier and inter-barrier) and GeSn well was calculated as 17 meV; while the barrier height at

GeSn well/Ge top barrier interface was 93 meV. In the VB, the residual strain results in the split of HH and light hole (LH) bands. The barrier heights at GeSn barrier/GeSn well and GeSn well/Ge barrier interfaces were 54 and 160 meV, respectively. In Figure 5-10(d), the barrier heights between GeSn barrier and GeSn well at L-valley and LH band were less than 5 meV; while at the GeSn well/Ge barrier interface, the barrier heights were calculated as 33 and 49 meV at L-valley and LH band, respectively.

Since the 17 meV (0.66 $k_B T$) barrier height between GeSn barriers and GeSn well in the Γ valley does not provide surfficient electron confinement, the electrons at $n_{1\Gamma}$ could gain thermal energy and populate the Γ valleys in the GeSn barrier layers at room temperature. In addition, the first quantized energy level in L valley was only a few meV above $n_{1\Gamma}$ in GeSn well, the electrons could also be thermally excited to populate the L valley, followed by populating the L valleys in the GeSn barriers due to weak carrier confinement. The re-distributed electrons leading to the recombinations could occur between different energy bands (including L valley to VB with phonon assistance) in multiple layers, resulting in the optical transitions being originated from multiple recombination mechanisms. Figure 5-10 (a)-(d) illustrate the possible transitions.

Figure 5-10(e)-(h) illustrate the band structures and possible optical transitions of sample B. The energy separation between Γ-L valley of direct bandgap $Ge_{0.847}Sn_{0.153}$ well was calculated as 52 meV, which was higher than that of sample A due to the higher Sn composition. It is worth noting that the $Ge_{0.906}Sn_{0.094}$ barrier also featured direct bandgap, as the Γ valley was 19 meV below the L valley. In Figure 5-10(e), in the CB, the barrier heights at GeSn barrier/GeSn well and GeSn well/Ge barrier interfaces were calculated as 35 and 99 meV in Γ valley, respectively; while in the VB the barrier heights are 54 and 166 meV at HH band,

respectively. The improved electron confinement in Γ valley and HH band compard to sample A was mainly due to the higher Sn composition and thicker GeSn well layer of sample B. The barrier heights in L valley and LH band were less than 5 meV between GeSn barriers and well, as shown in Figure 5-10(f) and (g).

Although the improved barrier height between GeSn barriers and GeSn well in the Γ valley was 35 meV (1.35 $k_B T$) at room temperature, some electrons at $n_{1\Gamma}$ could be thermally excited to populate the Γ valley in the GeSn barrier layers, leading to the multiple recombination mechanisms. Moreover, since there was almost no carrier confinement in the L valley and LH band between GeSn barrier and well, the carriers could flow from one to the other, resulting in the phonon assisted optical transitions that could occur in both layers. The detailed transition mechanism is discussed in the following section via the PL spectra analysis.

5.2.4 Photoluminescence Spectra Analysis

To adequately determine if the wells were direct band gap, PL spectra analysis was done on both samples A and B (Figures 5-11 and 5-12). Each peak of the associated spectra was fit using Gaussian fitting and the integrated intensity was plotted in Figure 5-13. Figure 5-11(a) shows the normalized temperature-dependent PL spectra of sample A using a 532-nm CW laser. The spectra were stacked for clarity. At 300 K, a major higher energy peak at 2220 nm (0.558 eV) and a small lower energy shoulder at 2560 nm (0.484 eV) were observed. As the temperature decreased, both peaks shifted toward shorter wavelength. For the higher energy peak, the peak intensity decreased as the temperature decreased. At temperatures below 100 K, the higher energy peak almost disappeared; while for the lower energy peak, the intensity increased significantly as the temperature decreased. This lower energy peak was assigned to the QW emission as the emission energy of 0.484 eV at 300 K was consistent with the calculated

value of 0.486 eV shown in Fig. 5-10(a).

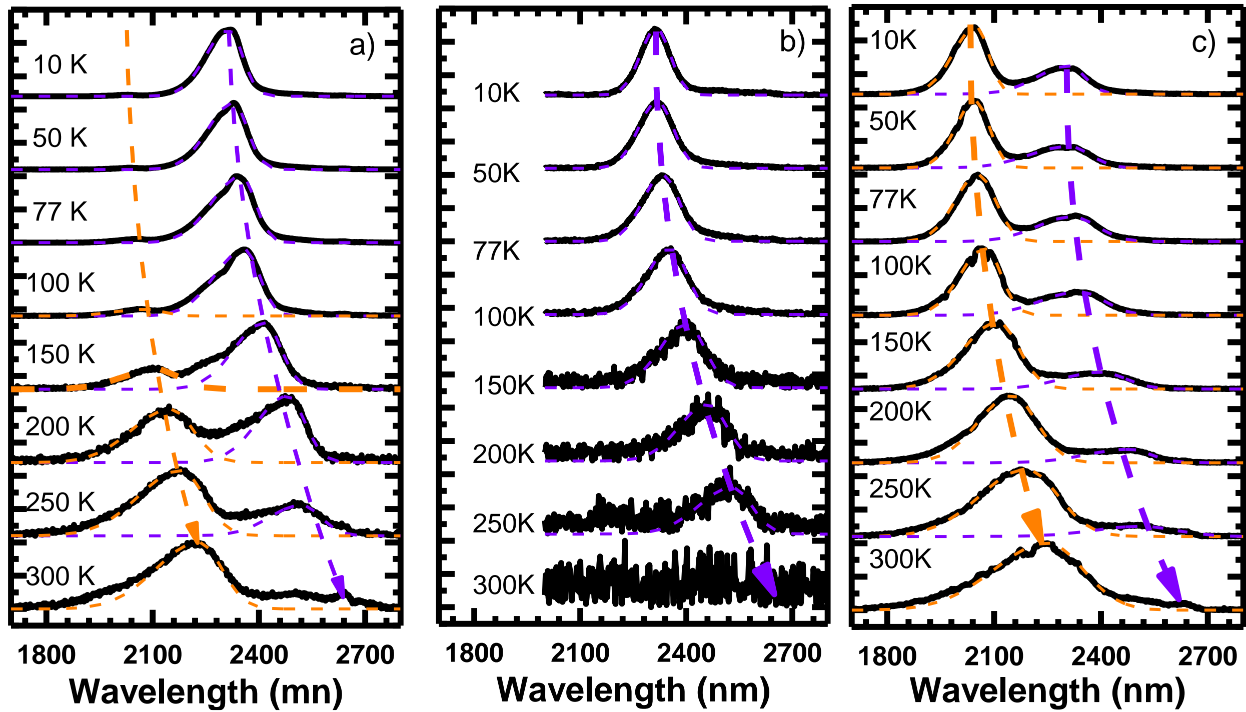

Figure 5-11: Temperature dependent PL of sample A using multiple pumping sources. a) 532 nm, b) 1550 nm, and c) 1064 nm.

At 10 K, the integrated PL intensity was over 100 times higher than that at 300 K, as shown in Fig. 5-13(a). The significantly increased PL intensity at lower temperature clearly indicated the direct bandgap material nature, matching well with band structure calculation. The higher energy peak was mainly attributed to Γ-HH transitions at GeSn barriers since the transition energy (0.558 eV) was very close to calculated one (0.557 eV). However, due to the thermally re-distributed carriers, the Γ-LH (0.565 eV) and L-HH (0.555 eV) transitions at GeSn barriers, and L-LH transition (0.568 eV) at Ge barrier could also have contributed to the PL, i.e., the higher energy peak might consist of multiple peaks with partial overlap. These peaks could not be further identified due to their small energy separation. Note that at 300 K the multi-peak

feature at ~2700 nm was due to the CO_2 absorption peak, which disappeared at lower temperature due to peak blue-shift. Such peak does not affect the PL spctra analysis.

It is worth noting that previous QW study of this research group showed that the GeSn barrier emission almost disappeared below 70 K [263]; while in this work, under the same pumping condition, the temperature at which barrier emission disappeared increased to 100 K. This revealed that by using higher Sn buffer, the significant reduction of thermally activated carriers occurs at higher temperature compared to previous QW results, indicating the improved carrier confinement.

Since the penetration depth of the 532-nm laser was only ~21 nm, the major absorption occurred only in the Ge top barrier and the QW and barrier emission were due to the carrier redistribution. To further analyze the optical transitions, a 1550-nm CW laser and a 1064-nm pulsed laser were used as pumping sources, which feature more than 400 nm penetration depth (see Table I) and, therefore, each layer could be involved in light absorption. Figure 5-11(b) shows the normalized temperature-dependent PL spectra of sample A using a 1550-nm CW laser. At 300 K, the peak feature was unclear due to lower signal–to–noise ratio because of lower light absorption under 1550-nm pumping than that under 532-nm pumping. Below 250 K, a single peak at each temperature was observed. The temperature-dependent peak position and shift were very similar to the lower energy peak shown in Fig. 5-11(a), indicating that this peak was due to the QW emission. As can be seen in Fig. 5-13(a), the integrated PL intensity increased 40 times from 250 to 10 K. Note that the emission from any other transitions was not observed under 1550-nm laser, which can be interpreted as follows: the increased penetration depth of 1550-nm laser beam enhanced the light absorption in the GeSn barriers. At lower temperature, the photo generated carriers would flow into the GeSn well region due to the

improved carrier confinement because of reduced thermal energy $k_B T$, which minimized the emission from barrier and consequently led to enhanced QW emission.

Figure 5-11(c) shows the normalized temperature-dependent PL spectra of sample A using a 1064-nm pulse laser. At each temperature, two clear peaks were obtained. The peak position and shift as temperature decreased were very close to those under 532-nm laser pumping, indicating that the higher and lower energy peaks were attributed to transition from barriers and well, respectively. Note that the peak intensity from barriers was always higher than that from well. This was due to the high injection level (see Table 2) under pulsed pumping by the 1064-nm laser and its deep penetration depth; a huge number of photo-generated carriers populated the GeSn well, GeSn and Ge barriers simultaneously. Electron-hole recombination in GeSn and Ge barriers could have occurred before the carriers re-distributed to the GeSn well via the carrier confinement effect, resulting in the PL spectra consisting of emissions from barriers and well with more pronounced contribution from GeSn and Ge barrier layers. Moreover, in Fig. 5-13(a) it can be seen that the integrated PL intensity of barriers emission increased 2.2 times as the temperature decreased from 300 to 10 K, while the well emission increased 8.6 times. This can be explained as the better carrier confinement at low temperature due to reduced $k_B T$ which enhanced the QW emission.

The normalized temperature-dependent PL spectra of sample B using 532-nm CW, 1550-nm CW, and 1064-nm pulse lasers are shown in Fig. 5-12(a), (b), and (c), respectively. In Fig. 5-12(a), at 300 K, two peaks at 2330 nm (0.532 eV) and 2800 nm (0.443 eV) were observed. As temperature decreased, both peaks exhibit blue-shift as expected. The higher energy peak features reduced intensity and disappeared below 150 K; while the lower energy peak showed dramatically increased intensity, as the integrated PL intensity at 10 K was over 450 times higher

than that at 300 K as shown in Fig. 5-13(b), indicating the direct bandgap material nature. The lower energy peak was assigned to QW emission. Compared to the calculated value of transition energy (0.433 eV), the deviation of 0.01 eV was mainly from the error of Gaussian fitting due to the weak peak intensity. The higher energy peak was mainly attributed to Γ-HH transitions at GeSn barrier as the transition energy (0.532 eV) matched well with calculated value of 0.531 eV. However, the broadened peak linewidth suggests that other transitions could have contributed to the PL as well, including Γ-LH (0.542 eV) and L-HH (0.550 eV) transitions at GeSn barriers, and L-LH (0.562 eV) Γ-LH transition (0.547 eV) at Ge barrier. Note that the temperature of barrier emission disappearing of sample B was 150 K, which was higher than that of sample A (100 K) and our previously reported QW (70 K, ref. 266). This implies that: i) by using high Sn buffer, both sample A and B features improved carrier confinement compared to previous reported QW; ii) compared to sample A, sample B exhibited further improved carrier confinement by using thicker GeSn well that further eased the compressive strain. The experimental evidence confirmed the band structure calculation results shown in Figure 5-10.

Figure 5-12(b) shows the normalized temperature-dependent PL spectra of sample B using a 1550-nm CW laser. The similar single peak feature as sample A was obtained. Based on the peak energy and shift trend, this peak was assigned to QW emission. The broadened peak line-width at 250, 200, and 150 K was mainly due to the partial overlay of emissions from QW and defects. Below 150 K, the dramatically increased intensity of QW peak led to a non-observable defect peak. As shown in Figure 5-13(b), the integrated PL intensity increased 150 times from 250 to 10 K.

Figure 5-12(c) shows the normalized temperature-dependent PL spectra of sample B using a 1064-nm pulse laser. At 300 K, the intensity of GeSn barrier peak was higher than that

of GeSn well. As temperature decreased, since the GeSn barrier and well were both direct bandgap material according to band structure calculation, both peak intensities increased with more rapid growth of QW peak than the barrier peak. Below 100 K, the emission from GeSn well was stronger than that from GeSn barriers. At 10 K, the integrated PL intensities increased 16 and 3 times for well and barrier, respectively, as shown in Figure 5-13(b).

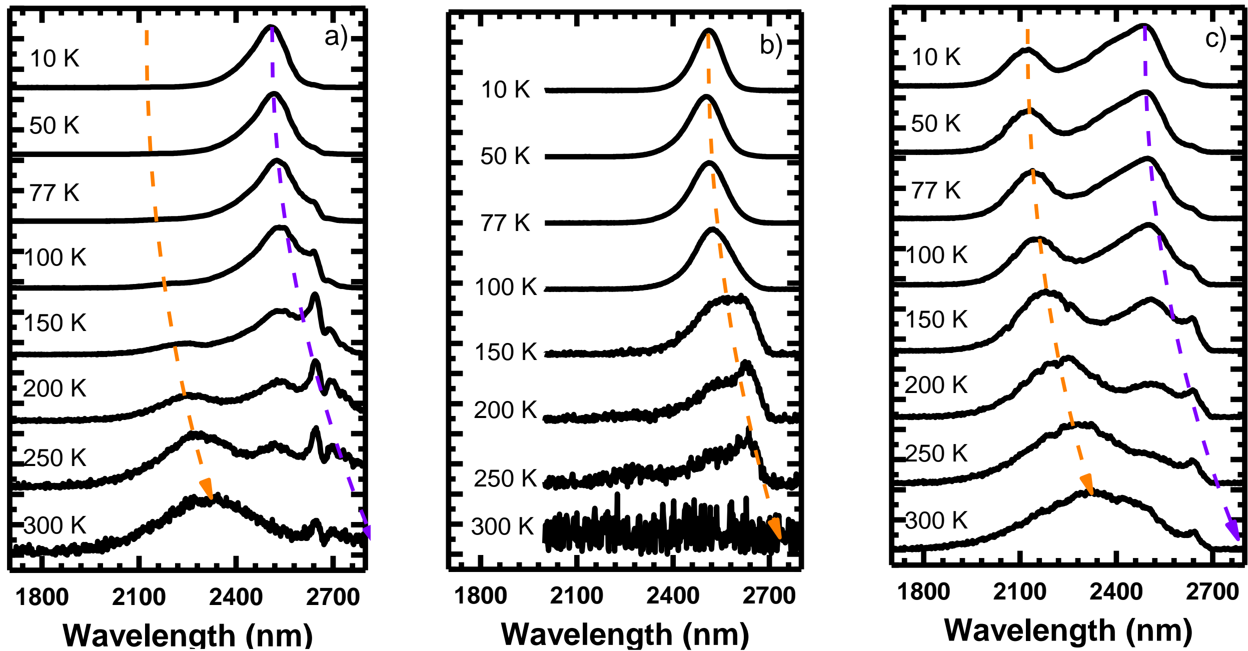

Figure 5-12: Temperature dependent PL using multiple laser pumping a) 532 nm, b)1550 nm, and c) 1064 nm.

The strong QW emission can be explained as follows: since the QW structure of sample B provided sufficient carrier confinement at lower temperature, most photo-generated carriers eventually tended to populate the Γ valleys in GeSn well, resulting in majority emissions from band-to-band transitions in the well. However, due to the high injection level, some electron-hole pairs could recombine before flowing into the well region, leading to the emissions from Ge and GeSn barriers.

It is worth noting that compared to sample A, the sample B exhibited dramatically

enhanced emission from QW, as QW peak dominated the PL below 100 K (for sample A, the barrier emission always dominated the PL). This was mainly due to the thicker GeSn well of sample B further relaxing the material and, consequently, lowering the first quantized energy level in the well resulting in improved carrier confinement compared to sample A.

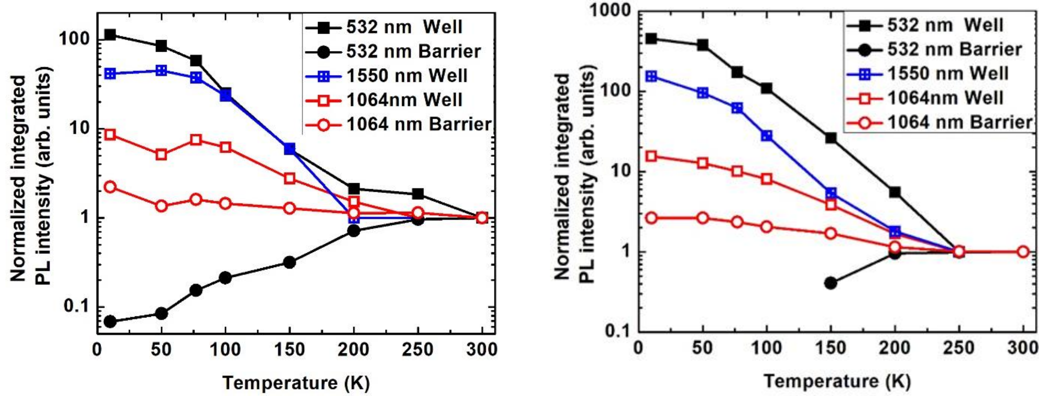

Figure 5-13: Integrated PL intensity of (a) sample A; and (b) sample B.

5.2.5 Conclusion

In conclusion, two GeSn/GeSn double QW samples with different well thicknesses were grown and analyzed in depth. By using relaxed GeSn buffer with higher Sn composition, improved carrier confinement was achieved, which was revealed by band structure calculation and confirmed by temperature-dependent PL spectra. At 300 K, the QW emission peaks at 2560 nm and 2800 nm for samples A and B were observed, respectively. The peak intensity increased dramatically as temperature decreased to 10 K, indicating a typical direct bandgap behavior. The transitions from Ge and GeSn barriers were also obtained and the peaks are partially overlapped due to small energy separation. Comparing samples B to A, the higher Sn composition in the well and increased well layer thickness lead to more direct bandgap and significantly enhanced carrier confinement of sample B. Particularly at lower temperature, the sufficient carrier confinement of sample B resulted in hundreds of times integrated PL intensity increase under

CW pump lasers, and in the QW emissions dominating the PL under both CW and pulse pump lasers.

5.3 Summary

In this chapter GeSn/GeSn QW's with both SQW and DQW structures were studied. The SQW structure showed direct bandgap and with type-I band alignment. Increasing the Sn in the buffer allowed for more Sn in the well as was shown in the DQW samples. Samples with a wide DQW structure reduced the quantized energy state and increased the carrier confinement. Using this method and the high Sn composition recently demonstrated, the possibilities of obtaining QW emitters in the mid-infrared regime have become more realistic.

Chapter 6 SiGeSn/GeSn Quantum Wells

6.1 Introduction

Group IV light emitters such as light emitting diodes (LEDs) and lasers have long been wanted for the development of optoelectronic integrated circuits. Photonic integration on Si got a breath of life with the recent development of group IV-based GeSn growth technique [213, 229, 264]. Development of the GeSn material system to produce direct bandgap material and devices based off of the direct bandgap including GeSn LEDs and optically pumped lasers has demonstrated the vast potential for Si-based emitters [170, 175, 177, 205, 230, 234]. Over the last few years, GeSn double heterostructures (DHS) [160, 200, 202, 230, 234, 246, 248, 251, 265] and quantum wells (QWs) [179, 181, 185, 187, 189, 250–254] have been reported. The motivation to demonstrate Ge/GeSn/Ge QW structure is based on the general acknowledgement that application of QW structures to LEDs and lasers could improve device performance. However, the detailed analysis suggested that using Ge as a barrier did not provide the desired carrier confinement due to the relative large lattice mismatch between Ge and GeSn [190]. Previous studies contained in Chapters 5 showed that the GeSn/GeSn material systems could be used to develop direct bandgap type I QW structures that enhance the emission over that of traditional bulk films [264].

The limitations using Ge and relaxed GeSn as barriers promote the use of the ternary material SiGeSn as the barrier, due to the ability to independently engineer the bandgap energy and lattice constant of the SiGeSn alloys. The SiGeSn/GeSn/SiGeSn QWs were grown and characterized recently [193, 194, 250, 251]. The carrier confinement in the QW was improved by using SiGeSn as barrier compared to those using Ge and GeSn by tuning the Si and Sn compositions to targeted compositions. Furthermore, to improve the device performance such as

light emission efficiency, the direct bandgap well is necessarily required, which can be achieved by using high-Sn GeSn material. To date, there are no known systematic studies which have been performed on direct bandgap type-I band alignment GeSn QW utilizing SiGeSn as a barrier layer.

Control of the compressive strain is critical to the achievement of direct bandgap type-I band alignment necessary for efficient GeSn LED and laser devices as the compressive strain moves the GeSn bandgap more toward indirect in nature. The relatively large lattice constant of high composition GeSn increases the challenge to keep the compressive strain under control. In this work, a series of SiGeSn/GeSn QW samples were examined including: i) three single quantum wells; ii) a double quantum well; and iii) a multiple quantum well with four wells. Similar to the GeSn/GeSn quantum wells shown in Chapter 5, these samples were also grown on a relaxed $Ge_{0.925}Sn_{0.085}$ buffer layer to reduce the strain in the well regions. The single quantum well samples were grown with increasing thickness. By increasing the well thickness, the quantized energy state was reduced near the bulk band-edge thus extending the wavelength as well as increasing the carrier confinement. The double and multiple quantum well structures are based on the thickest single quantum well studied. Clear QW emissions were seen in the temperature-dependent PL spectra of all samples. Direct bandgap of the GeSn QW was confirmed by significantly increased PL intensity at low temperatures and the increased ratio of integrated PL intensity at 10 K / 200 K, compared to that of the thinner well sample, indicated improved carrier confinement.

6.1.1 Experimental Details

6.1.2 Material Growth and Calculations

A commercial ASM Epsilon 2000–plus standard RPCVD system was used to grow the

QW samples studied in this work. Low-cost commercially available SiH_4, GeH_4, and $SnCl_4$ were used as Si, Ge, and Sn precursors, respectively. A 700-nm-thick Ge buffer layer was grown prior to QW growth by a two-step growth method. The nominal designed QW structures consisted of the following from the bottom to top: i) the 600-nm-thick $Ge_{0.915}Sn_{0.085}$ buffer for samples; ii) the SiGeSn barrier layers; and iii) GeSn wells. Each sample will be discussed in more detail before presenting characterization results. The detailed growth method has been described elsewhere. [214]

Following growth, the Si and Sn compositions and the degree of strain of each layer were ascertained by SIMS, HRXRD 2θ-ω scan, and RSM. The GeSn lattice bowing parameter of -0.066 was used for deriving the Sn composition from the RSM. The cross sectional TEM measurement was employed to validate the layer thickness and material quality.

6.1.3 Band Structure Calculation

The band diagrams of the QW samples at 300 K were calculated using the measured QW structure data. The bandedge bowing parameters b_Γ=1.95 and b_L=0.68 were selected to determine the direct and indirect bandgap energies based on Vegard's law, which are valid for the high-Sn material. The effective mass approximation and the propagation matrix approach were used to calculate the electronic band structure and quantized energy levels. The band offsets for conduction band (CB) and valence band (VB) were calculated following the methods discussed in refs. 256 and 258.

6.1.4 Photoluminescence Study

The temperature-dependent PL measurements were performed using standard off-axis configuration with lock-in technique (optically chopped at 377 Hz). The emissions were collected using a grating based spectrometer equipped with a thermoelectrically cooled PbS

detector with cutoff at 3.0 μm. For this initial study, only the 532 nm laser was used with 500 mW of pumping power.

6.2 Single Quantum Wells (SQW)

A set of three single quantum wells were grown and characterized. These were grown with increasing nominal thickness, (10-, 15-, 20-nm for samples denoted as samples A, B, and C, respectively). The nominal designed QW structures consisted of the following from the bottom to top: i) 600-nm-thick $Ge_{0.915}Sn_{0.085}$ buffer for samples; ii) $Si_{005}Ge_{0.89}Sn_{0.06}$ barrier layers (60-nm in layer thickness; and iii) $Ge_{0.86}Sn_{0.14}$ wells. Figure 6-1 shows the designed sample structures for the single quantum wells studied.

Sample A	Sample B	Sample C
$Si_{0.05}Ge_{0.89}Sn_{0.06}$ 60 nm	$Si_{0.05}Ge_{0.89}Sn_{0.062}$ 60 nm	$Si_{0.05}Ge_{0.89}Sn_{0.06}$ 60 nm
$Ge_{0.85}Sn_{0.15}$ 10 nm	$Ge_{0.85}Sn_{0.15}$ 15 nm	$Ge_{0.85}Sn_{0.15}$ 20 nm
$Si_{0.05}Ge_{0.89}Sn_{0.06}$ 70 nm	$Si_{0.05}Ge_{0.89}Sn_{0.06}$ 70 nm	$Si_{0.05}Ge_{0.89}Sn_{0.06}$ 70 nm
$Ge_{0.91.5}Sn_{0.085}$ buffer 600 nm	$Ge_{0.91.5}Sn_{0.085}$ buffer 600 nm	$Ge_{0.91.5}Sn_{0.085}$ buffer 600 nm
Ge buffer 700nm	Ge buffer 700nm	Ge buffer 700nm
Si Substrate	Si Substrate	Si Substrate

Figure 6-1: Sample structures for the single quantum wells.

6.2.1 Material Characterization

Material characterization was performed to fully understand the QW structure to produce simulations that correctly modeled the samples. Several characterization techniques were used to verify the composition of Sn and Si and strain in each structural layer. Figures 6-2, 6-3, and 6-4 show the SIMS profiles for the grown samples.

The SIMS profiles for samples A and B in Figures 6-2 and 6-3 show the Sn composition in each layer was uniform. The transition was graded and not abrupt however, the buffer,

barrier, and well regions could be clearly distinguished. The compositions of Sn and Si in the layers agreed well with the designed sample structures shown in Figure 6-1, implying strictly controlled material growth processes.

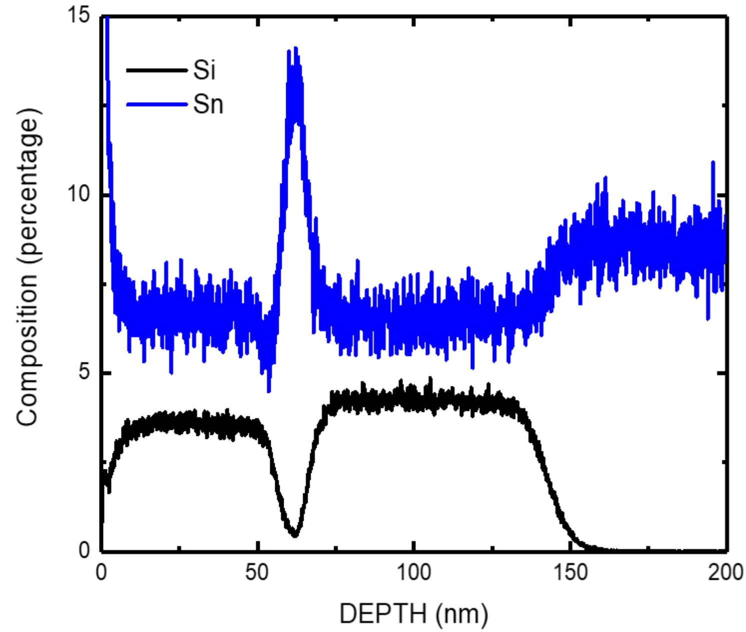

Figure 6-2: SIMS profile for sample A.

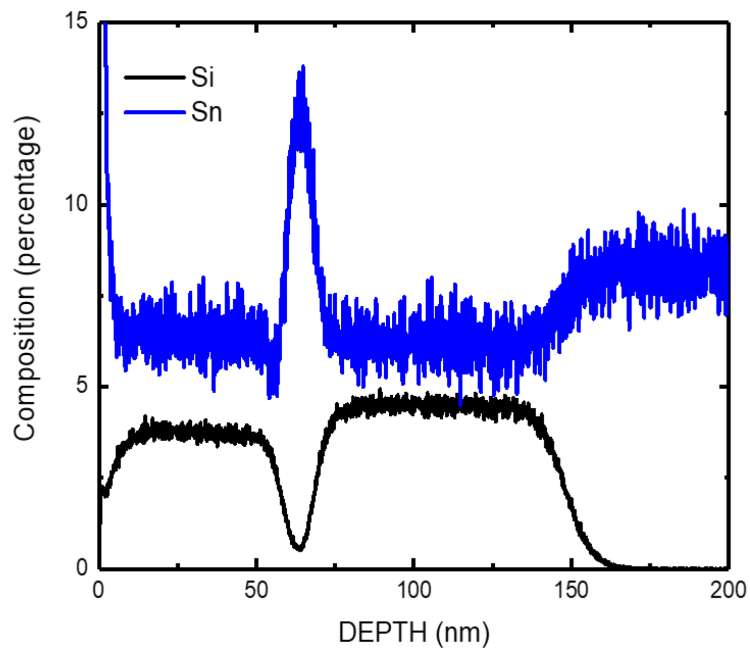

Figure 6-3: SIMS profile for sample B.

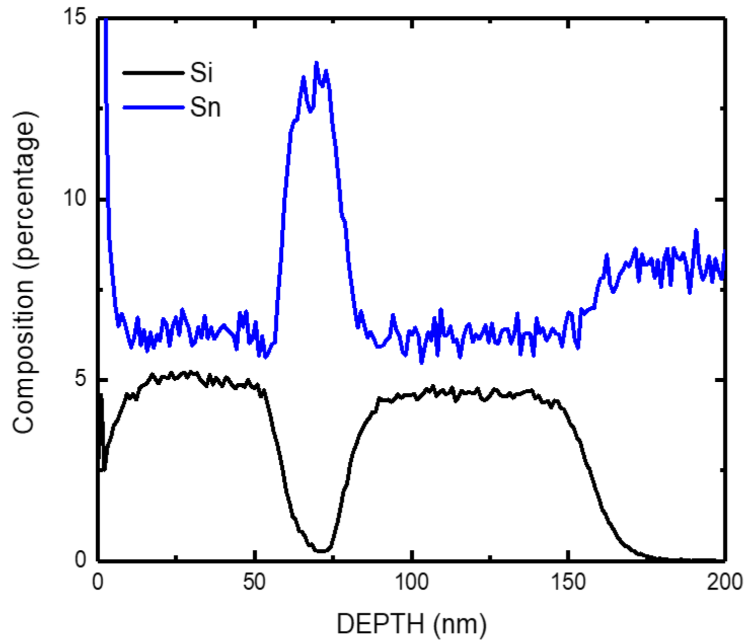

Figure 6-4: SIMS profile for sample C.

Samples A and B are seen to been very similar in thickness, however, sample C was considerably thicker. Further confirmation of the Sn incorporation and strain of the layers was accomplished using HRXRD shown in Figures 6-5, 6-6, and 6-7.

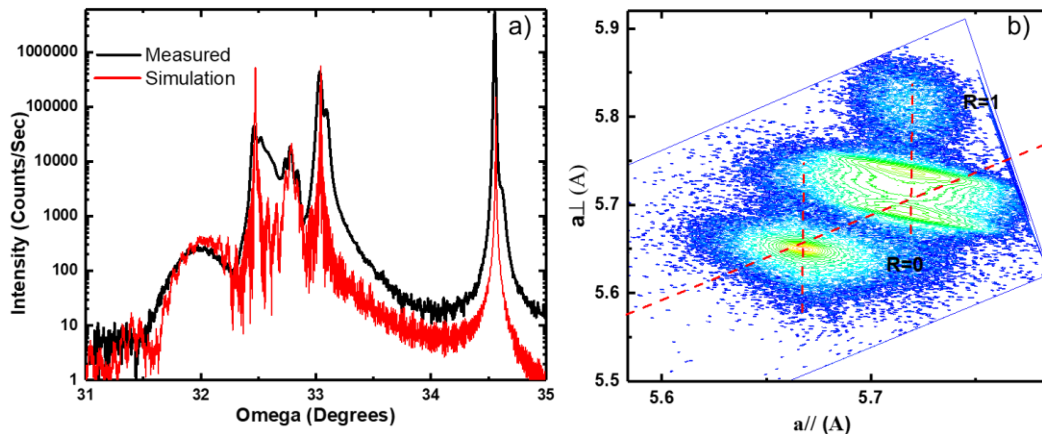

Figure 6-5: a) HRXRD rocking curve with simulation. b) RSM of sample A.

The HRXRD 2θ-ω scans are shown in Figures 6-5(a) for sample A. The black and red curves are the measured data and simulation results, respectively. In Figure 6-5(a), the peak at

~66° indicated the Ge buffer. A small peak located at ~66.5° was associated with the tensile strained SiGeSn barrier layers. The peaks at ~65.0° and ~64.0° corresponded to GeSn buffer (measured as 9.4% Sn for the buffer and 15% for the well). The XRD 2θ-ω simulation was conducted to further analyze the QW, by which the lattice constant and layer thickness could be determined.

The RSM shown in Figure 6-5(b) shows the clear four regions. The bottom region corresponded to the Ge buffer layers. The region above the Ge indicated the contour plot of the almost relaxed $Ge_{0.91}Sn_{0.09}$ buffer with the residual compressive strain of 0.15%. Directly below the GeSn buffer region, the tensile strained SiGeSn barriers, while the top region was the $Ge_{0.85}Sn_{0.15}$ well. It is shown that both barrier and well were psuedomorphic to the relaxed $Ge_{0.91}Sn_{0.09}$ buffer.

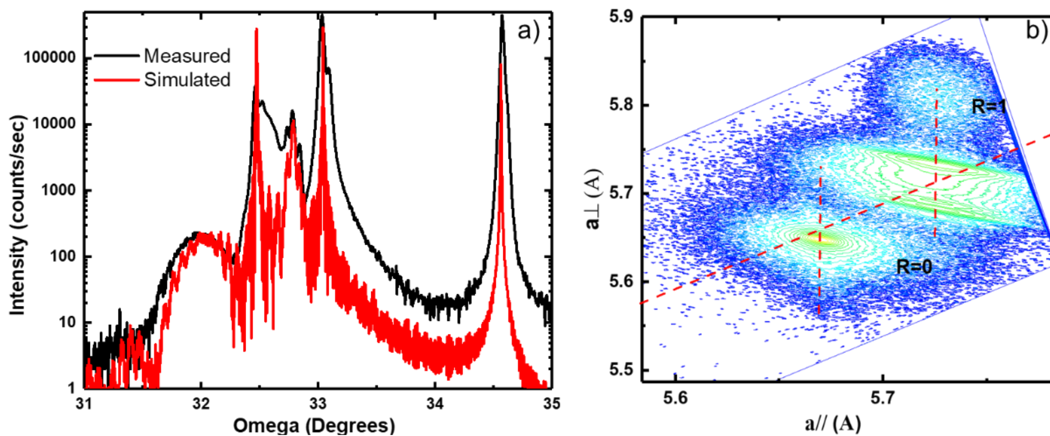

Figure 6-6: a) HRXRD rocking curve with simulation. b) RSM of sample B.

Figure 6-6(a) and (b) shows the XRD results of sample B. The similar 2θ-ω scan and RSM plot were obtained with the only exception being since the measured Sn compositions and well (15.2%) of sample B were higher than those of sample A, the GeSn peaks in 2θ-ω scan exhibited at 63.9°, shifting toward lower angles as expected.

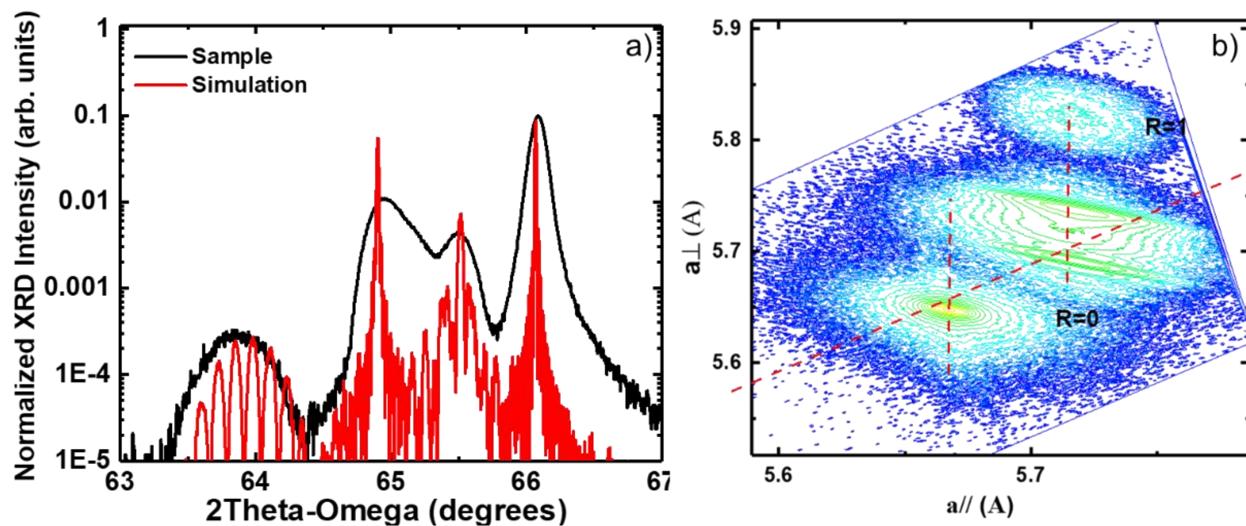

Figure 6-7: a) HRXRD rocking curve with simulation. B) RSM of sample C.

Figure 6-7(a) and (b) show the XRD results of sample C. Similar 2θ-ω scan and RSM plot showed that increased Sn in the well for sample C further shifted the well peak to lower angles, displaying at 63.8°. The increased thickness in the well region pushes the critical thickness and partial relaxation was shown, Figure 6-7(b). To investigate the layered structure, TEM was performed on sample C, shown in Figure 6-8. A summary of the characterization results is given in Table 5.

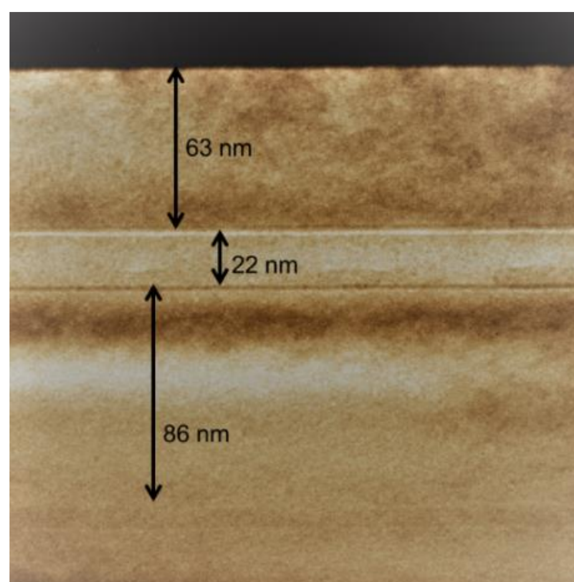

Figure 6-8: TEM image of sample C.

Table 5: Summary of SiGeSn/GeSn SQW sample information

Sample	Layer structure	Sn (%)		Si (%)		Thickness (nm)		Strain (%)
		Designed	Measured	Designed	Measured	Designed	Measured	
A	SiGeSn barrier	6	6.4	5	4.2	60	55	0.29
	GeSn well	15	15	0	0	10	11	-0.95*
	SiGeSn barrier	6	6.4	5	4.2	70	67	0.29
	GeSn buffer (bottom barrier)	8.5	9.3	0	0	600	600	-0.19*
	Ge buffer	0	0	0	0	700	700	0.17
B	SiGeSn Barrier	6	6.4	5	5	60	56	0.40
	GeSn well	15	15.2	0	0	15	14	-0.84*
	SiGeSn barrier	6	6.3	5	4.7	70	67	0.31
	GeSn buffer (bottom barrier)	8.5	9.4	0	0	600	600	-0.09*
	Ge buffer	0	0	0	0	700	700	0.19
C	SiGeSn barrier	6	6.4	5	5	60	65	0.22
	GeSn well	15	15.4	0	0	20	22	-1.03*
	SiGeSn barrier	6	6.3	5	4.7	70	86	0.22
	GeSn buffer	8.5	9	0	0	600	600	-0.29*
	Ge buffer	0	0	0	0	700	700	0.17

* Negative value indicates compressive strain.

6.2.2 Band Structure and Optical Transition Analysis

The bandedge diagrams of the QW samples at 300 K were calculated using the measured QW structure data shown in Table 5. Figure 6-9(a)-(d) illustrates the band structures at CB and

VB and possible optical transitions of sample A. Using selected bowing parameters and considering the compressive strain of 0.95%, the direct bandgap $Ge_{0.85}Sn_{0.15}$ well was obtained with the energy difference between Γ-L valley of 44 meV. Due to quantized energy levels in the well, the first energy levels in CB ($n_{1\Gamma}$) and VB (n_{1HH}) were calculated as 32 meV above the Γ valley minimum and 9 meV below the heavy hole (HH) band maximum, respectively. Figure 6-9 shows the barrier heights at each layer interface, which revealed that the type-I band alignment was achieved. In Figure 6-9(c), in the CB, the barrier height between SiGeSn barriers (including bottom barrier and top-barrier) and GeSn well was calculated as 28 meV to the L valley. In the VB, the residual strain resulted in the split of HH and light hole (LH) bands. The barrier heights at SiGeSn barriers/GeSn well was 81 meV to the light hole band in the tensile strained SiGeSn barriers.

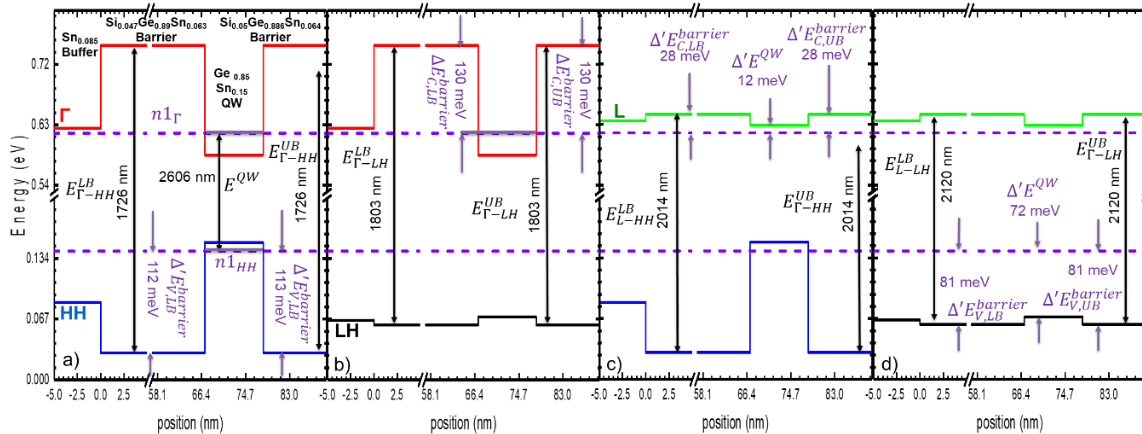

Figure 6-9: Bandedge diagram for sample A.

Since the L valley's first quantized energy level was only 12 meV above the $n_{1\Gamma}$ level in the CB in the GeSn well, as shown in Figure 6-9(c), at room temperature the electrons at $n_{1\Gamma}$ could be thermally excited to populate the L valley in the GeSn well and then populate the L valleys in the SiGeSn barriers. The barrier heights of 130 meV of the SiGeSn barriers provided sufficient electron confinement therefore limiting the electron population of the Γ valley of the

SiGesn barriers. However, the 28 meV barrier height was still insufficient to fully confine the carriers in the well. The re-distribution of electrons resulted in optical transitions that could have originated from multiple recombination mechanisms in different layers. While not expected, the possible transitions from the Γ valley to HH and LH were illustrated in Figures 6-9(a) and (b), respectively. On the other hand, the indirect bandgap transitions with phonon assistance could have occurred from the L valley to the VB. The corresponding transitions were shown in Figures 6-9(c) and (d). The detailed transition mechanism is discussed in the following section via the PL characterization.

Figure 6-10(a)-(d) illustrates the band structures at CB and VB and possible optical transitions of sample B. Using selected bowing parameters and considering the compressive strain of 0.84%, the direct bandgap $Ge_{0.848}Sn_{0.152}$ well was obtained with the energy difference between Γ-L valley of 47 meV. Due to quantized energy levels in the well, the first energy levels in CB ($n_{1\Gamma}$) and VB (n_{1HH}) were calculated as 24 meV above the Γ valley minimum and 6 meV below the heavy hole (HH) band maximum, respectively. Figure 6-10 shows the barrier heights at each layer interface, which revealed that the type-I band alignment was achieved. In Figure 6-10 (c), in the CB, the barrier height between SiGeSn barriers (including bottom barrier and top-barrier) and GeSn well was calculated as 40 meV to the L valley. In the VB, the residual strain resulted in the split of HH and light hole (LH) bands. The barrier heights at SiGeSn barriers/GeSn well was 75 meV to the light hole band in the tensile strained SiGeSn barriers.

Since the L valley's first quantized energy level was 23 meV above the $n_{1\Gamma}$ level in the CB in the GeSn well, as shown in Figure 6-10(c), room temperature electrons at $n_{1\Gamma}$ possessed the thermal energy to excite population of the L valley in the GeSn well. Thermal electrons had 26 meV of increased energy, therefore, barrier heights of 40 meV from the L valley in the

barriers improved the barrier height from Sample A but did not confine electrons to the well. The barrier heights of 164 meV of the SiGeSn barriers provided sufficient electron confinement, therefore limiting the electron population of the Γ valley of the SiGeSn barriers. While not expected, the possible transitions from the Γ valley to HH and LH are illustrated in Figures 6-10(a) and (b), respectively. On the other hand, the indirect bandgap transitions with phonon assistance could occur from the L valley to the VB. The corresponding transitions are shown in Figures 6-10(c) and (d). The detailed transition mechanism is discussed in the following section via the PL characterization.

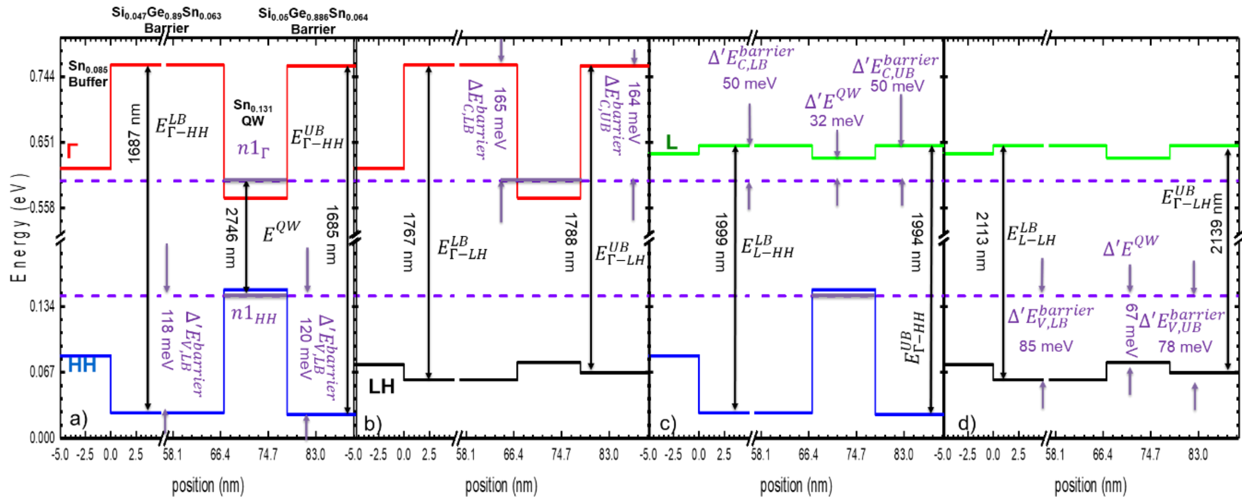

Figure 6-10: Bandedge diagram for sample B.

Figure 6-11(a)-(d) illustrates the band structures at CB and VB and possible optical transitions of sample C. Using selected bowing parameters and considering the compressive strain of 1.03%, the direct bandgap $Ge_{0.846}Sn_{0.154}$ well was obtained with the energy difference between Γ-L valley of 44 meV. Due to quantized energy levels in the well, the first energy levels in CB ($n_{1\Gamma}$) and VB (n_{1HH}) were calculated as 12 meV above the Γ valley minimum and 3 meV below the heavy hole (HH) band maximum, respectively. Figure 6-11 shows the barrier heights at each layer interface, which revealed that the type-I band alignment was achieved. In

Figure 6-11 (c), in the CB, the barrier height between SiGeSn barriers (including bottom barrier and top-barrier) and GeSn well was calculated as 50 meV to the L valley. In the VB, the residual strain resulted in the split of HH and light hole (LH) bands. The barrier heights at SiGeSn barriers/GeSn well was 103 meV to the light hole band in the tensile strained SiGeSn barriers.

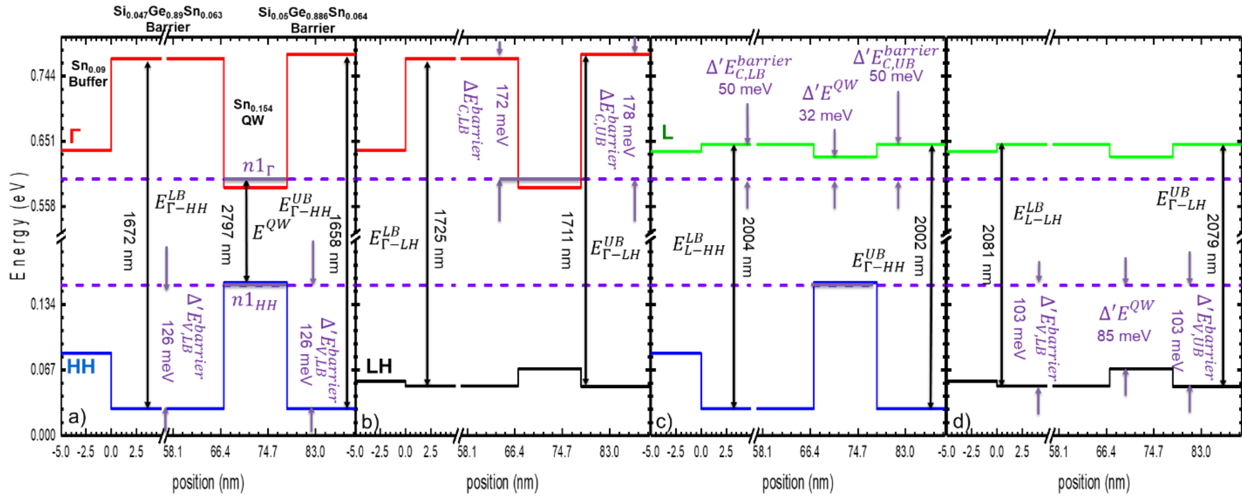

Figure 6-11: Bandedge diagram for sample C.

Since the L valley's first quantized energy level was 32 meV above the $n_{1\Gamma}$ level in the CB in the GeSn well, as shown in Figure 6-10(c), room temperature electrons at $n_{1\Gamma}$ should not possess the thermal energy to excite population of the L valley in the GeSn well. Thermal electrons had 26 meV of increased energy therefore, barrier heights of 50 meV from the L valley in the barriers may not have been populated with thermal electrons. The barrier heights of 172 meV of the SiGeSn barriers provided sufficient electron confinement, therefore limiting the electron population of the Γ valley of the SiGesn barriers. Successful confinement of electrons resulted in optical transitions that originated from the QW layer. While not expected, the possible transitions from the Γ valley to HH and LH are illustrated in Figures 6-10(a) and (b), respectively. The indirect bandgap transitions with phonon assistance was not expected due to stronger carrier confinement and greater energy to the L valley from the quantized energy state.

The corresponding transitions are shown in Figures 6-10(c) and (d). The detailed transition mechanism is discussed in the following section via the PL characterization.

6.2.3 Photoluminescence Spectra Analysis

The temperature-dependent PL study was performed using the standard off-axis and lock-in techniques. A 532-nm continuous-wave laser with 500 mW power and 65 µm spot size was used as the pumping source. The emissions were collected using a spectrometer equipped with a thermoelectrically cooled PbS detector with cutoff at 3.0 µm. Figure 6-12 shows the temperature-dependent PL spectra for all three samples which were stacked for clarity.

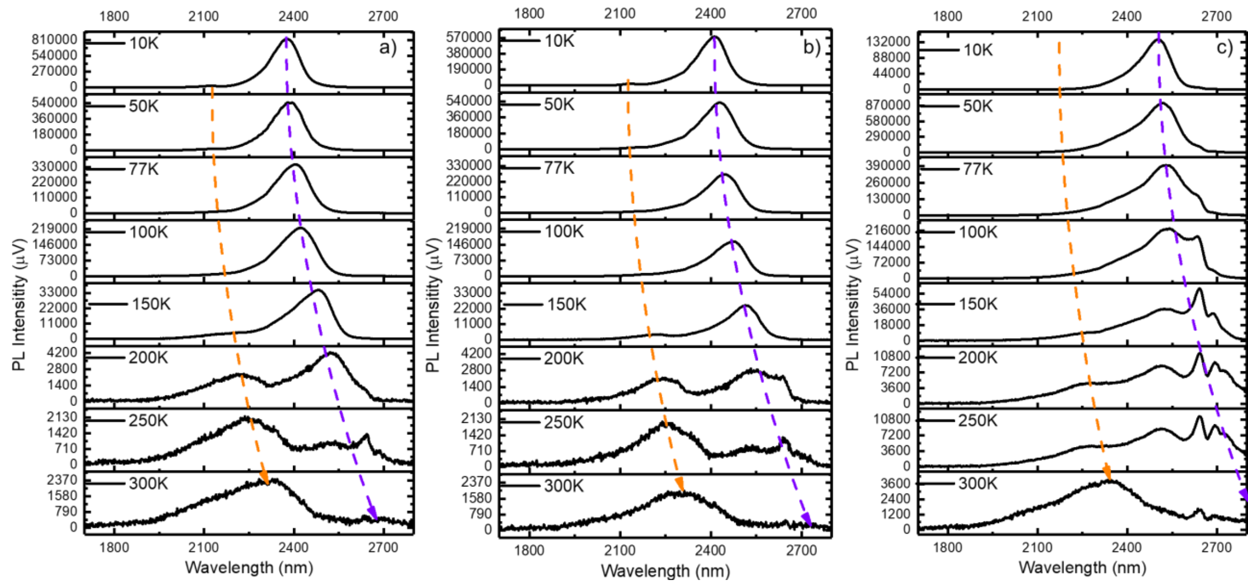

Figure 6-12: Temperature dependent PL spectra for (a) sample A, (b) sample B, and (c) sample C.

The multi-peak feature was observed at some temperatures. The Gaussian fitting was used to investigate each peak in terms of peak position, full width at half maximum (FWHM), and integrated PL intensity. However, strong atmospheric absorption occurred in the spectra beyond 2.6 µm thus interfering with the emission from the QW. This interfered with the data fitting of the PL spectra.

In Figure 6-12, a major peak in each spectrum is shown at ~ 2330 nm (0.532 eV) while the atmospheric absorption distorted the longer wavelength peak at 300K. As the temperature was decreased, both peaks shifted toward shorter wavelength. No additional peaks were seen in any spectra, contributing to the evidence that increased confinement of electrons suppressed transitions from the barrier layers as was seen in the GeSn/GeSn QWs shown in Chapter 5. Also different is that, even at increased temperatures and under atmospheric absorption the peak 2 continued to exhibit increased PL intensity over that of Peak 1. It was shown in Chapter 5 that the cross-over of peak intensity was 150 K or below. This suggests that more carriers were injected into the well due to stronger electron confinement. The atmospheric absorption plaguing the QW emission made fitting of the spectra difficult. To fit this part of the spectra, it was assumed that the emission contained only one peak as shown at low temperature and stayed consistently one peak until encountering atmospheric absorption at 2.6 μm. Peak positions from PL fitting are given in Figure 6-13.

Using the Varshni fitting formula allowed a means to roughly test the fitting of the PL information. Figure 6-13 shows the fitting for all three samples. The fitting based peak position for sample A agreed well with published data, while that of samples B and C did not agree well [220]. Elimination of the last two peak positions for sample C allowed for Varshni fitting that had better agreement to that of published literature. This suggests that the fitting at higher temperatures where the atmospheric absorption was detrimental to the obtained PL spectra was not accurate. The fitting parameters for the samples are given in Table 6. Sample C had the best carrier confinement and lowest transition energy thus making it the longest wavelength emitter of the three tested samples. This pushed it more toward the atmospheric absorption region and toward the detector cutoff. These two factors enhance the error in the fitting of PL data at the

upper temperature range.

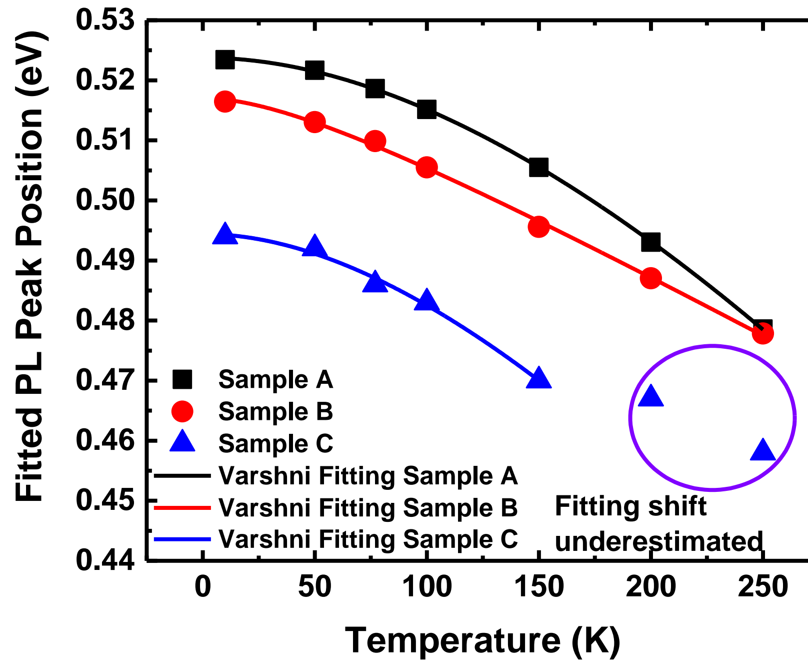

Figure 6-13: Peak positions of QW samples. Varshni fitting for each sample.

Table 6: Varshni fitting parameters derived from fitting PL spectra peaks.

Sample	E_0	A	B
Sample A	0.52377	6.78×10^{-4}	687
Sample B	0.51703	2.06×10^{-4}	77
Sample C - Before	0.49018	2.29×10^{13}	4.04×10^{19}
Sample C - After	0.49441	6.18×10^{-4}	421.07

The integrated intensity and FWHM fitting of the PL spectra are given in Figure 6-14. The normalized PL intensity in Figure 6-14a) shows that the integrated PL intensity for all three samples was strong at low temperature and reduced as the temperature was increased. The multiplied increase in integrated PL intensity of each sample from high temperature to low temperature was 556, 447, and 591 for samples A, B, and C, respectively.

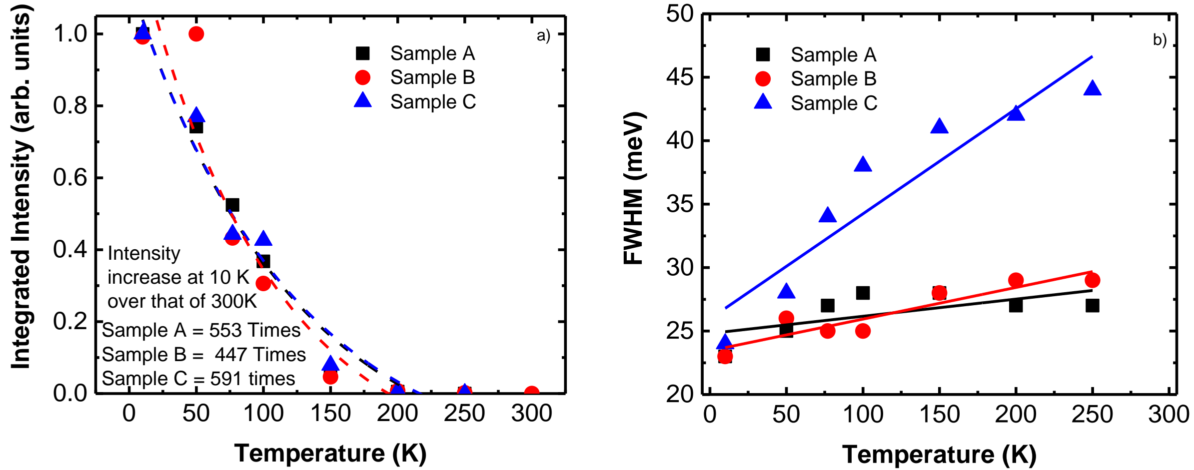

Figure 6-14: Normalized integrated PL intensity and FWHM of the PL spectra.

The FWHM of the samples in Figure 6-14b) shows all samples possessed narrow line widths with samples A and B showing narrower line width than sample C. Sample C was a thicker well than the other samples, A and B, and had more inconsistency in the peak fitting due to the atmospheric absorption. This could account for the increased line width at higher temperatures. The temperature dependent PL of the samples show that all three samples were direct bandgap QWs as was suggested from the band structure simulation in Figures 6-9, 6-10, and 6-11.

6.2.4 Conclusion

In conclusion, three SiGeSn/GeSn single QW samples with different well thicknesses were grown and analyzed in depth. By using relaxed GeSn buffer, the direct bandgap well and type-I band alignment were achieved, which were revealed by band structure calculation and confirmed by temperature-dependent PL spectra. At 300 K, the QW emission peaks at 2610, 2750, and 2800 nm for samples A, B, and C were observed, respectively. The peak intensity increased dramatically as temperature decreased to 10 K, indicating typical direct bandgap behavior. Comparing samples C to A and B, the higher Sn composition in the well and increased

well layer thickness led to more bandgap directness and significantly enhanced carrier confinement of sample C. While all samples showed considerable carrier confinement, sample C posted the strongest carrier confinement and resulted in the largest increase in integrated intensity from high temperature to low temperature at 591 times.

6.3 Double Quantum Wells (DQW)

In this section we examine a double quantum well sample based on sample C, from Section 6.3. Sample C with its thicker wells and increased Sn% in the well was calculated to have the highest carrier confinement and showed the strongest PL from the SQW set. The nominally designed QW structures consisted of the following from the bottom to top: i) the 600-nm-thick $Ge_{0.915}Sn_{0.085}$ buffer for samples; ii) the $Si_{005}Ge_{0.89}Sn_{0.06}$ barrier layers (60-nm in layer thickness; and iii) $Ge_{0.85}Sn_{0.15}$ wells (20 nm in layer thickness). Figure 6-15 shows the designed sample structures for the double quantum well studied.

Layer	Thickness
$Si_{0.05}Ge_{0.89}Sn_{0.06}$	60 nm
$Ge_{85}Sn_{15}$	20 nm
$Si_{0.05}Ge_{0.89}Sn_{0.06}$	60 nm
$Ge_{87.7}Sn_{12.7}$	20 nm
$Si_{0.05}Ge_{0.89}Sn_{0.06}$	60 nm
$Ge_{91.5}Sn_{8.5}$	600 nm
Ge	700 nm

Figure 6-15: Nominal sample structure for the SiGeSn/GeSn DQW

6.3.1 Material Characterization

Material characterization was performed to fully understand the QW structure to produce simulations that correctly models the samples. Several characterization techniques were used to

verify the composition of Sn and Si and strain in each structural layer. Figure 6-16 shows the SIMS profiles for the grown sample (annotated as Sample D).

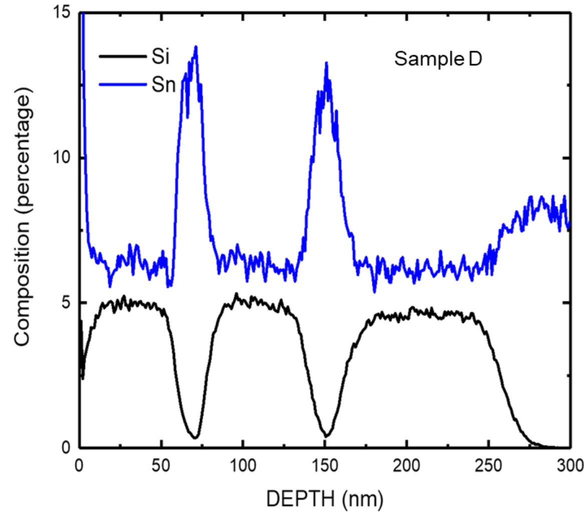

Figure 6-16: SIMS profile of the SiGeSn/GeSn DQW.

The SIMS profiles for sample D in Figure 6-16 show the Sn composition in each layer was uniform. The transition was graded and not abrupt however, the buffer, barrier, and well regions could be clearly distinguished. The compositions of Sn and Si in the layers agreed well with the designed sample structures, implying strictly controlled material growth processes. Further confirmation of the Sn incorporation and strain of the QW and buffer layers was accomplished using HRXRD shown in Figures 6-17.

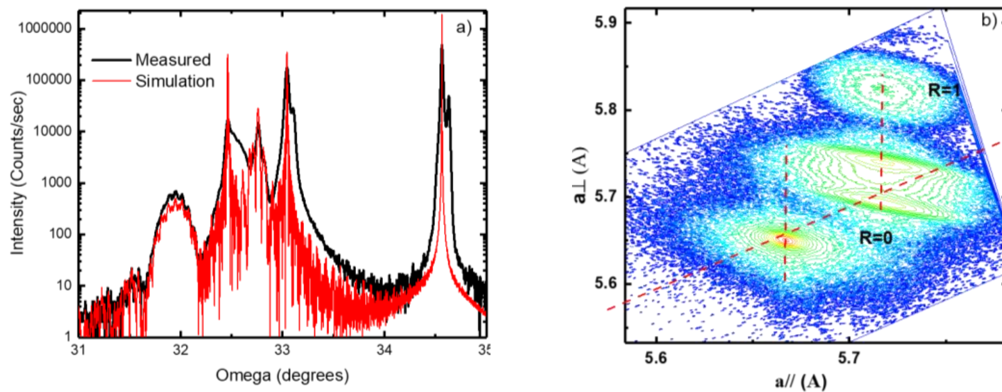

Figure 6-17: HRXRD rocking curve with simulation and RSM of sample D.

The HRXRD ω-2θ scans are shown in Figures 6-17(a). The black and red curves are the measured data and simulation results. In Figure 6-17(a), the peak at ~33° indicated the Ge buffer. A small peak located at ~32.75° was associated with the tensile strained SiGeSn barrier layers. The peaks at ~32.5° and ~31.9° correspond to GeSn buffer (measured as 9% Sn for the buffer and 15.5% for the well). The multiple oscillations were associated with thickness fringes of the multi-layered structure suggesting high quality of the layer interfaces. The XRD ω-2θ simulation was conducted to further analyze the QW, by which the lattice constant and layer thickness could be determined. The RSM in Figure 6-17(b) shows the clear four regions. The bottom region corresponded to the Ge buffer layers. The region above the Ge indicated the contour plot of the almost relaxed $Ge_{0.91}Sn_{0.09}$ buffer with the residual compressive strain of 0.2%. Directly below the GeSn buffer region, the tensile strained SiGeSn barriers, while the top region was the $Ge_{0.84.5}Sn_{0.15.5}$ well. It is shown that both barrier and well were psuedomorphic to the relaxed $Ge_{0.91}Sn_{0.09}$ buffer. The increased thickness in well region pushed the critical thickness and partial relaxation began to be seen, Figure 6-17(b). To investigate the layered structure, cross sectional TEM was done on Sample D, shown in Figure 6-18.

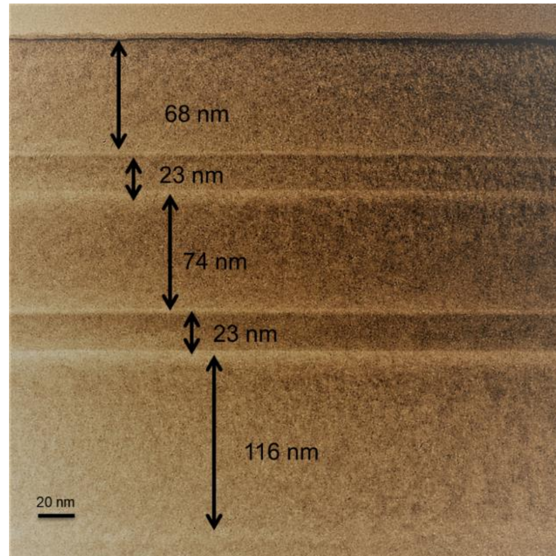

Figure 6-18: TEM image of sample D.

The TEM imaging accomplished on sample D shows clearly defined layers near the designed thickness, indicating precise control of the growth. Layer interfaces were smooth, and no threading dislocations could be seen in the image, demonstrating high quality material. This was particularly interesting for sample D, due to the $Ge_{0.85}Sn_{0.15.5}$ well layer featuring partial relaxation. The measured thickness of each layer from TEM images was consistent with the value that was extracted from the simulated XRD ω-2θ scan curve. Material characterization results are summarized in Table 7.

Table 7: Summary of SiGeSn/GeSn DQW sample information

Sample	Layer structure	Sn (%)		Si (%)		Thickness (nm)		Strain (%)
		Designed	Measured	Designed	Measured	Designed	Measured	
D	SiGeSn barrier	6	6.2	5	4.6	60	68	0.26
	GeSn well	15	15	0	0	20	23	-1.03*
	SiGeSn barrier	6	6.2	5	4.6	60	74	0.26
	GeSn well	15	15	0	0	20	23	-1.03*
	SiGeSn barrier	6	6.2	5	4.6	100	116	0.26
	GeSn buffer (bottom barrier)	8.5	9	0	0	600	600	-0.26
	Ge buffer	0	0	0	0	700	700	0.17

* Negative value indicates compressive strain.

6.3.2 Band Structure and Optical Transition Analysis

The bandedge diagrams of the QW samples at 300 K were calculated using the measured QW structure data shown in Table 7. Figure 6-19(a)-(d) illustrates the band structures at CB and VB and possible optical transitions of sample D. Using selected bowing parameters and

considering the compressive strain of 1.03%, the direct bandgap $Ge_{0.845}Sn_{0.155}$ well was obtained with the energy difference between Γ-L valley of 46 meV. Due to quantized energy levels in the well, the first energy levels in CB ($n_{1\Gamma}$) and VB (n_{1HH}) were calculated as 10 meV above the Γ valley minimum and 2 meV below the heavy hole (HH) band maximum, respectively. Figure 6-19 shows the barrier heights at each layer interface, which revealed that the type-I band alignment was achieved. In Figure 6-19(c), in the CB, the barrier height between SiGeSn barriers (including bottom barrier and top-barrier) and GeSn well was calculated as 35 meV to the L valley. In the VB, the residual strain results in the split of HH and light hole (LH) bands. The barrier heights at SiGeSn barriers/GeSn well is 85 meV to the light hole band in the tensile strained SiGeSn barriers.

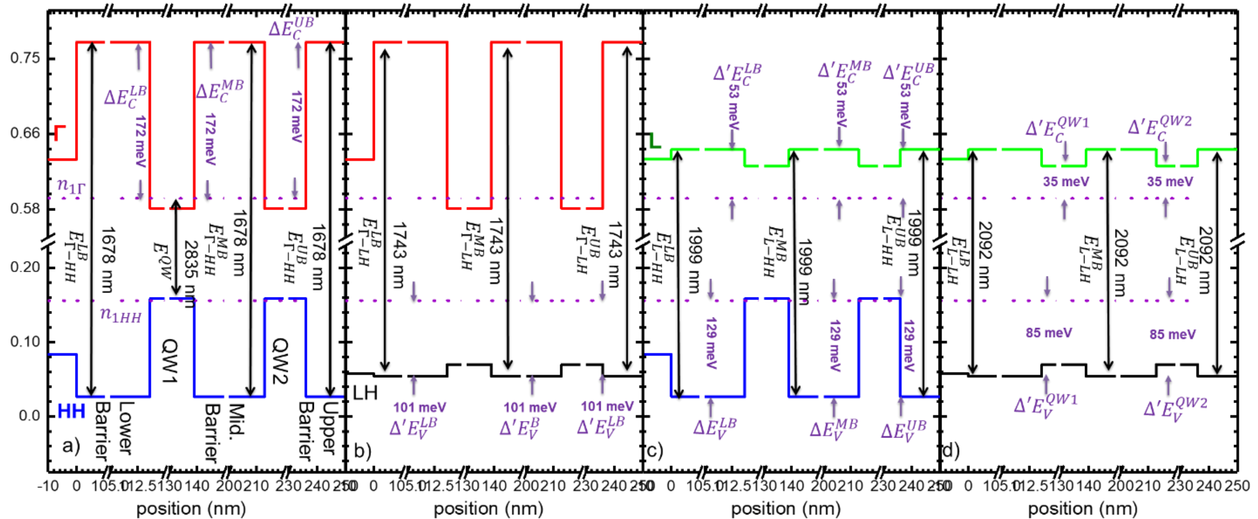

Figure 6-19: Bandedge diagram for sample D.

Since the L valley's first quantized energy level was 35 meV above the $n_{1\Gamma}$ level in the CB in the GeSn well, as shown in Figure 6-19(c), at room temperature the electrons at $n_{1\Gamma}$ could be thermally excited to populate the L valley in the GeSn well and then populate the L valleys in the SiGeSn barriers. The barrier heights of 172 meV of the SiGeSn barriers provided sufficient

electron confinement therefore limiting the electron population of the Γ valley of the SiGesn barriers. The 53 meV barrier height should have been sufficient to fully confine the carriers in the well. While not expected, the possible transitions from the Γ valley to HH and LH were illustrated in Figures 6-19(a) and (b), respectively. On the other hand, the indirect bandgap transitions with phonon assistance could occur from the L valley to the VB. The corresponding transitions are shown in Figures 6-19(c) and (d). The detailed transition mechanism is discussed in the following section via the PL characterization.

6.3.3 Photoluminescence Spectra Analysis

The temperature-dependent PL study was performed using the standard off-axis and lock-in techniques. A 532-nm continuous-wave laser with 500 mW power and 65 μm spot size was used as the pumping source. The emissions were collected using a spectrometer equipped with a thermoelectrically cooled PbS detector with cutoff at 3.0 μm. Figure 6-20 shows the temperature-dependent PL spectra for sample D stacked for clarity.

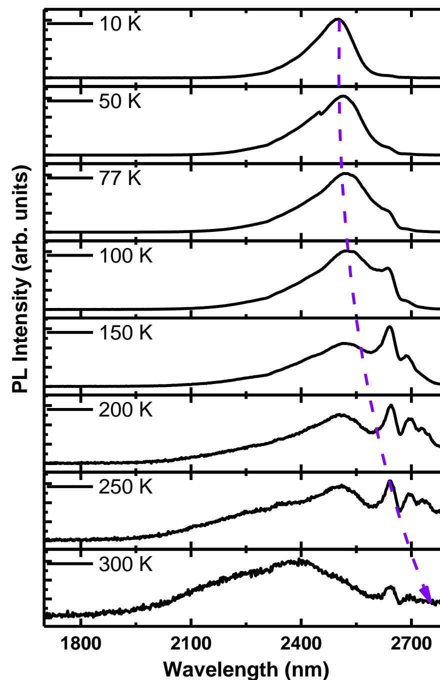

Figure 6-20: Temperature dependent PL of sample D.

The multi-peak feature observed in the SQW samples weren't observed for sample D. The Gaussian fitting was used to investigate each peak in terms of peak position, FWHM, and integrated PL intensity. However, strong atmospheric absorption occurred in the spectra beyond 2.6 µm thus interfering with the emission from the QW. This interfered with the data fitting of the PL spectra.

The temperature dependent PL shown in Figure 6-20, was affected by atmospheric absorption in all the spectra except for the 10 K measurement. This atmospheric absorption made obtaining spectral information impossible. However, some deductions were made about the sample, including: i) Sample D was direct band gap with type-I band alignment (based on the Sn composition and strain), ii) carrier confinement was significant as only one peak was observed, (all other GeSn/GeSn and SiGeSn/GeSn studies so far show GeSn buffer emission), iii) observed PL emission corresponded well to expected emission, even-though true peak could not be observed through the atmospheric absorption, and iv) the 10 K FWHM of the spectra was measured at 26 meV (similar to that of SQW samples).

6.3.4 Conclusion

In this section, the material characterization, bandedge structure simulation, and the temperature dependent PL optical characterization of a SiGeSn/GeSn double QW were presented. The grown structure was close to the desired structure showing good control of the growth process. The band edge structure suggested direct bandgap QW with type-I band alignment to the SiGeSn barriers. Calculation of carrier confinement suggested the effective confinement of carriers to the wells. PL emission was strongly affected by CO_2 atmospheric absorption limiting the ability to fit the PL spectra. Limited information gained from the low temperature measurement agreed with simulation of structure.

6.4 Multiple Quantum Wells 4x (MQW)

In this section, a 4x multiple quantum well (MQW) sample based on Sample C, from Section 6.3 (annotated as sample E) was examined. Sample C with its thicker wells and increased Sn% in the well was calculated to have the highest carrier confinement and showed the strongest PL from the SQW set. The nominally designed QW structure consisted of the following from the bottom to top: i) 600-nm-thick $Ge_{0.915}Sn_{0.085}$ buffer for samples; ii) $Si_{005}Ge_{0.89}Sn_{0.06}$ barrier layers (60-nm in layer thickness; and iii) $Ge_{0.85}Sn_{0.15}$ wells (20 nm in layer thickness). Figure 6-21 shows the designed sample structures for the multiple quantum well studied.

Layer	Thickness	
$Si_{0.05}Ge_{0.89}Sn_{0.06}$	60 nm	
$Ge_{0.85}Sn_{0.15}$	20 nm	4x
$Si_{0.05}Ge_{0.89}Sn_{0.06}$	60 nm	
$Ge_{0.915}Sn_{0.085}$	600 nm	
Ge	700 nm	

Figure 6-21: Nominal sample structure for the SiGeSn/GeSn MQW.

6.4.1 Material Characterization

Material characterization was performed to fully understand the QW structure to produce simulations that correctly modeled the samples. Several characterization techniques were used to verify the composition of Sn and Si and strain in each structural layer. Figures 6-22 shows the SIMS profiles for the grown sample.

The SIMS profiles for Sample E, shown in Figure 6-22, suggested that the Sn composition in each layer was not uniform. To confirm if this was the case, further characterization was needed. The transition was graded and not abrupt, however, the buffer,

barrier, and well regions could be clearly distinguished.

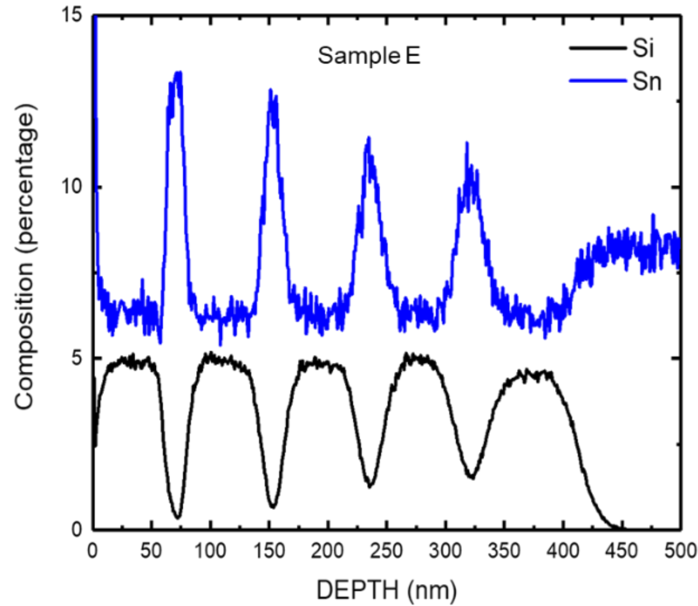

Figure 6-22: SIMS Profile of 4x multiple quantum well sample.

The compositions of Sn and Si in the layers agreed well with the designed sample structures, implying strictly controlled material growth processes. Further confirmation of the Sn in corporation and strain of the QW and buffer layers was accomplished using HRXRD shown in Figures 6-23.

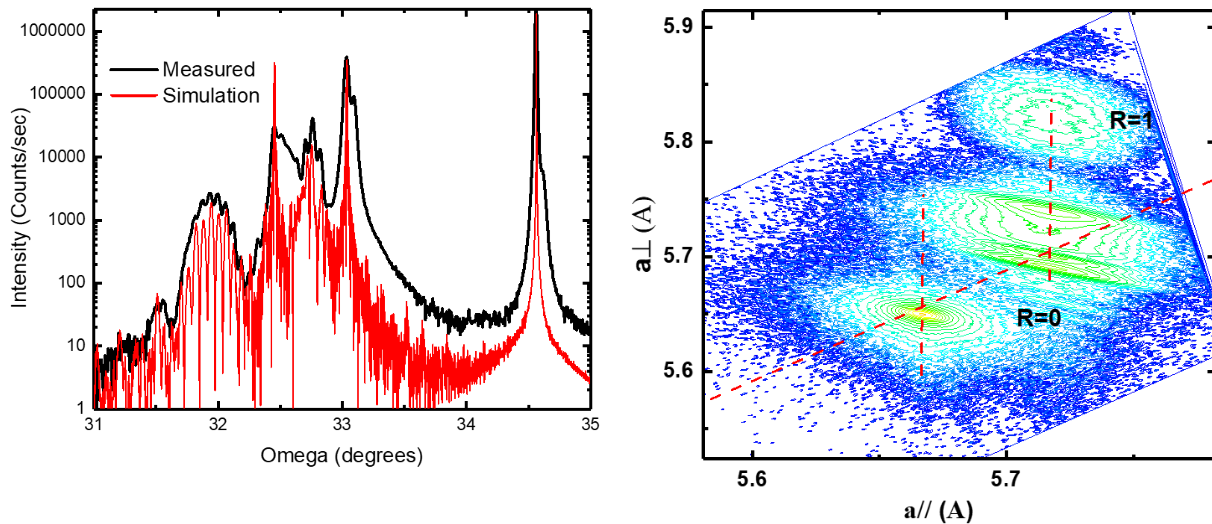

Figure 6-23: HRXRD rocking curve with simulation and RSM of sample E.

The HRXRD ω-2θ scans are shown in Figures 6-23(a). The black and red curves are the measured data and simulation results. In Figure 6-23(a), the peak at ~33° indicated the Ge buffer. A small peak located at ~32.75° was associated with the tensile strained SiGeSn barrier layers. The peaks at ~32.5° and ~31.9° corresponded to GeSn buffer (measured as 9.4% Sn for the buffer and 15.5% for the well). The multiple oscillations seen were associated with thickness fringes of the multi-layered structure suggesting high quality of the layer interfaces. The XRD ω-2θ simulation was conducted to further analyze the QW, by which the lattice constant and layer thickness could be determined. The RSM in Figure 6-23(b) showed the clear four regions. The bottom region corresponded to the Ge buffer layers. The region above the Ge indicated the contour plot of the almost relaxed $Ge_{0.906}Sn_{0.094}$ buffer with the residual compressive strain of 0.2%. Directly below the GeSn buffer region was tensile strained SiGeSn barriers, while the top region was the $Ge_{0.84.5}Sn_{0.15.5}$ well. It is shown that both barrier and well were psuedomorphic to the relaxed $Ge_{0.91}Sn_{0.09}$ buffer. The increased thickness in the well region pushed the critical thickness and partial relaxation began to be seen, Figure 6-23(b). To investigate the layered structure, TEM was performed on Sample E, shown in Figure 6-24.

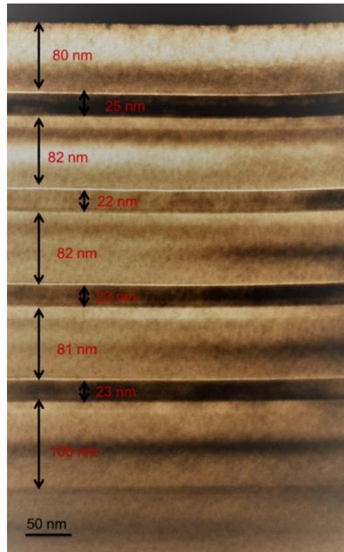

Figure 6-24: TEM image of sample E.

The TEM imaging performed on Sample E shows clearly defined layers near the designed thickness, indicating precise control of the growth. Layer interfaces were smooth, and no threading dislocations could be seen in the image, demonstrating high quality material. This was particularly interesting for sample E, due to the $Ge_{0.85}Sn_{0.15.5}$ well layer features partial relaxation. The measured thickness of each layer from TEM images was consistent with the value that was extracted from the simulated XRD ω-2θ scan curve. Material characterization results are summarized in Table 8.

Table 8: Summary of SiGeSn/GeSn 4x MQW sample information

Sample	Layer structure	Sn (%)		Si (%)		Thickness (nm)		Strain (%)
		Designed	Measured	Designed	Measured	Designed	Measured	
E	SiGeSn barrier	6	6.4	5	5	80	80	0.17
	GeSn well	15	15.5	0	0	20	25	-1.02*
	SiGeSn barrier	6	6.4	5	5	80	82	0.17
	GeSn well	15	15.5	0	0	20	22	-1.02*
	SiGeSn barrier	6	6.4	5	5	80	82	0.17
	GeSn well	15	15.5	0	0	20	23	-1.02*
	SiGeSn barrier	6	6.4	5	5	80	81	0.17
	GeSn well	15	15.5	0	0	20	23	-1.02*
	SiGeSn barrier	6	6.4	5	4.5	100	100	0.25
	GeSn buffer (bottom barrier)	8.5	9.5	0	0	600	600	-0.21
	Ge buffer	0	0	0	0	700	700	0.17

* Negative value indicates compressive strain.

6.4.2 Band Structure and Optical Transition Analysis

The bandedge diagrams of the QW samples at 300 K were calculated using the measured QW structure data shown in Table 6. Figure 6-25(a)-(d) illustrates the band structures at CB and VB and possible optical transitions of sample E. Using selected bowing parameters and considering the compressive strain of 1.02%, the direct bandgap $Ge_{0.845}Sn_{0.155}$ well was obtained with the energy difference between the Γ-L valley of 46 meV. Due to quantized energy levels in the well, the first energy levels in CB ($n_{1\Gamma}$) and VB (n_{1HH}) were calculated as 10 meV above the Γ valley minimum and 2 meV below the heavy hole (HH) band maximum, respectively. Figure 6-25 shows the barrier heights at each layer interface, which revealed that the type-I band alignment was achieved. In Figure 6-25(c), in the CB, the barrier height between SiGeSn barriers (including bottom barrier and top-barrier) and GeSn well was calculated as 36 meV to the L valley. In the VB, the residual strain results in the split of HH and light hole (LH) bands. The barrier heights at SiGeSn barriers/GeSn well was 85 meV to the light hole band in the tensile strained SiGeSn barriers.

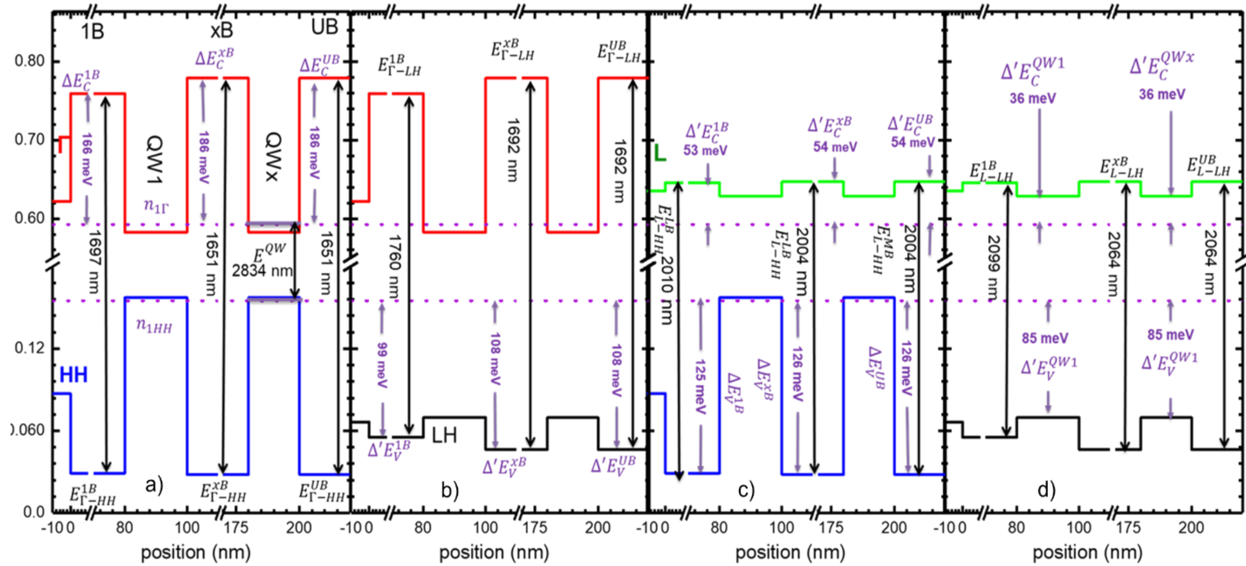

Figure 6-25: Bandedge diagram for Sample E.

Since the L valley's first quantized energy level is 35 meV above the $n_{1\Gamma}$ level in the CB in the GeSn well, as shown in Figure 6-25(c), at room temperature the electrons at $n_{1\Gamma}$ could be thermally excited to populate the L valley in the GeSn well and then populate the L valleys in the SiGeSn barriers. The barrier heights of 186 meV of the SiGeSn barriers provided sufficient electron confinement therefore limiting the electron population of the Γ valley of the SiGesn barriers. The 54 meV barrier height should have been sufficient to fully confine the carriers in the well. While not expected, the possible transitions from the Γ valley to HH and LH are illustrated in Figures 6-25(a) and (b), respectively. On the other hand, the indirect bandgap transitions with phonon assistance could occur from the L valley to the VB. The corresponding transitions are shown in Figures 6-25(c) and (d). The detailed transition mechanism is discussed in the following section via the PL characterization.

6.4.3 Photoluminescence Spectra Analysis

The temperature-dependent PL study was performed using the standard off-axis and lock-in techniques. A 532-nm continuous-wave laser with 500 mW power and 65 µm spot size was used as the pumping source. The emissions were collected using a spectrometer equipped with a thermoelectrically cooled PbS detector with cutoff at 3.0 µm. Figure 6-26 shows the temperature-dependent PL spectra for sample E stacked for clarity. The multi-peak feature observed in the SQW samples wasn't observed for sample E. The Gaussian fitting was used to investigate each peak in terms of peak position, full width at half maximum (FWHM), and integrated PL intensity. However, strong atmospheric absorption occurred in the spectra beyond 2.6 µm thus interfering with the emission from the QW. This interfered, with the data fitting of the PL spectra.

The temperature dependent PL shown in Figure 6-26 was affected by atmospheric

absorption in the majority of the spectra. This atmospheric absorption made obtaining spectral information impossible at the upper temperature range. Fitting was accomplished at 10 K where the wavelength was out of the absorption band.

Some deductions were made about the sample, including: i) Sample E was direct band gap with type-I band alignment (based on the Sn composition and strain), ii) carrier confinement was significant as only one peak was observed, (similar to DQW in Chapter 6.4), iii) observed PL emission corresponded well to expected emission, even-though true peak could not be observed through the atmospheric absorption, and iv) 10 K FWHM of the spectra was measured at 24 meV (similar to that of SQW samples).

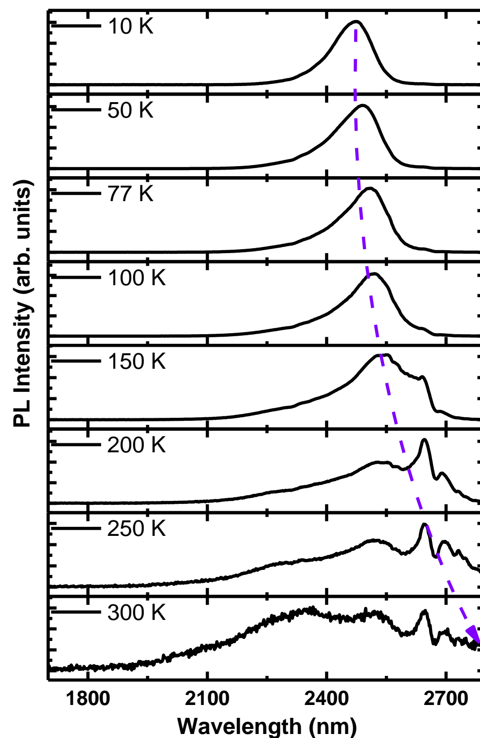

Figure 6-26: Temperature dependent PL of Sample E.

6.4.4 Conclusion

In this section, the material characterization, bandedge structure simulation, and the temperature dependent PL optical characterization of a SiGeSn/GeSn 4x multiple QW were

presented. The grown structure was close to the desired structure showing good control of the growth process. The band edge structure suggested direct bandgap QW with type-I band alignment to the SiGeSn barriers. Calculation of carrier confinement suggested the effective confinement of carriers to the wells. PL emission was strongly affected by CO_2 atmospheric absorption limiting the ability to fit the PL spectra. Limited information gained from the low temperature measurement agreed with simulation of structure.

6.5 Summary

This chapter presented five examples of SiGeSn/GeSn QW structures, including: i) three single quantum wells, ii) one double quantum well, iii) one 4x multiple quantum well. All QWs, presented both through bandedge calculation and temperature dependent PL, were shown to be direct band gap material exhibiting type-I band alignments. Carrier confinement in the SiGeSn samples was calculated to be much higher than that of GeSn/GeSn QWs. With increasing carrier confinement more intense PL was observed. The observed PL was consistent with the calculated emission. Atmospheric absorption caused by CO_2 made higher temper fitting of long wavelength PL difficult if not impossible.

Chapter 7 Dissertation Summary, Conclusion, and Future Work

7.1 Summary

This dissertation has presented information on two separate topics: i) the UHV-CVD growth from Ge to high quality GeSn with incorporations approaching 10% Sn and ii) the characterization of a set of GeSn/GeSn and SiGeSn/GeSn QWs.

The UHV-CVD growth started with the growth of Ge as this was the base material for the desired alloy. Dilute GeSn was then explored to determine differences between the low temperature growth of Ge and GeSn. The Sn composition was limited to less than 1% to provide a Ge-like alloy. This growth showed that, with the introduction of the $SnCl_4$ precursor, the growth rate of the material increased but showed a delay in beginning growth. The material quality from low temperature GeSn surpassed that of Ge also suggesting a change in the growth condition. This change in growth condition was attributed to excess heat from the production of HCl during GeSn deposition using GeH_4 and $SnCl_4$ precursors.

The growth of plasma enhanced GeSn was performed. This showed a 200 to 400 times increase in the growth rate. Growth temperature reduction was performed and a crystalline-to-amorphous transition was observed below 325 °C. Up to 5% Sn was incorporated, showing the ability to improve growth.

Most of the GeSn growth in the community is on Ge buffers instead of directly on Si. The growth of high quality GeSn is obtained on Ge buffers due to: i) lattice mismatch between Si and GeSn (at least 4.2%), ii) HCl etching of Si roughens the surface before GeSn can begin deposition resulting in poor material, and iii) the effect of strain limiting the Sn incorporation of the grown material. This prompted the development of a Ge buffer on Si for the growth of GeSn. The buffer development was limited due to lack of an annealing step, however, it still

produced a high-quality Ge buffer with TDD of 1.1 x 10^7 cm^{-2}. This TDD is near the level shown in literature to be considered high-quality.

GeSn growth on the developed buffers was then accomplished. The beginning growth was accomplished in a Sn overpressure condition to observe the effect of Sn. This limited the amount of Sn in the bulk of the deposited material with the surface covered by Sn segregation and agglomeration. Material and optical characterizations showed that while the growth temperature dependence on Sn incorporation was observed, the film was mostly depleted of Sn with the temperature dependent Sn incorporation forming near the droplet of Sn on the surface. Efforts were then focused to reduce the Sn molar flow fraction to result in high-quality GeSn films. Once the high-quality film was produced, the growth temperature was continued to be reduced to where Sn coverage was present on the surface again. This showed that the growth of GeSn at each growth temperature had a small window of gas flows that would produce high-quality material. Multipeak spectra demonstrated in the optimized growth window exhibited PL similar to samples that undergo spontaneous relaxation enhanced epitaxy with a lower composition first layer and second high composition layer. Photoconductor devices were fabricated from grown material, showing the improvement in growth of GeSn toward device quality materials.

The second major direction of this research characterized GeSn and SiGeSn barriered GeSn QWs. Material characterization, simulation, and optical characterization was performed. All samples studied were shown to be direct band gap QWs with type-I band alignment to the respective barrier. However, it was shown that the SiGeSn barriered QWs were superior in the carrier confinement. It was shown that by increasing the Sn in the buffer layer that higher amounts of Sn could be incorporated into the well region. This should be the case for both GeSn

and SiGeSn barriers. Combining this knowledge with the strategy of high Sn composition should pave a path to mid-infrared emitters. A summary of the 10 K PL spectra of all QWs presented in Chapters 5 and 6 is shown in Figure 7-1.

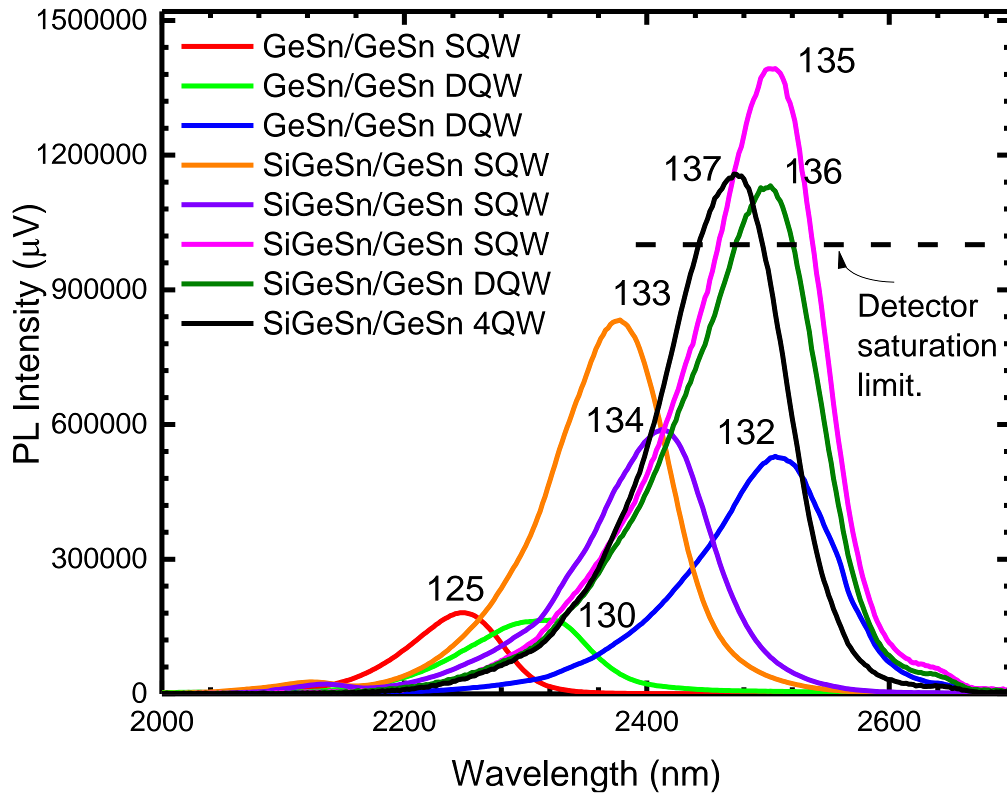

Figure 7-1: Summary of 10 K PL of all studied QW samples.

In Figure 7-1, both GeSn and SiGeSn barriered GeSn QWs are presented. The lowest PL observed came from the GeSn/GeSn SQW (annotated 125) and DQW thin well (annotated 130). The GeSn/GeSn DQW with thicker wells (annotated as 132) displayed higher carrier confinement and has PL emission that was larger than all other GeSn/GeSn samples and had PL emission close to that of the lowest PL intensity from SiGeSn/GeSn barriered SQW (annotated 134). The highest emission seen was from SiGeSn/GeSn with the thick wells annotated (135). The SiGeSn/GeSn DQW (annotated 136) and 4x MQW (annotated 137) were in the same range of PL intensity as 135. Samples 135, 136, and 137 all had PL intensities above the saturation

limit of the detector and had to be filtered. The sample PL intensity was expected to be higher for 136 and 137 than for 135 but this wasn't seen. This was attributed to the short pumping depth of the 532 nm laser. The penetration depth of 532 nm laser was calculated to be close to 20 nm and possibly a bit longer in SiGeSn. At this pumping depth it is likely that majority of emission was from the uppermost well.

7.2 Conclusion

In this work, a method of producing high quality GeSn on Ge buffers was developed. This was documented from Ge growth all the way to high-quality GeSn near 10% Sn incorporation. The research performed showed that a small growth window exists for a specific composition of Sn, with the $SnCl_4$ precursor molar flow fraction determining: i) no growth occurs (too low molar flow fraction) or, ii) layer depletion, surface segregation, and agglomeration (too high molar flow fraction). The GeH_4 molar flow fraction was the dominant mechanism controlling the growth rate at a given temperature. The lowest available gas flow fraction of Sn that could be experimentally produced limited the temperature that high-quality growth could occur. This research pushed the growth chamber to its limits and will require upgrades to continue pushing the Sn incorporation higher.

Direct-bandgap QWs with type-I band alignment were characterized. The GeSn/GeSn barriered SQW studied in Chapter 5 was the first GeSn QW to be characterized as direct bandgap with type-I band alignment. This research built on that success to further improve performance. SiGeSn barriers provided higher carrier confinement and produced more intense PL than GeSn barriers. Thicker wells were shown to increase the confinement further for both GeSn and SiGeSn barriered QWs. Double and multiple QWs were examined and showed that well stability could be controlled for the growth of higher number QW samples and superlattices

without degradation of the sample.

7.3 Future work

7.3.1 Ex-situ Gas Mixing

It was shown in this research that the lowest molar flow fraction achievable by the current set up would not allow $SnCl_4$ flow fractions low enough to push growth to higher incorporation amounts. Further reduction through the dilution of the source gas entering the chamber with Ar would only result in reduced film thickness and not lower the $SnCl_4$ molar flow fractions to the desired levels. Therefore, an alternate method to control the precursor composition going into the chamber is required to further push Sn incorporation to higher incorporation without sacrificing film thickness. An ex-situ gas mixing system has already been constructed (described in Chapter 2) and is awaiting restart of growth to begin testing with the system. The ability to control the molar flow fractions of the precursor gases entering the chamber will allow follow-on growers the capability to achieve higher Sn incorporations with better control of the growth rate.

7.3.2 GeSn on Ge Substrate

One alternate method of growing GeSn was briefly investigated. For these growths, the growth of GeSn was attempted on Ge wafers 6° offcut toward [111]. These are the dominant Ge wafers on the market as the majority of Ge wafers are used in III-V material integration and is required to avoid anti-phase domains. The growth of these materials did not turn out well. As this was not the direct focus of this work, characterization was limited. There was material deposition, however, it did not show room temperature PL suggesting poor quality of the film. Further improvements to the growth process are needed to improve the material growth directly

on offcut Ge.

7.3.3 Plasma Enhanced GeSn on Ge Buffered Si Substrate

From the stable recipe that produced 8% Sn incorporation, GeSn plasma enhanced growth was attempted to boost the growth rate. This was achieved as the films were shown to be much thicker. However, all films produced were shown to be amorphous and not crystalline. The reason for this was attributed to the boost in growth rate as the residence time for adatoms was reduced thus reducing the opportunity to find energetically favorable locations to reside before being locked into place by the next layer of growth. The GeH_4 flow rate can be reduced to lower the growth rate and a more optimal window for growth found.

7.3.4 Growth of SiGeSn

Based on the developed GeSn recipe for ~8% Sn, a single growth of SiGeSn was accomplished. The only change from the GeSn recipe was the introduction of 10 sccm of SiH_4 to the gas mixture. Initial characterization showed that Si had been incorporated into the growing films. However, the surface of the sample appeared ringed, such as a tree has rings. It has been reported that the growth of SiGeSn is difficult due to the repulsive nature of Si and Sn. This effect could be the cause of the ring shape seen in the surface of the grown film. As this research was beyond this documented work, in-depth characterization was not performed. However, based on this work, development of SiGeSn has a base starting point.

References

[1] M. A. Green, "The path to 25% silicon solar cell efficiency: History of silicon cell evolution," *Prog. Photovoltaics Reaserch Appl.*, vol. 17, pp. 183–189, 2009.

[2] M. E. Groenert, C. W. Leitz, A. J. Pitera, V. Yang, H. Lee, R. J. Ram, and E. A. Fitzgerald, "Monolithic integration of room-temperature cw GaAs/AlGaAs lasers on Si substrates via relaxed graded GeSi buffer layers," *J. Appl. Phys.*, vol. 93, no. 1, pp. 362–367, 2003.

[3] P. Moontragoon, R. A. Soref, and Z. Ikonic, "The direct and indirect bandgaps of unstrained SixGe1-x-y Sny and their photonic device applications," *J. Appl. Phys.*, vol. 112, no. 7, p. 073106, 2012.

[4] B. R. Conley, "GeSn Devices for Short-Wave Infrared Optoelectronics," 2011.

[5] J. Margetis, S. A. Ghetmiri, W. Du, B. R. Conley, A. Mosleh, R. A. Soref, G. Sun, L. Domulevica, H. A. Naseem, S.-Q. Yu, and J. Tolle, "Growth and Characterization of Epitaxial GeSn alloys and heterostructures Using a Commercial CVD System," *ECS Trans.*, vol. 64, no. 6, pp. 711–720, 2014.

[6] E. Cohen and C. van Eyk, "On the Enantiotropy of Tin," *K. Ned. Akad. van Wet. Proc. Ser. B Phys. Sci.*, vol. 2, pp. 77–80, 1899.

[7] E. Cohen and J. Olie Jr., "Huygens Institute - Royal Netherlands Academy of Arts and Sciences (KNAW)," in *Proceedings of the Royal Netherlands Academy of Arts nd Sciences*, 1909, pp. 437–445.

[8] A. J. Bijl and N. H. Kolkmeijer, "Investigation by means of x-rys of the crystal structure of white and grey tin. III. The structure of Grey Tin," in *Knaw*, 1919, vol. 21, pp. 501–504.

[9] A. J. Bijl, "Investigations by means of X-rays of the cryst-structure of white and grey tin. II The structure of white tin," *Knaw*, vol. 21, pp. 494–500, 1919.

[10] A. J. Bijl and N. H. Kolkmeijer, "Investigations by means of X-rays of the crystal-structure of white and grey tin," in *Knaw*, 1919, no. 21, pp. 405–408.

[11] K. Honda, "Die thermomagtnetischen Eigenschaften der Elemente," *Ann. Phys.*, vol. 337, no. 10, pp. 1027–1063, 1910.

[12] M. Owens, "Magnetochemische Untersuchungen. Die thermomagnetischen Eigenschaften der Elemente. II," *Ann. Phys.*, vol. 37, p. 657, 1912.

[13] S. R. Rao, "Magnetism of Tin," in *Proceedings of the Indian Academy of Sciences*, 1934, pp. 123–142.

[14] L. D. Brownlee, “Lattice Constant of Grey Tin,” *Nature*, vol. 166, p. 482, 1950.

[15] G. Busch, J. Wieland, and H. Zoller, “Versuche Zur Messung der Elecktrischen Leitfahigkeit des grauen Zinns,” *Helv. Phys. Acta*, vol. 25, no. 5, pp. 528–530, 1950.

[16] R. R. Rogers and J. F. Fydell, “Effect of Germanium on the Transformation of White Gray Tin , at Comparatively Low Temperature Zn + 4 ~,” *J. Electrochem. Soc.*, pp. 161–164, 1953.

[17] R. R. Rogers and J. F. Fydell, “Factors Affecting the Transformation of Gray Tin at Low Temperatures,” *J. Electrochem. Soc.*, vol. 100, pp. 383–387, 1953.

[18] A. W. Ewald, “Germanium-stabilized gray tin,” *J. Appl. Phys.*, vol. 25, no. 11, pp. 1436–1437, 1954.

[19] J. Fleeman, “Effect of Reactor irradiation on the White-to-Grey Tin Transition,” *J. Appl. Phys.*, vol. 26, p. 652, 1955.

[20] W. G. Burgers and L. J. Groen, “Mechanism and kinetics of the allotropic transformation of tin,” in *Discussions of the Faraday Society*, 1957, vol. 23, no. 0, p. 183.

[21] G. V. Raynor and R. W. Smith, “The Transition Temperature of the Transition between Grey and White Tin,” in *Proceedings of the Royal Society of London. Series A, Mathematical and Physical Sciences*, 1958, vol. 244, no. 1236, pp. 101–109.

[22] J. T. Kendall, “Electronic conduction in grey Tin,” *London, Edinburgh, Dublin Philos. Mag. J. Sci.*, vol. 45, no. 361, pp. 9–11, 1954.

[23] A. W. Ewald and E. E. Kohnke, “Measurements of electrical conductivity and magnetoresistance of gray tin filaments,” *Phys. Rev.*, vol. 97, no. 3, pp. 607–613, 1955.

[24] A. W. Ewald and O. N. Tufte, “Gray tin single crystals,” *J. Appl. Phys.*, vol. 29, no. 7, pp. 1007–1009, 1958.

[25] E. E. Kohnke and A. W. Ewald, “Hall Effect in Gray Tin Filaments,” *Phys. Rev.*, vol. 102, no. 6, pp. 1481–1486, 1956.

[26] A. N. Goland and A. W. Ewald, “Theremoelectric power of grey tin,” *Phys. Rev.*, vol. 104, no. 4, pp. 948–953, 1956.

[27] L. J. Groen, “Formation of Compact Pieces of Grey Sn,” *Nature*, vol. 174, p. 836, 1954.

[28] R. W. Smith, “The Grey Tin White Tine Transition in Tin-Mercury Alloys,” *Can. J. Phys.*, vol. 37, no. 10, pp. 1079–1084, 1959.

[29] R. W. Smith, “The white tin + grey t i n transition in tin-mercury alloys’,” *Can. J. Phys.*,

vol. 38, pp. 588–592, 1960.

[30] J. H. Becker, “On the quality of gray tin crystals and their rate of growth,” *J. Appl. Phys.*, vol. 29, no. 7, pp. 1110–1121, 1958.

[31] G. A. Busch and R. Kebn, “Semiconducting Properties of Gray Tin,” *Solid State Phys. - Adv. Res. Appl.*, vol. 11, no. C, pp. 1–40, 1960.

[32] R. G. Wolfson, M. E. Fine, and A. W. Ewald, “Transformation studies of gray tin single crystals,” *J. Appl. Phys.*, vol. 31, no. 11, pp. 1973–1977, 1960.

[33] W. E. Blumberg and J. Eisinger, “Effective mass in gray tin from knight shift measurements,” *Phys. Rev.*, vol. 120, no. 6, pp. 1965–1968, 1960.

[34] B. L. Booth and A. W. Ewald, “Anisotropy of the Gray-Tin Gamma 8+ Conduction Band,” *Phys. Rev.*, vol. 168, no. 3, p. 805, 1968.

[35] M. Cardona and D. L. Greenaway, “Reflectivity of gray tin single crystals in the fundamental absorption region,” *Phys. Rev.*, vol. 125, no. 4, pp. 1291–1296, 1962.

[36] R. E. Lindquist and A. W. Ewald, “Optical constants of single-crystal gray tin in the infrared,” *Phys. Rev.*, vol. 135, no. 1A, 1964.

[37] E. D. Hinkley and A. W. Ewald, “Oscillatory magnetoresistance in gray tin,” *Phys. Rev.*, vol. 134, no. 5A, 1964.

[38] M. J. P. Musgrave, “On the Relation between Grey and White Tin,” in *Proceedings of the Royal Society of London. Series A, Mathematical and Physical Sciences*, 1963, vol. 272, no. 1351, pp. 503–528.

[39] S. Groves and W. Paul, “Band Structure of Gray Tin,” *Phys. Rev. Lett.*, vol. 11, no. 5, pp. 194–196, 1963.

[40] F. Bassani and L. Liu, “Electronic Band Structure of Gray Tin,” *Phys. Rev.*, vol. 132, no. 5, pp. 2047–2050, 1963.

[41] D. D. Koellengf and D. Dean, “Symmetrized Relativistic Augmented-Plane-Wave Method: Gray Tin and the Warped Muffin-Tin Potential,” *Phys. Reivew*, vol. 188, no. 3, 1970.

[42] F. H. Pollack, M. Cardona, and C. W. Higginbotham, “Energy-Band Structure of Optical Spectrum of Grey Tin,” *Phys. Rev. B*, vol. 2, no. 2, pp. 352–363, 1970.

[43] J. G. Broerman, “Ionized-Impurity-Limited Mobility of alpha-Sn in the Random-Phase Approximation,” *Phys. Rev. B.*, vol. 1, no. 12, pp. 4568–4572, 1970.

[44] J. G. Broerman, "Anomalous Mobility and Dielectric Singularity of a-Sn," *Phys. Rev. Lett.*, vol. 24, no. 9, pp. 450–451, 1970.

[45] B. L. Booth and A. W. Ewald, "Screening Enhanced Shubnikov de Haas Oscillation in Sb Doped Gray Tin," *Phys. Rev. Lett.*, vol. 18, no. 13, pp. 491–493, 1967.

[46] B. L. Booth and A. W. Ewald, "Nonparabolicity of the Gray-Tin Gamma 8+ Conduction Band," *Phys. Rev.*, vol. 168, no. 3, p. 796-804, 1968.

[47] B. L. Booth and A. W. Ewald, "Spin splitting of landau levels and the effective G factor in gray tin," *Phys. Rev.*, vol. 186, no. 3, pp. 770–774, 1969.

[48] T. Hanyu, "Optical Constants of Gray Tin Single Crystals from 1.18 to 4.95 eV," *J. Phys. Soc. Japan*, vol. 31, no. 6, pp. 1738–1747, 1971.

[49] B. J. Roman and A. W. Ewald, "Stress-Induced Band Gap and Related Phenomena in Gray Tin," *Phys. Rev. B*, vol. 5, no. 10, pp. 3914–3932, 1972.

[50] M. Iliev, M. Sinyukov, and M. Cardona, "Resonant first-and second-raman scattering in gray tin," *Phys. Rev. B*, vol. 16, no. 12, p. 5350-5355, 1977.

[51] W. Weber, "Adiabatic bond charge model for the phonons in diamond, Si, Ge, and α-Sn," *Phys. Rev. B*, vol. 15, no. 10, pp. 4789–4803, 1977.

[52] S. Guilj and R. M. Pick, "Sound Propagation in α-Sn," Le Journal De Physique, vol. 38, no. 2, pp. 221-229, 1977.

[53] J. Ihm and M. L. Cohen, "Equilibrium properties and the phase transition of grey and white tin," *Phys. Rev. B*, vol. 23, no. 4, p. 1576, 1981.

[54] R. M. Friedman, R. E. Watson, J. Hudis, and M. L. Perlman, "Electron binding in metals: Grey and white tin," *Phys. Rev. B*, vol. 8, no. 8, pp. 3569–3575, 1973.

[55] L. Liu, "Magnetic Subband Structure of alpha-Sn," *Phys. Rev. B*, vol. 8, no. 8, pp. 3811–3816, 1973.

[56] D. L. Price, J. M. Rowe, and R. M. Nicklow, "Lattice dynamics of grey tin and indium antimonide," *Phys. Rev. B*, vol. 3, no. 4, pp. 1268–1279, 1971.

[57] C. J. Buchenauer, M. Cardona, F. H. Pollak, J. H. Parker, D. W. Feldman, M. Ashkin, T. R. Hart, R. L. Aggarwal, B. Lax, P. Bev, by G. B Wright Springer, S. S. Mitra, O. Brafman, W. B. Daniels, E. Anastasakis, A. Pinczuk, E. Burstein, and D. H. Qlson, "Raman Scattering in Gray Tin," *Phys. Rev. B Phys. Bev. Phys. Bev. Phys. Rev. B*, vol. 3, no. 4, pp. 1243–1244, 1971.

[58] L. J. Chen and L. M. Falicov, "Psuedopotential calculation of the stacking fault energy in

diamond, Germanium, and Grey Tin," *Philosophical Magazine*, 1974.

[59] D. H. Bilderback and R. Colella, "Valence Charge Densit in Grey Tin: X-ray determination of the (222) 'forbiden' reflection and its temperture dependence," *Phys. Rev. B*, vol. 11, no. 2, pp. 793–797, 1974.

[60] R. P. Gupta, S. K. Sinha, J. P. Walter, and M. L. Cohen, "Dielectric Function and Phonon Spectrum of Grey Tin," *Solid State Commun.*, vol. 14, pp. 1313–1316, 1974.

[61] T. Soma, "Lattice Vibation Spectra in α-Sn," *J. Phys. Soc. Japan*, vol. 36, no. 5, pp. 1301–1303, 1974.

[62] R. F. C. Farrow, D. S. Robertson, G. M. Williams, A. G. Cullis, G. R. Jones, I. M. Young, and P. N. J. Dennis, "The growth of metastable, heteroepitaxial films of α-Sn by metal beam epitaxy," *J. Cryst. Growth*, vol. 54, no. 3, pp. 507–518, 1981.

[63] S. Takatani and Y. W. Chung, "Thin-film quantization studies of grey tin epitaxially grown on CdTe(111)," *Phys. Rev. B*, vol. 31, no. 4, pp. 2290–2293, 1985.

[64] B. I. Craig and B. J. Garrison, "Theoretical examination of the quantum-size effect in thin grey-tin films," *Phys. Rev. B*, vol. 33, no. 12, pp. 8130–8135, 1986.

[65] W. M. T. Gallerneault, F. Vnuk, and R. W. Smith, "Silicon-stabilized grey tin," *J. Appl. Phys.*, vol. 54, no. 7, pp. 4200–4201, 1983.

[66] F. Vnuk, A. DeMonte, and R. W. Smith, "The composition dependence of the grey tin → white tin transition in dilute tin-germanium alloys," *Mater. Lett.*, vol. 2, no. 1, pp. 67–70, 1983.

[67] G. P. Srivastava, "Electronic structure and total energy of Si, Ge and a-Sn by the self-consistent local pseudopotential method," *J. Phys. C*, vol. 15, pp. 707–719, 1982.

[68] G. P. Srivastava, "Self-consistent pseudopotential calculations for the electronic structure of bulk and (111) surface of α- Sn," *J. Phys. C*, Vol. 15, no. 4. pp. 699–706, 1982.

[69] G. P. Srivastava, "Self-consistent non-local pseudopotential calculations for the ground-state properties of α-Sn," *J. Phys. C*, vol. 16, no. 9 pp.1649-1657, 1983.

[70] L. Vina, H. Höchst, and M. Cardona, "Dielectric function of alpha-Sn and its temperature dependence," *Phys. Rev. B*, vol. 31, no. 2. pp. 958–967, 1985.

[71] T. Kinoshita, S. Kono, and T. Sagawa, "Angle-resolved photoelectron-spectroscopy study of the Si(111) √3×√3-Sn surface: Comparison with Si(111) √3×√3-Al, -Ga, and -In surfaces," *Phys. Rev. B*, vol. 34, no. 4, 1986.

[72] A. Svane, "Hartree-Fock band-structure calculations with the linear muffin-tin-orbital

method: Application to C, Si, Ge, and α-Sn," *Phys. Rev. B*, vol. 35, no. 11, pp. 5496–5502, 1987.

[73] H. U. Middelmann, L. Sorba, V. Hinkel, and K. Horn, "Valence-band structure of a-Sn determined by angle-resolved photoemission," *Phys. Rev. B*, vol. 35, no. 2, pp. 718–722, 1987.

[74] L. W. Tu, G. K. Wong, and J. B. Ketterson, "Observation of quantum size effect in the resistivity of thin, gray tin epilayers," *Appl. Phys. Lett.*, vol. 55, no. 13, pp. 1327–1329, 1989.

[75] S. Adachi, "Optical properties of α-Sn," *J. Appl. Phys.*, vol. 66, no. 2, pp. 813–819, 1989.

[76] M. Tang, D. W. Niles, I. Hernández-Calderón, and H. Höchst, "Angle-resolved photoemission study of the α-Sn/CdTe(100) interface," *Phys. Rev. B*, vol. 36, no. 6, pp. 3336–3343, 1987.

[77] Y. Kasukabe, M. Iwai, and T. Osaka, "The dynamical observation of α-sn (111) this films grown on insb (1̄;1̄;1̄;) by rheed," *Jpn. J. Appl. Phys.*, vol. 27, no. 7A, pp. L1201–L1203, 1988.

[78] D. H. Rich, T. Miller, A. Samsavar, H. F. Lin, and T. C. Chiang, "Adsorption and growth of Sn on Si(100) from synchrotron photoemission studies," *Phys. Rev. B*, vol. 37, no. 17, pp. 10221–10228, 1988.

[79] L. W. Tu, G. K. Wong, and J. B. Ketterson, "Growth of n-type heteroepitaxial films of gray tin on (001) CdTe by molecular beam epitaxy," *Appl. Phys. Lett.*, vol. 54, no. 11, pp. 1010–1012, 1989.

[80] R. F. C. Farrow, "The stabilization of metastable phases by epitaxy," *J. Vac. Sci. Technol. B Microelectron. Nanom. Struct.*, vol. 1, no. 2, p. 222, 1983.

[81] H. Hochst, D. W. Niles, and I. Hernández-Calderón, "Interface and growth studies of alpha-Sn /CdTe (110) superlattices," *J. Vac. Sci. Technol. B*, vol. 6, no. 4, pp. 1219–1223, 1988.

[82] L. W. Tu, G. K. Wong, S. N. Song, Z. Zhao, and J. B. Ketterson, "Shubnikov-de Haas effect in thin epitaxial films of gray tin," *Appl. Phys. Lett.*, vol. 55, no. 25, pp. 2643–2645, 1989.

[83] P. John, T. Miller, and T. Chiang, "Core-Level Photoemission Studies of the α-Sn/InSb(100) heterostructure system," *Phys. Rev. B*, vol. 39, no. 5, pp. 3223-3229, 1989.

[84] J. Olajos, P. Vogl, W. Wegscheider, and G. Abstreiter, "Infrared Optical Properties and Band Structure of a-Sn/Ge Superlattices on Ge Substrates," *Phys. Rev. Lett.*, vol. 67, no. 22, p. 3164-3167, 1991.

[85] W. T. Yuen, W. K. Liu, S. N. Holmes, and R. A. Stradling, “First observation of a two dimensional electron gas at the interface of akfa-Sn/InSb (100) grown by Molecular Beam Epitaxy,” *Semicond. Sci. Technol.*, vol. 819, no. 001, 1989.

[86] W. T. Yuen, W. K. Liu, B. A. Joyce, and R. A. Stradling, “RHEED studies of the surface morphology of a-Sn pseudomorphically grown on lnSb (100) by MBE-a new kind of non-polar / polar system,” *Semicond. Sci. Technol.*, vol. 373, no. 100, 1990.

[87] L. W. Tu, G. K. Wong, S. N. Song, Z. Zhao, and J. B. Ketterson, “Growth and characterisation of substrate-stabilised heteroepitaxial grey tin films,” *Semicond. Sci. Technol.*, vol. 5, no. 3 S, pp. 244–247, 1990.

[88] W. Wegscheider, K. Eberl, U. Menczigar, and G. Abstreiter, “Single-crystal Sn/Ge superlattices on Ge substrates: Growth and structural properties,” *Appl. Phys. Lett.*, vol. 57, no. 9, pp. 875–877, 1990.

[89] M. Kimata, T. Suzuki, K. Saino, K. Kawamura, and A. Hobbs, “Stabilized α-Sn grown at high temperature by molecular beam epitaxy,” *J. Vac. Sci. Technol. B Microelectron. Nanom. Struct.*, vol. 12, no. 2, p. 1184, 1994.

[90] J. Zi, K. Zhang, and X. Xide, “Strained a-Sn/Ge superlattices: Geometrical structures and phonon spectra,” *Phys. Rev. B*, vol. 45, no. 15, pp. 8397–8403, 1992.

[91] A. Continenza and A. J. Freeman, “Band lineup and electric fields in (a-Sn)m/(CdTe)n [001] and [110] superlattices,” *Phys. Rev. B*, vol. 45, no. 11, pp. 5953–5960, 1992.

[92] J. Olajos, W. Wegscheider, and G. Abstreiter, “Interband absorption in α-Sn/Ge short-period superlattices,” *Appl. Phys. Lett.*, vol. 61, no. 26, pp. 3130–3132, 1992.

[93] J. Zi, K. Zhang, and X. Xie, “Vibrational properties of Si/Ge and ±-Sn/Ge superlattices with intermixed interfaces,” *Phys. Rev. B*, vol. 47, no. 15, pp. 9937–9939, 1993.

[94] R. Schorer, W. Wegscheider, and G. Abstreiter, “Raman scattering of α-Sn/Ge superlattices on Ge (001),” *J. Vac. Sci. Technol. B Microelectron. Nanom. Struct.*, vol. 11, no. 3, p. 1069, 1993.

[95] K. S. Min and H. A. Atwater, “Ultrathin pseudomorphic Sn/Si and SnxSi1-x/Si heterostructures,” *Appl. Phys. Lett.*, vol. 72, no. 15, pp. 1884–1886, 1998.

[96] I. Hernandez-Calderon and H. Hochst, “Anomalous Fermi level emission during the initial growth of epitaxial alpha -Sn/CdTe(111) heterostructures,” *J. Phys. Condens. Matter*, vol. 5, no. 33 A, pp. 10–12, 1993.

[97] K. Yamamoto and K. Kobayashi, “Electronic structure and EPC stability of the α-Sn/InSb(111)A nonpolar-polar heterojunction interface,” *Phys. Rev. B - Condens. Matter*

Mater. Phys., vol. 53, no. 8, pp. 4539–4543, 1996.

[98] A. Continenza and A. J. Freeman, "Structural and electron properties of a-Sn, CdTe, and their [100] mololayer superlattices," *Phys. Rev. B*, vol. 43, no. 11, pp. 8951–8961, 1991.

[99] T. Osaka, H. Omi, K. Yamamoto, and A. Ohtake, "Surface phase transition and interface interaction in the -Sn/InSb{111} system," *Phys. Rev. B*, vol. 50, no. 11, pp. 7567–7572, 1994.

[100] H. Omi, H. Saito, and T. Osaka, "Polarity propagation in the InSb/α-Sn/InSb heterostructure," *Phys. Rev. Lett.*, vol. 72, no. 16, pp. 2596–2599, 1994.

[101] Z.-Y. Lu, G. Chiarotti, S. Scandolo, and E. Tosatti, "Atomic and electronic structure of ideal and reconstructed alpha -Sn (100) surfaces," *Phys. Rev. B*, vol. 58, no. 20, p. 13698, 1998.

[102] T. Eguchi, J. Nakamura, and T. Osaka, "Structure and Electronic States of the *α* -Sn(111)-(**2×2**) Surface," *J. Phys. Soc. Japan*, vol. 67, no. 2, pp. 381–384, 1998.

[103] C. H. L. Goodman, "Direct-gap group IV semiconductors based on tin," *IEEE Proc. I (Solid-State Electron Devices)*, vol. 129, no. 5, pp. 189–192, 1982.

[104] S. I. Shah, J. E. Green, L. L. Abels, Y. Yao, and P. M. Raccah, "Growth of single-crystal metastable Ge1-xSnx alloys on Ge(100) and GaAs(100) substrates," *J. Cryst. Growth*, vol. 83, no. 1, pp. 3–10, 1987.

[105] I. Chambouleyron and F. C. Marques, "Use of hydrogenation in the study of the properties of amorphous germanium tin alloys," *J. Appl. Phys.*, vol. 65, no. 4, pp. 1591–1597, 1989.

[106] I. Chambouleyron, F. C. Marques, P. H. Dionisio, I. J. R. Baumvol, and R. A. Barrio, "Mössbauer study of hydrogenated amorphous germanium-tin thin-film alloys," *J. Appl. Phys.*, vol. 66, no. 5, pp. 2083–2090, 1989.

[107] H. Höchst, M. A. Engelhardt, and I. Hernandez-Calderan, "Angle-resolved photoemission study of thin molecular-beam-epitaxy-grown -Sn1-xGex films with x0.5," *Phys. Rev. B*, vol. 40, no. 14, pp. 9703–9708, 1989.

[108] C. A. Hoffman, J. R. Meyer, R. J. Wagner, F. J. Bartoli, M. A. Engelhardt, and H. Hochst, "Three-band transport and cyclotron resonance in alpha-Sn and alpha-Sn1-xGex grown by molecular-beam epitaxy," *Phys. Rev. B*, vol. 40, no. 17, pp. 693–700, 1989.

[109] H. Hochst, M. A. Engelhardt, R. C. Bowman, and P. M. Adams, "Characterisation of MBE-grown α-Sn films and α-$Sn_{1-x}Ge_x$ alloys," *Semicond. Sci. Technol.*, vol. 5, no. 3 pp. S240-S244, 1990.

[110] E. R. Youngdale, C. A. Hoffman, J. R. Meyer, and F. J. Bartoli, "Nonlinear optical

properties of a-Sn and Sn1-xGex," in *Ouantum Electronics and Laser Science Conference*, 1989, pp. 1–2.

[111] R. C. Bowman Jr., P. M. Adams, M. A. Engelhart, and H. Hochst, "Structural characterization of α-Sn and α-Sn1−x Gex alloys grown by molecular beam epitaxy on CdTe and InSb," *J. Vac. Sci. Technol. A Vacuum, Surfaces, Film.*, vol. 8, no. 3, p. 1577, 1990.

[112] R. A. Soref and L. Friedman, "Direct-gap Ge/GeSn/Si and GeSn/Ge/Si heterostructures," *Superlattices Microstruct.*, vol. 14, no. 2–3, pp. 189–193, 1993.

[113] X. Deng, B.-K. Yang, S. Hackney, M. Krishnamurthy, and D. Williams, "Formation of Self-Assembled Quantum Wires during Epitaxial Growth of Strained GeSn Alloys on Ge(100): Trench Excavation by Migrating Sn Islands," *Phys. Rev. Lett.*, vol. 80, no. 5, pp. 1022–1025, 1998.

[114] T. Maruyama and H. Akagi, "Thin Films of Amorphous Germanium-Tin Alloys Prepared by Radio-Frequency Magnetron Sputtering," *J. Electrochem. Soc.*, vol. 145, no. 4, pp. 1303-1305, 1998.

[115] R. W. Schmude and K. A. Gingerich, "Thermodynamic investigation of small germanium-tin clusters with a mass spectrometer," *J. Chem. Phys.*, vol. 109, no. 8, pp. 3069–3071, 1998.

[116] R. Ragan and H. A. Atwater, "Measurement of the direct energy gap of coherently strained Sn_xGe_{1-x}/Ge(001) heterostructures," *Appl. Phys. Lett.*, vol. 77, no. 21, pp. 3418-3420, 2000.

[117] J. Taraci, S. Zollner, M. R. McCartney, J. Menendez, M. A. Santana-Aranda, D. J. Smith, A. Haaland, A. V. Tutukin, G. Gundersen, G. Wolf, and J. Kouvetakis, "Synthesis of silicon-based infrared semiconductors in the Ge-Sn system using molecular chemistry methods," *J. Am. Chem. Soc.*, vol. 123, no. 44, pp. 10980–10987, 2001.

[118] J. Taraci, S. Zollner, M. R. Mccartney, J. Menendez, D. J. Smith, J. Tolle, E. Duda, N. V Edwards, and J. Kouvetakis, "Optical Vibrational and Structural Properties of GeSn alloys by UHV-CVD," *MRS Online Proc. Libr. Arch.*, vol. 692, pp. 631–636, 2001.

[119] J. Taraci, J. Tolle, J. Kouvetakis, M. R. McCartney, D. J. Smith, J. Menendez, and M. A. Santana, "Simple chemical routes to diamond-cubic germanium-tin alloys," *Appl. Phys. Lett.*, vol. 78, no. 23, pp. 3607–3609, 2001.

[120] M. R. Bauer, J. Tolle, a. V. G. Chizmeshya, S. Zollner, J. Menendez, and J. Kouvetakis, "New Ge-Sn materials with adjustable bandgaps and lattice constants," *MRS Proc.*, vol. 744, no. 100, pp. 3–8, 2002.

[121] M. Bauer, J. Taraci, J. Tolle, a. V. G. Chizmeshya, S. Zollner, D. J. Smith, J. Menendez,

C. Hu, and J. Kouvetakis, “Ge-Sn semiconductors for band-gap and lattice engineering,” *Appl. Phys. Lett.*, vol. 81, no. 16, pp. 2992–2994, 2002.

[122] M. R. Bauer, C. S. Cook, P. Aella, J. Tolle, J. Kouvetakis, P. A. Crozier, A. V. G. Chizmeshya, D. J. Smith, and S. Zollner, “SnGe superstructure materials for Si-based infrared optoelectronics,” *Appl. Phys. Lett.*, vol. 83, no. 17, pp. 3489–3491, 2003.

[123] A. V. G. Chizmeshya, M. R. Bauer, and J. Kouvetakis, “Experimental and theoretical study of deviations from Vegard’s law in the Sn_xGe_{1-x}system,” *Chem. Mater.*, vol. 15, no. 13, pp. 2511–2519, 2003.

[124] M. R. Bauer, J. Tolle, C. Bungay, A. V. G. Chizmeshya, D. J. Smith, J. Menéndez, and J. Kouvetakis, “Tunable band structure in diamond-cubic tin-germanium alloys grown on silicon substrates,” *Solid State Commun.*, vol. 127, no. 5, pp. 355–359, 2003.

[125] V. G. Deibuk and Yu. G. Korolyuk, “Thermodynamic stability of bulk and epitaxial Ge 1 − x Sn x semiconductor alloys,” Semiconductors, vol 36. no. 10. pp. 1073–1076, 2002.

[126] N. Bouarissa and F. Annane, “Electronic properties and elastic constants of the ordered Ge1-xSnx alloys,” *Mater. Sci. Eng. B*, vol. 95, no. 2, pp. 100–106, 2002.

[127] R. Ragan, C. C. Ahn, and H. A. Atwater, “Nonlithographic epitaxial SnxGe1-x dense nanowire arrays grown on Ge(001),” *Appl. Phys. Lett.*, vol. 82, no. 20, pp. 3439–3441, 2003.

[128] R. Ragan, J. E. Guyer, E. Meserole, M. S. Goorsky, and H. A. Atwater, “Kinetics governing phase separation of nanostructured Snx Ge1-x alloys,” *Phys. Rev. B - Condens. Matter Mater. Phys.*, vol. 73, no. 23, pp. 1–11, 2006.

[129] R. Ragan, K. S. Min, and H. A. Atwater, “Direct energy gap group IV semiconductor alloys and quantum dot arrays in SnxGe1−x/Ge and SnxSi1−x/Si alloy systems,” *Mater. Sci. Eng. B*, vol. 87, no. 3, pp. 204–213, 2001.

[130] R. Ragan and H. A. Atwater, “Diamond cubic Sn-rich nanocrystals: Synthesis, microstructure and optical properties,” *Appl. Phys. A Mater. Sci. Process.*, vol. 80, no. 6, pp. 1335–1338, 2005.

[131] J. Blacksburg, L. D. Bell, and S. Nikzad, “Structural and Optical Properties of SnGe thin films and Quantum Dots,” in *Bullitin of the American Physcial Society*, 2005.

[132] N. Naruse, Y. Mera, Y. Nakamura, M. Ichikawa, and K. Maeda, “Fourier-transform photoabsorption spectroscopy of quantum-confinement effects in individual GeSn nanodots,” *Appl. Phys. Lett.*, vol. 94, no. 9, pp. 94–97, 2009.

[133] Y. Nakamura, N. Fujinoki, and M. Ichikawa, “Photoluminescence from Si-capped GeSn nanodots on Si substrates formed using an ultrathin SiO2 film technique,” *J. Appl. Phys.*,

vol. 106, no. 1, pp. 04309-1 - 04309-4, 2009.

[134] K. A. Bratland, Y. L. Foo, P. Desjardins, and J. E. Greene, “Sn-enhanced epitaxial thickness during low-temperature Ge(001) molecular-beam epitaxy,” *Appl. Phys. Lett.*, vol. 82, p. 4247-4249, 2003.

[135] K. A. Bratland, Y. L. Foo, T. Spila, H.-S. Seo, R. T. Haasch, P. Desjardins, and J. E. Greene, “Sn-mediated Ge/Ge(001) growth by low-temperature molecular-beam epitaxy: Surface smoothening and enhanced epitaxial thickness,” *J. Appl. Phys.*, vol. 97, no. 4, p. 044904-1 - 044904-10, 2005.

[136] S. Takeuchi, A. Sakai, K. Yamamoto, O. Nakatsuka, M. Ogawa, and S. Zaima, “Growth and structure evaluation of strain-relaxed $Ge_{1-x}Sn_x$ buffer layers grown on various types of substrates,” *Semicond. Sci. Technol.*, vol. 22, no. 1, pp. S231–S235, 2007.

[137] A. Sakai, Y. Ohara, T. Ueda, E. Toyoda, K. Izunome, S. Takeuchi, Y. Shimura, O. Nakatsuka, M. Ogawa, S. Zaima, and S. Kimura “Interface and defect control for group IV channel engineering,” *ECS Trans.*, vol. 16, no. 10, pp. 687–698, 2008.

[138] A. Sakai, S. Takeuchi, O. Nakatsuka, and S. Zaima, “Growth and characterization of tensile strained Ge on Ge 1-x Sn x buffers for novel channel layers,” no. 001, pp. 6–10, 2008.

[139] Y. Shimura, N. Tsutsui, O. Nakatsuka, A. Sakai, and S. Zaima, “Control of Sn precipitation and strain relaxation in compositionally step-graded Ge1-xSnx buffer layers for tensile-strained ge layers,” *Jpn. J. Appl. Phys.*, vol. 48, no. 4 PART 2, 2009.

[140] J. Tolle, a. V. G. Chizmeshya, Y.-Y. Fang, J. Kouvetakis, V. R. D’Costa, C.-W. Hu, J. Menéndez, and I. S. T. Tsong, “Low temperature chemical vapor deposition of Si-based compounds via $SiH_3SiH_2SiH_3$: Metastable SiSn/GeSn/Si(100) heteroepitaxial structures,” *Appl. Phys. Lett.*, vol. 89, no. 23, p. 231924, 2006.

[141] J. Kouvetakis and A. V. G. Chizmeshya, “New classes of Si-based photonic materials and device architectures via designer molecular routes,” *J. Mater. Chem.*, vol. 17, no. 17, p. 1649, 2007.

[142] J. Kouvetakis, J. Menendez, and A. V. G. Chizmeshya, “Tin-Based Group IV Semiconductors: New Platforms for Opto- and Microelectronics on Silicon,” *Annu. Rev. Mater. Res.*, vol. 36, no. 1, pp. 497–554, 2006.

[143] J. Tolle, R. Roucka, A. V. G. Chizmeshya, J. Kouvetakis, V. R. D’Costa, and J. Menéndez, “Compliant tin-based buffers for the growth of defect-free strained heterostructures on silicon,” *Appl. Phys. Lett.*, vol. 88, no. 25, p. 252112, 2006.

[144] R. Roucka, J. Tolle, C. Cook, a. V. G. Chizmeshya, J. Kouvetakis, V. D’Costa, J. Menendez, Z. D. Chen, and S. Zollner, “Versatile buffer layer architectures based on Ge_{1-}

$_x$Sn$_x$ alloys," *Appl. Phys. Lett.*, vol. 86, p. 191912, 2005.

[145] R. Roucka, J. Xie, J. Kouvetakis, J. Mathews, V. D'Costa, J. Menéndez, J. Tolle, and S.-Q. Yu, "$Ge_{1-y}Sn_y$ photoconductor structures at 1.55 μm: From advanced materials to prototype devices," *J. Vac. Sci. Technol. B Microelectron. Nanom. Struct.*, vol. 26, no. 6, p. 1952, 2008.

[146] J. Mathews, R. Roucka, J. Xie, S. Q. Yu, J. Meńndez, and J. Kouvetakis, "Extended performance GeSn/Si(100) p-i-n photodetectors for full spectral range telecommunication applications," *Appl. Phys. Lett.*, vol. 95, no. 13, pp. 11–14, 2009.

[147] I. S. Yu, K. Y. Wu, K. Y. Wang, T. H. Wu, H. H. Cheng, V. Ulyanov, V. I. Mashanov, and O. P. Pchelyakov, "Strained Ge1-xSnxthin film on Ge (100) with low temperature Ge buffer layer," *INEC 2010 - 2010 3rd Int. Nanoelectron. Conf. Proc.*, no. 100, pp. 1329–1330, 2010.

[148] W. Wang, S. J. Su, J. Zheng, G. Z. Zhang, Y. H. Zuo, B. W. Cheng, and Q. M. Wang, "High quality epitaxial Ge0.22Sn alloy films on Si with a Ge buffer by molecular beam epitaxy with combined sources," *Gr. IV Photonics (GFP), 2010 7th IEEE Int. Conf.*, pp. 347–349, 2010.

[149] H. H. Cheng, G. Sun, and R. A. Soref, "Tin-based IV-IV heterostructures by using Molecular Beam Epitaxy," *DOD project report, Project#:AOARD-09-4108*, 2010.

[150] O. Nakatsuka, N. Tsutsui, Y. Shimura, S. Takeuchi, A. Sakai, and S. Zaima, "Mobility behavior of Ge1-xSnx layers grown on silicon-on-insulator substrates," *Jpn. J. Appl. Phys.*, vol. 49, no. 4 PART 2, pp. 1–4, 2010.

[151] Y. Huo, R. Chen, H. Lin, T. I. Kamins, and J. S. Harris, "MBE growth of high Sn-percentage GeSn alloys with a composition-dependent absorption-edge shift," *IEEE Int. Conf. Gr. IV Photonics GFP*, pp. 344–346, 2010.

[152] J. Mathews, R. T. Beeler, J. Tolle, C. Xu, R. Roucka, J. Kouvetakis, and J. Meńndez, "Direct-gap photoluminescence with tunable emission wavelength in Ge 1-y Sny alloys on silicon," *Appl. Phys. Lett.*, vol. 97, no. 22, pp. 19–22, 2010.

[153] Y. Chibane and M. Ferhat, "Electronic structure of Snx Ge1-x alloys for small Sn compositions: Unusual structural and electronic properties," *J. Appl. Phys.*, vol. 107, no. 5, pp. 1–8, 2010.

[154] B. Vincent, F. Gencarelli, H. Bender, C. Merckling, B. Douhard, D. H. Petersen, O. Hansen, H. H. Henrichsen, J. Meersschaut, W. Vandervorst, M. Heyns, R. Loo, and M. Caymax, "Undoped and in-situ B doped GeSn epitaxial growth on Ge by atmospheric pressure-chemical vapor deposition," *Appl. Phys. Lett.*, vol. 99, no. 15, p. 152103, 2011.

[155] W. Wang, S. Su, J. Zheng, G. Zhang, C. Xue, Y. Zuo, B. Cheng, and Q. Wang,

"Flattening of low temperature epitaxial Ge1−xSnx/Ge/Si(100) alloys via mass transport during post-growth annealing," *Appl. Surf. Sci.*, vol. 257, no. 9, pp. 4468–4471, 2011.

[156] W. Wang, S. J. Su, J. Zheng, G. Z. Zhang, Y. H. Zuo, B. W. Cheng, and Q. M. Wang, "Strained and strain-relaxed epitaxial Ge1-xSnxalloys on Si(100) substrates," *Chinese Phys. B*, vol. 20, no. 6, pp. 4–9, 2011.

[157] S. Su, W. Wang, B. Cheng, G. Zhang, W. Hu, C. Xue, Y. Zuo, and Q. Wang, "Epitaxial growth and thermal stability of Ge1−xSnx alloys on Ge-buffered Si(001) substrates," *J. Cryst. Growth*, vol. 317, no. 1, pp. 43–46, 2011.

[158] R. Beeler, R. Roucka, A. V. G. Chizmeshya, J. Kouvetakis, and J. Menéndez, "Nonlinear structure-composition relationships in the GeSn/Si(001)system," *Phys. Rev. B - Condens. Matter Mater. Phys.*, vol. 84, no. 3, pp. 1–8, 2011.

[159] G. Han, S. Su, C. Zhan, Q. Zhou, Y. Yang, L. Wang, P. Guo, W. Wei, C. P. Wong, Z. X. Shen, B. Cheng, and Y. C. Yeo, "High-mobility germanium-tin (GeSn) P-channel MOSFETs featuring metallic source/drain and sub-370°C process modules," *Tech. Dig. - Int. Electron Devices Meet. IEDM*, no. 2010, pp. 402–404, 2011.

[160] S. Su, B. Cheng, C. Xue, W. Wang, Q. Cao, H. Xue, W. Hu, G. Zhang, Y. Zuo, and Q. Wang, "GeSn p-i-n photodetector for all telecommunication bands detection.," *Opt. Express*, vol. 19, no. 7, pp. 6400–6405, 2011.

[161] M. Oehme, J. Werner, M. Gollhofer, M. Schmid, M. Kaschel, E. Kasper, and J. Schulze, "Room Temperature Electroluminescence from GeSn Light Emitting pin Diodes on Si (August 2011)," *IEEE Photonics Technol. Lett.*, vol. 23, pp. 1751–1753, 2011.

[162] F. Gencarelli, B. Vincent, L. Souriau, O. Richard, W. Vandervorst, R. Loo, M. Caymax, and M. Heyns, "Low-temperature Ge and GeSn Chemical Vapor Deposition using Ge2H6," *Thin Solid Films*, vol. 520, pp. 3211–3215, 2012.

[163] S. Wirths, D. Buca, A. T. Tiedemann, B. Hollander, P. Bernardy, T. Stoica, D. Grutzmacher, and S. Mantl, "Epitaxial Growth of Gesn with high Sn content by RPCVD," in *ECS Prime*, 2012, vol. 742, no. June, pp. 2–3.

[164] R. T. Beeler, C. Xu, D. J. Smith, G. Grzybowski, J. Menéndez, and J. Kouvetakis, "Compositional dependence of the absorption edge and dark currents in Ge1−x−ySixSny/Ge(100) photodetectors grown via ultra-low-temperature epitaxy of Ge4H10, Si4H10, and SnD4," *Appl. Phys. Lett.*, vol. 101, no. 22, p. 221111, 2012.

[165] G. Han, S. Su, Y. Yang, P. Guo, X. Gong, L. Wang, W. Wang, C. Guo, G. Zhang, C. Xue, B. Cheng, and Y.-C. Yeo, "High Hole Mobility in Strained Germanium-Tin (GeSn) Channel pMOSFET Fabricated on (111) Substrate," *ECS Trans.*, vol. 50, no. 9, pp. 943–948, 2012.

[166] G. Han, S. Su, L. Wang, W. Wang, X. Gong, Y. Yang, P. Guo, C. Guo, G. Zhang, J. Pan,

Z. Zhang, C. Xue, B. Cheng, and Y. Yeo, “Strained Germanium-Tin (GeSn) N-channel MOSFETs featuring Low Temperature N + / P Junction Formation and GeSnO 2 Interfacial Layer,” *Mater. Res.*, pp. 97–98, 2012.

[167] Y. Yang, S. Su, P. Guo, W. Wang, X. Gong, L. Wang, K. L. Low, G. Zhang, C. Xue, B. Cheng, G. Han, and Y. C. Yeo, “Towards direct band-to-band tunneling in P-channel tunneling field effect transistor (TFET): Technology enablement by Germanium-tin (GeSn),” *Tech. Dig. - Int. Electron Devices Meet. IEDM*, pp. 379–382, 2012.

[168] M. Oehme, M. Schmid, M. Kaschel, M. Gollhofer, D. Widmann, E. Kasper, and J. Schulze, “GeSn p-i-n detectors integrated on Si with up to 4% Sn,” *Appl. Phys. Lett.*, vol. 101, no. 14, pp. 3–7, 2012.

[169] G. He and H. A. Atwater, “Interband Transitions in Sn_{x}Ge_{1-x} Alloys,” *Phys. Rev. Lett.*, vol. 79, no. 10, pp. 1937–1940, 1997.

[170] H. Lin, R. Chen, W. Lu, Y. Huo, T. I. Kamins, and J. S. Harris, “Investigation of the direct band gaps in Ge1-xSnxalloys with strain control by photoreflectance spectroscopy,” *Appl. Phys. Lett.*, vol. 100, no. 10, 2012.

[171] V. R. D’Costa, C. S. Cook, A. G. Birdwell, C. L. Littler, M. Canonico, S. Zollner, J. Kouvetakis, and J. Menéndez, “Optical critical points of thin-film Ge1-y Sny alloys: A comparative Ge1-y Sny Ge1-x six study,” *Phys. Rev. B - Condens. Matter Mater. Phys.*, vol. 73, no. 12, pp. 1–16, 2006.

[172] S. A. Ghetmiri, W. Du, J. Margetis, A. Mosleh, L. Cousar, B. R. Conley, L. Domulevicz, A. Nazzal, G. Sun, R. A. Soref, J. Tolle, B. Li, H. A. Naseem, and S.-Q. Yu, “Direct-bandgap GeSn grown on silicon with 2230nm photoluminescence Direct-bandgap GeSn grown on silicon with 2230 nm photoluminescence,” *Appl. Phys. Lett.*, vol. 105, no. 15, p. 151109, 2014.

[173] M. Oehme, D. Buca, K. Kostecki, S. Wirths, B. Holländer, E. Kasper, and J. Schulze, “Epitaxial growth of highly compressively strained GeSn alloys up to 12.5% Sn,” *J. Cryst. Growth*, vol. 384, pp. 71–76, 2013.

[174] F. Gencarelli, B. Vincent, J. Demeulemeester, A. Vantomme, A. Moussa, A. Franquet, A. Kumar, H. Bender, J. Meersschaut, W. Vandervorst, R. Loo, M. Caymax, K. Temst, and M. Heyns, “Crystalline Properties and Strain Relaxation Mechanism of CVD Grown GeSn,” in *ECS Prime*, 2012, vol. 2, no. 4, pp. P134–P137.

[175] W. Dou, M. Benamara, A. Mosleh, J. Margetis, P. Grant, Y. Zhou, S. Al-Kabi, W. Du, J. Tolle, B. Li, M. Mortazavi, and S. Q. Yu, “Investigation of GeSn Strain Relaxation and Spontaneous Composition Gradient for Low-Defect and High-Sn Alloy Growth,” *Sci. Rep.*, vol. 8, no. 1, pp. 1–11, 2018.

[176] S. Wirths, R. Geiger, N. von den Driesch, G. Mussler, T. Stoica, S. Mantl, Z. Ikonic, M.

Luysberg, S. Chiussi, J. M. Hartmann, H. Sigg, J. Faist, D. Buca, and D. Grützmacher, "Lasing in direct-bandgap GeSn alloy grown on Si," *Nat. Photonics*, vol. 9, no. 2, pp. 88–92, 2015.

[177] S. Al-Kabi, S. A. Ghetmiri, J. Margetis, T. Pham, Y. Zhou, W. Dou, B. Collier, R. Quinde, W. Du, A. Mosleh, J. Liu, G. Sun, R. A. Soref, J. Tolle, B. Li, M. Mortazavi, H. A. Naseem, and S. Q. Yu, "An optically pumped 2.5 μ m GeSn laser on Si operating at 110 K," *Appl. Phys. Lett.*, vol. 109, no. 17, pp. 171105-1–171105-4, 2016.

[178] J. Margetis, S. Al-Kabi, W. Du, W. Dou, Y. Zhou, T. Pham, P. Grant, S. Ghetmiri, A. Mosleh, B. Li, J. Liu, G. Sun, R. Soref, J. Tolle, M. Mortazavi, and S.-Q. Yu, "Si-Based GeSn Lasers with Wavelength Coverage of 2–3 μm and Operating Temperatures up to 180 K," *ACS Photonics*, vol. 5, no. 3, pp. 827–833, 2017.

[179] G. Sun, R. A. Soref, and H. H. Cheng, "Design of an electrically pumped SiGeSn/GeSn/SiGeSn double-heterostructure midinfrared laser," *J. Appl. Phys.*, vol. 108, no. 3, p. 033107, 2010.

[180] G. Sun, R. A. Soref, and H. H. Cheng, "Design of a Si-based lattice-matched room-temperature GeSn/GeSiSn multi-quantum-well mid-infrared laser diode.," *Opt. Express*, vol. 18, no. 19, pp. 19957–19965, 2010.

[181] G.-E. Chang, S.-W. Chang, and S.-L. Chuang, "Strain-Balanced Multiple-Quantum-Well Lasers," *IEEE J. Quantum Electron.*, vol. 46, no. 12, pp. 1813–1820, 2010.

[182] a Gassenq, F. Gencarelli, J. Van Campenhout, Y. Shimura, R. Loo, G. Narcy, B. Vincent, and G. Roelkens, "GeSn/Ge heterostructure short-wave infrared photodetectors on silicon.," *Opt. Express*, vol. 20, no. 25, pp. 27297–303, 2012.

[183] R. Chen, S. Gupta, Y. Huang, Y. Huo, C. W. Rudy, E. Sanchez, Y. Kim, T. I. Kamins, K. C. Saraswat, and J. S. Harris, "Demonstration of a Ge / GeSn / Ge Quantum-Well Microdisk Resonator on Silicon : Enabling high- quality Ge (Sn) materials for micro and nanophotonics," *Nano Lett.*, vol. 14, pp. 37–43, 2014.

[184] H. Li, C. Chang, T. P. Chen, H. H. Cheng, Z. W. Shi, and H. Chen, "Characteristics of Sn segregation in Ge/GeSn heterostructures," *Appl. Phys. Lett.*, vol. 105, no. 15, pp. 151906-1–151906-4, 2014.

[185] J.-Z. Chen, H. Li, H. H. Cheng, and G.-E. Chang, "Structural and optical characteristics of Ge_1−xSnx/Ge superlattices grown on Ge-buffered Si(001) wafers," *Opt. Mater. Express*, vol. 4, no. 6, p. 1178, 2014.

[186] M. Oehme, D. Widmann, K. Kostecki, P. Zaumseil, B. Schwartz, M. Gollhofer, R. Koerner, S. Bechler, M. Kittler, E. Kasper, and J. Schulze, "GeSn/Ge multiquantum well photodetectors on Si substrates.," *Opt. Lett.*, vol. 39, no. 16, pp. 4711–4, 2014.

[187] A. A. Tonkikh, C. Eisenschmidt, V. G. Talalaev, N. D. Zakharov, J. Schilling, G. Schmidt, and P. Werner, "Pseudomorphic GeSn / Ge (001) quantum wells : Examining indirect band gap bowing Pseudomorphic GeSn / Ge (001) quantum wells : Examining indirect band gap bowing," *Appl. Phys. Lett.*, vol. 103, p. 032106, 2013.

[188] B. Schwartz, M. Oehme, K. Kostecki, D. Widmann, M. Gollhofer, R. Koerner, S. Bechler, I. a Fischer, T. Wendav, E. Kasper, J. Schulze, and M. Kittler, "Electroluminescence of GeSn/Ge MQW LEDs on Si substrate," *Opt. Lett.*, vol. 40, no. 13, pp. 3209–3212, 2015.

[189] Y. G. Sadofyev, V. P. Martovitsky, M. A. Bazalevsky, A. V. Klekovkin, D. V. Averyanov, and I. S. Vasil'evskii, "Ge/GeSn heterostructures grown on Si (100) by molecular-beam epitaxy," *Semiconductors*, vol. 49, no. 1, pp. 124–129, 2015.

[190] D. Stange, N. von den Driesch, D. Rainko, C. Schulte-Braucks, S. Wirths, G. Mussler, A. T. Tiedemann, T. Stoica, J. M. Hartmann, Z. Ikonic, S. Mantl, D. Grützmacher, and D. Buca, "Study of GeSn based heterostructures: towards optimized group IV MQW LEDs," *Opt. Express*, vol. 24, no. 2, pp. 1358–1367, 2016.

[191] D. Buca, S. Wirths, D. Stange, A. T. Tiedemann, G. Mussler, Z. Ikonic, S. Chiussi, J. M. Hartman, D. Grutzmacher, and S. Mantl, "Si-Ge-Sn heterostructures: growth and applications," in *7th International Silicon-Germanium Technology and Device Meeting*, 2014, pp. 163–164.

[192] V. Chakraborty, B. Mukhopadhyay, and P. K. Basu, "Study of GeSn/SiGeSn RCE photodetectors based on Franz-Keldysh effect and quantum confined Stark effect," *Opt. Quantum Electron.*, vol. 47, no. 8, pp. 2381–2389, 2015.

[193] W. Dou, S. A. Ghetmiri, S. Al-Kabi, A. Mosleh, Y. Zhou, B. Alharthi, W. Du, J. Margetis, J. Tolle, A. Kuchuk, M. Benamara, B. Li, H. A. Naseem, M. Mortazavi, and S. Q. Yu, "Structural and Optical Characteristics of GeSn Quantum Wells for Silicon-Based Mid-Infrared Optoelectronic Applications," *J. Electron. Mater.*, vol. 45, no. 12, pp. 6265–6272, 2016.

[194] S. A. Ghetmiri, Y. Zhou, J. Margetis, S. Al-Kabi, W. Dou, A. Mosleh, W. Du, A. Kuchuk, J. Liu, G. Sun, R. A. Soref, J. Tolle, H. A. Naseem, B. Li, M. Mortazavi, and S.-Q. Yu, "Study of a SiGeSn/GeSn/SiGeSn structure toward direct bandgap type-I quantum well for all group-IV optoelectronics," *Opt. Lett.*, vol. 42, no. 3, p. 387, 2017.

[195] W. Du, S. A. Ghetmiri, J. Margetis, S. Al-Kabi, Y. Zhou, J. Liu, G. Sun, R. A. Soref, J. Tolle, B. Li, M. Mortazavi, and S.-Q. Yu, "Investigation of optical transitions in a SiGeSn/GeSn/SiGeSn single quantum well structure," *J. Appl. Phys.*, vol. 122, no. 12, p. 123102, 2017.

[196] P. A. Folkes, P. Taylor, C. Rong, B. Nichols, H. Hier, and M. Farrell, "Raman Scattering from Tin," *Army Res. Lab Rep.*, 2015.

[197] W. H. Bragg and W. L. Bragg, "The Refelection of X-rays by Crystals," *Proc. R. Soc. London. Ser. A, Contain. Pap. a Matheatical Phys. Character*, vol. 88, no. 605, pp. 428–438, 1913.

[198] A. Mosleh, "Epitaxial Growth of Si-Ge-Sn Alloys for Optoelectronic Device Applications," A dissertation submitted in partial fulfillment of the requirements for the degree of Doctor of Philosophy in Microelectronics-Photonics, University of Arkansas," 2015.

[199] W. Du, S. A. Ghetmiri, B. R. Conley, A. Mosleh, A. Nazzal, R. A. Soref, G. Sun, J. Tolle, J. Margetis, H. A. Naseem, and S.-Q. Yu, "Competition of optical transitions between direct and indirect bandgaps in Ge1−xSnx," *Appl. Phys. Lett.*, vol. 105, no. 5, p. 051104, 2014.

[200] N. von den Driesch, D. Stange, S. Wirths, G. Mussler, B. Holländer, Z. Ikonic, J. M. Hartmann, T. Stoica, S. Mantl, D. Grützmacher, and D. Buca, "Direct Bandgap Group IV Epitaxy on Si for Laser Applications," *Chem. Mater.*, p. 4693-4702, 2015.

[201] Y. Zhou, W. Dou, W. Du, T. Pham, S. A. Ghetmiri, S. Al-Kabi, A. Mosleh, M. Alher, J. Margetis, J. Tolle, G. Sun, R. Soref, B. Li, M. Mortazavi, H. Naseem, and S. Q. Yu, "Systematic study of GeSn heterostructure-based light-emitting diodes towards mid-infrared applications," *J. Appl. Phys.*, vol. 120, no. 2, pp. 1–8, 2016.

[202] M. Oehme, K. Kostecki, T. Arguirov, G. Mussler, K. Ye, M. Gollhofer, M. Schmid, M. Kaschel, R. A. K\"{o}rner, M. Kittler, D. Buca, E. Kasper, and J. Schulze, "GeSn heterojunction LEDs on Si substrates," *IEEE Photonics Technol. Lett.*, vol. 26, no. 2, pp. 187–189, 2014.

[203] J. P. Gupta, N. Bhargava, S. Kim, T. Adam, and J. Kolodzey, "Infrared electroluminescence from GeSn heterojunction diodes grown by molecular beam epitaxy," *Appl. Phys. Lett.*, vol. 102, no. 2013, pp. 2011–2015, 2013.

[204] T. Pham, B. R. Conley, J. Margetis, H. Tran, S. A. Ghetmiri, A. Mosleh, W. Du, G. Sun, R. A. Soref, J. Tolle, H. A. Naseem, B. Li, and S. Yu, "Photoconductors by Integration of Interdigitated Electrodes," in *CLEO*, San Jose, CA, May 10-15, 2015.

[205] B. R. Conley, A. Mosleh, S. A. Ghetmiri, W. Du, R. a Soref, G. Sun, J. Margetis, J. Tolle, H. a Naseem, and S.-Q. Yu, "Temperature dependent spectral response and detectivity of GeSn photoconductors on silicon for short wave infrared detection," *Opt. Express*, vol. 22, no. 13, pp. 15639–52, 2014.

[206] S. Al-Kabi, S. A. Ghetmiri, J. Margetis, T. Pham, Y. Zhou, W. Dou, B. Collier, R. Quinde, W. Du, A. Mosleh, J. Liu, G. Sun, R. A. Soref, J. Tolle, B. Li, M. Mortazavi, H. A. Naseem, and S. Q. Yu, "An optically pumped 2.5 um GeSn laser on Si operating at 110 K," *Appl. Phys. Lett.*, vol. 109, no. 17, 2016.

[207] P. Tao, L. Huang, H. H. Cheng, H.-H. Wang, and X.-S. Wu, "Epitaxial growth of Ge 1– x Sn x films with x up to 0.14 grown on Ge (00l) at low temperature," *Chinese Phys. B*, vol. 23, no. 8, p. 088112, 2014.

[208] O. Gurdal, P. Desjardins, J. R. a. Carlsson, N. Taylor, H. H. Radamson, J.-E. Sundgren, and J. E. Greene, "Low-temperature growth and critical epitaxial thicknesses of fully strained metastable Ge[sub 1−x]Sn[sub x] (x≲0.26) alloys on Ge(001)2×1," *J. Appl. Phys.*, vol. 83, no. 1, p. 162, 1998.

[209] R. Chen, H. Lin, Y. Huo, C. Hitzman, T. I. Kamins, and J. S. Harris, "Increased photoluminescence of strain-reduced, high-Sn composition Ge 1-xSnx alloys grown by molecular beam epitaxy," *Appl. Phys. Lett.*, vol. 99, no. 18, pp. 2013–2016, 2011.

[210] J. Werner, M. Oehme, M. Schmid, M. Kaschel, a. Schirmer, E. Kasper, and J. Schulze, "Germanium-tin p-i-n photodetectors integrated on silicon grown by molecular beam epitaxy," *Appl. Phys. Lett.*, vol. 98, no. 6, pp. 2011–2014, 2011.

[211] M. Coppinger, J. Hart, N. Bhargava, S. Kim, and J. Kolodzey, "Photoconductivity of germanium tin alloys grown by molecular beam epitaxy," *Appl. Phys. Lett.*, vol. 102, no. 14, pp. 2013–2016, 2013.

[212] S. Wirths, D. Buca, G. Mussler, A. T. Tiedemann, B. Hollander, P. Bernardy, T. Stoica, D. Grutzmacher, and S. Mantl, "Reduced Pressure CVD Growth of Ge and Ge1-xSnx Alloys," *ECS J. Solid State Sci. Technol.*, vol. 2, no. 5, pp. N99–N102, 2013.

[213] A. Mosleh, M. a. Alher, L. C. Cousar, W. Du, S. A. Ghetmiri, T. Pham, J. M. Grant, G. Sun, R. a. Soref, B. Li, H. a. Naseem, and S.-Q. Yu, "Direct Growth of Ge1−xSnx Films on Si Using a Cold-Wall Ultra-High Vacuum Chemical-Vapor-Deposition System," *Front. Mater.*, vol. 2, no. April, pp. 1–7, 2015.

[214] J. Margetis, S. A. Ghetmiri, W. Du, B. R. Conley, A. Mosleh, R. A. Soref, G. Sun, L. Domulevicz, H. A. Naseem, S.-Q. Yu, and J. Tolle, "Growth and characterization of epitaxial," *ECS Trans.*, vol. 64, no. 6, pp. 711–720, 2014.

[215] A. Mosleh, M. Alher, L. Cousar, H. Abu-safe, W. Dou, P. C. Grant, S. Al-Kabi, S. A. Ghetmiri, B. Alharthi, H. Tran, W. Du, M. Benamara, B. Li, M. Mortazavi, S.-Q. Yu, and H. A. Naseem, "Enhancement of Material Quality of (Si)GeSn Films Grown By $SnCl_4$ Precursor A. Mosleh," vol. 69, no. 5, pp. 279–286, 2015.

[216] S. Wirths, R. Geiger, Z. Ikonie, C. Schulie-Braucks, D. Stange, N. Von Den Driesch, J. M. Hartmann, S. Mantl, H. Sigg, D. Buca, and D. Grutzmacher, "The GeSn laser - Enabler for monolithic integration of photonics on Si," *IEEE Int. Conf. Gr. IV Photonics GFP*, vol. 2015–Octob, pp. 165–166, 2015.

[217] Y. Bogumilowicz, J. M. Hartmann, R. Truche, Y. Campidelli, G. Rolland, and T. Billon, "Chemical vapour etching of Si, SiGe and Ge with HCl; applications to the formation of

thin relaxed SiGe buffers and to the revelation of threading dislocations," *Semicond. Sci. Technol.*, vol. 20, no. 2, pp. 127–134, 2004.

[218] M. Hierlemann, H. Simka, K. Jensen F., and M. Utz, "Kinetic Modeling of the Gas Phase Decomposition of Germane by Computational Chemistry Techniques," *J. Phys. IV Fr.*, vol. 05, no. C5, pp. C5-71-C5-77, 1995.

[219] A. Mosleh, S. A. Ghetmiri, B. R. Conley, M. Hawkridge, M. Benamara, A. Nazzal, J. Tolle, S. Q. Yu, and H. a. Naseem, "Material characterization of Ge1-x Sn x alloys grown by a commercial CVD system for optoelectronic device applications," *J. Electron. Mater.*, vol. 43, no. 4, pp. 938–946, 2014.

[220] S. A. Ghetmiri, W. Du, B. R. Conley, A. Mosleh, A. Nazzal, G. Sun, R. A. Soref, J. Margetis, J. Tolle, H. A. Naseem, and S.-Q. Yu, "Shortwave-infrared photoluminescence from Ge1−xSnx thin films on silicon," *J. Vac. Sci. Technol. B, Nanotechnol. Microelectron. Mater. Process. Meas. Phenom.*, vol. 32, no. 6, p. 060601, 2014.

[221] R. People and J. C. Bean, "Calculation of critical layer thickness versus lattice mismatch for GexSi1-2/Si strianed-layer heterostructures," *Appl. Phys. Lett.*, vol. 47, p. 322, 1985.

[222] P. C. Grant, W. Dou, B. Alharthi, J. M. Grant, A. Mosleh, W. Du, B. Li, M. Mortazavi, H. A. Naseem, and S. Q. Yu, "Comparison study of the low temperature growth of dilute GeSn and Ge," *J. Vac. Sci. Technol. B*, vol. 35, no. 6, p. 061204, 2017.

[223] J. Margetis, S.-Q. Yu, N. Bhargava, B. Li, W. Du, and J. Tolle, "Strain Engineering in Epitaxial GexSn1-x: a Path towards Low-defect and High Sn-content Layers," *Semicond. Sci. Technol.*, 2017.

[224] E. A. Fitzgerald, Y. -H. Xie, M. L. Green, D. Brasen, A. R. Kortan, J. Michel, Y. -. Mii, and B. E. Weir, "Totally relaxed Ge $_x$ Si $_{1-x}$ layers with low threading dislocation densities grown on Si substrates," *Appl. Phys. Lett.*, vol. 59, no. 7, pp. 811–813, 1991.

[225] H.-C. Luan, D. R. Lim, K. K. Lee, K. M. Chen, J. G. Sandland, K. Wada, and L. C. Kimerling, "High-quality Ge epilayers on Si with low threading-dislocation densities," *Appl. Phys. Lett.*, vol. 75, no. 1999, p. 2909, 1999.

[226] T. A. Langdo, C. W. Leitz, M. T. Currie, E. A. Fitzgerald, A. Lochtefeld, and D. A. Antoniadis, "High quality Ge on Si by epitaxial necking," *Appl. Phys. Lett.*, vol. 76, no. 25, pp. 3700-3702, 2000.

[227] J. Margetis, S. A. Ghetmiri, W. Du, B. R. Conley, A. Mosleh, R. A. Soref, G. Sun, L. Domulevicz, H. A. Naseem, S.-Q. Yu, and J. Tolle, "Growth and characterization of epitaxial," *ECS Trans.*, vol. 64, no. 6, pp. 711–720, 2014.

[228] Z. Liu, C. He, D. Zhang, C. Li, C. Xue, Y. Zuo, and B. Cheng, "Temperature dependent direct-bandgap light emission and optical gain of Ge," *Chinese Phys. B*, vol. 25, no. 5, p.

057804, 2016.

[229] N. a. Riordan, C. Gogineni, S. R. Johnson, X. Lu, T. Tiedje, D. Ding, Y. H. Zhang, R. Fritz, K. Kolata, S. Chatterjee, K. Volz, and S. W. Koch, "Temperature and pump power dependent photoluminescence characterization of MBE grown GaAsBi on GaAs," *J. Mater. Sci. Mater. Electron.*, vol. 23, no. 10, pp. 1799–1804, Mar. 2012.

[230] R. R. Lieten, K. Bustillo, T. Smets, E. Simoen, J. W. Ager, E. E. Haller, and J. P. Locquet, "Photoluminescence of bulk germanium," *Phys. Rev. B - Condens. Matter Mater. Phys.*, vol. 86, no. 3, pp. 1–5, 2012.

[231] K. Toko, R. Yoshimine, K. Moto, and T. Suemasu, "High-hole mobility polycrystalline Ge on an insulator formed by controlling precursor atomic density for solid-phase crystallization," *Sci. Rep.*, vol. 7, no. 1, pp. 1–7, 2017.

[232] R. Soref, D. Buca, and S.-Q. Yu, "Group IV Photonics," *Opt. Photonics News*, vol. 27, no. 1, pp. 32–39, 2016.

[233] S. Q. Yu, S. A. Ghetmiri, W. Du, J. Margetis, Y. Zhou, A. Mosleh, S. Al-Kabi, A. Nazzal, G. Sun, R. A. Soref, J. Tolle, B. Li, and H. A. Naseem, "Si based GeSn light emitter: mid-infrared devices in Si photonics," *Proc. SPIE 9367, Silicon Photonics X*, vol. 9367, no. 479, p. 93670R, 2015.

[234] S. Gupta, R. Chen, B. Magyari-Kope, H. Lin, B. Yang, A. Nainani, Y. Nishi, J. S. Harris, and K. C. Saraswat, "GeSn technology: Extending the Ge electronics roadmap," *Tech. Dig. - Int. Electron Devices Meet. IEDM*, pp. 398–401, 2011.

[235] S. Sant and A. Schenk, "Band-offset engineering for GeSn-SiGeSn hetero tunnel FETs and the role of strain," *IEEE J. Electron Devices Soc.*, vol. 3, no. 3, pp. 164–175, 2015.

[236] S. A. Ghetmiri, W. Du, J. Margetis, A. Mosleh, L. Cousar, B. R. Conley, L. Domulevicz, A. Nazzal, G. Sun, R. A. Soref, J. Tolle, B. Li, H. A. Naseem, and S. Q. Yu, "Direct-bandgap GeSn grown on silicon with 2230 nm photoluminescence," *Appl. Phys. Lett.*, vol. 105, no. 15, pp. 151109-1 - 151109-4, 2014.

[237] W. Du, Y. Zhou, S. A. Ghetmiri, A. Mosleh, B. R. Conley, A. Nazzal, R. A. Soref, G. Sun, J. Tolle, J. Margetis, H. A. Naseem, and S. Q. Yu, "Room-temperature electroluminescence from Ge/Ge1-xSn x/Ge diodes on Si substrates," *Appl. Phys. Lett.*, vol. 104, no. 24, pp. 241110-4–241110-4, 2014.

[238] D. Stange, S. Wirths, R. Geiger, C. Schulte-Braucks, B. Marzban, N. V. Den Driesch, G. Mussler, T. Zabel, T. Stoica, J. M. Hartmann, S. Mantl, Z. Ikonic, D. Grützmacher, H. Sigg, J. Witzens, and D. Buca, "Optically Pumped GeSn Microdisk Lasers on Si," *ACS Photonics*, vol. 3, no. 7, pp. 1279–1285, 2016.

[239] A. Mosleh, M. Alher, L. C. Cousar, W. Du, S. A. Ghetmiri, S. Al-Kabi, W. Dou, P. C.

Grant, G. Sun, R. A. Soref, B. Li, H. A. Naseem, and S. Q. Yu, "Buffer-Free GeSn and SiGeSn Growth on Si Substrate Using In Situ SnD4 Gas Mixing," *J. Electron. Mater.*, vol. 45, no. 4, pp. 2051–2058, 2016.

[240] J. Margetis, A. Mosleh, S. Al-Kabi, S. A. Ghetmiri, W. Du, W. Dou, M. Benamara, B. Li, M. Mortazavi, H. A. Naseem, S. Q. Yu, and J. Tolle, "Study of low-defect and strain-relaxed GeSn growth via reduced pressure CVD in H2and N2carrier gas," *J. Cryst. Growth*, vol. 463, pp. 128–133, 2017.

[241] B. R. Conley, J. Margetis, W. Du, H. Tran, A. Mosleh, S. A. Ghetmiri, J. Tolle, G. Sun, R. Soref, B. Li, H. A. Naseem, and S. Q. Yu, "Si based GeSn photoconductors with a 1.63 A/W peak responsivity and a 2.4 µ m long-wavelength cutoff," *Appl. Phys. Lett.*, vol. 105, no. 22, pp. 221117-1 - 221117-42014.

[242] W. Dou, Y. Zhou, J. Margetis, S. Ghetmiri, W. Du, J. Liu, G. Sun, R. Soref, J. Tolle, B. Li, M. Mortazavi, and S. Q. Yu, "Optically Pumped GeSn-edge-emitting Laser with Emission at," in *CLEO*, San Jose, CA, May 10-15, 2018.

[243] J. Liu, "Monolithically Integrated Ge-on-Si Active Photonics," *Photonics*, vol. 1, no. 3, pp. 162–197, 2014.

[244] R. Geiger, T. Zabel, and H. Sigg, "Group IV Direct Band Gap Photonics: Methods, Challenges, and Opportunities," *Front. Mater.*, vol. 2, July, 2015.

[245] S. Dominici, H. Wen, F. Bertazzi, M. Goano, and E. Bellotti, "Numerical study on the optical and carrier recombination processes in GeSn alloy for E-SWIR and MWIR optoelectronic applications," *Opt. Express*, vol. 24, no. 23, pp. 26363–26381, 2016.

[246] R. Soref, "Mid-infrared photonics in silicon and germanium," *Nat. Photonics*, vol. 4, no. 8, pp. 495–497, 2010.

[247] J. Liu, L. C. Kimerling, and J. Michel, "Monolithic Ge-on-Si lasers for large-scale electronic-photonic integration," *Semicond. Sci. Technol.*, vol. 27, no. 9, pp. 1-13, 2012.

[248] B. Dutt, H. Lin, D. S. Sukhdeo, B. M. Vulovic, S. Gupta, D. Nam, K. C. Saraswat, and J. S. Harris, "Theoretical analysis of GeSn alloys as a gain medium for a Si-compatible laser," *IEEE J. Sel. Top. Quantum Electron.*, vol. 19, no. 5, p. 1502706, 2013.

[249] M. Oehme, J. Werner, M. Gollhofer, M. Schmid, M. Kaschel, E. Kasper, and J. Schulze, "Room-Temperature Electroluminescence From GeSn Light-Emitting Pin Diodes on Si," *IEEE Photonics Technol. Lett.*, vol. 23, no. 23, pp. 19–21, 2011.

[250] H. H. Tseng, K. Y. Wu, H. Li, V. Mashanov, H. H. Cheng, G. Sun, and R. A. Soref, "Mid-infrared electroluminescence from a Ge/Ge0. 922Sn0. 078/Ge double heterostructure pin diode on a Si substrate," *Appl. Phys. Lett.*, vol. 102, no. 18, p. 182106, 2013.

[251] C. L. Senaratne, J. D. Gallagher, T. Aoki, and J. Kouvetakis, “Advances in Light Emission from Group-IV Alloys via Lattice Engineering and n-Type Doping Based on Custom-Designed Chemistries,” *Chem. Mater.*, vol. 26, pp. 6033–6041, 2014.

[252] C. Y. Lin, C. H. Huang, S. H. Huang, C. C. Chang, C. W. Liu, Y. C. Huang, H. Chung, and C. P. Chang, “Photoluminescence and electroluminescence from Ge/strained GeSn/Ge quantum wells,” *Appl. Phys. Lett.*, vol. 109, no. 9, pp. 187-189, 2016.

[253] J. D. Gallagher, C. L. Senaratne, P. Sims, T. Aoki, J. Menéndez, and J. Kouvetakis, “Electroluminescence from GeSn heterostructure pin diodes at the indirect to direct transition,” *Appl. Phys. Lett.*, vol. 106, no. 9, pp. 091103-1 - 191103-4, 2015.

[254] N. von den Driesch, D. Stange, S. Wirths, D. Rainko, I. Povstugar, A. Savenko, U. Breuer, R. Geiger, H. Sigg, Z. Ikonic, J. M. Hartmann, D. Grützmacher, S. Mantl, and D. Buca, “SiGeSn Ternaries for Efficient Group IV Heterostructure Light Emitters,” *Small*, vol. 13, no. 16, pp. 1–9, 2017.

[255] D. Stange, N. von Den Riesch, D. R. Ainko, S. Roesgaard, I. Povstugar, J.-M. Hartmann, T. Stoica, Z. Ikonic, S. Mantl, D. Grützmacher, and D. Buca, “Short-wave infrared LEDs from GeSn / SiGeSn multiple quantum wells,” *Optica*, vol. 4, no. 2, pp. 185–188, 2017.

[256] J. Zheng, S. Wang, H. Cong, C. S. Fenrich, Z. Liu, C. Xue, C. Li, Y. Zuo, B. Cheng, J. S. Harris, and Q. Wang, “Characterization of a Ge1-x-ySiySnx/Ge1-xSnx multiple quantum well structure grown by sputtering epitaxy,” *Opt. Lett.*, vol. 42, no. 8, pp. 1608–1611, 2017.

[257] Y.-H. Huang, G.-E. Chang, H. Li, and H. H. Cheng, “Sn-based waveguide p-i-n photodetector with strained GeSn / Ge multiple-quantum-well active layer,” *Opt. Lett.*, vol. 42, no. 9, pp. 1652–1655, 2017.

[258] I. A. Fischer, T. Wendav, L. Augel, S. Jitpakdeebodin, F. Oliveira, A. Benedetti, S. Stefanov, S. Chiussi, G. Capellini, K. Busch, and J. Schulze, “Growth and characterization of SiGeSn quantum well photodiodes,” *Opt. Express*, vol. 23, no. 19, p. 25048, 2015.

[259] M. Oehme, K. Kostecki, T. Arguirov, G. Mussler, K. Ye, M. Gollhofer, M. Schmid, M. Kaschel, R. A. Korner, M. Kittler, D. Buca, E. Kasper, and J. Schulze, “GeSn heterojunction LEDs on Si substrates,” *IEEE Photonics Technol. Lett.*, vol. 26, no. 2, pp. 187–189, 2014.

[260] G. Sun, R. A. Soref, and H. H. Cheng, “Design of a Si-based lattice-matched room-temperature GeSn / GeSiSn multi-quantum-well mid-infrared laser diode,” *Opt. Express*, vol. 18, no. 19, pp. 19957–19965, 2010.

[261] R. Beeler, R. Roucka, A. V. G. Chizmeshya, J. Kouvetakis, and J. Menéndez, “Nonlinear structure-composition relationships in the Ge 1-ySny/Si(100) (y<0.15) system,” *Phys. Rev. B - Condens. Matter Mater. Phys.*, vol. 84, no. 3, pp. 1–8, 2011.

[262] M. Jaros, “Simple analytic model for heterojunction band offsets,” *Phys. Rev. B*, vol. 37, no. 12, pp. 7112–7114, 1988.

[263] H. Tran, W. Du, S. A. Ghetmiri, A. Mosleh, G. Sun, R. A. Soref, J. Margetis, J. Tolle, B. Li, H. A. Naseem, and S.-Q. Yu, “Systematic study of Ge$_{1-x}$Sn$_x$ absorption coefficient and refractive index for the device applications of Si-based optoelectronics,” *J. Appl. Phys.*, vol. 119, no. 10, p. 103106, 2016.

[264] P. C. Grant, J. Margetis, Y. Zhou, W. Dou, G. Abernathy, A. Kuchuk, W. Du, B. Li, J. Tolle, J. Liu, G. Sun, R. A. Soref, M. Mortazavi, and S. Q. Yu, “Direct bandgap type-I GeSn/GeSn quantum well on a GeSn- and Ge- buffered Si substrate,” *AIP Adv.*, vol. 8, no. 2, pp. 025108-1 - 025108-6, 2018.

[265] R. A. Soref and C. H. Perry, “Predicted band gap of the new semiconductor SiGeSn,” *J. Appl. Phys.*, vol. 69, no. 1, pp. 539–541, 1991.

[266] V. Reboud, A. Gassenq, N. Pauc, J. Aubin, L. Milord, Q. M. Thai, M. Bertrand, K. Guilloy, D. Rouchon, J. Rothman, T. Zabel, F. Armand Pilon, H. Sigg, A. Chelnokov, J. M. Hartmann, and V. Calvo, “Optically pumped GeSn micro-disks with 16% Sn lasing at 3.1 μ m up to 180 K,” *Appl. Phys. Lett.*, vol. 111, no. 9, 2017.

[267] C. Chang, H. Li, S. H. Huang, L. C. Lin, and H. H. Cheng, “Temperature-dependent electroluminescence from GeSn heterojunction light-emitting diode on Si substrate,” *Jpn. J. Appl. Phys.*, vol. 55, no. 4, 2016.

[268] S. Wirths, R. Geiger, Z. Ikonic, A. T. Tiedemann, G. Mussler, M. Hartmann, S. Mantl, H. Sigg, D. Grützmacher, D. Buca, P. Grünberg, and F. Juelich, “Epitaxy and Photoluminescence Studies of High Quality GeSn Heterostructures with Sn Concentrations up to 13 at .%,” in *Group IV Photonics (GFP), 2014 IEEE 11th International Conference*, 2014, vol. 2, pp. 15–16.

[269] C. L. Senaratne, P. M. Wallace, J. D. Gallagher, P. E. Sims, J. Kouvetakis, and J. Menendez, “Direct gap Ge1-ySny alloys: Fabrication and design of mid-IR photodiodes,” *J. Appl. Phys.*, vol. 120, no. 2, p. 025701, 2016.

Appendix A: Description of Research for Popular Publication

Bridging the gap between electronics and optoelectronics

Since the invention of the transistor radio, electronics has become an increasing part of everyday life. With billions of cell phones in use, Facebook® users, personal wearable electronics (Fitbit®), and the rise of automation, the impact of electronics on today's societies is undeniable. Optoelectronics (devices that produce or detect light) have also expanded their reach into our daily lives, such as TV remotes, home and vehicle lighting, and the fiber optic systems that have vastly improved the ability to send and receive information. Optoelectronics covers most of the wavelengths of light from the UV, through the visible, and out toward the infra-red. Infra-red optoelectronics operate in regions beyond the visible spectrum and are currently used for a host of devices, such as gas detectors, fiber optic lasers, space communication devices, etc. Most of the advancement in human society over the last 50 years can be directly linked to the rise of these two technologies. However, there is a gap between the two technologies that has yet to be filled.

Silicon is the main material used for most electronics found in the world today. Decades of progress in electronics has increased the speed of the systems and reduced device footprint to meet the ever-increasing demand from consumers. Silicon, however, has an indirect band-gap thus making its optical properties poor in comparison of III-V materials, such as gallium arsenide, that make up the optoelectronics industry. III-V materials are direct band-gap which increases the amount of light that can be emitted from the material, however, these materials are inherently expensive. This increase in efficiency of light generation in III-V materials has been the biggest barrier to silicon-based devices becoming competitive in the optoelectronic market. One method to try and bridge the gap between electronics and optoelectronics has been to pursue

III-V material and devices integrated on silicon substrates. While there has been good progress in this direction, the incompatibility of III-V material to the silicon processing has made it difficult to achieve an integration strategy that will allow III-V materials to bridge the gap. The other method is called group IV photonics. This method proposes to use only group IV elements, such as silicon, to make infra-red optoelectronic devices. Researchers have made major efforts in using silicon and germanium as optoelectronic devices. However, this is limited in that silicon stays an indirect band-gap semiconductor, limiting light generation efficiency. Germanium, while an indirect band-gap material, has been shown to become direct band-gap material under strain, thus increasing light generation efficiency, but it has limited range in which the semiconductor can operate.

P.C. Grant, μEP student of Dr. Fisher Yu, Electrical Engineering at the University of Arkansas has recently performed research into making the next generation of cheaper infra-red optoelectronic devices. P.C. said, "The germanium-tin material can bridge the gap between the traditional electronics and the infra-red optoelectronics worlds. This cool material can achieve all the benefits of traditional III-V materials but is compatible with silicon processing. It's like having the best of both worlds." The alloying of germanium and tin has produced direct band-gap material like traditional III-V materials and can cover the same spectrum all from a silicon substrate without extraordinary processing methods. Devices from the germanium-tin material has already been used to make a number of optically active devices, such as LEDs and lasers. Several industries can be disrupted by consumer products based on this material. Infra-red imaging currently uses III-V devices to generate images, with modern infrared cameras being several thousand dollars in cost. The germanium-tin material can compete in this field with a large reduction in cost due to being silicon-based instead of III-V based. The silicon processing

even can produce an infra-red camera small enough and cheap enough to be put in cell phones. This will effectively put night vision technology in the hands of the individual consumer.

Using this technology, first responders to any disaster can have one more tool at their disposal. Infrared imaging can be used to see through dust, fog, or smoke assisting the first responders to be more aware of their environment. Internal injuries are also visible under infra-red light thus making it easier to diagnose injuries that occur from an accident. Food services can see issues with food before sending it out to the public, such as bruising in fresh fruit. Another application that infra-red optoelectronics based on silicon can play a major role in that of computing. Currently all information in a computer is stored, transmitted, and processed using electronics. This generates heat in the system which all people who use computers know they have a fan used to cool the processor. Infra-red optoelectronic based on silicon can increase the speed of computers and reduce the operating temperature because the system could use light instead of electrons to transmit data. P.C. said, "It's like taking the fiber optic systems used to transmit data around the country and shrinking it down to the computer chip." This shrinking of the fiber optic system to the chip level can lead to more efficient computers that have increased speed.

The infra-red optoelectronics market is ready for the next generation of emitters and detectors to fill the increasing demand from consumers. The next generation of infra-red optoelectronics needs to be efficient and inexpensive as this will be the only way to supplant the existing technology. The germanium-tin material has shown its potential to compete with and possibly out-perform traditional III-V infra-red optoelectronic devices.

Appendix B: Executive Summary of Newly Created Intellectual Property

Newly created intellectual property is as follows:

i) New method to produce gaseous HCl. This was accomplished using the following reaction $GeH_4 + SnCl_4 \rightarrow GeSn + 4\ HCl$ at temperatures > 250 °C.

ii) Low temperature (250 °C) CVD growth of GeSn on Ge buffers using UHV-CVD in conjunction with commercial precursors (GeH_4 and $SnCl_4$). Continued reduction in growth temperature is foreseeable.

iii) Plasma enhancement for CVD growth of GeSn directly on Si or Ge buffered Si.

iv) Discovered Sn over-pressure leaves droplets on the surface and the size of droplet can be controlled by Sn overpressure. Sn over-pressure also depletes GeSn films to 1% Sn incorporation regardless of growth temperature.

Appendix C: Potential Patent and Commercialization Aspects of Listed Intellectual Property Item

C. 1 Patentability of Intellectual Property (Could Each Item be Patented)

Each piece of created IP was first examined if it could be patented.

i) The production method of HCl can be patented.

ii) The growth temperature value cannot be patented.

iii) The plasma enhancement can be patented.

iv) Depletion of GeSn films by Sn over-pressure cannot be patented. The Sn droplets cannot be patented.

C. 2 Commercialization Prospects (Should Each Item Be Patented)

i) No. Commercial industry already has more efficient and safer methods of HCl than produced through this method.

ii) Not applicable.

iii) No. Verification of compliance of a patent across the industry would not be cost effective.

iv) Not applicable

C. 3 Possible Prior Disclosure of IP

i) Not applicable

ii) Not applicable

iii) Not applicable

iv) Not applicable

Appendix D: Broader Impact of Research

D. 1 Applicability of Research Methods to Other Problems

High quality GeSn could become a disruptive technology within the infra-red optoelectronics market. The research methods used in development of high quality GeSn material could be applied to other problems. The method most applicable to other problems involved a rapid feedback mechanism for the grower. The feedback mechanism for each grown sample involved four characterization techniques applied to give four important pieces of information (surface clarity, film thickness, film crystallinity, and Sn composition/material quality). The feedback mechanism was performed in a single day following the growth. The information collected every day was documented for reference. When samples displayed desired properties from the feedback mechanism, more involved characterization techniques were planned. This type of feedback mechanism that collects several pieces of information in a short period of time, and is then documented for a grower, keeps the grower on track to the goal.

D. 2 Impact of Research Results on U.S. and Global Society

Development of the GeSn material as part of the SiGeSn material systems greatly impacts U.S. and global society. Infra-red optoelectronics have been limited in their integration into the mass markets due to their high cost, however, the ability to grow GeSn on silicon substrates will lead a reduction in cost of devices by more than 50%. In the U.S., computers, cell phones, and personal electronics have become commonplace. GeSn on Si has already been shown to produce all the single devices to make an on-chip optical signal transfer. This advancement will lead to more efficient computers that operate at faster speeds. Infra-red optoelectronics devices can be used to help see in the dark, through smoke, or fog making them useful for individuals to navigate during these conditions. With self-driving cars making their entrance into the market, optoelectronics that can see in these conditions will increase the safety

of these automobiles. GeSn devices have the potential to disrupt the existing infra-red optoelectronic market with inexpensive and efficient devices. This will allow for new companies to enter into markets that has been dominated by III-V materials for decades.

D. 3 Impact of Research Results on the Environment

The research performed can impact the environment in many ways. Development of Si-based light sources will reduce the need to mine for rare materials, thus reducing the damage to the environment and ecosystems where these minerals exist. Increased efficiency in any electronic based system is beneficial to the environment. Less energy used by electronic systems results in a decrease in the demand on natural resources used to develop energy, traditionally coal, oil, or gas. Increasing the infra-red absorption in the materials also offers the possibility of more efficient solar cells, that can maintain cost effectiveness for use in terrestrial applications. Each of these benefits of developing the GeSn material show how improving the electronic systems that are currently used will ultimately make this world a better place to be.

Appendix E: Microsoft Project for MS MicroEP Degree Plan

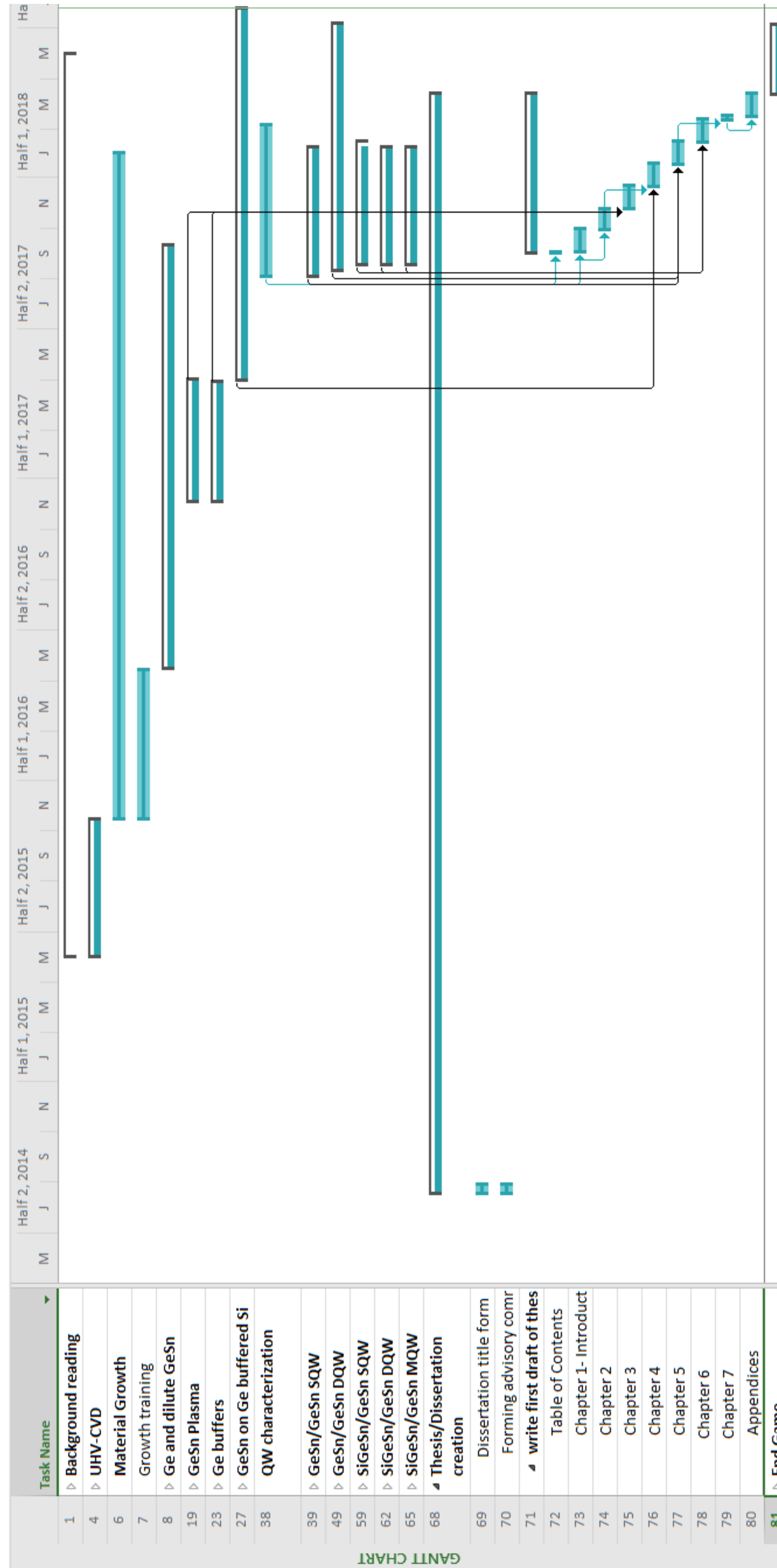

Appendix F: Identification of All Software Used in Research and Dissertation Generation

Computer #1:
    Model Number: Satellite C75D-A7310
    Serial Number: ZD099158C
    Location: Personal laptop
    Owner: Perry C. Grant
Software #1:
    Name: Microsoft Office 2016
    Purchased by: Electrical Engineering Department, University of Arkansas
Software #2:
    Name: Microsoft Project 2016
    Provided by: Electrical Engineering Department, University of Arkansas
Software #3:
    Name: Mendeley
    Purchased by: Free download available from Mendeley.com
Software #4:
    Name: Matlab R2017a Student Version
    Provided by: University of Arkansas
Software #5
    Name: OriginPro 2017
    Purchased by Perry C. Grant

Computer #2:
    Model Number: Dell Vostro
    Serial Number: 52M6XK1
    Location: ENRC Room 2923
    Owner: Dr. Shui-Qing Yu
Software #1:
    Name: SynerJY with built-in Origin software
    Purchased by: Dr. Shui-Qing Yu

Computer #3:
    Model Number: Dell Inspiron
    Serial Number: 52M6XK1
    Location: ENRC Room 2923
    Owner: Dr. Shui-Qing Yu
Software #1:
    Name: SynerJY with built-in Origin software
    Purchased by: Dr. Shui-Qing Yu

Appendix G: All Publications Published, Submitted, and Planned

i. Articles in Refereed Journals

2018

19 **P.C. Grant**, W. Dou, B. Alharthi, J.M. Grant, H. Tran, G. Abernathy, A. Mosleh, W. Du, M. Mortazavi, H.A. Naseem, S.-Q. Yu "UHV-CVD Growth of High Quality GeSn Using SnCl4: From Growth Optimization to Prototype Devices" arXiv:1810.02523 [cond-mat.mtrl-sci]

18 Wei Dou, Bader Alharthi, **Perry C. Grant**, Joshua M. Grant, Aboozar Mosleh, Huong Tran, Wei Du, Mansour Mortazavi, Baohua Li, Hameed Naseem, Shui-Qing Yu "Crystalline GeSn Growth by Plasma Enhanced Chemical Vapor Deposition" Optical Materials Express, vol. 8, no. 10, pp. 3320-3229

17 **Perry C. Grant**, Joe Margetis, Wei Du, Yiyin Zhou, Wei Dou, Grey Abernathy, Andrian Kuchuk, Baohua Li, John Tolle, Jiefeng Liu, Greg Sun, Richard A. Soref, Mansour Mortazavi, Shui-Qing Yu, "Study of Direct Bandgap Type-I GeSn/GeSn Double Quantum Well with Improved Carrier Confinement" Nanotechnology, vol. 29, no. 46, pp. 465201

16 Huong Tran, Thach Pham, Wei Du, Yang Zhang, **Perry C. Grant**, Joshua M. Grant, Greg Sun, Richard A. Soref, Joe Margetis, John Tolle, Baohua Li, Mansour Mortazavi, Shui-Qing Yu, "High performance $Ge_{0.89}Sn_{0.11}$ photodiodes for low-cost shortwave infrared imaging" Journal of Applied Physics, vol. 124, no. 1, pp. 013101

15 Wei Dou, Mourad Benamara, Aboozar Mosleh, Joe Margetis, **Perry Grant**, Yiyin Zhou, Sattar Al-Kabi, Wei Du, John Tolle, Baohua Li, Mansour Mortazavi, Shui-Qing Yu, "Investigation of GeSn Strain Relaxation and Spontaneous Composition Gradient for Low-Defect and High-Sn Alloy Growth" Scientific Reports, vol 8 no 1, pp. 5640-5650, 2018.

14 Bader Alharthi, Joshua M. Grant, Wei Dou, **Perry C. Grant**, Aboozar Mosleh, Wei Du, Mansour Mortazavi, Baohua Li, Hameed Naseem, Shui-Qing Yu, "Heteroepitaxial Growth of Germanium-on-Silicon Using Ultrahigh-Vacuum Chemical Vapor Deposition with RF Plasma Enhancement" Journal of Electronic Materials, vol. 47 pp. 4561, 2018.

13 **Perry C. Grant,** Joe Margetis, Yiyin Zhou, Wei Dou, Grey Abernathy, Andrian Kuchuk, Wei Du, Baohua Li, John Tolle, Jifeng Liu, Greg Sun, Richard Soref, Mansour Mortazavi, Shui-Qing Yu, "Direct Bandgap Type-I GeSn/GeSn Quantum Well on GeSn and Ge buffered Si Substrate" AIP Advances, vol. 8 no. 2, pp. 025104, 2018.

2017

12 **Perry C. Grant**, Wei Dou, Bader Alharthi, Joshua M Grant, Aboozar Mosleh, Wei Du, Baohua Li, Mansour Mortazavi, Hameed A Naseem, Shui-Qing Yu, "Comparison study of the low temperature growth of dilute GeSn and Ge", Journal of Vacuum Science and Technology B, vol 35, no. 6, pp. 061204, 2017.

11 A Bachri, A Elmhamdi, M Hawron, **P Grant**, B Zazoum, C Martin, "High-pressure xenon time projection Titanium chamber: a methodology for detecting background radiation in neutrinoless double-beta decay experiments", Journal of Instrumentation, vol. 12 no. 10, pp. T10004, 2017.

10 Joe Margetis, Sattar Al-Kabi, Wei Du, Wei Dou, Yiyin Zhou, Thach Pham, **Perry Grant**, Seyed Ghetmiri, Aboozar Mosleh, Baohua Li, Jifeng Liu, Greg Sun, Richard Soref, John Tolle, Mansour Mortazavi, Shui-Qing Yu, "Si-based GeSn lasers with wavelength coverage of 2 to 3 μm and operating temperatures up to 180 K", ACS Photonics, vol. 5, no. 3, pp. 827-833, 2017.

2016

9 Aboozar Mosleh, Murtadha Alher, Larry C Cousar, Wei Du, Seyed Amir Ghetmiri, Sattar Al-Kabi, Wei Dou, **Perry C Grant**, Greg Sun, Richard A Soref, Baohua Li, Hameed A Naseem, Shui-Qing Yu, "Buffer-Free GeSn and SiGeSn Growth on Si Substrate Using In Situ SnD_4 Gas Mixing", Journal of Electronic Materials, vol 45, no. 4, pp. 2051-2058, 2016.

8 A. Mosleh, M. Alher, W. Du, L. Cousar, S.A. Ghetmiri, S. Al-Kabi, W. Dou, **P. Grant**, G. Sun, R. Soref, B. Li, H. Naseem, and S.-Q.Yu. "SiyGe1−x−ySnx films grown on Si using a cold-wall ultrahigh-vacuum chemical vapor deposition system", Journal of Vacuum Science & Technology B, vol. 34, no. 1, pp. 011201, 2016.

2015

7 A. Mosleh, M. Alher, L. Cousar, H. Abusafe, W. Dou, **P. Grant**, S. Al-Kabi, S. A. Ghetmiri, B. Alharthi, H. Tran, W. Du, M. Benamara, B. Li, M. Mortazavi, S.-Q. Yu, and H. A. Naseem. "Enhancement of Material Quality of (Si)GeSn Films Grown by $SnCl_4$ Precursor", ECS Transactions, vol. 69, no. 5, pp. 279-286, 2015.

6 J. A, Steele, Josip Horvat, Roger A. Lewis, M. Henini, D. Fan, Yu I. Mazur, V. G. Dorogan, **P. C. Grant**, S-Q. Yu, and G. J. Salamo. "Mechanism of periodic height variations along self-aligned VLS-grown planar nanostructures." Nanoscale 7, no. 48 (2015): 20442-20450.

5 M. Alher, A. Mosleh, L. Cousar, W. Dou, **P. Grant**, S. A. Ghetmiri, S. Al-Kabi, W. Du, M. Benamara, B. Li, M. Mortazavi, S.-Q. Yu and H. A. Naseem."CMOS Compatible Growth of High Quality Ge, SiGe and SiGeSn for Photonic Device Applications",ECS Transactions, vol. 69, no. 5, pp. 269-278, 2015.

2014

4 J. A. Steele, R. A. Lewis, M. Henini, O. M. Lemine, A. Alkaoud, D. Fan, Yu. I. Mazur, V. G. Dorogan, **P. C. Grant**, S.-Q. Yu, and G. J. Salamo. "*Raman reveals strong LO-phonon-hole-plasmon coupling in undoped GaAsBi*", Optics Express, Vol. 22, No. 10, 11680-11689 (2014).

3 **P. C. Grant**, Dongsheng Fan, Aboozar Mosleh, Shui-Qing Yu, Vitaliy G. Dorogan, Michael E. Hawkridge, Yuriy I. Mazur, Mourad Benamara, Gregory J. Salamo, and Shane R. Johnson. "Rapid thermal annealing effect on GaAsBi/GaAs single quantum wells grown by

molecular beam epitaxy" Journal of Vacuum Science & Technology B, vol. 32, no. 2, pp. 02C119, 2014.

2013

2 D. Fan, **P. Grant**, and S. Yu, V.G. Dorogan, X. Hu, Z. Zeng, C. Li, M. E. Hawkridge, M. Benemara, Yu. I. Mazur, G. J. Salamo, S. R. Johnson, and Z. M. Wang. "MBE Grown GaAsBi/GaAs Double Quantum Well Separate Confinement Heterostructures", Journal of Vacuum Science and Technology, vol. 31, issue 3, pp. 03C105, May 2013.

2011

1 **P. Grant**, A. Bachri, and A. Goldschmidt. "Analysis of Gamma Rays and Cosmic Muons with a Single Detector", The Journal of the Arkansas Academy of Science, vol. 64, pp. 27-32, 2011.

ii. Articles and Abstracts in Conference Proceedings

2018

19 **Perry C. Grant**, Joshua M. Grant, Wei Dou, Bader Alharthi, Huong Tran, Aboozar Mosleh, Wei Du, Baohua Li, Mansour Mortizavi, Hameed Naseem, Shui-Qing Yu, **"**Growth and characterization of GeSn using UHV-CVD system, submitted to MIOMD-XIV conference, Flagstaff, AZ, OCT 7-10, 2018

18 Wei Dou, Yiyin Zhou, Huong Tran, Thach Pham, **Perry Grant**, Shui-Qing Yu, Seyed Ghetmiri, Aboozar Mosleh, Mansour Mortazavi, Wei Du, Greg Sun, Richard Soref, Joe Maregtis, John Tolle, Boahua Li "Development of SiGeSn Technique Towards Integrated Mid-Infrared Photonics Applications" IEEE Photonics Society Summer Topical Meeting Series (SUM), Waikoloa, HI, July 9-11, 2018

17 Perry **C. Grant,** Joe Margetis, Yiyin Zhou, Wei Dou, Grey Abernathy, Andrian Kuchuk, Wei Du, Seyed A. Ghetmiri, Baohua Li, John Tolle, Jifeng Liu, Greg Sun, Richard A. Soref, Mansour Mortazavi, Shui-Qing Yu, "Direct Bandgap Type-I GeSn Quantum Well toward Si-based Optoelectronics" CLEO: Science and Innovation, San Jose, CA, May 10-15, 2018.

16 Huong Tran, Thach Pham, Wei Du, Yang Zhang, Seyed Amir Ghetmiri, Perry C. Grant, Joshua M. Grant, Greg Sun, Richard A. Soref, Joe Margetis, JohnTolle, Baohua Li, Mansour Mortazavi, and Shui-Qing Yu, "Systematic Study of Ge0.89Sn0.11 Photodiodes for Low-Cost Shortwave Infrared Imaging" CLEO: Science and Innovation, San Jose, CA, May 10-15, 2018.

2017

15 P. **Grant,** W. Dou, B. Alharthi, J. Grant, W. Du, B. Li, M. Mortazavi, H.A. Naseem. "The Growth of Dilute GeSn: A Comparison with Low Temperature Germanium Growth" 59th Annual Electronic Materials Conference, South Bend, IN, Jun 29-30, 2017.

14 B. Alharthi, Joshua M. Grant, Wei Dou, **Perry C. Grant**, Aboozar Mosleh, Wei Du, Mansour Mortazavi, Baohua Li, Hameed Naseem, Shui-Qing Yu, "Low Temperature Ge

Growth Using Plasma Enhanced CVD Technique, 59th Annual Electronic Materials Conference, South Bend, IN, Jun 29-30, 2017.

13 Joe Margetis, John Tolle, Wei Du, Seyed Ghetmiri, Mansour Mortazavi, Sattar Al-Kabi, Yiyin Zhou, Huong Tran, Thach Pham, Wei Dou, **Perry Grant**, Shui-Qing Yu, Greg Sun, Richard Soref, Baohua Li, "GeSn-based light sources and photoconductors towards integrated photonics for the mid-infrared", IEEE Photonics Society Summer Topical Meeting Series (SUM), San Juan, PR, July 10-12, 2017.

12 Thach Pham, Huong Tran, Wei Du, Joe Margetis, Yiyin Zhou, **Perry Grant**, Gregory Sun, Richard Soref, John Tolle, Baohua Li, Mansour Mortazavi, Shui-Qing Yu, "Investigation of Si-based Ge 0.89 Sn 0.11 Photoconductors with 3.0 μm photoresponse", CLEO: Science and Innovation, San Jose, CA, May 14-19, 2017.

2015

11 A. Mosleh, M. Alher, L. Cousar, H. Abu-safe, W. Dou, **P. C. Grant**, S. Al- Kabi,, S.A. Ghetmiri, B. Alharthi, H. Tran, W. Du, M. Benamara, B. Li ,M. Mortazavi, S.-Q. Yu, and H. Naseem, Enhancement of Material Quality of (Si)GeSn Films Grown By $SnCl_4$ Precursor, 2015 ECS fall (228th meeting), October 11-16, Phoenix, AZ (2015).

10 M. Alher, A. Mosleh, L. Cousar, W. Dou, **P. C. Grant**, S.A. Ghetmiri, S. Al-Kabi, W. Du, M. Benamara, B. Li, M. Mortazavi, S.-Q. Yu, and H. A. Naseem, CMOS Compatible Growth of High Quality Ge, SiGe and SiGeSn for Photonic Device Applications, 2015 ECS fall (228th meeting), October 11-16, Phoenix, AZ (2015).

9 Aboozar Mosleh, Murtadha Alher, Wei Du, Larry C. Cousar, Seyed Amir Ghetmiri, Sattar Al-Kabi, Wei Dou, **Perry C. Grant**, Benjamin R. Conley, Greg Sun, Richard A. Soref, Baohua Li, Hameed A. Naseem, and Shui-Qing Yu, Growth and characterization of buffer-free SiGeSn epitaxial layers on Si for photonic applications, 2015 Electronic Material Conference, June 24~26, Columbus, OH (2015).

2014

8 **Perry C. Grant**, Wei Dou, Dongsheng Fan, Yuriy I. Mazur, Vitaliy Dorogan, Shui-Qing Yu, Gregory J. Salamo, Band offsets in GaAs1-xBix ($0<x<3.6\%$) Grown by Molecular Beam Epitaxy, 18th International MBE conference, Flagstaff, Arizona (2014).

2013

7 **P.C. Grant**, D.S. Fan, A. Mosleh, V.G. Dorogan, M.E. Hawkridge, Y.I. Mazur, M. Benamara, S.-Q. Yu, G.J. Salamo, Photoluminescence Studies of the Effects of Rapid Thermal Annealing on Molecular Beam Epitaxy Grown GaAs1-xBix/GaAs Heterostructures, 30th North American Molecular Beam Epitaxy Conference (NAMBE), Banff, Alberta from October 5-11, 2013.

6 **P.C. Grant**, D. Fan, A. Mosleh, M. Hawkridge, Y. Mazur, M. Benemara, V. Dorogan, S.-Q. Yu, G. Salamo, Investigation of Rapid Thermal Annealing on GaAs1-xBix/GaAs

Heterostructures, 4th International Workshop on Bismuth-Containing Semiconductors (4th BCS), Fayetteville, AR, USA, July 14-17, 2013.

2012

5 D. Fan, Z. Zeng, X. Hu, V.G. Dorogan, Y. Hirono, C. Li, **P. C. Grant**, M. Benamara, M. Hawkridge, Y.I. Mazur, S.-Q. Yu, S.R. Johnson, Z.M. Wang, G.J. Salamo, High Optical Quality GaAsBi/GaAs/AlGaAs Separate Confinement Heterostructures, 17th International Conference on Molecular Beam Epitaxy (MBE 2012), Nara, Japan, September 23-28, 2012.

4 D. Fan, Z. Zeng, X. Hu, V. G. Dorogan, Y. Hirono, C. Li, **P. C. Grant**, M. Benamara, M. E. Hawkridge, Yu, I. Mazur, S.-Q. Yu, S. R. Johnson, Zh. M. Wang, and G. J. Salamo, Molecular Beam Epitaxy Growth of GaAsBi/GaAs/AlGaAs Separate Confinement Heterostructures, 3rd International Workshop on Bismuth-Containing Semiconductors (3rd BCS), Victoria B.C., Canada, July 15-18, 2012.

3 D. Fan, **P. C. Grant**, Z. Zeng, X. Hu, C. Li, V. G. Dorogan, M. E. Hawkridge, Yu, I. Mazur, S.-Q. Yu, S. R. Johnson, Zh. M. Wang, and G. J. Salamo, GaAsBi/GaAs Multiple Quantum Wells Grown by Molecular Beam Epitaxy, 29th North American Molecular Beam Epitaxy Conference (NAMBE), Atlanta GA, October 14-17, 2012.

2010

2 **P. Grant**, A. Bachri, and A. Goldschmidt. “Background from Low Energy Neutrons in a High-Pressure Xenon Time Projection Chamber for Neutrinoless Double Beta Decay”, Arkansas INBRE Conference, Fayetteville, AR, October 2010.

1 **P.Grant**, A. Bachri, and A. Goldschmidt. “Analysis of Gamma Rays and Cosmic Muons with a Single Detector”, Arkansas Academy of Science, Little Rock, AR, March 2010.

Appendix H: Publishing Agreements/Permissions

JVSTB

Article re-use permission for Dissertation
AIPRights Permissions <Rights@aip.org>

Mon 11/26, 9:42 AM

Perry Grant

Dear Dr. Grant:

Thank you for requesting permission to reproduce material from AVS publications.

Material to be reproduced:

"Comparison study of the low temperature growth of dilute GeSn and Ge" P.C. Grant, W. Dou, B. Alharthi, J. M. Grant, A. Mosleh, W. Du, B. Li, M. Mortazavi, H. A. Naseem, S.-Q. Yu,
JVST (B), vol 35, no. 6, 061204, (2017)

For use in the following manner:

Reproduced in your dissertation.

Permission is granted subject to these conditions:

1. The AVS grants you non-exclusive world rights in all languages and media. This permission extends to all subsequent and future editions of the new work.

2. The following notice must appear with the material (please fill in the citation information):

"Reproduced from [FULL CITATION], with the permission of the American Vacuum Society."

When reusing a full article, the notice must be printed on the first page of the reprinted article or book chapter.

3. If the material is published in electronic format, we ask that a link be created pointing back to the abstract of the article on the journal website using the article's DOI.

4. This permission does not apply to any materials credited to another source.

For the second article, "Direct bandgap type-I GeSn/GeSn quantum well on a GeSn- and Ge- buffered Si substrate," from AIP Advances, vol. 8, no. 2, (2018), no formal permission is needed as the article was published open access under a Creative Commons CC BY license, the terms of which do not require

written permission for reuse.

Please let us know if you have any questions.

Sincerely,
Susann Brailey
Manager, Rights & Permissions

AIP Publishing
1305 Walt Whitman Road | Suite 300 | Melville NY 11747-4300 | USA
t +1.516.576.2268
rights@aip.org | [publishing.aip.org]publishing.aip.org
Follow us: Facebook | **Twitter** | **LinkedIn**

AIP Advances

This License to Publish must be signed, either electronically within the Peer X-Press manuscript submission system, or as a PDF to be uploaded into Peer X-Press as an alternate form, before the manuscript can be published. If you have questions about how to submit the form, please contact the journal's editorial office. For questions regarding the copyright terms and conditions of this License, please contact AIP Publishing LLC's Office of Rights and Permissions, 1305 Walt Whitman Road, Suite 300, Melville, NY 11747-4300 USA; Phone 516-576-2268; Email: rights@aip.org.
Article Title ("Work"):
____
____
(Please indicate the final title of the Work. Any substantive changes made to the title after acceptance of the Work may require the completion of a new agreement.)
All Author(s):
____
____
(Please list **al**l the authors' names in order as they will appear in the Work. All listed authors must be fully deserving of authorship and no such authors should be omitted. For large groups of authors, attach a separate list to this form.)
Journal: ____
Manuscript ID# ____
All Copyright Owner(s), if not Author(s):
____
____
(Please list **al**l copyright owner(s) by name. In the case of a Work Made for Hire, the employer(s) or commissioning party(ies) are the copyright owner(s). For large groups of copyright owners, attach a separate list to this form.)

Copyright Ownership and Grant of Rights

For the purposes of this License, the "Work" consists of all content within the article itself and made available as part of the article, including but not limited to the abstract, tables, figures, graphs, images, and multimedia files, as well as any subsequent errata. The Work refers to the content contained in both the Accepted Manuscript (AM) and the Version of Record (VOR). "Supplementary Material" consists of material that is associated with the article but linked to or accessed separately (available electronically only), including but not limited to data sets and any additional files.
This Agreement is an Exclusive License to Publish not a Transfer of Copyright. Copyright to the Work remains with the Author(s) or, in the case of a Work Made for Hire, with the Author(s)' employer(s). AIP Publishing LLC shall own and have the right to register in its name the copyright to the journal issue or any other collective work in which the Work is included. Any rights granted under this License are contingent upon acceptance of the Work for publication by AIP Publishing. If for any reason and at its own discretion AIP Publishing decides not to publish the Work, this License is considered void.
Each Copyright Owner hereby grants to AIP Publishing LLC the following irrevocable rights for the full term of United States and foreign copyrights (including any extensions):
1. The exclusive right and license to publish, reproduce, distribute, transmit, display, store, translate, edit, adapt, and create derivative works from the Work (in whole or in part) throughout the world in all formats and media whether now known or later developed, and the nonexclusive right and license to do the same with the Supplementary Material.
2. The right for AIP Publishing to freely transfer and/or sublicense any or all of the exclusive rights listed in #1 above. Sublicensing includes the right to authorize requests for reuse of the Work by third parties.
3. The right for AIP Publishing to take whatever steps it considers necessary to protect and enforce, at its own expense, the exclusive rights granted herein against third

parties.

Author Rights and Permitted Uses

Subject to the rights herein granted to AIP Publishing, each Copyright Owner retains ownership of copyright and all other proprietary rights such as patent rights in the Work.

Each Copyright Owner retains the following nonexclusive rights to use the Work, without obtaining permission from AIP Publishing, in keeping with professional publication ethics, and provided clear credit is given to its first publication in an AIP Publishing journal. Any reuse must include a full credit line acknowledging AIP Publishing's publication and a link to the VOR on AIP Publishing's site.

Each Copyright Owner may:

1. Reprint portions of the Work (excerpts, figures, tables) in future works created by the Author, in keeping with professional publication ethics.
2. Post the Accepted Manuscript (AM) to their personal web page or their employer's web page immediately after acceptance by AIP Publishing.
3. Deposit the AM in an institutional or funder-designated repository immediately after acceptance by AIP Publishing.
4. Use the AM for posting within scientific collaboration networks (SCNs). For a detailed description of our policy on posting to SCNs, please see our Web Posting Guidelines (https://publishing.aip.org/authors/web-posting-guidelines).
5. Reprint the Version of Record (VOR) in print collections written by the Author, or in the Author's thesis or dissertation. It is understood and agreed that the thesis or dissertation may be made available electronically on the university's site or in its repository and that copies may be offered for sale on demand.
6. Reproduce copies of the VOR for courses taught by the Author or offered at the institution where the Author is employed, provided no fee is charged for access to the Work.
7. Use the VOR for internal training and noncommercial business purposes by the Author's employer.
8. Use the VOR in oral presentations made by the Author, such as at conferences, meetings, seminars, etc., provided those receiving copies are informed that they may not further copy or distribute the Work.
9. Distribute the VOR to colleagues for noncommercial scholarly use, provided those receiving copies are informed that they may not further copy or distribute the Work.
10. Post the VOR to their personal web page or their employer's web page 12 months after publication by AIP Publishing.
11. Deposit the VOR in an institutional or funder-designated repository 12 months after publication by AIP Publishing.
12. Update a prior posting with the VOR on a noncommercial server such as arXiv, 12 months after publication by AIP Publishing.

Author Warranties

Each Author and Copyright Owner represents and warrants to AIP Publishing the following:

1. The Work is the original independent creation of each Author and does not infringe any copyright or violate any other right of any third party.
2. The Work has not been previously published and is not being considered for publication elsewhere in any form, except as a preprint on a noncommercial server such as arXiv, or in a thesis or dissertation.
3. Written permission has been obtained for any material used from other sources, and copies of the permission grants have been supplied to AIP Publishing to be included in the manuscript file.
4. All third-party material for which permission has been obtained has been properly credited within the manuscript.
5. In the event that an Author is subject to university open access policies or other institutional restrictions that conflict with any of the rights or provisions of this License, such Author has obtained the necessary waiver from his or her university or institution.

This License must be signed by the Author(s) and, in the case of a Work Made for Hire, also by the Copyright Owners. One Author/Copyright Owner may sign on behalf of all the contributors/owners only if they all have authorized the signing, approved of the License, and agreed to be bound by it. The signing Author and, in the case of a Work Made for Hire, the signing Copyright Owner warrants that he/she/it has full authority to enter into this License and to make the grants this License contains.

1. The Author must please sign here (*except* if an Author is a U.S. Government employee, then please sign under #3 below):

Author Signature Print Name Date

2. The Copyright Owner (if different from the Author) must please sign here:

Name of Copyright Owner Authorized Signature and Title Date

3. If an Author is a U.S. Government employee, such Author must please sign below.

The signing Author certifies that the Work was written as part of his/her official duties and is therefore not eligible for copyright protection in the United States.

Name of U.S. Government Institution (e.g., Naval Research Laboratory, NIST)

Author Signature Print Name Date

PLEASE NOTE: NATIONAL LABORATORIES THAT ARE SPONSORED BY U.S. GOVERNMENT AGENCIES BUT ARE INDEPENDENTLY RUN ARE NOT CONSIDERED GOVERNMENT INSTITUTIONS. (For example, Argonne, Brookhaven, Lawrence Livermore, Sandia, and others.) Authors at these types of institutions should sign under #1 or #2 above.

If the Work was authored under a U.S. Government contract, and the U.S. Government wishes to retain for itself and others acting on its behalf, a paid-up, nonexclusive, irrevocable, worldwide license in the Work to reproduce, prepare derivative works from, distribute copies to the public, perform publicly, and display publicly, by or on behalf of the Government, please check the box below and add the relevant Contract numbers.

- Contract #(s**)** ____ **[1.16.1]**

Nanotechnology

Assignment of copyright and publication agreement IOP Publishing Limited (“IOP”) agrees to publish:
Manuscript Title: Study of Direct Bandgap Type-I GeSn/GeSn Double Quantum Well with Improved Carrier Confinement (the “Article”) written by
Names of all authors: Grant, Perry; Margetis, Joe; Du, Wei; Zhou, Yiyin; Dou, Wei; Abernathy, Grey; Kuchuk, Andrian; Li, Baohua; Tolle, John; Liu, Jifeng; Sun, Greg; Soref, Richard; Mortazavi, Mansour; Yu, Shui-Qing (“the Named Authors”) in the following journal
Nanotechnology (“the Journal”)
Name of copyright owner(s) (if not the Named Author(s) – see Important Information above):
(“the Copyright Owner”)

IOP Ref: NANO-117955.R1

Part 1 - Publication on a Subscription basis
1.1 In consideration for acceptance and publication of the Article, the Named Authors of the Article and/or the Copyright Owner hereby assign, where necessary by present assignment of future copyright, to IOP with full title guarantee the entire copyright in all original material published as part of the Article (which expression includes but is not limited to the text, abstract, tables, figures and graphs, related corrigenda or “comments” and multimedia content but excludes any other item referred to as supplementary material and/or any video abstract) throughout the world for the full term of copyright (including any extensions or renewals thereof) for all media and formats, whether known or unknown.
Such assignment shall be effective only if the Article (or any resubmission of the Article) is accepted for publication. For the avoidance of doubt, copyright does not subsist in any fundamental data underlying the Article and nothing in this agreement is intended to limit access to or use of such data.
1.2 If the Article, or any part of it, is protected by Crown copyright, in consideration for acceptance and publication of the Article, the relevant Named Authors and the relevant originating department or agency hereby grant IOP a non-exclusive royalty-free worldwide freely-transferrable licence for the full term of copyright (including any extensions or renewals thereof) for all media and formats, whether known or unknown, to do in relation to the Article all acts restricted by copyright worldwide including, but not limited to, the right of action under section 101A of the Copyright Designs and Patents Act 1988. Such licence shall be effective only if the Article is accepted for publication.
1.3 If all the Named Authors are employees of the US Government, they represent and warrant to IOP that the Article was prepared as part of their official duties. In such circumstances, or where the Article was created as part of a work for hire, none of the original content within the Article is subject to copyright protection as it is in the public domain.
1.4 In consideration for acceptance and publication of the Article, the Named Authors

and/or the Copyright Owner hereby grant IOP a royalty-free non-exclusive worldwide freely transferrable licence for the full term of copyright (including any extensions or renewals thereof) to do in relation to any supplementary material not deemed to be part of the Article and/or any video abstract all acts restricted by copyright worldwide. This shall include, but not be limited to, making the material available under any licence that IOP deems appropriate for purposes including, but not limited to, the maximisation of visibility and the long term preservation of the content.
1.5 Each of the Named Authors consents to all publication and processing of their personal data by IOP, as that data is displayed on the Article, including, but not limited to, the names and email addresses of the Named Authors. Accordingly, the Named Authors shall not object on data protection grounds to the use of their personal data on the Article wherever IOP chooses to display it, whether itself or via a third party.

Representations and warranties
2.1 The Copyright Owner and/or the Submitting Author on behalf of the Named Authors (as appropriate) represent and warrant that:
2.1.1 the Article is the original work of the Named Authors;
2.1.2 the Article has not been published previously in any form, other than in accordance with our Preprint pre-publication policy;
2.1.3 each of the Named Authors has made a material contribution to the conception and/or writing of the Article, has received the final version of the Article, has agreed to its submission on the terms contained herein and takes responsibility for it and submission has been approved as necessary by the authorities at the establishment where the research was carried out;
2.1.4 the Submitting Author completes and returns this agreement as authorised agent for and on behalf of all the Named Authors and the Copyright Owner (as applicable) and has the full power to enter into this agreement and to make the grants and assignments it contains;
2.1.5 the Article has not been and shall not be submitted to another publisher prior to withdrawal or rejection by IOP;
2.1.6 the Article does not infringe any third party rights, it contains nothing libellous or unlawful, all factual statements are to the best of the Named Authors' knowledge true or based on valid research conducted according to accepted norms and all required permissions have been obtained in writing;
2.1.7 the Article expressly acknowledges any third party funding and/or potential conflicts of interest; and
2.1.8 any supplementary material or video abstract is the original work of the Named Authors, or is the property of the Copyright Owner, or permission has been obtained from its owner(s) for its publication by IOP and permission has been obtained for the inclusion of any third party content.
2.2 The Named Authors and/or the Copyright Owner (as appropriate) indemnify and will keep indemnified IOP against all costs and expenses suffered or incurred by IOP as a result of and/or arising out of any breach of the representations and/or warranties in this section 2.

The Named Authors' rights

3.1 IOP grants the Named Authors the rights specified in paragraphs 3.2 and 3.3. All such rights must be exercised solely for non-commercial purposes. Where possible, any use should display citation information and IOP's copyright notice, and, for electronic use, best efforts must be made to include a link to the online abstract in the Journal. Exercise of the rights in paragraph 3.2 may use the peer reviewed, edited, formatted and typeset version of the Article including any tagging, indexing and other enhancements published by IOP and/or its licensors ("Final Published Version").
Exercise of the rights referred to in paragraph 3.3 must not use the Final Published Version and extend only to the version of the Article accepted for publication including all changes made as a result of the peer review process, and which may also include the addition to the article by IOP of a header, an article ID, a cover sheet and/or an 'Accepted Manuscript' watermark, but excluding any other editing, typesetting or other changes made by IOP and/or its licensors (the "Accepted Manuscript") and must be accompanied by the following statement of provenance:
'This is the Accepted Manuscript version of an article accepted for publication in Nanotechnology. IOP Publishing Ltd is not responsible for any errors or omissions in this version of the manuscript or any version derived from it. The Version of Record is available online at [insert DOI].'
3.2 The rights are:
3.2.1 To make copies of the Final Published Version of the Article (all or part) for teaching purposes;
3.2.2 To include the Final Published Version of the Article (all or part) in a research thesis or dissertation provided it is not then published commercially;
3.2.3 To make oral presentation of the Final Published Version of the Article (all or part) and to include a summary and/or highlights of it in papers distributed at such presentations or in conference proceedings; and
3.2.4 To use original figures and text from the Final Published Version of the Article falling within the quota outlined in and subject to the STM Permissions Guidelines (http://www.stmassoc.org/permissions-guidelines/) at the relevant time in force.
For the avoidance of doubt, the Named Authors retain all proprietary rights in the Article other than copyright.
3.3 Additional rights of the Named Authors are to:
3.3.1 Use the Accepted Manuscript (all or part) without modification in personal compilations of the Named Authors' own works (provided not created by a third party publisher); and 3.3.2 Include the Accepted Manuscript (all or part) on the Named Authors' own Personal Website(s), institutional website(s), repositories, Scientific Social Networks and third party websites provided that this is fully in accordance with the Author Rights set out at the following url legal.ioppublishing.org/author-rights on the date of submission of the agreement.

Miscellaneous
4. To the extent that there are moral rights in the Article, all the Named Authors expressly reserve and assert their moral rights to be identified as the authors of the Article.
5. The Named Authors and/or the Copyright Owner shall execute such further documents, and take such actions and do such things, as may be requested by IOP at IOP's reasonable expense to give full effect to the terms of the agreement.

6. For the avoidance of doubt, the grants and assignment envisaged herein shall become effective only upon acceptance of the Article for publication. In the event that the Article is withdrawn prior to acceptance, or is rejected, this agreement shall have no effect and no party shall be bound by it.
7. The agreement shall be governed by English Law and subject to the non-exclusive jurisdiction of the English courts.

Confirmation
8. By selecting to publish on a subscription basis, the Submitting Author is responsible for ensuring that, where relevant all Named Authors, who are affiliated to a university/institution which has an open access policy which is incompatible with IOP's green open access policy, obtain a waiver for the Article from their institution or university's open access policy and retain such waiver as evidence of compliance. These Named Authors agree that they shall obtain such waivers and provide them to IOP promptly on request.
9. By typing the Submitting Author's name into the box at Part 3 below and clicking "Submit", the Named Authors agree to these terms. The Authorised Signatories of any third party Copyright Owner(s) and/or the Submitting Author agree, on behalf of such Copyright Owner(s), to these terms by typing the Copyright Owner's name into the "Copyright Owner" box at the top of the page.